Università degli Studi di Ferrara

DOCTORAL COURSE IN
ENGINEERING SCIENCE
CIVIL ENGINEERING CURRICULUM
CYCLE XXXII

Director: Prof. Stefano TRILLO

1D augmented fluid-structure interaction systems with viscoelasticity: from water pipelines to blood vessels

---

SCIENTIFIC/DISCIPLINARY SECTOR (SDS) ICAR/01

Candidate:
Giulia BERTAGLIA

Supervisors:
Prof. Alessandro VALIANI

Prof. Valerio CALEFFI

Years 2016/2019

"Learn how to see.
Realize that everything connects to everything else."

Leonardo da Vinci

Abstract

Nowadays, mathematical models and numerical simulations are widely used in the whole fluid dynamics research field. They represent a powerful resource to better understand phenomena and processes and to significantly reduce the costs that would otherwise be necessary for carrying out laboratory experiments (sometimes even allowing to obtain useful data that could not be collected by measurements).
Currently there are many important industries of hydraulic systems which, for the correct analysis of the behavior of the designed systems, require the preventive use of an accurate mathematical model, able to describe the trend of the properties of the fluid in the pipelines. On the other hand, the availability of robust and efficient mathematical instruments, together with the engineering know-how in the fluid mechanics sector, represents an invaluable tool for a consistent support even in hemodynamics studies, providing practical approaches for the quantification of variables involved in the cardiovascular fluid dynamics.
The correct characterization of the interactions occurring between the fluid and the wall that circumscribes the motion of the fluid itself, is a fundamental aspect in all the contexts involving deformable ducts, which requires the utmost attention at every stage of both the development of the computational scheme and the interpretation of the results and at their application to cases of practical interest.
In this PhD Thesis, innovative mathematical models able to predict the behavior of the fluid-structure interaction mechanism that underlies the dynamics of flows in different compliant ducts is presented. Starting from the purely civil engineering sector, with the study of plastic water pipelines, the final application of the proposed tool is linked to the medical research field, to reproduce the mechanics of blood flow in both arteries and veins. With this aim, various linear viscoelastic models, from the simplest to the more sophisticated, have been applied and extended to obtain augmented fluid-structure interaction systems in which the constitutive equation of the material is directly inserted into the system as partial differential equation. These systems are solved recurring to second-order Finite Volume Methods that take into account the recent evolution in the computational literature of hyperbolic balance laws systems. The models have been extensively validated through different types of test cases, highlighting the advantages of using the augmented formulation of the system of equations. Numerical results have been compared with quasi-exact solutions of idealized time-dependent tests for situations close to reality or with reference values obtained with numerical schemes generally adopted in the specific research field investigated. Furthermore, comparisons with experimental data have been considered both for the water pipelines scenario and the blood flow modeling, recurring to ad hoc in-vivo measurements for the latter. Accuracy and efficiency analyses have been performed in different contexts, as well as a sensitivity analysis with regards to the final part of the project, related to a more applicative study on arterial hypertension.

Sommario

Oggigiorno, modelli matematici e simulazioni numeriche sono ampiamente utilizzati nell'intero campo della ricerca fluidodinamica. Essi rappresentano una potente risorsa per comprendere meglio i fenomeni e i processi e per ridurre significativamente i costi che sarebbero altrimenti necessari per la realizzazione di esperimenti di laboratorio (a volte anche per ottenere utili dati che non potrebbero essere raccolti mediante misurazioni).
Attualmente esistono molte importanti industrie di sistemi idraulici che, per la corretta analisi del comportamento dei sistemi progettati, richiedono l'uso preventivo di un accurato modello matematico, in grado di descrivere l'andamento delle proprietà del fluido nelle tubazioni. D'altra parte, la disponibilità di strumenti matematici robusti ed efficienti, insieme al know-how ingegneristico nel settore della fluidodinamica, rappresenta uno strumento inestimabile per un supporto costante anche negli studi emodinamici, fornendo approcci pratici per la quantificazione delle variabili coinvolte nella fluidodinamica cardiovascolare.
La corretta caratterizzazione delle interazioni tra il fluido e la parete che ne circoscrive il moto, è un aspetto fondamentale in tutti i contesti di condotte deformabili, che richiede la massima attenzione in ogni fase dello sviluppo dello schema di calcolo e della interpretazione dei risultati e nella loro applicazione a casi di interesse pratico.
In questa Tesi di Dottorato vengono presentati innovativi modelli matematici in grado di prevedere il comportamento del meccanismo di interazione fluido-struttura che sta alla base della dinamica dei flussi in diverse condotte deformabili. Partendo dal settore dell'ingegneria puramente civile, con lo studio di condotte idrauliche in plastica, l'applicazione finale dello strumento proposto è legata al campo della ricerca medica, per riprodurre la meccanica del flusso sanguigno sia nelle arterie che nelle vene. A tal fine, sono stati applicati ed estesi diversi modelli viscoelastici lineari, dai più semplici ai più sofisticati, per ottenere sistemi aumentati di interazione fluido-struttura in cui l'equazione costitutiva del materiale è direttamente inserita nel sistema come equazione alle derivate parziali. Questi sistemi sono risolti ricorrendo a Metodi ai Volumi Finiti al secondo ordine che tengono conto della recente evoluzione della letteratura computazionale dei sistemi iperbolici di leggi di bilancio. I modelli sono stati ampiamente validati attraverso diversi tipi di casi test, evidenziando i vantaggi dell'utilizzo del sistema di equazioni in forma aumentata. I risultati numerici sono stati confrontati con soluzioni quasi esatte di problemi ideali dipendenti dal tempo per situazioni vicine alla realtà o con valori di riferimento ottenuti con schemi numerici adottati solitamente nello specifico campo di ricerca indagato. Inoltre, sono stati presi in considerazione confronti con dati sperimentali sia per lo scenario delle condotte idriche che per la modellazione del flusso sanguigno, ricorrendo a misurazioni in-vivo ad hoc per quest'ultimo. Sono state effettuate analisi di accuratezza ed efficienza in diversi contesti, nonché un'analisi di sensitività per quanto riguarda la parte finale del progetto, relativa ad uno studio più applicativo sull'ipertensione arteriosa.

Acknowledgements

First and foremost, I would like to thank my family, for the continuous support they showed me. Thank you, in particular, to my parents, for having always given me the opportunity to choose my future, knowing how to direct me, as only a parent can do, towards the path that best suits me without ever invading my freedom. I would like to dedicate a special thanks to my dad, because he has always been my very first fan. You and mom have always believed in my abilities, more than I have ever believed in myself, always encouraging me to achieve my goals. I will be grateful to you for that forever.

Thanks to my fantastic sister, who was able to console me those nights that I came home dejected, for making me laugh even during the most difficult days, and for always being the first to celebrate my successes with. The two years of my PhD spent under the same rooftop with you only are undoubtedly part of the moments that I will always lovingly remember in life.

A huge thank you goes to all of my friends, from the lifelong ones to the last ones who entered in my life. I honestly believe to be surrounded by the most wonderful people in the world and I know that I have had a great fortune in this. Thanks especially to the most adorable, hilarious and supportive friends ever, Ale e Frency, because they have always been there for me, and I know they always will.

A thought goes to Marco, who (I still don't know how) managed to withstand all my mood swings, remaining by my side even when I myself could no longer stand me anymore. Thank you for your constant love and support and for always putting our well-being first.

I am very grateful to my supervisors, Prof. A. Valiani and Prof. V. Caleffi, first of all for giving me the chance to join this PhD program with your oversight. Thank you for always having an open door for me, for the many fruitful conversations and for the time you have devoted to help me. I feel deeply enriched by everything I have learned from you in these years and I sincerely feel lucky to have had you as tutors.

I would like to thank Prof. J. Murillo and Prof. P. Garcia-Navarro for welcoming me to the Department of Science and Technology of Materials and Fluids (EINA) of the University of Zaragoza for my visiting period. My stay at your institute and the work carried out in Zaragoza has been an essential part of this research project. A special thanks goes to Eng. A. Navas-Montilla, Ph.D., and the whole GHC research group of the University of Zaragoza, for making me incredibly enjoy the months spent there. It would have never been so amazing without the continuous support and contagious willingness of each one of you. You made me feel at home from the very first moment, and this is priceless.

I am pleased to acknowledge Dr. M. I. Monge García (Intensive Care Unit, Hospital SAS, Jerez de la Frontera) for offering me the opportunity to visit the Intensive Care Unit of the Hospital SAS of Jerez and for collecting in-vivo Doppler and tonometer measurements used in this work. Thank you also for the inspiring discussion about the research world we had while sipping a cup of coffee.

I would like to express my sincere appreciation to Prof. E. F. Toro (Laboratory of Applied Mathematics, University of Trento) and Eng. L. O. Müller, Ph.D. (Department of Mathematics, University of Trento), for permitting me to use the global blood flow model and for the willingness shown in sharing your deep knowledge with me. All the discussions with you have been a great starting point for me to enter into the blood flow modeling research and to realize the multitude of applications related to this field. Thank you also to M. Celant for the valuable work done in support of the research project on the Selfish Brain Hypotesis presented in this Thesis.

I would like to warmly thank Prof. L. Pareschi (Department of Mathematics, University of Ferrara) for the very helpful and dispassionate discussions that contributed to the linearization of the IMEX algorithm presented in this Thesis.

I would like to acknowledge the assistance of Prof. M. Dumbser (Department of Civil, Environmental and Mechanical Engineering, University of Trento), for the advices on problems and doubts encountered during part of the water pipeline project, and Eng. M. Ioriatti, Ph.D. (Department of Civil, Environmental and Mechanical Engineering, University of Trento), for the precious work on the Semi-Implicit method and on the ODE friction model discussed in this Thesis.

I would like to express my gratefulness to Eng. A. Leopardi, Ph.D., and Prof. G. de Marinis (Department of Civil and Mechanical Engineering, University of Cassino and Southern Lazio) for providing the experimental data of the water hammer problems used in this work and to Prof. S. Alvisi (Department of Engineering, University of Ferrara) for sharing the SCE-UA algorithm, written in MATLAB Language, adopted for part of the calibrations.

Finally, I would like to thank all the PhD colleagues and young researchers I had the privilege to meet during these years. Thank you for not only being colleagues, but also friends, and for making my workspace such a cozy place to be. Each one of you, in one way or another, has been able to give me a little extra energy to achieve the ultimate goal. If the research world is so stimulating it is mainly thanks to the people who represent it.

Contents

Scientific production

Journal articles published during this PhD research project:

Bertaglia, G., A. Navas-Montilla, A. Valiani, M. I. Monge García, J. Murillo, and V. Caleffi (2020). "Computational hemodynamics in arteries with the one-dimensional augmented fluid-structure interaction system: viscoelastic parameters estimation and comparison with in-vivo data". In: *Journal of Biomechanics* 100.C, 109595.

Bertaglia, G., V. Caleffi, and A. Valiani (2020). "Modeling blood flow in viscoelastic vessels: the 1D augmented fluid-structure interaction system". In: *Computer Methods in Applied Mechanics and Engineering* 360.C, 112772.

Bertaglia, G., M. Ioriatti, A. Valiani, M. Dumbser, and V. Caleffi (2018). "Numerical methods for hydraulic transients in visco-elastic pipes". In: *Journal of Fluids and Structures* 81.C, pp. 230-254.

Conference contributes related to this PhD research project:

Müller, L. O., M. Celant, E. F. Toro, P. J. Blanco, **G. Bertaglia**, V. Caleffi, and A. Valiani (2019). "The Selfish-Brain Hypothesis as possible cause of arterial hypertension: a modeling study". *6th International Conference on Computational and Mathematical Biomedical Engineering*, Tohoku University, Sendai City, Japan.

Bertaglia, G., V. Caleffi, A. Valiani, A. Navas-Montilla, and J. Murillo (2019). "The augmented FSI system for blood flow in viscoelastic vessels solved with IMEX schemes". *Workshop on Efficient high-order time discretization methods for PDEs*, Villa Orlandi, Anacapri, Italy.

Bertaglia, G., V. Caleffi, and A. Valiani (2019). "Accuracy-preserving IMEX schemes applied to the augmented FSI system for blood flow in viscoelastic vessels". *European Workshop on High Order Numerical Methods for Evolutionary PDEs: Theory and Applications*, Escuela Técnica Superior de Ingenieros de Minas y Energía, Universidad Politécnica de Madrid, Spain.

Bertaglia, G., M. Ioriatti, A. Valiani, M. Dumbser, and V. Caleffi (2018). "Modelli numerici per lo studio di fenomeni transitori idraulici in condotte viscoelastiche". *XXXVI Convegno Nazionale di Idraulica e Costruzioni Idrauliche*, Universitá Politecnica delle Marche, Ancona, Italy.

Bertaglia, G., A. Valiani, and V. Caleffi (2018). "The augmented FSI system for blood flow in compliant vessels". *5th IAHR Europe Congress, New challenges in hydraulic research and engineering*, University of Trento, Italy.

Bertaglia, G., M. Ioriatti, A. Valiani, M. Dumbser, and V. Caleffi (2018). "A comparison of numerical methods for compressible flows in viscoelastic pipes". *5th IAHR Europe Congress, New challenges in hydraulic research and engineering*, University of Trento, Italy.

Bertaglia, G., M. Ioriatti, A. Valiani, M. Dumbser, and V. Caleffi (2018). "Numerical methods for compressible flows in compliant tubes". *Workshop on Numerical Aspects of Hyperbolic Balance Laws and Related Problems*, University of Ferrara, Italy.

List of Figures

List of Tables

List of Abbreviations

1D	**1**-**D**imensional
3D	**3**-**D**imensional
ADER	**A**rbitrary high-order **DER**ivatives
a-FSI	**a**ugmented **F**luid-**S**tructure **I**nteraction
AP	**A**symptotic **P**reserving
BA	**B**asilar **A**rtery
BSA	**B**ody **S**urface **A**rea
CCA	**C**ommon **C**arotid **A**rtery
CFA	**C**ommon **F**emoral **A**rtery
cfPWV	**c**arotid-**f**emoral **P**ulse **W**ave **V**elocity
CI	**C**ardiac **I**ndex
CO	**C**ardiac **O**utput
CoW	**C**ircle **o**f **W**illis
CSF	**C**erebro**s**pinal **F**luid
CPU	**C**entral **P**rocessing **U**nit
CVR	**C**erebro**v**ascular **R**esistance
DOT	**D**umbser-**O**sher -**T**oro
EKG	**E**lectrocardio**g**raphy
EOS	**E**quation **O**f **S**tate
ESC	**E**uropean **S**ociety of **C**ardiology
ESH	**E**uropean **S**ociety of **H**ypertension
FSI	**F**luid-**S**tructure **I**nteraction
FVM	**F**inite **V**olume **M**ethod
g-KV	**g**eneralized **K**elvin-**V**oigt
HDPE	**H**igh-**D**ensity **P**oly**e**thylene
HR	**H**eart **R**ate
HTN	**H**yper**ten**sive
IMEX	**IM**plicit-**EX**plicit
KV	**K**elvin-**V**oigt
LD	**L**inearly **D**egenerate
LSE	**L**east **S**quare **E**rror
LTS	**L**ocal **T**ime **S**tepping
MAP	**M**ean **A**rterial **P**ressure
MMS	**M**ethod of **M**anufactured **S**olutions
MOC	**M**ethod **O**f **C**haracteristics
MX	**M**ax**x**ell
NTN	**N**ormo**ten**sive
NTS	**N**ucleus **T**ractus **S**olitarii
ODE	**O**rdinary **D**ifferential **E**quation
PcoA	**P**osterior **co**mmunicating **A**rtery
PDE	**P**artial **D**ifferential **E**quation

PE	**P**oly**e**thylene
PVC	**P**oly**v**inyl **C**hloride
RI	**R**iemann **I**nvariant
RK	**R**unge-**K**utta
RP	**R**iemann **P**roblem
SCE-UA	**S**huffled **C**omplex **E**volution - **U**niversity of **A**rizona
SI	**S**emi-**I**mplicit
SLS	**S**tandard **L**inear **S**olid
SSP	**S**trong-**S**tability-**P**reserving
TA	**T**horacic **A**orta
TVD	**T**otal **V**ariation **D**iminishing
VA	**V**ertebral **A**rtery
VAH	**V**ertebral **A**rtery **H**ypoplasia
VMC	**V**aso**m**otor **C**enter

List of Symbols

A	area	m^2
A_0	equilibrium area	m^2
$A^{(*)}$	parameter of the weighting function	-
a	wave speed/celerity	$m\ s^{-1}$
$B^{(*)}$	parameter of the weighting function	-
C	capacitance related to the wall compliance in the RCR circuit	$Pa^{-1}\ m^3\ (kg^{-1}\ m^4\ s^2)$
CFL	Courant-Friedrichs-Lewy number	-
c	celerity contribute related to fluid-structure interaction	$m\ s^{-1}$
c_0	reference celerity	$m\ s^{-1}$
c_s	speed of sound	$m\ s^{-1}$
c_s'	celerity contribute related to fluid compressibility	$m\ s^{-1}$
D	diameter	m
D_0	equilibrium diameter	m
E	Young/elastic modulus of the material	$Pa\ (kg\ m^{-1}\ s^{-2})$
E_0	instantaneous Young/elastic modulus of the material	$Pa\ (kg\ m^{-1}\ s^{-2})$
E_∞	asymptotic Young/elastic modulus of the material	$Pa\ (kg\ m^{-1}\ s^{-2})$
F_R	friction term	$Pa\ m\ (kg\ s^{-2})$
f	friction factor	-
g	gravity acceleration	$m\ s^{-2}$
H	total head	m
$\mathcal{H}$	Heaviside step function	-
h	piezometric head	m
h_0	equilibrium piezometric head	m
J	creep of the material	$Pa^{-1}\ (kg^{-1}\ m\ s^2)$
J_0	instantaneous creep of the material	$Pa^{-1}\ (kg^{-1}\ m\ s^2)$
j	frictional head loss coefficient	-
K	stiffness parameter of the pipe/vessel	$Pa\ (kg\ m^{-1}\ s^{-2})$
K_c	cavitation constant	$Pa^{-1}\ (kg^{-1}\ m\ s^2)$
K_e	bulk modulus of elasticity	$Pa\ (kg\ m^{-1}\ s^{-2})$
L	length of the domain	m
$\mathcal{L}$	inductance related to the fluid inertia in the RCR model	$Pa\ m^{-3}\ s^2\ (kg\ m^{-4})$
m	vessel wall parameter	-
$m^{(*)}$	coefficient of the weighting function	-
N_G	number of nodes of the Gauss-Legendre quadrature	-
N_{KV}	number of Kelvin-Voigt units	-
N_w	number of weighting points	-
N_x	number of cells in the mesh	-
n	vessel wall parameter	-
$n^{(*)}$	coefficient of the weighting function	-
P	ratio between diffusion and wave time scale in a pipe	-

p	pressure	Pa (kg m^{-1} s^{-2})
p_0	equilibrium pressure	Pa (kg m^{-1} s^{-2})
p_C	pressure at the capacitor in the RCR model	Pa (kg m^{-1} s^{-2})
p_D	diastolic pressure	Pa (kg m^{-1} s^{-2})
p_{el}	elastic component of the pressure	Pa (kg m^{-1} s^{-2})
p_{ext}	external pressure	Pa (kg m^{-1} s^{-2})
p_{IC}	intracranial pressure	Pa (kg m^{-1} s^{-2})
p_{out}	outlet pressure	Pa (kg m^{-1} s^{-2})
p_S	systolic pressure	Pa (kg m^{-1} s^{-2})
p_v	vapor pressure	Pa (kg m^{-1} s^{-2})
q	flow rate	m^3 s^{-1}
q_{in}	inlet flow rate	m^3 s^{-1}
q_{out}	outlet flow rate	m^3 s^{-1}
R	inner radius	m
R_0	equilibrium inner radius	m
$R_{0,in}$	equilibrium inner radius at the inlet	m
$R_{0,out}$	equilibrium inner radius at the outlet	m
R_1	first resistance related to the fluid viscosity in the RCR circuit	Pa m^{-3} s (kg m^{-4} s^{-1})
R_2	second resistance related to the fluid viscosity in the RCR circuit	Pa m^{-3} s (kg m^{-4} s^{-1})
R_e	external radius	m
R_T	total viscous resistance of the flow in the RCR circuit	Pa m^{-3} s (kg m^{-4} s^{-1})
R_v	gas constant	K^{-1} m^2 s^{-2}
Re	Reynolds number	-
r	radial coordinate	m
s	node of the Gauss-Legendre quadrature	-
s_0	thickness	m
T_0	reference temperature	K
t	time variable	s
t_{end}	final time	s
t'	integral variable of time	s
u	velocity	m s^{-1}
u_0	initial velocity	m s^{-1}
u_{in}	inlet velocity	m s^{-1}
W	geometry parameter of the pipe/vessel	-
w	weighting function	-
x	space variable	m
Z_0	characteristic impedance of the vessel	Pa m^{-3} s (kg m^{-4} s^{-1})
α	adimensional area	-
α_c	Coriolis coefficient	-
α_{pc}	adimensional axial pipe-constraint parameter	-
Γ	viscous parameter of the vessel wall in the Kelvin-Voigt model	kg s^{-1}
Δx	mesh spacing size	m
Δt	time step size	s
ϵ	strain	-
ϵ_D	strain related to the dashpot	-
ϵ_e	elastic/instantaneous strain	-
ϵ_r	retarded strain	-
ζ	polynomial order of the friction model	-

η	viscosity coefficient of the material	Pa s (kg m^{-1} s^{-1})
θ	implicitness parameter of the θ-method	-
μ	dynamic viscosity of the fluid	Pa s (kg m^{-1} s^{-1})
ν	kinematic viscosity of the fluid	m^2 s^{-1}
ν_p	Poisson's ratio	-
ξ	celerity of the shock wave	m s^{-1}
ρ	density	kg m^{-3}
ρ_0	reference density	kg m^{-3}
ρ_v	vapor density	kg m^{-3}
σ	stress	Pa (kg m^{-1} s^{-2})
σ_D	stress related to the dashpot	Pa (kg m^{-1} s^{-2})
τ_c	creep/retardation time of the material	s
τ_r	relaxation time of the material	s
τ_s	quasi-steady wall shear stress	Pa (kg m^{-1} s^{-2})
τ_u	unsteady wall shear stress	Pa (kg m^{-1} s^{-2})
τ_w	wall shear stress	Pa (kg m^{-1} s^{-2})
φ	mass fraction of vapor	-
ψ_{el}	elastic contribute of the transmural pressure	Pa (kg m^{-1} s^{-2})
ω	weight of the Gauss-Legendre quadrature	-

To my father,
who knew I was going to be a PhD before I did.

Chapter 1

Introduction

1.1 Background and Motivation

Flexible plastic pipes are playing an increasingly important role in pressurized and non-pressurized hydraulic systems, often being preferred to other materials for the components of most water distribution and sewage networks, due to their cost-effectiveness and ease of installation. Currently there are many important industries of hydraulic systems which, for the correct analysis of the behavior of the systems themselves, require the preventive use of an accurate mathematical model, able to describe the trend of the properties of the fluid in the pipelines already in the design phase. With computational simulations, one must be able to verify the behavior of the networks especially in case of fast hydraulic transients. In addition, due to the increasing complexity of the industrial systems used, it is necessary to have more and more efficient numerical models and simulations, which will ensure the increasingly stringent standards of safety and environmental protection.
The effects of fluid-structure interaction, in situations of hydraulic transients, have not yet been fully studied for pipelines that manifest a complex mechanical behavior. Some researches have been performed with reference to systems consisting of a single pipe, very few investigating the behavior of networks of systems using viscoelastic models (already proven in this context significantly more efficient than linear elastic models), which better take into account the real compliance of the plastic material (Evangelista et al., 2015; Meniconi et al., 2014; Meniconi, Brunone, and Ferrante, 2012; Covas et al., 2004; Covas et al., 2005; Ramos et al., 2004).
The possibility of analyzing the results of mathematical models suitably adaptable to a wide range of mechanical behaviors would have a very strong impact on the industrial level. The most onerous situations of complex pipelines could be verified, possible leakages could be foreseen, pressure involved in the event of water hammers could be defined more precisely, strengthening the guarantee conditions in a functional way, both for producers and purchasers.

The same studies can be applied not only in the case of water supply or drainage systems, but in a wide range of cases in the analysis of fluid dynamics systems. In particular, reference is made to the fact that in the last twenty years, the research in the field of hydrodynamics of pressure waves (and also the research interested by various mathematics fields) approached the research in the medical sector, giving rise to stimulating interactions both in the choice of topics to be investigated and in the refinement of techniques to approach new challenging problems (Alastruey et al., 2011; Alastruey, Parker, and Sherwin, 2012; Müller and Toro, 2013; Müller and Toro, 2014a; Mynard and Smolich, 2015). The knowledge and modeling of computational fluid dynamics, able to give quantitative and not only qualitative responses to the problems studied, have been used, for example,

to support research conducted in support of the analysis of particular diseases still incurable, hypothetically related to abnormalities in the venous system (Toro, 2016). In fact, it has been proven that arteries and veins can be seen, with the due corrections specifically provided by hemodynamics, as highly flexible, viscoelastic tubes, tending almost to collapse under certain physiological conditions in the case of veins, when the transmural pressure reaches negative values (Spiller et al., 2017).
The application of fluid mechanics studies in the development of mathematical models able to reproduce the behavior of the cardiovascular system, would lead to the achievement of essential quantitative results in medical researches. Numerical simulations could indeed provide efficient approaches for the quantification of fluid dynamics phenomena in the cardiovascular network, supplying meaningful data that otherwise would require invasive techniques (or simply would not be available with general clinical measurements) and even help the prediction of the possible onset of diseases and development of pathologies (Liang, Guan, and Alastruey, 2018; Müller et al., 2019).

1.2 Aims and Objectives

This PhD research aims at realizing a mathematical model able to predict different behaviors, first elastic and then viscoelastic, of the fluid-structure mechanism characterizing various flexible ducts. The desired model should be able to provide celerity of the propagating waves, pressure and deformation state of the system, which are the typical features in fluid transients events, as well as to correctly capture, with high resolution, the profiles of the shock waves, rarefactions and contact discontinuities that may occur during these phenomena. The correct characterization of the interactions between the fluid and the wall, when the latter is deformable, is a fundamental aspect of the method, which requires the utmost attention at every stage of both the development of the computational scheme and the interpretation of the results and at their application to cases of practical interest. This goal can be achieved recurring to second-order numerical schemes that take into account the recent evolution in the computational literature concerning hyperbolic balance laws systems.
Starting from the purely civil engineering sector, with the study of plastic water pipelines, the final application of the proposed tool is expected to interact with the field of hemodynamics, to reproduce the behavior of the human cardiovascular network. The most ambitious goal of this research would therefore be part of a multidisciplinary project in which the joint use of mathematics, physics and engineering on the one hand and of physiology and medicine on the other, should contribute to the solution of problems of great interest for the improvement of human health and quality of life for patients suffering from serious diseases or otherwise potentially disabling.

1.3 Thesis Outline

This PhD Thesis is structured in four main Chapters, which guide the reader from a general introduction of the theory underlying the viscoelastic behavior of the materials under interest, to the development of the mathematical model of fluid-structure interactions valid first for water pipelines and then for blood flow in arteries and veins, to the final real application study cases.
In Chapter 2, a necessary overview of the theory of linear viscoelasticity is presented.

The phenomenological aspects underlying the behavior of the wide field of viscoelastic materials are first discussed. Furthermore, the main mathematical models used to simulate linear viscoelastic materials are analyzed. Starting from the Maxwell and the Kelvin-Voigt model, defined by solely two parameters, the discussion ends with the presentation of the generalized Kelvin-Voigt chain, in which the number of base elements (and, by consequence, of the parameters) is extended to allow a more flexible response of the model, possibly closer to the real response of the material.
In Chapter 3, the fluid-structure interaction model of water flow in compliant pipelines is presented, with a specific characterization made for each numerical scheme, constitutive law and friction model adopted for the numerical analyses. An original extension of existing techniques for the numerical treatment of multi-parameter viscoelastic models is also introduced. Three different numerical models are chosen to solve the resulting hyperbolic system of partial differential equations: the standard Method of Characteristics, a second-order Explicit path-conservative Finite Volume Method and a second-order staggered Semi-Implicit Finite Volume Method. After a focused calibration of the viscoelastic parameters involved, the performance of these three schemes is compared in terms of accuracy, efficiency and robustness through different test cases concerning hydraulic transients phenomena, including cross-sectional changes, highly flexible materials and cavitation episodes. Moreover, two water hammer tests in high-density polyethylene pipes are designed to compare numerical solutions with the experimental data provided. A specific Section is entirely dedicated to the analysis of the relevance of the unsteady friction effects, with respect to the quasi-steady ones, and to the validation of the ODE friction model, for the first time applied to turbulent flow cases.
The innovative augmented fluid-structure interaction system of blood flow is derived and discussed in Chapter 4, together with the description of the constitutive laws chosen for the characterization of the vessel wall mechanics, whether elastic or viscoelastic. A second-order Implicit-Explicit Runge-Kutta scheme, for applications to hyperbolic systems with stiff relaxation terms, is chosen for the resolution of the system. The proposed model is validated through very demanding Riemann Problems, C-property tests (providing also the analytical proof of the well-balancing of the model) and problems designed with the Method of Manufactured Solutions. The expected order of accuracy of the proposed scheme is then verified through a focused analysis, comparing the results with those that would be obtained if a simple Splitting-technique were used to treat stiff problems like those considered in this work. The computational code, written in MATLAB (MathWorks Inc.) language, with the implementation of the above discussed tests, is made available in Mendeley Data repository (Bertaglia, Caleffi, and Valiani, 2020). Further tests are designed to evaluate the applicability of the model to real case studies in single vessels, assessing its capability to serve as valuable tool even for practical medical applications. Hence, numerical results concerning the blood flow in the upper thoracic aorta and in the common carotid artery are compared to literature benchmark solutions which were obtained with six different one-dimensional schemes and a three-dimensional one. Furthermore, specific test cases regarding the common carotid artery and the common femoral artery are designed starting from in-vivo data recorded in six volunteers: using the velocity waveform extrapolated from Doppler measurements as inlet boundary and comparing the pressure waveforms measured by a PulsePen tonometer with the computed pressures. In-vivo data acquisition and extrapolation methodologies are discussed in a separate Section. Finally, a preliminary effective procedure to estimate the fluid-structure parameters of the proposed model, returning hysteresis curves dissipating energy fraction in line with literature values, is provided.

In Chapter 5 an application study on essential arterial hypertension related to the Selfish Brain Hypothesis is discussed. In this Chapter, the potential of a mathematical instrument such as the Müller-Toro model, a global multi-scale closed-loop mathematical model of the entire human circulation, composed by a one-dimensional representation of the network of major arteries and major veins and lumped-parameter models for microvasculature (arterioles, capillaries and venules), heart, pulmonary circulation and cerebrospinal fluid circulation, is assessed. In the study here presented, the Müller-Toro model is developed to permit simulations of adult healthy subjects (and not only young subjects) and hypertensive patients, with a proper recalibration of the network parameters involved in the aging and hypertensive process and a thorough sensitivity analysis of the model. Furthermore, to analyze the effects of the presence of congenital cerebrovascular abnormalities, in connection with the development of a persistent high arterial pressure state (as according to the Selfish Brain Hypothesis of essential hypertension), a preliminary computational study is conducted, taking into account three different configurations of anatomical cerebrovascular variants.
Finally, Chapter 6 provides a general discussion of issues arising from this Thesis, including an assessment of the strengths and limitations of the proposed models, an overview of the main findings and suggested directions for future work.

Chapter 2

Viscoelastic Materials

2.1 Introduction

The study of viscoelasticity is of interest in several contexts. Materials used in engineering may exhibit a viscoelastic behavior that has a profound influence on the performance of that material and, in applications, one may consider viscoelasticity of specific materials in the design process to achieve a particular goal. Furthermore, the mathematics underlying viscoelasticity theory is of interest within the applied mathematics community and, overall, viscoelastic materials are of interest in some branches of materials science, metallurgy, and solid state physics. In common metals, such as steel or aluminum, as well as in quartz, at room temperature and at small strain, the behavior does not deviate much from the behavior of linearly elastic materials. Synthetic polymers, wood, and biological tissues, as well as uncommon metals, at high temperature manifest large viscoelastic effects. The study of viscoelasticity is therefore pertinent even to applications concerning medical diagnosis, injury prevention, and, more in general, anatomy and biology. In some applications, even a small viscoelastic response can be significant and an analysis or design involving such materials must incorporate their viscoelastic behavior (Lakes, 2009).

2.2 Phenomenological aspects

A material that exhibits both elastic and viscous characteristics when undergoing deformation, responding to external forces in an intermediate manner between the behavior of an elastic solid and a viscous liquid, is termed viscoelastic material (Gurtin and Sternberg, 1962; Christensen, 1982; Lakes, 2009). The mechanical characterization of these materials often consists on performing uniaxial tensile tests similar to those used for elastic solids, but modified so as to enable the observation of the time dependency of the material response due to its intrinsic nature. In viscoelastic materials, the energy put into the system during the loading phase is not totally recovered during relaxation. Viscoelasticity, therefore, results in materials with memory since the strain depends on the history of stresses (and vice-versa). To study and define the mechanics of a viscoelastic material, three primary features need to be considered and verified: creep, stress relaxation and hysteresis. Creep describes a material in continuous deformation over time when it is maintained under constant stress; stress relaxation refers to the decrease of stress over time when it is maintained under constant strain; lastly, the hysteresis loop (schematically represented in Fig. 2.1) describes the dissipation of energy when a material undergoes cyclic loading and unloading (Battista, 2015). The energy dissipation

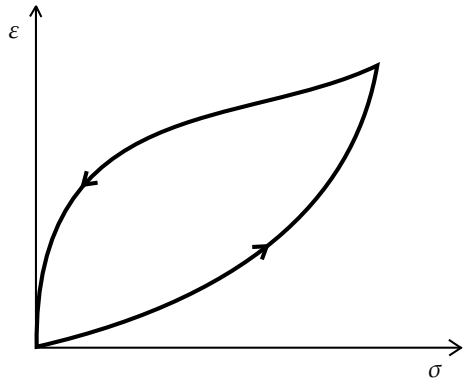

FIGURE 2.1: *Schematic representation of a hysteresis loop described by loading and unloading phase of a viscoelastic material.*

associated with hysteresis makes the construction and simulation of viscoelastic systems a nontrivial task.

2.2.1 Creep

In Fig. 2.2, on the left, the typical response of a viscoelastic material to a creep-recovery test (consisting in a constant load and subsequent removal of that load) is shown. Creep describes a material in continuous deformation over time when it is maintained under constant stress. A viscoelastic material, indeed, first suffers an instantaneous strain upon loading, increasing then it over time with an ever decreasing strain rate. Only part of the strain accumulated during the loading is recovered during the unloading phase, with an immediate recovery of the elastic (instantaneous) strain and a delayed recovery of the anelastic deformation over time. A permanent strain may then be left in the material.
In one-dimension (1D), the history of stress σ depends on the time t through the unit Heaviside step function $\mathcal{H}(t)$, defined as 0 for $t < 0$, 1 for $t > 0$ and $1/2$ for $t = 0$, with magnitude σ_0 (Lakes, 2009):

$$\sigma(t) = \sigma_0 \mathcal{H}(t). \tag{2.1}$$

The strain, also depending on time, $\epsilon(t)$, defines the so-called creep compliance (Lakes, 2009):

$$J(t) = \epsilon(t)\sigma_0. \tag{2.2}$$

In linearly viscoelastic materials, the creep compliance does not depend on the stress level, but solely on time.

2.2.2 Relaxation

Stress relaxation refers to the decrease of stress over time (with an exponential decay) when the material is maintained under constant strain, after an instantaneous initial peak.
If we suppose the strain history to be a step function with magnitude ϵ_0 beginning at $t = 0$ (Lakes, 2009),

$$\epsilon(t) = \epsilon_0 \mathcal{H}(t), \tag{2.3}$$

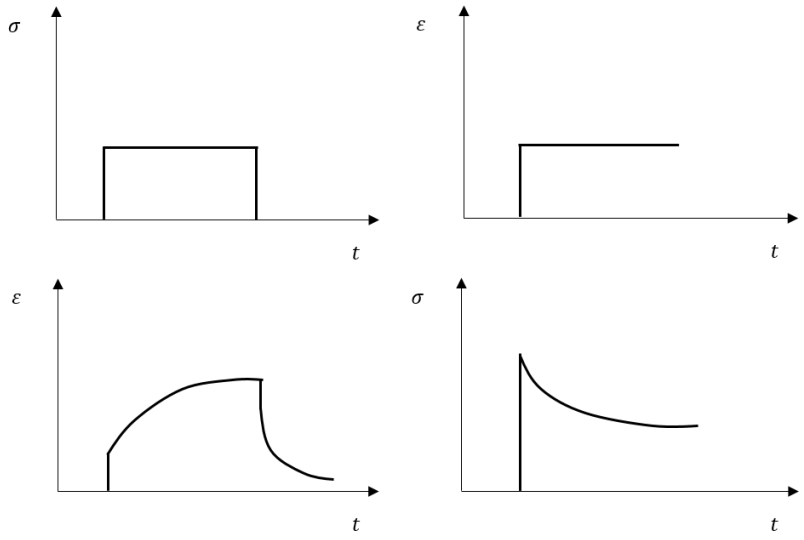

FIGURE 2.2: *Schematic representation of the behavior of a viscoelastic material. On the left, the material is maintained under constant stress, presenting a continuous variation of the deformation over time (creep), composed by an elastic instantaneous strain and a retarded damping effect. On the right, the material is maintained under constant deformation, exhibiting an exponential relaxation of the stress over time (stress relaxation) after an instantaneous peak.*

the stress $\sigma(t)$ will decrease as shown in Fig. 2.2, on the right. The ratio

$$E(t) = \frac{\sigma(t)}{\epsilon_0} \tag{2.4}$$

is called relaxation modulus and in linear materials is independent on the stress level (Lakes, 2009).

2.3 Mathematical Models for Linear Viscoelasticity

Even if only a few of the existent viscoelastic materials behave in a linear way, the theory of linear viscoelasticity provides a usable engineering approximation for many applications in polymer and composites engineering. Even in instances requiring more elaborate treatments, the linear viscoelastic theory has been demonstrated to be a useful starting point for a variety of actual materials and significant problems (Gurtin and Sternberg, 1962).

A constitutive relation of linear viscoelasticity is built up considering the material as a sum of linear elastic springs, each one defined by a Young modulus E, and linear viscous dashpots, characterized by a viscosity coefficient η, to take into account also the time dependent relaxation of the wall and its damping effect. In general, the more elements we have, the more accurate the model will be in describing the real response of the material. But the more complex the model, the more material parameters there will be that need to be accurately calibrated. The determination of a large number of parameters may in fact become a very difficult task.

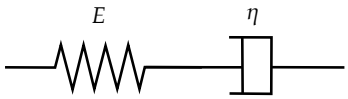

FIGURE 2.3: *Scheme of the Maxwell model.*

2.3.1 Maxwell Model

The Maxwell (MX) model consists on a spring and a dashpot in series, as presented in Fig. 2.3 (Lakes, 2009). The total strain ϵ of the unit will be the sum of two different contributes, one deriving from the deformation of the spring (ϵ_1) and one deriving from the deformation of the dashpot (ϵ_2):

$$\epsilon = \epsilon_1 + \epsilon_2.$$

The total stress σ will be, instead, the same in both elements:

$$\sigma = \sigma_1 = \sigma_2.$$

The constitutive equation of a linear elastic solid coincides with Hooke's law (Avallone and Baumeister III, 1916), which can simply be express as:

$$\sigma = E\epsilon. \tag{2.5}$$

On the other hand, to define the behavior of a linear dashpot, we have to consider the mechanics of a piston moving in an ideal incompressible viscous (Newtonian) fluid. For this dashpot, the rheological law results (Gurtin and Sternberg, 1962):

$$\sigma = \eta \frac{\mathrm{d}\epsilon}{\mathrm{d}t}, \tag{2.6}$$

which means, the larger the stress, the faster the material deforms.
Therefore, considering the two contributes in the MX model, the following system of three equations in four unknowns (σ, ϵ, ϵ_1, ϵ_2) is obtained:

$$\begin{aligned} \epsilon &= \epsilon_1 + \epsilon_2 \\ \sigma &= E\epsilon_1 \\ \sigma &= \eta \frac{\mathrm{d}\epsilon_2}{\mathrm{d}t}. \end{aligned}$$

With algebraic manipulations, it is possible to rewrite this system in one rheological equation, relating total stress to total strain, which represents the constitutive law of the MX model:

$$\frac{\mathrm{d}\sigma}{\mathrm{d}t} = E\frac{\mathrm{d}\epsilon}{\mathrm{d}t} - \frac{1}{\tau_r}\sigma. \tag{2.8}$$

with τ_r called relaxation time and in this model defined $\tau_r = \eta/E$. The response of the model to a sudden load, maintained constant in time, reflects an instantaneous deformation of the spring followed by the additional strain of the dashpot, which takes time to react. Once the load is removed, the spring reacts again immediately, relaxing, but the dashpot does not have any tendency to recover. Thus, the system remains with a "creep" strain due to the dashpot.

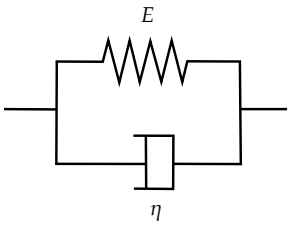

FIGURE 2.4: *Scheme of the Kelvin-Voigt model.*

The creep response of the MX model is defined in time by the function (Lakes, 2009):

$$J(t) = \frac{1}{E} + \frac{t}{\eta}, \tag{2.9}$$

which describes the primary creep through an unrealistic straight line. Otherwise, if a step strain is applied to the unit, the relaxation response results (Lakes, 2009):

$$E(t) = Ee^{-\frac{t}{\tau_r}}. \tag{2.10}$$

2.3.2 Kelvin-Voigt Model

If a single spring and a dashpot are connected in parallel, so that they both experience the same strain,

$$\epsilon = \epsilon_1 = \epsilon_2,$$

while the total stress is the sum of the stresses in each element,

$$\sigma = \sigma_1 + \sigma_2,$$

we have what is known as Kelvin-Voigt (KV) model, shown in Fig. 2.4 (Lakes, 2009). Considering again, as for the MX model, the contributes of both spring and dashpot, the following system of equations is obtained for the definition of the KV unit:

$$\begin{aligned} \sigma &= \sigma_1 + \sigma_2 \\ \sigma_1 &= E\epsilon \\ \sigma_2 &= \eta \frac{\mathrm{d}\epsilon}{\mathrm{d}t}. \end{aligned}$$

Rewriting this system in a single equation, relating total stress to total strain, leads to the following constitutive equation:

$$\sigma = E\epsilon + \eta \frac{\mathrm{d}\epsilon}{\mathrm{d}t}. \tag{2.12}$$

When the KV model is suddenly loaded with a constant stress over time, the spring cannot immediately deform because is held back by the dashpot. Hence, this model is not able to describe an instantaneous elastic strain, since the stress is initially totally absorbed by the dashpot, being transferred to the spring only successively in time. Also when unloading the unit, the dashpot does not permit to the spring to instantaneously relax and no permanent strain is left.

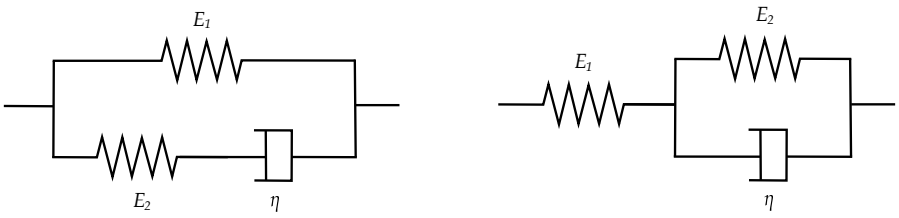

FIGURE 2.5: *Schemes of the Standard Linear Solid Model, with Maxwell unit on the left and with Kelvin-Voigt unit on the right.*

The creep function of the KV model results (Lakes, 2009):

$$J(t) = \frac{1}{E}\left(1 - e^{-\frac{t}{\tau_c}}\right), \tag{2.13}$$

with τ_c called retardation/creep time and here defined $\tau_c = \eta/E$.
On the other hand, if we consider the behavior of the KV unit when loaded by a step strain, it can be demonstrated that the model cannot describe a realistic relaxation response, which represents the main weakness of the model. In this system, indeed, the relaxation of the material is defined by an impulse plus a constant (Lakes, 2009).

2.3.3 Standard Linear Solid Model

If a linear elastic spring is added in parallel to a MX unit or in series to a KV unit, the so-called Standard Linear Solid (SLS) model is obtained, as presented in Fig. 2.5. it can be demonstrated that both the versions of the SLS model reproduce exactly the same behavior of the material (Lakes, 2009; Gurtin and Sternberg, 1962). Starting analyzing the SLS model in its formulation with a MX unit, the following system has to be considered:

$$\begin{aligned}
&\epsilon = \epsilon_1 = \epsilon_2 + \epsilon_D \\
&\sigma = \sigma_1 + \sigma_2 = \sigma_1 + \sigma_D \\
&\sigma_1 = E_1\epsilon_1 \\
&\sigma_2 = E_2\epsilon_2 \\
&\sigma_D = \eta\frac{\mathrm{d}\epsilon_D}{\mathrm{d}t},
\end{aligned}$$

where the subscript D identifies the contributes given by the dashpot and the subscripts 1 and 2 identify those given by each spring, as from Fig. 2.5 left. If the SLS model with a KV unit is studied, the system of equations to be taken into account results as follows:

$$\begin{aligned}
&\epsilon = \epsilon_1 + \epsilon_2 = \epsilon_1 + \epsilon_D \\
&\sigma = \sigma_1 = \sigma_2 + \sigma_D \\
&\sigma_1 = E_1\epsilon_1 \\
&\sigma_2 = E_2\epsilon_2 \\
&\sigma_D = \eta\frac{\mathrm{d}\epsilon_D}{\mathrm{d}t}.
\end{aligned}$$

When manipulating the previous systems, in both the cases the same constitutive law, valid for a general SLS model, is obtained:

$$\frac{\mathrm{d}\sigma}{\mathrm{d}t} = E_0 \frac{\mathrm{d}\epsilon}{\mathrm{d}t} - \frac{1}{\tau_r}(\sigma - E_\infty \epsilon), \tag{2.16}$$

where E_0 is the instantaneous Young modulus and E_∞ is the asymptotic Young modulus. In the MX unit case, the instantaneous Young modulus, the asymptotic Young modulus, the relaxation time and the retardation/creep time result, respectively:

$$E_0 = E_1 + E_2, \qquad E_\infty = E_1, \qquad \tau_r = \frac{\eta}{E_2}, \qquad \tau_c = \eta \frac{E_1 + E_2}{E_1 E_2}; \tag{2.17}$$

while with the KV unit:

$$E_0 = E_1, \qquad E_\infty = \frac{E_1 E_2}{E_1 + E_2}, \qquad \tau_r = \frac{\eta}{E_1 + E_2}, \qquad \tau_c = \frac{\eta}{E_2}. \tag{2.18}$$

This model is able to realistically exhibit all the three primary features of a viscoelastic material: creep, stress relaxation and hysteresis. Analyzing first the mechanics of the model in its MX configuration, it can be noticed that when the system is suddenly loaded, the two springs are immediately strained, while only successively the load is distributed also to the dashpot. The instantaneous elastic modulus of the system, indeed, takes into account both the contributes of the two springs, E_1 and E_2. If the same load is applied to the SLS model with the KV unit, the instantaneous response is attributed solely to the first spring, being indeed $E_0 = E_1$. The dashpot then takes up the stress, transferring the load to the second spring as it slowly opens over time. If the load is maintained constant in time, in the SLS model with the MX unit tends asymptotically to reach a state in which the elastic response is governed only by E_1, while in the second configuration, with the KV unit, the two springs collaborate as if there were only the two of them in series: $1/E_\infty = 1/E_1 + 1/E_2$. While reaching this asymptotic state, in the first configuration, the creep is attributed to the joint reaction of the two springs, while, in the second case, only to the one in parallel with the dashpot. Finally, when unloading the system, considering both the formulations of the SLS model, the first spring relax immediately while the second reacts slowly, being held back by the dashpot.
Applying the Laplace transform theory it is possible to derive the creep response of this model, represented by the following function (Lakes, 2009):

$$J(t) = \frac{1}{E_0} e^{-\frac{t}{\tau_c}} + \frac{1}{E_\infty}\left(1 - e^{-\frac{t}{\tau_c}}\right). \tag{2.19}$$

It is also possible to define the relaxation function (Lakes, 2009), which describes, through the relaxation time τ_r, how the stiffness of the material changes in time, starting from the instantaneous value and reaching the asymptotic one:

$$E(t) = E_0 e^{-\frac{t}{\tau_r}} + E_\infty \left(1 - e^{-\frac{t}{\tau_r}}\right). \tag{2.20}$$

2.3.4 Generalized Kelvin-Voigt chain

Starting from the SLS in its configuration with a KV element, it is possible to extend the number of KV units obtaining the so-called generalized Kelvin-Voigt (g-KV) chain,

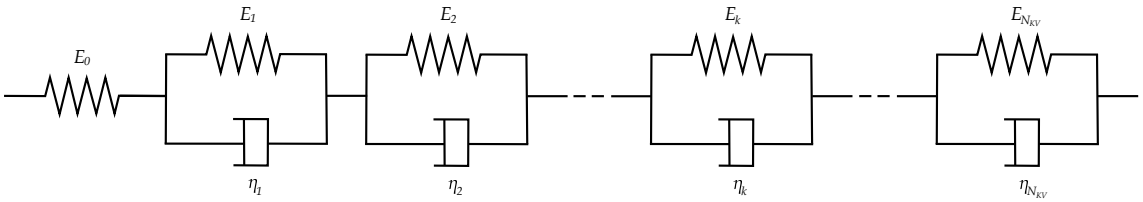

FIGURE 2.6: *Scheme of the generalized Kelvin-Voigt chain.*

shown in Fig. 2.6. With this system we obtain the following equations for the basic stress-strain relations, with the subscript k referring to parameters of the k^{th} element (with N_{KV} number of total KV units in series with a single spring) and the additional subscript D identifying the contributes given by the dashpot:

$$\begin{aligned}
\epsilon &= \epsilon_0 + \sum_{k=1}^{N_{KV}} \epsilon_k \\
\sigma &= \sigma_0 = \sigma_k + \sigma_{k,D} \\
\sigma_0 &= E_0 \epsilon_0 \\
\sigma_k &= E_k \epsilon_k \\
\sigma_{k,D} &= \eta_k \frac{\mathrm{d}\epsilon_k}{\mathrm{d}t}.
\end{aligned}$$

The algebraic manipulation of this system, leads to:

$$\frac{\mathrm{d}\epsilon}{\mathrm{d}t} = \frac{\mathrm{d}\epsilon_0}{\mathrm{d}t} + \sum_{k=1}^{N_{KV}} \frac{\mathrm{d}\epsilon_k}{\mathrm{d}t} = \frac{1}{E_0}\frac{\mathrm{d}\sigma}{\mathrm{d}t} + \sum_{k=1}^{N_{KV}} \left(\frac{\sigma - E_k \epsilon_k}{\eta_k} \right)$$

and thus,

$$\frac{\mathrm{d}\sigma}{\mathrm{d}t} = E_0 \frac{\mathrm{d}\epsilon}{\mathrm{d}t} + E_0 \left(\sum_{k=1}^{N_{KV}} \frac{E_k \epsilon_k}{\eta_k} - \sigma \sum_{k=1}^{N_{KV}} \frac{1}{\eta_k} \right). \tag{2.22}$$

The same procedure can be followed starting from the SLS model with a MX unit, extending the amount of MX elements in parallel with the single spring. Such models contain many parameters and exhibit a whole array of relaxation and retardation times.
The creep function of a g-KV chain is expressed by:

$$J(t) = J_0 + \sum_{k=1}^{N_{KV}} J_k \left(1 - e^{-\frac{t}{\tau_{ck}}} \right), \tag{2.23}$$

with $J_0 = 1/E_0$, $J_k = 1/E_k$ and the retardation/creep time of each KV element defined: $\tau_{ck} = \eta_k / E_k$. As a matter of fact, the relaxation function will be:

$$E(t) = E_0 + \sum_{k=1}^{N_{KV}} E_k \left(1 - e^{-\frac{t}{\tau_{rk}}} \right), \tag{2.24}$$

depending on the relaxation time of each KV unit.

Chapter 3

Viscoelasticity in pipelines

3.1 Introduction

Flexible plastic pipes in polyvinyl chloride (PVC), polyethylene (PE) and in particular high density polyethylene (HDPE) are gaining an increasingly important role in pressurized and not pressurized hydraulic systems, being often preferred to other materials (i.e. steel and concrete) for water distribution networks, irrigation plants and sewage systems. This trend is a consequence of the excellent mechanical and chemical properties of polymer materials, even more considering the easy and rapid process of installation required and the cheaper prices. Almost without exception, polymers belong to a class of substances that show viscoelastic properties, responding to external forces in an intermediate manner between the behavior of an elastic solid and a viscous liquid (Shaw and MacKnight, 2005), attributing to the material an elastic instantaneous strain together with a retarded dampening effect. This aspect is particularly visible in case of hydraulic transients, for which it has already been demonstrated that the classical Allievi-Joukowsky theory for water hammer, based on the assumption of a linear elastic wall behavior and quasi-steady friction losses (Chaudhry, 1979), fails in the prediction of the real pressure trend in flexible tubes (Covas et al., 2004; Covas et al., 2005). From the experimental point of view, a recent thorough work has been done by Ferràs et al. (2016) for the distinction of the main effects of dampening during hydraulic transients in PE pipes. Ramos et al. (2004) discussed the importance of the implementation of a viscoelastic constitutive law for plastic pipes and also the relevance of the unsteady friction with respect to the steady one. Their results show that the pressure wave dissipation is more sensitive to the viscoelastic damping effects than to the unsteady friction losses. Furthermore, Duan et al. (2010) demonstrated that the viscoelastic effects are deeply more significant when the retardation time is less than the wave travel time along the entire pipeline length. Other researches regarding the unsteady friction losses had already been done by Zielke (1968) and Franke and Seyler (1983), while recently Ioriatti, Dumbser, and Iben (2017) proposed a new more efficient approach for evaluating the convolution integral of the unsteady wall shear stress.

In many industrial applications involving the design of hydraulic networks, accurate computational models able to correctly a priori evaluate the behaviour of systems are required. The mathematical model has to properly describe the mechanics of the phenomenon also in terms of resistance and deformation of the pipe wall, especially in the event of water hammers which could seriously damage the whole system. Moreover, considering the increase in complexity of these systems, numerical simulations need to be more and more efficient and robust.

The main numerical method used for studies concerning hydraulic transients has always

been the Method of Characteristics (MOC) (Ghidaoui et al., 2005). Among these studies, a lot of research has been done for the single-pipe plastic system by Covas et al. (2004), Covas et al. (2005), Soares, Covas, and Reis (2008), and Apollonio et al. (2014). There are also applications performed with a 2D axially symmetric model in Duan et al., 2010; Pezzinga, 2014. Meniconi, Brunone, and Ferrante (2012) and Meniconi et al. (2014) analyzed the effects of water hammer pressure waves in case of sudden contraction or expansion of the cross-sectional area or with an in-line valve in the pipeline. Evangelista et al. (2015) even investigated the behavior of more complex hydraulic systems, with a Y-shaped configuration.
Other techniques are only seldom applied for the resolution of transient flows in pipelines (Seck, Fuamba, and Kahawita, 2017) and include in particular Finite Volume Methods (FVM). Starting from this consideration, in the present work the explicit path-conservative FVM associated with the Dumbser-Osher-Toro (DOT) Riemann solver proposed by Dumbser and Toro (2011a) and Dumbser and Toro (2011b) and the semi-implicit staggered FVM (further simply called SI) presented by Dumbser, Iben, and Ioriatti (2015) are tested, together with the MOC, for the simulation of two water hammer problems in single HDPE pipelines. Results are compared with experimental data and further methods are analyzed also in terms of efficiency. It has to be mentioned that the DOT solver had never been used before for this type of applications, only for frequency analysis by Leibinger et al. (2016), while the SI method had already been tested with hydraulic transients, but only considering an elastic tube wall behavior by Ioriatti, Dumbser, and Iben (2017). In the present research, water hammer test cases are performed taking into account different linear viscoelastic models: the SLSM and the g-KV chain (see Section 2.3), with the aim to evaluate if a more complex model is worth to be chosen to achieve a better agreement with experimental data. Furthermore, a comparison of the results obtained implementing a quasi-steady friction model and an unsteady friction model, with the approach proposed by Ioriatti, Dumbser, and Iben (2017), is evaluated in case of turbulent flow. To stress the investigated numerical schemes, in order to reveal their weaknesses, tests are executed also with three challenging Riemann problems (RP), adopting an elastic rheological behavior of the tube wall. The aim of the Riemann problems here presented is to evaluate the robustness of each scheme, pointing out the performance of every method in case of cross-sectional changes, when more flexible materials are considered and when cavitation occurs.

3.2 Methods

3.2.1 Mathematical model

The governing balance laws system of a compressible fluid through a flexible tube is obtained averaging the three-dimensional compressible Navier-Stokes equations over the cross-section under the assumption of axial symmetry of the geometry of the conduct and of the flow. The resulting simplified one-dimensional non-linear hyperbolic system of partial differential equations (PDE), composed by the continuity equation and by the momentum equation, reads (Ghidaoui et al., 2005):

$$\frac{\partial}{\partial t}(A\rho) + \frac{\partial}{\partial x}(A\rho u) = 0 \tag{3.1a}$$

$$\frac{\partial}{\partial t}(A\rho u) + \frac{\partial}{\partial x}(A\rho u^2 + Ap) - p\frac{\partial A}{\partial x} = F_R. \tag{3.1b}$$

where x is the space, t is the time, A is the cross-sectional area, ρ is the cross-sectional averaged density of the fluid, u is the averaged fluid velocity, p is the averaged fluid pressure and F_R is a model of the friction between fluid and tube wall, further presented in Section 3.2.1.2.
To close system (3.1), an equation of state (EOS) and a constitutive tube law must be added. In most of the technical applications it is usually sufficient to assume a barotropic behavior of the fluid, therefore $\rho = \rho(p)$. Nevertheless, taking into account the cavitation phenomena may be useful. An EOS for barotropic flow taking into account cavitation is presented in Section 3.2.1.1.
The tube law describes the relationship between the tube cross-section and the internal pressure, containing all the information about the rheological behavior of the pipe material. It can be expressed in different ways. To take into account the deformability and the flexibility of the tube wall, two different rheological models are here considered: the first one defining an elastic behavior and the second one for a more complex viscoelastic behavior, which is necessary to reproduce the real performance of plastic tubes (Evangelista et al., 2015; Covas et al., 2004; Covas et al., 2005). These models are presented in Section 3.2.1.3 and 3.2.1.4.

Returning to system of equations (3.1), it is possible to derive the classical water hammer equations in terms of piezometric head $h = p/\rho g$ and velocity u, when temperature changes can be neglected. From Eq. (3.1a),

$$\frac{\partial}{\partial t}(A\rho) + \frac{\partial}{\partial x}(A\rho u) = \rho\frac{\partial A}{\partial t} + A\frac{\partial \rho}{\partial t} + \rho u\frac{\partial A}{\partial x} + A\rho\frac{\partial u}{\partial x} + Au\frac{\partial \rho}{\partial x} = 0.$$

Gathering terms, we obtain:

$$\rho\left(\frac{\partial A}{\partial t} + u\frac{\partial A}{\partial x}\right) + A\left(\frac{\partial \rho}{\partial t} + u\frac{\partial \rho}{\partial x}\right) + A\rho\frac{\partial u}{\partial x} = 0. \tag{3.2}$$

On the other hand, manipulating Eq. (3.1b), considering a quasi-steady friction model, with g gravity acceleration and j frictional head loss coefficient per unit length (see Section 3.2.1.2),

$$\frac{\partial}{\partial t}(A\rho u) + \frac{\partial}{\partial x}(A\rho u^2) + A\frac{\partial p}{\partial x} = A\rho\frac{\partial u}{\partial t} + u\frac{\partial(A\rho)}{\partial t} + A\rho u\frac{\partial u}{\partial x} + u\frac{\partial(A\rho u)}{\partial x} + A\frac{\partial p}{\partial x} = -A\rho g j.$$

Dividing both members for $A\rho g$ and using Eq. (3.1a), follows:

$$\frac{1}{g}\left(\frac{\partial u}{\partial t} + u\frac{\partial u}{\partial x}\right) + \frac{1}{\rho g}\frac{\partial p}{\partial x} = -j. \tag{3.3}$$

Assuming that $\frac{1}{\rho g}\frac{\partial p}{\partial x} \approx \frac{\partial}{\partial x}(\frac{p}{\rho g})$, which means that the spatial variation of the density is negligible, Eq. (3.3) becomes:

$$\frac{1}{g}\left(\frac{\partial u}{\partial t} + u\frac{\partial u}{\partial x}\right) + \frac{\partial h}{\partial x} = -j. \tag{3.4}$$

A generic function $\mathcal{F}(x,t)$ that represents any characteristics of the pressure wave concerning water hammer problems is now introduced. Standing on the wave frame reference, the characteristic $\mathcal{F}$ remains constant in both time and space, thus it can be written

that:

$$\frac{\mathrm{d}\mathcal{F}}{\mathrm{d}t} = \frac{\partial \mathcal{F}}{\partial t} + \frac{\partial \mathcal{F}}{\partial x}\frac{\mathrm{d}x}{\mathrm{d}t} = 0,$$

being $a = {}^{dx}/_{dt}$ the wave speed. Rearranging this equation and dividing for the velocity in the duct, it results:

$$\frac{a}{u} = -\frac{\frac{\partial \mathcal{F}}{\partial t}}{u\frac{\partial \mathcal{F}}{\partial x}}. \tag{3.5}$$

Since, in a general water hammer problem in flexible tubes (and even more in rigid tube cases), a is considerably bigger than u (Wylie and Streeter, 1978), from Eq. (3.5) it follows that all the convective terms $u{}^{\partial \mathcal{F}}/_{\partial x}$ can be neglected compared to terms ${}^{\partial \mathcal{F}}/_{\partial t}$. Thus, system of equations (3.2) and (3.4) becomes:

$$\rho\frac{\partial A}{\partial t} + A\frac{\partial \rho}{\partial t} + A\rho\frac{\partial u}{\partial x} = 0 \tag{3.6a}$$

$$\frac{1}{g}\frac{\partial u}{\partial t} + \frac{\partial h}{\partial x} = -j. \tag{3.6b}$$

Manipulating again Eq. (3.6a), in order to write it in terms of piezometric head and velocity,

$$\frac{1}{A}\frac{\partial A}{\partial p}\frac{\partial p}{\partial t} + \frac{1}{\rho}\frac{\partial \rho}{\partial p}\frac{\partial p}{\partial t} + \frac{\partial u}{\partial x} = 0,$$

and considering again the assumption $\frac{1}{\rho g}\frac{\partial p}{\partial t} \approx \frac{\partial}{\partial t}(\frac{p}{\rho g})$, it follows that:

$$\rho g\left(\frac{1}{A}\frac{\partial A}{\partial p} + \frac{1}{\rho}\frac{\partial \rho}{\partial p}\right)\frac{\partial h}{\partial t} + \frac{\partial u}{\partial x} = 0. \tag{3.7}$$

To reduce terms in brackets, it is necessary to introduce Hooke's law (Avallone and Baumeister III, 1916):

$$\mathrm{d}p = K_e\frac{\mathrm{d}\rho}{\rho}, \tag{3.8}$$

with K_e water bulk modulus of elasticity. Considering a cylindrical tube with diameter D, and referring to Eq. (2.5), Hooke's law can also be written as:

$$\mathrm{d}\sigma = E_0\frac{dD}{D}, \tag{3.9}$$

with E_0 instantaneous Young (elastic) modulus of the wall material. Introducing then Barlow's formula (Avallone and Baumeister III, 1916):

$$pD = 2\sigma s_0, \tag{3.10}$$

with s_0 thickness of the tube (assumed constant in space and time) and σ tension stress, it immediately follows that

$$\mathrm{d}p = \frac{2s_0}{D}\mathrm{d}\sigma,$$

and applying Eq. (3.9),

$$\mathrm{d}p = \frac{2s_0E_0}{D^2}\mathrm{d}D. \tag{3.11}$$

Since $\frac{1}{A}\frac{\mathrm{d}A}{\mathrm{d}p} = \frac{2}{D}\frac{\mathrm{d}D}{\mathrm{d}p}$, substituting Eq. (3.11) and Eq. (3.8) into Eq. (3.7), we obtain:

$$\frac{\partial h}{\partial t} + \frac{1}{g}\frac{\frac{K_e}{\rho}}{\left(1 + \frac{D}{s_0}\frac{K_e}{E_0}\right)}\frac{\partial u}{\partial x} = 0. \tag{3.12}$$

Hence, the simplified unsteady pipe flow system of equations, in which the convective transport terms have been neglected, following the classical Allievi-Joukowsky theory, finally results:

$$\frac{\partial h}{\partial t} + \frac{a^2}{g}\frac{\partial u}{\partial x} = 0 \tag{3.13a}$$

$$\frac{1}{g}\frac{\partial u}{\partial t} + \frac{\partial h}{\partial x} = -j, \tag{3.13b}$$

where the general definition of a is given by:

$$a = \sqrt{\frac{\frac{\partial p}{\partial \rho}}{1 + \frac{\rho}{A}\frac{\partial A}{\partial p}\frac{\partial p}{\partial \rho}}} = \frac{c_s'}{\sqrt{1 + \frac{c_s'^2}{c^2}}} = \frac{1}{\sqrt{\frac{1}{c_s'^2} + \frac{1}{c^2}}}. \tag{3.14}$$

Here $c_s' = \sqrt{\partial p/\partial \rho}$ is the speed of sound, which represents the celerity contribute linked to the compressibility of the fluid. It results equal to c_s when cavitation episodes do not occur, hence when the fluid component is only liquid. On the other hand, c is the celerity contribute due to the fluid-structure interaction (FSI), hence due to the relation between inner pressure p and cross-sectional area A:

$$c = \sqrt{\frac{A}{\rho}\frac{\partial p}{\partial A}}. \tag{3.15}$$

It can be noticed that Eq. (3.14) can also be written as

$$\frac{1}{a^2} = \frac{1}{c_s'^2} + \frac{1}{c^2} \tag{3.16}$$

which recalls the sum of two resistances in parallel of an electric circuit. Therefore, we can see the total wave speed of the system a as the result of two resistances in parallel defined by the two celerity contributes c_s' and c.
Eq. (3.14) can be made explicit when suitable EOS and tube law are selected.

3.2.1.1 Equation of state

When considering a barotropic fluid, the density only depends on the pressure, hence $\rho = \rho(p)$. To take into account cases in which cavitation occurs means supposing to have cases in which $p < p_v$, where p_v is the vapor pressure. Thus, to account also for cavitation cases, the following equation of state with an homogeneous mixture approximation is

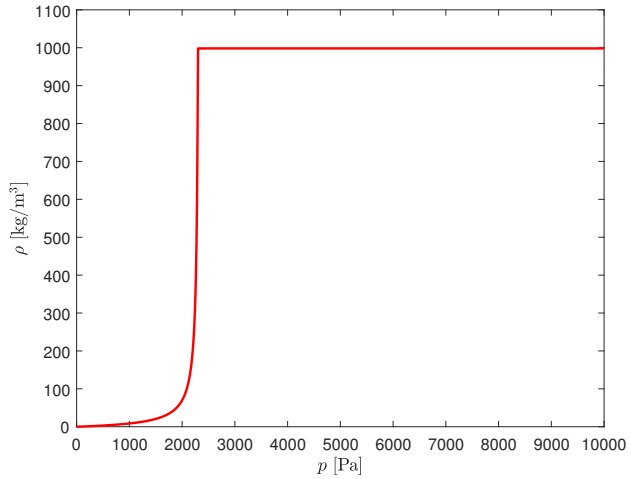

FIGURE 3.1: *Representation of the behavior described by the selected EOS. The density remains almost constant with decreasing pressure until the p_v value is reached, after which a very sharp decrease of the density occurs.*

selected (Dumbser, Iben, and Ioriatti, 2015):

$$\rho(p) = \begin{cases} \rho_0 + \frac{1}{c_s^2}(p - p_v) & \text{if} \quad p \geq p_v \\ \left[\frac{\varphi(p)}{\rho_v(p)} + \frac{1-\varphi(p)}{\rho_0}\right]^{-1} & \text{if} \quad 0 < p < p_v \end{cases} \tag{3.17}$$

with ρ_0 and p_0 the reference density and pressure in equilibrium state respectively, c_s the speed of sound in the fluid at reference conditions, $\varphi(p) = -K_c(p - p_v)$ the mass fraction of vapor, with K_c cavitation constant, and $\rho_v(p) = \frac{p}{R_v T_0}$ the vapor density, calculated considering the gas constant R_v at reference temperature T_0. The general behavior defined by the selected EOS is shown in Fig. 3.1.

3.2.1.2 Friction model

Concerning the friction model applied to water hammer problems, it is possible to define the parameter P as the ratio between the diffusion time scale and the wave time scale:

$$\mathsf{P} = \frac{2D/fu_0}{L/a}, \tag{3.18}$$

where L is the length of the pipe, f is the friction factor, as defined by the Darcy-Weisbach formula (Wylie and Streeter, 1978), u_0 is the initial velocity and a is given by Eq. (3.14). It has been shown that accurate physically based unsteady friction models are required if P is of order 1 or less (Ghidaoui, Mansour, and Zhao, 2002; Duan et al., 2010). If $\mathsf{P} \gg 1$, it is possible to consider only a quasi-steady friction model, for which the term F_R in Eq. (3.1b) reads:

$$F_R = -A\rho g j, \tag{3.19}$$

with the frictional head loss per unit length $j = \frac{f}{D}\frac{u|u|}{2g}$ and f friction coefficient. Considering a cylindrical tube with axially symmetric flow, the same quantity F_R can also be

expressed in terms of the wall shear stress τ_w as:

$$F_R = -2\pi R \tau_w, \tag{3.20}$$

where R is the pipe radius and with τ_w concerning only the quasi-steady contribute τ_s, hence:

$$\tau_w = \tau_s = f\frac{\rho u|u|}{8}. \tag{3.21}$$

If unsteadiness effects need to be taken into account, hence when $\mathsf{P} \ll 1$, the wall shear stress τ_w is written as sum of quasi-steady τ_s and unsteady contribute τ_u:

$$\tau_w = \tau_s + \tau_u. \tag{3.22}$$

Thus, considering the expression by Zielke (1968):

$$\tau_w = f\frac{\rho u|u|}{8} + \frac{2\mu}{R}\int_0^t w(t-t')\frac{\partial u}{\partial t}(t')\,\mathrm{d}t', \tag{3.23}$$

where μ is the dynamic viscosity, w is a weighting function and t' is the integral variable having dimension of time.

The evaluation of the convolution integral in Eq. (3.23) is very time consuming and several solutions have been proposed for it (see Urbanowicz and Zarzycki (2012) and Shamloo, Norooz, and Mousavifard (2015) for extensive summaries). The first who developed an effective method was Trikha (1975), while the most diffused formulation is the one proposed by Kagawa et al. (1983), who improved Trikha's approach. Recently, a novel approach has been proposed by Ioriatti, Dumbser, and Iben (2017) in the case of laminar flow. In particular, the solution of the convolution integral is reduced to the solution of a set of ordinary differential equations (ODEs). This solution allows to gain efficiency with respect to Kagawa's formula (which requests the evaluation of exponential functions). In the following, the ODE approach is extended, proposing the ODE friction model even for turbulent flow cases.
First, the weighting function in turbulent regime proposed by Urbanowicz and Zarzycki (2012), expressed as a series of exponential functions, is considered:

$$w(t) = \sum_{i=1}^{N_w} A^* m_i^* \exp\left[-(n_i^* + B^*)\frac{\nu t}{R^2}\right], \tag{3.24}$$

where $\nu = \mu/\rho$ is the kinematic viscosity of the fluid, $N_w = 16$, $(n_1^*, ..., n_{16}^*) = (4.78793, 51.0897, 210.868, 765.03, 2731.01, 9731.44, 34668.5, 123511, 440374, 1578229, 5481659, 18255921, 59753474, 192067361, 616415963, 1945566788)$ and $(m_1^*, ..., m_{16}^*) = (5.03392, 6.4876, 10.7735, 19.904, 37.4754, 70.7117, 133.460, 251.933, 476.597, 902.22, 1602.04, 2894.84, 5085.55, 9190.11, 16118.6, 29117.3)$. Since in this work only smooth pipes are considered, the parameters A^* and B^* are chosen as those proposed by Vardy and Brown (2003):

$$A^* = \sqrt{1/(4\pi)} \quad B^* = \mathsf{Re}^k/12.86 \quad \text{with} \quad k = \log_{10}(15.29/\mathsf{Re}^{0.0567}), \tag{3.25}$$

where $\mathrm{Re} = |u|D/\nu$ is the Reynolds number. Substituting Eq. (3.24) into the convolution integral, the unsteady wall shear stress is computed as:

$$\tau_u = \sum_{i=1}^{N_w} \tau_{u,i} = \sum_{i}^{N_w} \frac{2\mu}{R} \int_0^t A^* m_i^* \exp\left[-\frac{\nu(n_i^* + B^*)}{R^2}(t-t')\right] \frac{\mathrm{d}u}{\mathrm{d}t}(t')\,\mathrm{d}t'. \tag{3.26}$$

Then, the left and the right side of the i-th contribution in the last equation are derived with respect to the time. Applying the Leibniz rule yields the following ODE:

$$\frac{\mathrm{d}}{\mathrm{d}t}\tau_{u,i} = -\frac{(n_i^* + B^*)\nu}{R^2}\tau_{u,i} + \frac{2\mu}{R}\frac{\mathrm{d}u}{\mathrm{d}t} m_i^* A^*, \tag{3.27}$$

which is discretized in time using the implicit Euler method (Ioriatti, Dumbser, and Iben, 2017):

$$\frac{\tau_{u,i}^{n+1} - \tau_{u,i}^{n}}{\Delta t} = -\frac{(n_i^* + B^*)\nu}{R^2}\tau_{u,i}^{n+1} + \frac{2\mu}{R}\frac{u^{n+1} - u^n}{\Delta t} m_i^* A^*. \tag{3.28}$$

Finally, the total unsteady wall shear stress at time $t^{n+1} = t^n + \Delta t$ is computed as follows:

$$\tau_u^{n+1} = \sum_{i=1}^{N_w} \tau_{u,i}^{n+1} \quad \text{with} \quad \tau_{u,i}^{n+1} = \frac{\tau_{u,i}^{n} + \frac{2\mu}{R}(u^{n+1} - u^n) m_i^* A^*}{1 + \frac{(n_i^* + B^*)\nu}{R^2}\Delta t} \quad i = 1, 2, \ldots N_w. \tag{3.29}$$

3.2.1.3 Elastic constitutive tube law

To study water hammer events occurring in commercial pipes, it is usually sufficient to consider an elastic rheological behavior of the tube wall. This is valid in particular when dealing with steel ducts, but also to obtain a first fair approximation working with plastic pipes. To derive the well-known elastic tube law (also called Laplace law) Hooke's law (3.9) and Barlow's formula (3.10) need to be considered. The combination of these two equations leads to

$$\frac{\mathrm{d}A}{A} = \frac{D}{E_0 s_0}\mathrm{d}p,$$

from which it follows that:

$$\frac{\sqrt{\pi}}{2A\sqrt{A}}\mathrm{d}A = \frac{1}{E_0 s_0}\mathrm{d}p.$$

Integrating both members and linearizing (with Taylor series) the resulting equation, the linearized version of the Laplace law is obtained:

$$p = p_0 + \frac{K}{2}(\alpha - 1), \tag{3.30}$$

where $\alpha = A/A_0$ is the ratio between the cross-sectional area A and the equilibrium cross-sectional area of the tube A_0, being the latter related to the equilibrium pressure p_0. In this elastic constitutive equation the cross-sectional area only depends linearly on the pressure p through a coefficient K, which accounts for all the elastic properties of the material:

$$K = \frac{E_0 s_0}{R_0} = \frac{E_0}{W}, \tag{3.31}$$

with R_0 the radius that corresponds to the equilibrium area A_0 and

$$W = \frac{R_0}{s_0} \tag{3.32}$$

a geometry parameter.
As proposed by Leibinger et al. (2016), to derive the closure equation for system (3.1) in PDE form, we need to differentiate Eq. (3.30) with respect to t:

$$\frac{\partial p}{\partial t} = \frac{K}{2A_0}\frac{\partial A}{\partial t}.$$

Considering that

$$\frac{\partial p}{\partial t} = \frac{\partial p}{\partial \rho}\frac{\partial \rho}{\partial t} = c_s'^2\frac{\partial \rho}{\partial t} \tag{3.33}$$

and

$$\frac{\partial \rho}{\partial t} = \frac{1}{A}\left(\frac{\partial (A\rho)}{\partial t} - \rho\frac{\partial A}{\partial t}\right), \tag{3.34}$$

we can obtain:

$$c_s'^2\frac{\partial (A\rho)}{\partial t} = \left(\rho c_s'^2 + \frac{K\alpha}{2}\right)\frac{\partial A}{\partial t}.$$

Finally, recurring to the continuity equation (3.1a), leads to:

$$\frac{\partial A}{\partial t} + \frac{1}{\rho + \frac{K\alpha}{2c_s'^2}}\frac{\partial (A\rho u)}{\partial x} = 0, \tag{3.35}$$

where c_s' again depends on the selected EOS.

3.2.1.4 Viscoelastic constitutive tube law

To better reproduce the real behavior of a polymer material, as those used in industries, it is necessary to introduce a viscoelastic model. The simplest model yet able to correctly reproduce the stress-strain behavior of a polymer material is the Standard Linear Solid model, which can be structured with a Maxwell or a Kelvin-Voigt element (please refer to Section 2.3). The schematic representation of both the types is shown in Fig. 2.5. To obtain more complex models, it is possible to extend the chain of Maxwell or Kelvin-Voigt units up to an infinite number. In general, the more elements there are, the more accurate the model will be in describing the real response of the material. But that said, the more complex the model is, the more material parameters need to be evaluated by delicate calibrations.
A sensitivity analysis was carried out by Covas et al. (2005) to estimate the number of Kelvin-Voigt elements beyond which the accuracy of the results doesn't improve anymore, and the optimal number resulted equal to 4.
For the simulations here presented, first the SLS model has been considered. Then, to test the applicability of the extension to more complex models, some tests considering the generalized Kelvin-Voigt chain with 5 KV units have also been carried out.

The aim is to obtain the viscoelastic material closing equation for system (3.1). Thus, as previously done for the elastic case in Section 3.2.1.3, starting from the constitutive equation of the SLS model presented in Eq. (2.16) and applying Barlow's formula, Eq. (3.10), the linearized kinematic relation between the strain and the cross sectional area of

the pipe $\alpha = (1+\epsilon^2) \approx 1+2\epsilon$, and the continuity equation (3.1a), leads to (Leibinger et al., 2016):

$$\frac{\partial A}{\partial t} + \frac{1}{\rho + \frac{K\alpha}{2c_s'^2}} \frac{\partial (A\rho u)}{\partial x} = \frac{1}{\tau_r} \left[\frac{A(p-p_0)}{\rho c_s'^2 + \frac{K\alpha}{2}} - \frac{AKE_\infty(\alpha-1)}{2E_0\left(\rho c_s'^2 + \frac{K\alpha}{2}\right)} \right], \tag{3.36}$$

which represents the partial differential form of the SLS model constitutive equation. Comparing this equation to the Laplace PDE (3.35), it can be noticed that all the viscous properties of the material are totally enclosed in the source term.

Furthermore, it is possible to write Eq. (3.36) into an ODE considering that the PDE can be expressed as:

$$\frac{\partial A}{\partial t} = \frac{2A}{\tau_r K\alpha}(p-p_0) - \frac{2c_s'^2}{K\alpha}\left[\frac{\partial (A\rho u)}{\partial x} + \rho \frac{\partial A}{\partial t}\right] - \frac{A_0 E_\infty}{\tau_r E_0}(\alpha - 1). \tag{3.37}$$

From Eq. (3.33) and Eq. (3.34) it follows that

$$\frac{\partial p}{\partial t} = \frac{c_s'^2}{A}\left[\frac{\partial (A\rho)}{\partial t} - \rho \frac{\partial A}{\partial t}\right]$$

and recurring to the continuity equation (3.1a), it results:

$$\frac{\partial p}{\partial t} = -\frac{c_s'^2}{A}\left[\frac{\partial (A\rho u)}{\partial x} + \rho \frac{\partial A}{\partial t}\right].$$

If we use this last equation into (3.37), the SLS model ODE finally results:

$$\frac{\mathrm{d}A}{\mathrm{d}t} = \frac{2A}{K\alpha}\frac{\mathrm{d}p}{\mathrm{d}t} + \frac{1}{\tau_r}\left[\frac{2A(p-p_0)}{K\alpha} - \frac{A_0 E_\infty(\alpha-1)}{E_0}\right]. \tag{3.38}$$

To extend the applicability of Eq. (3.36) to viscoelastic models characterized by more than three parameters, an original formulation is proposed. Considering a generalized Kelvin-Voigt chain, with N_{KV} Kelvin-Voigt units in series and one isolated spring, as shown in Fig. 2.6, the procedure starts from the constitutive equation of the model, Eq. (2.22). Recurring to the same manipulations previously described for the SLS case, the following closure equation for the g-KV model is obtained:

$$\frac{\partial A}{\partial t} + \frac{1}{\rho + \frac{K\alpha}{2c_s'^2}} \frac{\partial (A\rho u)}{\partial x} = \frac{AE_0(p-p_0)}{\rho c_s'^2 + \frac{K\alpha}{2}} \sum_{k=1}^{N_{KV}} \frac{1}{\eta_k} - \frac{AK}{\rho c_s'^2 + \frac{K\alpha}{2}} \sum_{k=1}^{N_{KV}} \frac{\epsilon_k}{\tau_{ck}}. \tag{3.39}$$

in which η_k and E_k, $\tau_{ck} = \eta_k/E_k$, are the viscoelastic parameters of the k^{th} KV element (refer to Section 2.3.4) and ϵ_r represents the retarded strain of the system, equal to the sum of the strains of each KV unit: $\epsilon_r = \sum_{k=1}^{N_{KV}} \epsilon_k$. Again, it is possible to derive the corresponding ODE of (3.39), resulting:

$$\frac{\mathrm{d}A}{\mathrm{d}t} = \frac{2A}{K\alpha}\frac{\mathrm{d}p}{\mathrm{d}t} + \frac{2AE_0(p-p_0)}{K\alpha} \sum_{k=1}^{N_{KV}} \frac{1}{\eta_k} - 2A_0 \sum_{k=1}^{N_{KV}} \frac{\epsilon_k}{\tau_{ck}}. \tag{3.40}$$

On the other hand, when choosing to consider the system of the classical water-hammer equations, taking into account the viscoelasticity of the tube wall means that

a specific term must be added into the continuity equation (3.7), whereas the momentum equation (3.13b) remains unaltered (Covas, 2003), following:

$$\frac{\partial h}{\partial t} + \frac{a^2}{g}\frac{\partial u}{\partial x} = -\frac{2a^2}{g}\frac{\mathrm{d}\epsilon_r}{\mathrm{d}t}, \tag{3.41}$$

Boltzmann superposition principle states that for small strains each increment of load makes an independent and linearly additive contribution to the total deformation (Shaw and MacKnight, 2005). Hence, the elastic deformation results:

$$\epsilon_e(t) = J_0\sigma(t), \tag{3.42}$$

where J_0 is the instantaneous creep compliance ($J_0 = 1/E_0$ for linear viscoelastic materials), while the retarded deformation is defined as:

$$\epsilon_r(t) = \int_0^t \sigma(t-t')\frac{\partial J}{\partial t}(t')\,\mathrm{d}t', \tag{3.43}$$

with $J(t')$ creep function at time t'. The total deformation of the system is the sum of these two contributes, $\epsilon = \epsilon_e + \epsilon_r$. Applying Barlow's formula (3.10), the total circumferential strain can also be expressed as (Covas et al., 2005):

$$\epsilon = \epsilon_e + \epsilon_r = W\left[p(t) - p_0\right]J_0 + W\int_0^t \left[p(t-t') - p_0\right]\frac{\partial J(t')}{\partial t}\mathrm{d}t' \tag{3.44}$$

with the thickness s_0 considered constant in time. This equation is valid for a g-KV model with a selected N_{KV}, being the creep function of the pipe wall represented by a mathematical expression, Eq. (2.24), which can be implemented numerically.
It is worth to notice that, for the SLS model of KV type, N_{KV} is equal to 1 and it is possible to go back to the equations of this model directly starting from the generalized equations of the g-KV chain.

3.2.1.5 Complete coupled system of the FSI problem

As described in the previous Sections, the continuity and the momentum equations can be expressed in different forms. Moreover, the closure equations have different formulations depending on the assumed behavior of the pipe material and the relevance of the flow unsteadiness in the computation of friction effects. The more appropriate formulation of the system of governing equations depends on the chosen numerical integration technique. In this Section, we summarize, for each numerical method considered in this work, the most suited form of the complete system of equations.

To take into account the FSI, working in the context of an explicit Finite Volume Method (Leibinger et al., 2016), the PDE of the material model can be inserted into the system of averaged Navier-Stokes equations (3.1), obtaining and augmented FSI (a-FSI)

system:

$$\frac{\partial}{\partial t}(A\rho) + \frac{\partial}{\partial x}(A\rho u) = 0 \tag{3.45a}$$

$$\frac{\partial}{\partial t}(A\rho u) + \frac{\partial}{\partial x}(A\rho u^2 + Ap) - p\frac{\partial A}{\partial x} = F_R \tag{3.45b}$$

$$\frac{\partial}{\partial t}A + d\frac{\partial}{\partial x}(A\rho u) = S \tag{3.45c}$$

$$\frac{\partial}{\partial t}A_0 = 0. \tag{3.45d}$$

Equation (3.45c) unifies both the elastic and the viscoelastic wall models (Leibinger et al., 2016). The parameter d identifies the solely elastic contribute of the wall, having indeed the same formulation if choosing an elastic or a viscoelastic characterization, while the source term S takes into account the viscous information of the wall behavior. Hence, concerning the Laplace elastic law

$$d = \frac{1}{\rho + \frac{K\alpha}{2c_s'^2}}, \qquad S = 0. \tag{3.46}$$

For the viscoelastic SLS model

$$d = \frac{1}{\rho + \frac{K\alpha}{2c_s'^2}}, \qquad S = \frac{1}{\tau_r}\left[\frac{Ad}{c_s'^2}(p - p_0) - \frac{AdKE_\infty}{2c_s'^2 E_0}(\alpha - 1)\right], \tag{3.47}$$

being in general for a viscoelastic g-KV model

$$d = \frac{1}{\rho + \frac{K\alpha}{2c_s'^2}}, \qquad S = \frac{AdE_0}{c_s'^2}(p - p_0)\sum_{k=1}^{N_{KV}}\frac{1}{\eta_k} - \frac{AdK}{c_s'^2}\sum_{k=1}^{N_{KV}}\frac{\epsilon_k}{\tau_{ck}}. \tag{3.48}$$

It has to be remembered that if we are considering a thick-walled tube (which means that the ratio between external wall radius R_e and inner radius R is bigger than 1.2) Barlow's formula (3.10) is not valid anymore, and the geometry parameter W is defined as follows (Leibinger et al., 2016):

$$W = 2\frac{\left(\frac{R_e}{R}\right)(1 + \nu_p) + 1 - 2\nu_p}{\left(\frac{R_e}{R}\right)^2 - 1}. \tag{3.49}$$

with ν_p Poisson's ratio.

Eq. (3.45d) simply states that the spatially variable equilibrium cross-section A_0 is constant in time. This trivial equation is introduced to allow a formally correct treatment of discontinuous longitudinal changes of A_0. In fact, in case of discontinuous A_0, the system of governing equations is non-conservative and appropriate numerical techniques must be selected, as done in other contexts (Müller and Toro, 2013; Gallardo, Parés, and Castro, 2007). The explicit scheme proposed by Dumbser and Toro (2011b) and further discussed by (Leibinger et al., 2016) belongs to the family of the path-conservative schemes that have specifically been developed to address the problem of discontinuous variables arising in applications governed by non-conservative balance laws. The reader is addressed to Parés (2006) for the theory related to the path-conservative schemes.

Considering the semi-implicit numerical scheme proposed by Dumbser, Iben, and

Ioriatti (2015) for the resolution of the problem, we can more easily consider the standard two-equation system

$$\frac{\partial}{\partial t}(A\rho) + \frac{\partial}{\partial x}(A\rho u) = 0 \tag{3.50a}$$

$$\frac{\partial}{\partial t}(A\rho u) + \frac{\partial}{\partial x}(A\rho u^2) = -A\frac{\partial p}{\partial x} F_R, \tag{3.50b}$$

associated with the tube law expressed by Eq. (3.30) for an elastic wall model and the ODEs (3.38) and (3.40) when considering the viscoelastic SLS and g-KV models, respectively.

On the other hand, using the MOC for the discretization, the classical water hammer equations considering the FSI have the following final form (Covas, 2003):

$$\frac{\partial h}{\partial t} + \frac{a^2}{g}\frac{\partial u}{\partial x} = S_M \tag{3.51a}$$

$$\frac{1}{g}\frac{\partial u}{\partial t} + \frac{\partial h}{\partial x} = -\frac{4\tau_w}{\rho g D} = -j. \tag{3.51b}$$

with $S_M = 0$ for an elastic wall behavior and

$$S_M = -\frac{2a^2}{g}\frac{\mathrm{d}\epsilon_r}{\mathrm{d}t} \tag{3.52}$$

for a viscoelastic wall behavior. The retarded deformation ϵ_r in Eq. (3.52) is computed by (3.43), selecting the appropriate creep function (2.24) for the SLS and g-KV models.

Finally, in Eqs. (3.45b), (3.50b) and (3.51b) the friction term F_R is evaluated through Eq. (3.20), considering a wall shear stress τ_w computed with Eq. (3.21) if the quasi-steady model is applicable or using Eq. (3.23) if taking into account unsteady flow effects results necessary.

3.2.2 Numerical models

To solve the mathematical models presented in Section 3.2.1, three different numerical schemes have been chosen and compared. The standard way to solve the simplified system (3.51) in case of water hammer problems is recurring to the Method of Characteristics. Other two methods have been tested and compared, in terms of accuracy and efficiency, to the classical MOC: the explicit path-conservative FVM associated with the DOT Riemann solver presented in Dumbser and Toro (2011b) and Dumbser and Toro (2011a) and the semi-implicit FVM for axially symmetric compressible flows in compliant tubes proposed by Dumbser, Iben, and Ioriatti (2015).

3.2.2.1 Method of Characteristics

The simplified system (3.51), obtained by neglecting the convective terms and thus leading to approximately straight characteristic lines $\Delta x/\Delta t = \pm a$, can be solved with the numerical scheme proposed by Covas et al. (2005):

$$h_i^{n+1} - h_{i\mp1}^n \pm \frac{a}{g}\left(u_i^{n+1} - u_{i\mp1}^n\right) + \frac{2a^2\Delta t}{g}\left(\frac{\mathrm{d}\epsilon_r}{\mathrm{d}t}\right) \pm \frac{f\Delta x}{2gD} u_{i\mp1}^n \left|u_{i\mp1}^n\right| = 0 \tag{3.53}$$

valid along the characteristic lines, using a uniform grid of N_x elements with mesh spacing $\Delta x = x_{i+1} - x_i$ and a time step size $\Delta t = t^{n+1} - t^n$ which respects the Courant-Friedrichs-Lewy, CFL, condition (Toro, 2009):

$$\Delta t = \mathrm{CFL}\frac{\Delta x}{max|u \pm a|}. \tag{3.54}$$

Decoupling the problem we get:

$$u_i^{n+1} = \frac{u_{i-1}^n + u_{i+1}^n}{2} + \frac{g}{a}\left(\frac{h_{i-1}^n - h_{i+1}^n}{2}\right) - \frac{g\Delta x}{2a}\left(j_{i-1}^n + j_{i+1}^n\right), \tag{3.55a}$$

$$h_i^{n+1} = \frac{h_{i-1}^n + h_{i+1}^n}{2} + \frac{a}{g}\left(\frac{u_{i-1}^n - u_{i+1}^n}{2}\right) - \frac{\Delta x}{2}\left(j_{i-1}^n - j_{i+1}^n\right) - \frac{2a\Delta x}{g}\left(\frac{\mathrm{d}\epsilon_r^n}{\mathrm{d}t}\right), \tag{3.55b}$$

with

$$j_{i-1}^n = \frac{f}{2gD}u_{i-1}^n\left|u_{i-1}^n\right| \qquad \text{and} \qquad j_{i+1}^n = \frac{f}{2gD}u_{i+1}^n\left|u_{i+1}^n\right|.$$

Starting from Eq. (3.44), the time-derivative of ϵ_r is computed as a sum of each k^{th} Kelvin-Voigt element contribution at time n:

$$\frac{\mathrm{d}\epsilon_r^n}{\mathrm{d}t} = \sum_{k=1}^{N_{KV}}\frac{\mathrm{d}\epsilon_k^n}{\mathrm{d}t} = \sum_{k=1}^{N_{KV}}\left[W\rho g\frac{J_k}{\tau_{ck}}\left(h^n - h_0\right) - \frac{\epsilon_k^n}{\tau_{ck}}\right], \tag{3.56}$$

with h_0 equilibrium piezometric head and considering the numerical approximation of each retarded strain in each node as:

$$\epsilon_k^n \approx \tilde{\epsilon}_k^n = J_k\hat{F}^n - J_k e^{-\Delta t/\tau_{ck}}\hat{F}^{n-1} - J_k\tau_{ck}\left(1 - e^{-\Delta t/\tau_{ck}}\right)\frac{\hat{F}^n - \hat{F}^{n-1}}{\Delta t} + e^{-\Delta t/\tau_{ck}}\tilde{\epsilon}_k^{n-1}, \tag{3.57}$$

with the function $\hat{F}$ at time n defined by:

$$\hat{F}^n = W\rho g\frac{J_k}{\tau_{ck}}\left(h^n - h_0\right).$$

For further details about this scheme the reader can refer to Covas et al. (2005).
It is here specified that to obtain reliable results in the Riemann problems presented in Section 3.3.1, the Method of Specified Intervals has been applied, with a linear interpolation from the known values in the grid nodes at each time step (Wylie and Streeter, 1978).

3.2.2.2 Explicit Path-Conservative Finite Volume Method

A non-linear hyperbolic system of PDE with a conservative and a non-conservative part can be written in the following general form:

$$\frac{\partial \boldsymbol{Q}}{\partial t} + \frac{\partial}{\partial x}\boldsymbol{f}(\boldsymbol{Q}) + \boldsymbol{B}(\boldsymbol{Q})\frac{\partial \boldsymbol{Q}}{\partial x} = \boldsymbol{S}(\boldsymbol{Q}) \tag{3.58}$$

where $\boldsymbol{Q}$ is the conservative variables vector, $\boldsymbol{f}$ is the analytical fluxes vector related to the conservative part, $\boldsymbol{B}(\boldsymbol{Q})$ is the matrix related to the non-conservative part and $\boldsymbol{S}(\boldsymbol{Q})$ is the source term vector containing all the head losses and material viscosity information,

depending on the viscoelastic model adopted (see Section 3.2.1.5).
System (3.58) can also be written in the quasi-linear form,

$$\frac{\partial \boldsymbol{Q}}{\partial t} + \boldsymbol{A}(\boldsymbol{Q})\frac{\partial \boldsymbol{Q}}{\partial x} = \boldsymbol{S}(\boldsymbol{Q}), \tag{3.59}$$

in which the matrix $\boldsymbol{A}(\boldsymbol{Q}) = \partial \boldsymbol{f}/\partial \boldsymbol{Q} + \boldsymbol{B}(\boldsymbol{Q})$ is diagonalizable, with a diagonal matrix $\boldsymbol{\Lambda}(\boldsymbol{Q})$ containing all real eigenvalues λ_l and a complete set of linearly independent eigenvectors $\boldsymbol{R}(\boldsymbol{Q})$ (Leibinger et al., 2016).
Considering system (3.45),

$$\boldsymbol{Q} = \begin{pmatrix} A\rho \\ A\rho u \\ A \\ A_0 \end{pmatrix} \quad \boldsymbol{f}(\boldsymbol{Q}) = \begin{pmatrix} A\rho u \\ A\rho u^2 + Ap \\ 0 \\ 0 \end{pmatrix}, \quad \frac{\partial \boldsymbol{f}}{\partial \boldsymbol{Q}} = \begin{pmatrix} 0 & 1 & 0 & 0 \\ c_s'^2 - u^2 & 2u & p - \rho c_s'^2 & 0 \\ 0 & 0 & 0 & 0 \\ 0 & 0 & 0 & 0 \end{pmatrix},$$

$$\boldsymbol{B}(\boldsymbol{Q}) = \begin{pmatrix} 0 & 0 & 0 & 0 \\ 0 & 0 & -p & 0 \\ 0 & d & 0 & 0 \\ 0 & 0 & 0 & 0 \end{pmatrix}, \quad \boldsymbol{A}(\boldsymbol{Q}) = \begin{pmatrix} 0 & 1 & 0 & 0 \\ c_s'^2 - u^2 & 2u & -\rho c_s'^2 & 0 \\ 0 & d & 0 & 0 \\ 0 & 0 & 0 & 0 \end{pmatrix},$$

$$\boldsymbol{\Lambda} = \begin{pmatrix} 0 & 0 & 0 & 0 \\ 0 & 0 & 0 & 0 \\ 0 & 0 & u-a & 0 \\ 0 & 0 & 0 & u+a \end{pmatrix}, \quad \boldsymbol{R} = \begin{pmatrix} \frac{\rho c_s'^2}{c_s'^2 - u^2} & 0 & \frac{1}{d} & \frac{1}{d} \\ 0 & 0 & \frac{u-a}{d} & \frac{u+a}{d} \\ 1 & 0 & 1 & 1 \\ 0 & 1 & 0 & 0 \end{pmatrix},$$

with wave speed from Eq. (3.14) considering the linearized version of the Laplace law (3.30):

$$a = \sqrt{c_s'^2(1 - \rho d)} = \frac{c_s'}{\sqrt{1 + \frac{2\rho c_s'^2}{K\alpha}}}, \tag{3.60}$$

where

$$c_s' = \sqrt{\frac{\partial p}{\partial \rho}} = \begin{cases} c_s & \text{if} \quad p \geq p_v \\ \frac{(\rho_0 K R_v T_0 - Kp)(p - p_v) - p}{\sqrt{\rho_0 K(\rho_0 T_0 R_v p_v - p^2)}} & \text{if} \quad 0 < p < p_v \end{cases}. \tag{3.61}$$

The explicit second order total variation diminishing (TVD) finite volume discretization of system (3.45) is:

$$\boldsymbol{Q}_i^{n+1} = \boldsymbol{Q}_i^n - \frac{\Delta t}{\Delta x}\left(\boldsymbol{F}_{i+\frac{1}{2}} - \boldsymbol{F}_{i-\frac{1}{2}}\right) - \frac{\Delta t}{\Delta x}\left(\boldsymbol{D}_{i+\frac{1}{2}} + \boldsymbol{D}_{i-\frac{1}{2}}\right) - \Delta t \boldsymbol{B}\left(\boldsymbol{Q}_i^{n+\frac{1}{2}}\right)\frac{\Delta \boldsymbol{Q}_i^n}{\Delta x} + \Delta t \boldsymbol{S}\left(\boldsymbol{Q}_i^{n+\frac{1}{2}}\right), \tag{3.62}$$

with $\boldsymbol{F}_{i\pm\frac{1}{2}}$ numerical fluxes and $\boldsymbol{D}_{i\pm\frac{1}{2}}$ fluctuations, both evaluated at the cell interfaces, using a uniform grid of N_x elements with mesh spacing $\Delta x = x_{i+\frac{1}{2}} - x_{i-\frac{1}{2}}$ and a time step size $\Delta t = t^{n+1} - t^n$ that follows the CFL condition of Eq. (3.54). Here the slope $\Delta \boldsymbol{Q}_i^n$ is evaluated by using the classical minmod slope limiter (Toro, 2009) and variables at the intermediate time step $\Delta t/2$ are evaluated with the following equation:

$$\boldsymbol{Q}_i^{n+\frac{1}{2}} = \boldsymbol{Q}_i^n + \frac{1}{2}\Delta t \partial_t \boldsymbol{Q}_i^n, \tag{3.63}$$

with the time derivative

$$\partial_t \boldsymbol{Q}_i^n = -\frac{\boldsymbol{f}\left(\boldsymbol{Q}_i^n + \frac{1}{2}\Delta\boldsymbol{Q}_i^n\right) - \boldsymbol{f}\left(\boldsymbol{Q}_i^n - \frac{1}{2}\Delta\boldsymbol{Q}_i^n\right)}{\Delta x} - \boldsymbol{B}\left(\boldsymbol{Q}_i^n\right)\frac{\Delta\boldsymbol{Q}_i^n}{\Delta x} + \boldsymbol{S}\left(\boldsymbol{Q}_i^n\right). \tag{3.64}$$

The numerical flux is obtained applying the DOT solver as defined by Dumbser and Toro (2011a):

$$\boldsymbol{F}_{i\pm\frac{1}{2}} = \frac{1}{2}\left[\boldsymbol{f}\left(\boldsymbol{Q}_{i\pm\frac{1}{2}}^+\right) + \boldsymbol{f}\left(\boldsymbol{Q}_{i\pm\frac{1}{2}}^-\right)\right] - \frac{1}{2}\int_0^1 \left|\boldsymbol{A}\left(\Psi\left(\boldsymbol{Q}_{i\pm\frac{1}{2}}^-, \boldsymbol{Q}_{i\pm\frac{1}{2}}^+, s\right)\right)\right| \frac{\partial\Psi}{\partial s}\mathrm{d}s, \tag{3.65}$$

with a numerical dissipation related to matrix $\boldsymbol{A}$ including both conservative and non-conservative terms.
The fluctuations given by the non-conservative part then read (Dumbser and Toro, 2011b):

$$\boldsymbol{D}_{i\pm\frac{1}{2}} = \frac{1}{2}\int_0^1 \boldsymbol{B}\left(\Psi\left(\boldsymbol{Q}_{i\pm\frac{1}{2}}^-, \boldsymbol{Q}_{i\pm\frac{1}{2}}^+, s\right)\right)\frac{\partial\Psi}{\partial s}\mathrm{d}s. \tag{3.66}$$

The boundary-extrapolated values within cell i are given by:

$$\boldsymbol{Q}_{i+\frac{1}{2}}^- = \boldsymbol{Q}_i^n + \frac{1}{2}\Delta\boldsymbol{Q}_i^n + \frac{1}{2}\Delta t\partial_t\boldsymbol{Q}_i^n, \qquad \boldsymbol{Q}_{i-\frac{1}{2}}^+ = \boldsymbol{Q}_i^n - \frac{1}{2}\Delta\boldsymbol{Q}_i^n + \frac{1}{2}\Delta t\partial_t\boldsymbol{Q}_i^n. \tag{3.67}$$

The symbol Ψ stands for the path connecting left to right boundary values in the phase-space. In this work, a simple linear segment has been chosen (Parés, 2006), hence:

$$\Psi = \Psi\left(\boldsymbol{Q}_{i+\frac{1}{2}}^-, \boldsymbol{Q}_{i+\frac{1}{2}}^+, s\right) = \boldsymbol{Q}_{i+\frac{1}{2}}^- + s\left(\boldsymbol{Q}_{i+\frac{1}{2}}^+ - \boldsymbol{Q}_{i+\frac{1}{2}}^-\right). \tag{3.68}$$

For an extension to a non-linear path scheme, the reader can refer to applications for the Shallow Water Equations (Caleffi and Valiani, 2017). Approximating Eq. (3.65) and (3.66) with a Gauss-Legendre quadrature formula we get the final expressions to solve Eq. (3.62) numerically:

$$\boldsymbol{F}_{i+\frac{1}{2}} = \frac{1}{2}\left[\boldsymbol{f}\left(\boldsymbol{Q}_{i+\frac{1}{2}}^+\right) + \boldsymbol{f}\left(\boldsymbol{Q}_{i+\frac{1}{2}}^-\right)\right] - \frac{1}{2}\sum_{j=1}^{N_G}\left[\omega_j\left|\boldsymbol{A}\left(\Psi\left(\boldsymbol{Q}_{i+\frac{1}{2}}^-, \boldsymbol{Q}_{i+\frac{1}{2}}^+, s_j\right)\right)\right|\right]\left(\boldsymbol{Q}_{i+\frac{1}{2}}^+ - \boldsymbol{Q}_{i+\frac{1}{2}}^-\right) \tag{3.69}$$

$$\boldsymbol{D}_{i+\frac{1}{2}} = \frac{1}{2}\sum_{j=1}^{N_G}\left[\omega_j\boldsymbol{B}\left(\Psi\left(\boldsymbol{Q}_{i+\frac{1}{2}}^-, \boldsymbol{Q}_{i+\frac{1}{2}}^+, s_j\right)\right)\right]\left(\boldsymbol{Q}_{i+\frac{1}{2}}^+ - \boldsymbol{Q}_{i+\frac{1}{2}}^-\right), \tag{3.70}$$

where ω_j and s_j are the weights and nodes of the Gauss-Legendre quadrature, in the present work chosen with 3 nodes ($N_G = 3$).
For the evaluation of the source term related to the tube wall viscosity, it has to be noticed that, when choosing the g-KV model, ϵ_{rk} in Eq. (3.48) can be calculated with the numerical approximation already presented in Eq. (3.57).

3.2.2.3 Semi-Implicit Finite Volume Method

To solve the problem a semi-implicit numerical method, it is considered that along the pipe of length L there are N_x intervals of constant length $\Delta x = L/N_x$. The one-dimensional domain is composed by two overlapping grids according to the staggered approach: one is for the evaluation of pressure, called main grid, and the other is for the

evaluation of the fluxes, the dual mesh. The pressure is located at the cell barycenter x_i, meanwhile the velocities and the mass fluxes are defined at the edges $x_{i\pm\frac{1}{2}}$ of each cell. Then, to easily achieve second order of accuracy in time, the so called θ-method is used (Ioriatti, Dumbser, and Iben, 2017). θ is an implicitness parameter chosen in the interval $0.5 \leq \theta \leq 1$ for stability. In particular, when $\theta = 1$ the scheme is first order accurate in time and when $\theta = 0.5$ the method corresponds to a Crank-Nicolson type scheme of the second order. In the latter situation, the scheme is non-monotone and spurious oscillations could appear near strong discontinuities (Toro, 2009). To have an example, the θ-method applied to the pressure leads to:

$$p_i^{n+\theta} = \theta p_i^{n+1} + (1-\theta) p_i^n.$$

The continuity equation is discretized in the main grid in a semi-implicit way:

$$\rho A\left(p_i^{n+1}\right) = \rho A\left(p_i^n\right) - \frac{\Delta t}{\Delta x}\left(Q_{i+\frac{1}{2}}^{n+\theta} - Q_{i-\frac{1}{2}}^{n+\theta}\right), \tag{3.71}$$

where $\rho A\left(p_i\right) = \rho\left(p_i\right) A\left(p_i\right)$ and the mass flow rate $Q_{i+\frac{1}{2}}^{n+1} = \rho_{i+\frac{1}{2}}^n A_{i+\frac{1}{2}}^n u_{i+\frac{1}{2}}^{n+1}$, expressing $\rho_{i+\frac{1}{2}}^n = \frac{1}{2}\rho\left(p_i^n\right) + \frac{1}{2}\rho\left(p_{i+1}^n\right)$ and $A_{i+\frac{1}{2}}^n = \frac{1}{2}A\left(p_i^n\right) + \frac{1}{2}A\left(p_{i+1}^n\right)$.
Then, the semi-implicit discretization of the momentum equation yields to:

$$\frac{Q_{i+\frac{1}{2}}^{n+1} - FQ_{i+\frac{1}{2}}^n}{\Delta t} = -A_{i+\frac{1}{2}}^n \frac{\Delta t}{\Delta x}\left(p_{i+1}^{n+\theta} - p_i^{n+\theta}\right) - 2\pi R_{i+\frac{1}{2}}^n \left(\tau_w^n\right)_{i+\frac{1}{2}}, \tag{3.72}$$

where, as from Eq. (3.22),

$$\left(\tau_w^n\right)_{i+\frac{1}{2}} = \left(\tau_s^n\right)_{i+\frac{1}{2}} + \left(\tau_u^n\right)_{i+\frac{1}{2}} = f_{i+\frac{1}{2}}^n \frac{\rho_{i+\frac{1}{2}}^n u_{i+\frac{1}{2}}^n u_{i+\frac{1}{2}}^{n+1}}{8} + \left(\tau_u^n\right)_{i+\frac{1}{2}}$$

and τ_u^n computed with the approximation of the Zielke integral presented in Section 3.2.1.2. Furthermore, FQ is an explicit and nonlinear operator for the convective terms. Here it is considered a robust explicit upwind approach based on the Rusanov method which allows also to keep the well-balancing properties of the flux as done by Dumbser, Iben, and Ioriatti (2015) and Ioriatti, Dumbser, and Iben (2017):

$$FQ_{i+\frac{1}{2}}^n = Q_{i+\frac{1}{2}}^n - \frac{\Delta t}{\Delta x}\left(f_{i+1}^{Rus,n} - f_i^{Rus,n}\right), \tag{3.73}$$

with

$$f_i^{Rus,n} = \frac{1}{2}\left(u_{i+\frac{1}{2}}^n Q_{i+\frac{1}{2}}^n + u_{i-\frac{1}{2}}^n Q_{i-\frac{1}{2}}^n\right) - \frac{1}{2} S_{\max}\left(Q_{i+\frac{1}{2}}^n - Q_{i-\frac{1}{2}}^n\right), \tag{3.74}$$

$$S_{\max} = 2\max\left(|u_{i-\frac{1}{2}}^n|, |u_{i+\frac{1}{2}}^n|\right). \tag{3.75}$$

In addition, Eq. (3.72) is manipulated resulting:

$$Q_{i+\frac{1}{2}}^{n+1} = G_{i+\frac{1}{2}}^n - \theta A_{i+\frac{1}{2}}^n \frac{\Delta t}{\Delta x}\left(p_{i+1}^{n+1} - p_i^{n+1}\right) - \Delta t \gamma_{i+\frac{1}{2}}^n Q_{i+\frac{1}{2}}^{n+1}, \tag{3.76}$$

where the term $\gamma^n_{i+\frac{1}{2}} = \frac{2\pi R^n_{i+\frac{1}{2}} f^n_{i+\frac{1}{2}} |u^n_{i+\frac{1}{2}}|}{8A^n_{i+\frac{1}{2}}} \geq 0$ accounts for the explicit contribution of the quasi-steady friction and $G^n_{i+\frac{1}{2}}$ collects all the explicit terms:

$$G^n_{i+\frac{1}{2}} = FQ^n_{i+\frac{1}{2}} - (1-\theta)\, A^n_{i+\frac{1}{2}} \frac{\Delta t}{\Delta x} \left(p^n_{i+1} - p^n_i\right) - 2\pi R^n_{i+\frac{1}{2}} \left(\tau_u\right)^n_{i+\frac{1}{2}} \Delta t. \tag{3.77}$$

Collecting all the quantities with $Q^{n+1}_{i+\frac{1}{2}}$ on the left side member yields to the following expression:

$$Q^{n+1}_{i+\frac{1}{2}} = \left(\frac{G}{1+\Delta t\gamma}\right)^n_{i+\frac{1}{2}} - \theta \frac{\Delta t}{\Delta x} \left(\frac{A}{1+\Delta t\gamma}\right)^n_{i+\frac{1}{2}} \left(p^{n+1}_{i+1} - p^{n+1}_i\right). \tag{3.78}$$

Coupling Eq. (3.78) with Eq. (3.71) gives:

$$\rho A \left(p^{n+1}_i\right) - \theta^2 \frac{\Delta t^2}{\Delta x^2} \left[\left(p^{n+1}_{i+1} - p^{n+1}_i\right) \left(\frac{A}{1+\Delta t\gamma}\right)^n_{i+\frac{1}{2}} - \left(p^{n+1}_i - p^{n+1}_{i-1}\right) \left(\frac{A}{1+\Delta t\gamma}\right)^n_{i-\frac{1}{2}}\right] = b^n_i, \tag{3.79}$$

with the known right hand side,

$$b^n_i = \rho A \left(p^n_i\right) + \left(\frac{G}{1+\Delta t\gamma}\right)^n_{i+\frac{1}{2}}.$$

Eq. (3.79) can also be written in the following mildly non-linear form,

$$\rho \boldsymbol{A}\left(\boldsymbol{p}^{n+1}\right) + \boldsymbol{T}\boldsymbol{p}^{n+1} = \boldsymbol{b}^n, \tag{3.80}$$

where $\rho \boldsymbol{A}$ is the non-linear diagonal contribution, $\boldsymbol{T}$ is the linear and symmetric three-diagonal matrix and $\boldsymbol{p}^{n+1}$ is the unknown vector pressure and $\boldsymbol{b}^n$.
System (3.80) can be solved by using a Newton-type algorithm such as the one proposed by Brugnano and Casulli (2008) and Brugnano and Casulli (2009) or the more general one by Casulli and Zanolli (2010) and Casulli and Zanolli (2012). For more details the reader can refer to Ioriatti, Dumbser, and Iben (2017), Dumbser, Iben, and Ioriatti (2015), Tavelli, Dumbser, and Casulli (2013), Fambri, Dumbser, and Casulli (2014), and Casulli, Dumbser, and Toro (2012). The density is updated using the closure EOS presented in Eq. (3.17) while the cross-sectional area is updated using the Laplace law (3.30) or the ODE versions of Eq. (3.38) and Eq. (3.40), respectively discretized as follows:

$$A^{n+1}_i = A^n_i + \frac{2A^n_i}{K\alpha^n_i} \left(p^{n+1}_i - p^n_i\right) + \frac{\Delta t}{\tau_r} \left[\frac{2A^n_i (p^{n+1}_i - p_0)}{K\alpha^n_i} - \frac{A_0 E_\infty (\alpha^n_i - 1)}{E_0}\right] \tag{3.81}$$

$$A^{n+1}_i = A^n_i + \frac{2A^n_i}{K\alpha^n_i} \left(p^{n+1}_i - p^n_i\right) + \Delta t \left[\frac{2A^n_i E_0 (p^{n+1}_i - p_0)}{K\alpha^n_i} \sum_{k=1}^{N_{KV}} \frac{1}{\eta_k} - 2A_0 \sum_{k=1}^{N_{KV}} \frac{\epsilon_{rk}}{\tau_{rk}}\right]. \tag{3.82}$$

Also in this case, ϵ_{rk} in Eq. (3.82) is evaluated with the numerical approximation presented in Eq. (3.57).

Finally, the velocity is computed as:

$$u_{i+\frac{1}{2}}^{n+1} = \frac{Q_{i+\frac{1}{2}}^{n+1}}{\rho_{i+\frac{1}{2}}^{n} A_{i+\frac{1}{2}}^{n}}.$$

The time step Δt for the semi-implicit model is the one given by the stability condition for the computation of the non-linear convective terms. In this case we have that

$$\Delta t = \mathsf{CFL}\frac{\Delta x}{2|u_{max}|},$$

instead of the standard CFL condition defined in Eq. (3.54). It is worth underling that this condition is based only on the fluid velocity and not taking into account the wave speed, which makes this method very efficient especially in the low Mach number regime. In addition, for some simulations, the contribution of the convective terms can be neglected, resulting $FQ = Q$, and the scheme becomes unconditionally stable. However, it is important to properly choose the time step Δt to reduce the numerical viscosity of the method.

3.2.3 Unsteady friction effects and ODE friction model validation

In order to better analyze the effects of the unsteady friction term and to validate the ODE friction model presented in Section 3.2.1.2 for turbulent flow cases, a water hammer test case is analyzed assuming, as first attempt, that the pressure damping is determined only by friction losses, neglecting viscoelastic effects. In Fig. 3.2 the classical water hammer solution obtained considering only the quasi-steady friction term in Eq. (3.22) is presented together with the solutions derived taking into account the complete expression of the equation, using different unsteady friction models. Reference solutions are represented by Brunone's model, Thrika's and Kagawa's formulation. In the same figure, the experimental curve is also shown.
Simulations are run only using the explicit path-conservative method presented in Section 3.2.2.2, since the unsteady friction models behave in the same way in all the numerical schemes, not being affected by the chosen numerical discretization.

Brunone's model (Brunone et al., 2000) belongs to the Instantaneous Acceleration (IA) methods, based on the hypothesis that the unsteady wall shear stress is directly proportional to the acceleration of the flow, thus:

$$\tau_u = \frac{\rho D K_{Bru}}{4}\left[\frac{\partial u}{\partial t} + sign\left(u\frac{\partial u}{\partial x}\right)c_s\frac{\partial u}{\partial x}\right], \tag{3.83}$$

considering for the coefficient K_{Bru} the expression suggested by Vardy and Brown (Vardy and Brown, 1995):

$$K_{Bru} = 0.5\sqrt{\frac{7.41}{\mathsf{Re}^{\chi}}}, \qquad \chi = \log\left(\frac{14.3}{\mathsf{Re}^{0.05}}\right). \tag{3.84}$$

Trikha's and Kagawa's formulations belong to the class of the Convolution Integral (CI) methods, as the ODE friction model presented in this work, for which the analytic expression for the unsteady losses is given by Zielke's convolution integral, Eq. (3.23). To solve this integral in turbulent flow conditions, firstly Trikha (1975) proposed to use the same approach adopted for the laminar case with the following approximated weighting

function:

$$w(t) = \sum_{i=1}^{N_w} m_i \exp\left(-n_i \frac{\nu t}{R^2}\right) \tag{3.85}$$

with N_w = 3, (m_1, m_2, m_3) = (40.0, 8.1, 1) and (n_1, n_2, n_3) = (8000, 200, 26.4). Writing the weighting function as a series of exponential functions, the unsteady wall shear stress calculated with Trikha's formulation becomes:

$$\tau_u^{n+1} \approx \frac{2\mu}{R} \sum_{i=1}^{3} \tau_i^{n+1} = \frac{2\mu}{R} \left[\sum_{i=1}^{3} \exp\left(-n_i \frac{\nu t}{R^2}\right) \tau_i^n + \sum_{i=1}^{3} m_i \left(u^{n+1} - u^n\right) \right]. \tag{3.86}$$

Successively, Kagawa et al. (1983) proposed a more efficient formulation to approximate the convolution integral. Considering the weighting function for turbulent cases presented in in Eq. (3.24) with Urbanowicz and Zarzycki coefficients (Urbanowicz and Zarzycki, 2012), Kagawa's solution becomes:

$$\tau_u^{n+1} \approx \frac{2\mu}{R} \left[\sum_{i=1}^{N_w} \exp\left(-(n_i^* + B^*) \frac{\nu t}{R^2}\right) \tau_i^n + \sum_{i=1}^{N_w} A^* m_i^* \exp\left(-(n_i^* + B^*) \frac{\nu t}{R^2}\right) \left(u^{n+1} - u^n\right) \right]. \tag{3.87}$$

It can easily be observed from Fig. 3.2 that with none of the friction formulations it is possible to correctly reproduce the dampening behavior of an HDPE pipe in case of hydraulic transients, confirming that viscoelastic effects must be taken into account if realistic solutions are expected. It is possible to observe that the shape of the pressure wave appears significantly different than the reference solution. In particular, Brunone's model has a less smooth behavior, as already highlighted by other publications (Brunone et al., 2000; Ioriatti, Dumbser, and Iben, 2017). This particular shape of the wave is a feature of all the IA methods. There is also a small disagreement between Trikha's and Kagawa's formulations that can be attributed to the different sets of parameters adopted in each case for the weighting function (Ioriatti, Dumbser, and Iben, 2017; Urbanowicz and Zarzycki, 2012).
Nevertheless, with this test, it can be confirmed that the ODE friction model reproduces reliable results if compared to the other unsteady friction models. As expected, adopting the ODE friction model the same solution given by Kagawa's formulation is obtained. Both these two unsteady friction models, indeed, belong to the CI methods category and are based on the same weighting function and coefficients. The advantage of choosing the ODE friction model lies in the reduced computational cost, as already discussed in (Ioriatti, Dumbser, and Iben, 2017) for laminar flow cases.

3.2.4 Viscoelastic parameters calibration

For the water hammer test cases, a calibration of the viscoelastic parameters is necessary to accurately reproduce the behavior of the pipe material. The instantaneous elastic modulus E_0 is estimated accordingly to the reference elastic wave speed of each test. As a matter of fact, knowing the mean value of the wave speed, estimated by observing the oscillation period on the basis of experimental measurements, and using definition in Eq. (3.60), it is possible to obtain the proper value of E_0 (Evangelista et al., 2015). Concerning the rest of the viscoelastic parameters, for a g-KV model, while τ_k are fixed as in references (Covas et al., 2005; Evangelista et al., 2015), E_k are calibrated by minimizing

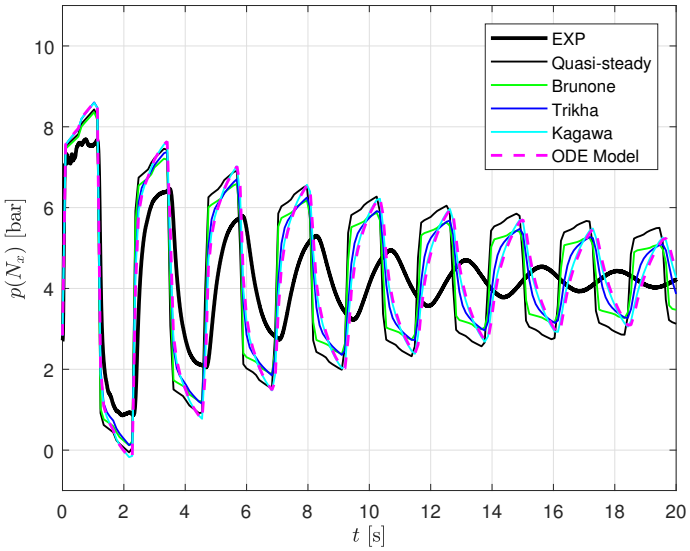

FIGURE 3.2: *Experimental data compared with numerical results obtained using different friction models for the water hammer problem in a HDPE DN50 smooth-wall pipe with turbulent flow (Q_0 = 2,00 l/s, Re $\approx$ 51000). Pressure $p(N_x)$ at the downstream.*

the least square error (LSE) between numerical and experimental pressure at the downstream end of the pipe, considering the entire time interval and not the single peaks. The same principle is followed for the calibration of E_∞ and η with the SLS model. To perform these optimizations, the SCE-UA (Shuffled Complex Evolution - University of Arizona) algorithm, a general purpose global optimization method originally developed by Duan, Sorooshian, and Gupta (1992) and Duan, Gupta, and Sorooshian (1993), is used.
Two main approaches are followed to calibrate the creep function and test the numerical models. Having observed in Section 3.2.3 that in general the unsteady friction term cannot extensively describe the dissipation of transient waves in HDPE pipes, in the first calibration unsteady friction effects are neglected, considering only the pipe wall viscoelasticity as diffusive effect. In the second calibration, instead, unsteady friction losses are considered as part of the damping. It has been noticed that the calibration of viscoelastic parameters is not independent of the specific test facilities, in terms of diameter and length of the tube, wall thickness and anchors. Hence, in order to achieve the best fitting between numerical and experimental results, a specific calibration has been made for each test analyzed, considering not to have parameters generally valid for a given material. Moreover, it is worth to mention that the existence of different combinations of viscoelastic parameters that can describe the behavior of a plastic tube, with the same sum of squared errors against experimental data, has been confirmed by Ferrante and Capponi (2017) when using the SLS model. Viscoelastic calibrated parameters are further presented in Section 3.3.2 for each water hammer test case.

3.3 Numerical results and Discussion

To compare the three numerical methods, two different types of problems are selected. The first kind of test cases regards three different Riemann problems (i.e. initial value problems governed by conservation laws with piece-wise constant initial data

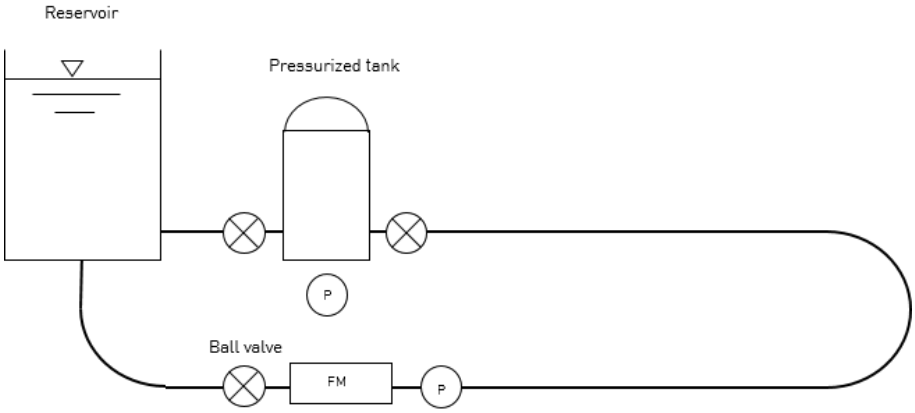

FIGURE 3.3: *Schematic representation of the experimental setup of water hammer tests. The supply system is provided by a centrifugal pump submerged in a water reservoir with a capacity of 5 m^3. At the upstream of the pipe there is a pressurized tank of galvanized steel with 500 l volume and 8 bars nominal pressure. Pressure transmitters (P) and a flow meter (FM) are employed for the data acquisition. The closure of a downstream ball valve is used to recreate hydraulic transients.*

having a single discontinuity), solved only in the elastic case, for which a quasi-exact solution is available (Dumbser, Iben, and Ioriatti, 2015). Furthermore, two water hammer problems in HDPE tubes are presented, for which experimental data already used by Pignatelli (2014) and Evangelista et al. (2015) were provided and assumed as reference. A sketch of the experimental setup is shown in Fig. 3.3. For this kind of tests, viscoelastic parameters calibration is also discussed.

In all the simulations presented in this chapter the following assumptions are considered: CFL = 0.9, $\nu_p = 0.4$, $\rho_0 = 998.2$ kg m^{-3}, $p_0 = 10^5$ Pa, $c_s = 1400$ m s^{-1}, $T_0 = 293$ K, $p_v = 2300$ Pa, $R_v = 303$ K^{-1} m^2 s^{-2} and $K_c = 10^{-6}$ Pa $^{-1}$.

3.3.1 Riemann Problems

The chosen Riemann problems are very demanding test cases, selected to stress numerical schemes and evaluate their possible weaknesses. The first two Riemann problems, RP1 and RP2, are designed considering a sudden increment of the cross-section of the conduct in the middle of the domain and differ each other only for the material of the pipe taken into account, hence for the Young modulus. Precisely, this information is contained within the parameter K, defined in Eq. (3.31). While in RP1 $K = 2.40 \cdot 10^8$ Pa/m^2, corresponding to an elastic modulus typical of polymer materials, in RP2 $K = 2.40 \cdot 10^6$

Case	p_L [Pa]	u_L [m/s]	A_{0L} [cm^2]	p_R [Pa]	u_R [m/s]	A_{0R} [cm^2]	K [Pa]	t_{end} [s]	N_x [-]
RP1	$100 \cdot \gamma_0$	0.0	15.00	$20 \cdot \gamma_0$	0.0	34.00	$2.40 \cdot 10^8$	0.3	400
RP2	$100 \cdot \gamma_0$	0.0	15.00	$20 \cdot \gamma_0$	0.0	34.00	$2.40 \cdot 10^6$	3.0	400
RP3	10^5	0.0	0.50265	10^2	0.0	0.50265	$10.053 \cdot 10^8$	0.0005	500

TABLE 3.1: *Initial states for the Riemann problems, with $\gamma_0 = \rho_0 g$. Subscripts L and R stand respectively for left and right state of the piece-wise constant initial values typical of Riemann problems.*

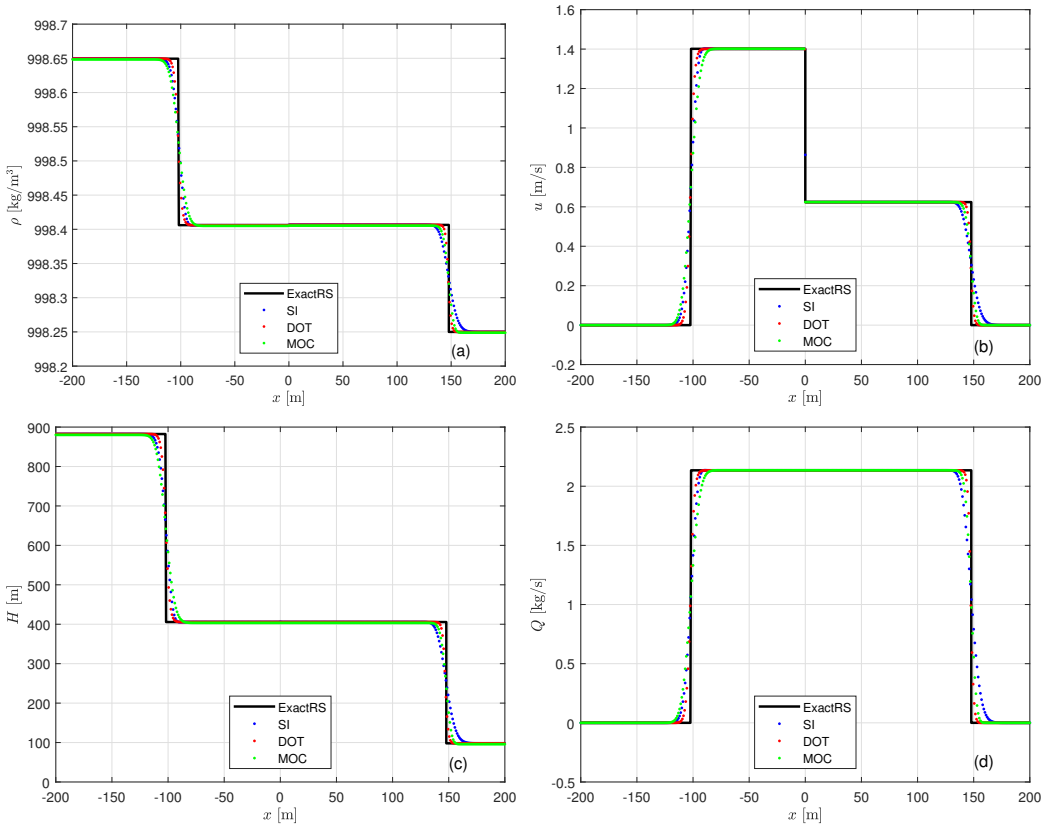

FIGURE 3.4: *Comparison of the numerical results obtained with MOC, DOT and SI against the quasi-exact solution (ExactRS) in Riemann problem RP1 at time t_{end} in terms of (a) density, (b) velocity, (c) total head and (d) flow rate.*

Pa/m^2, which corresponds to a typical elastic modulus of a rubber material. To have higher stiffness means to have higher wave speeds (with a flow velocity that becomes negligible in comparison with the celerity itself) and a substantial non-variance of the celerity across the rarefaction and the shock waves, which relates exactly to a linear behavior. To confirm this assertion, the trend of the celerity in RP1 and RP2 is presented in Fig. 3.6, focusing on the concept of non-variance just discussed. In the same figure, velocity values are also shown to compare them to the celerity ones. The solution of the problem consists of a rarefaction wave, propagating to the left, followed by a stationary contact discontinuity in the middle of the domain, where there is the cross-sectional jump, and a final shock wave, propagating to the right. The differences between the two solutions are connected to the different material properties: only concerning a very flexible material the rarefaction wave appears well extended (while in the first case the rarefaction could be confused with a shock wave) and the central contact discontinuity is stronger in RP2 than in RP1.

The last Riemann problem, RP3, concerns a general elastic flexible pipe in which cavitation occurs: the initial left state is liquid, while the right state is in the wet steam region, with $p_R < p_v$. In this test, therefore, there is a very large pressure drop across the two phases, of three orders of magnitude. Moreover, a very strong rarefaction traveling also through the phase change, followed by an equally severe shock wave, is observed.

All of the RP tests are solved only considering the Laplace constitutive law, to make it possible to compare the results with a quasi-exact solution (Dumbser, Iben, and Ioriatti,

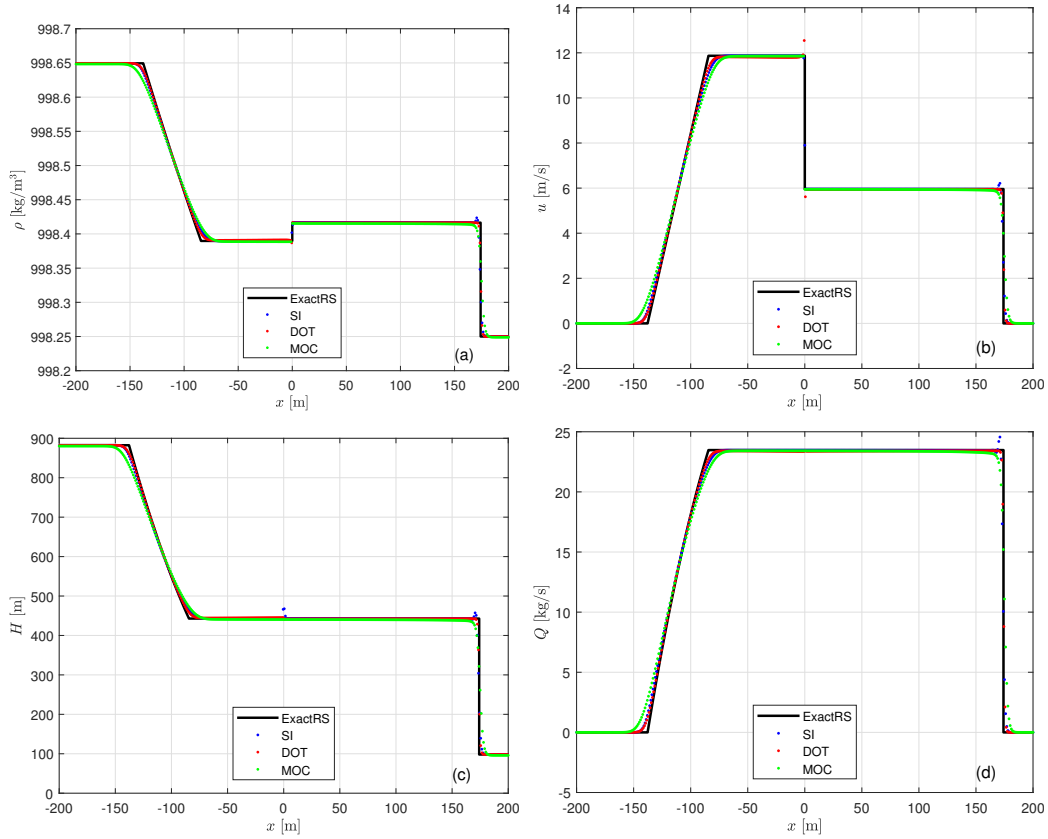

FIGURE 3.5: *Comparison of the numerical results obtained with MOC, DOT and SI against the quasi-exact solution (ExactRS) in Riemann problem RP2 at time t_{end} in terms of (a) density, (b) velocity, (c) total head and (d) flow rate.*

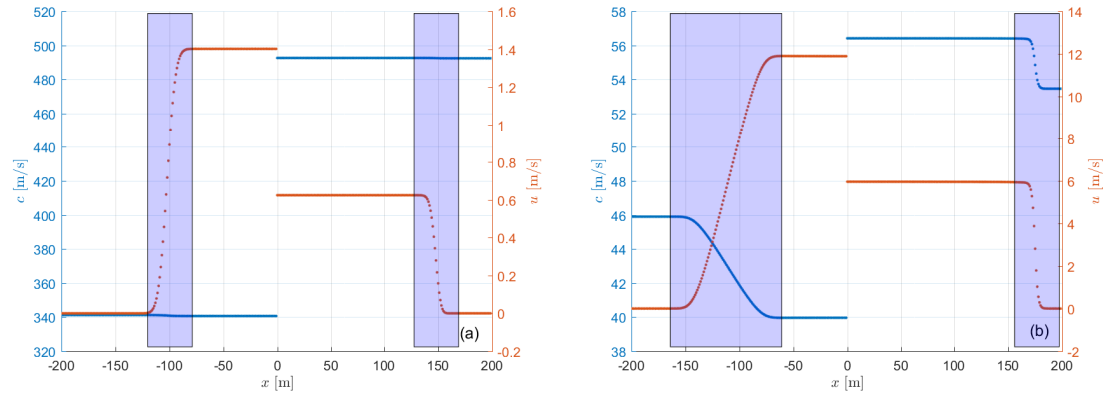

FIGURE 3.6: *Celerity and velocity values in RP1 (a) and RP2 (b). Position of the rarefaction and of the shock wave highlighted in each case. The light blue dotted line represents the celerity while the orange dotted line represents the velocity. While in RP1 numerical methods works in a weakly non-linear context, in RP2 the more flexible material returns a fully non-linear response.*

2015). Initial data of each Riemann problem are presented in Tab. 4.1 and the final results are shown in figures from 4.6 to 4.8. Concerning the SI scheme, $\Delta t_{max} = 10^{-3}$ s in RP1 and

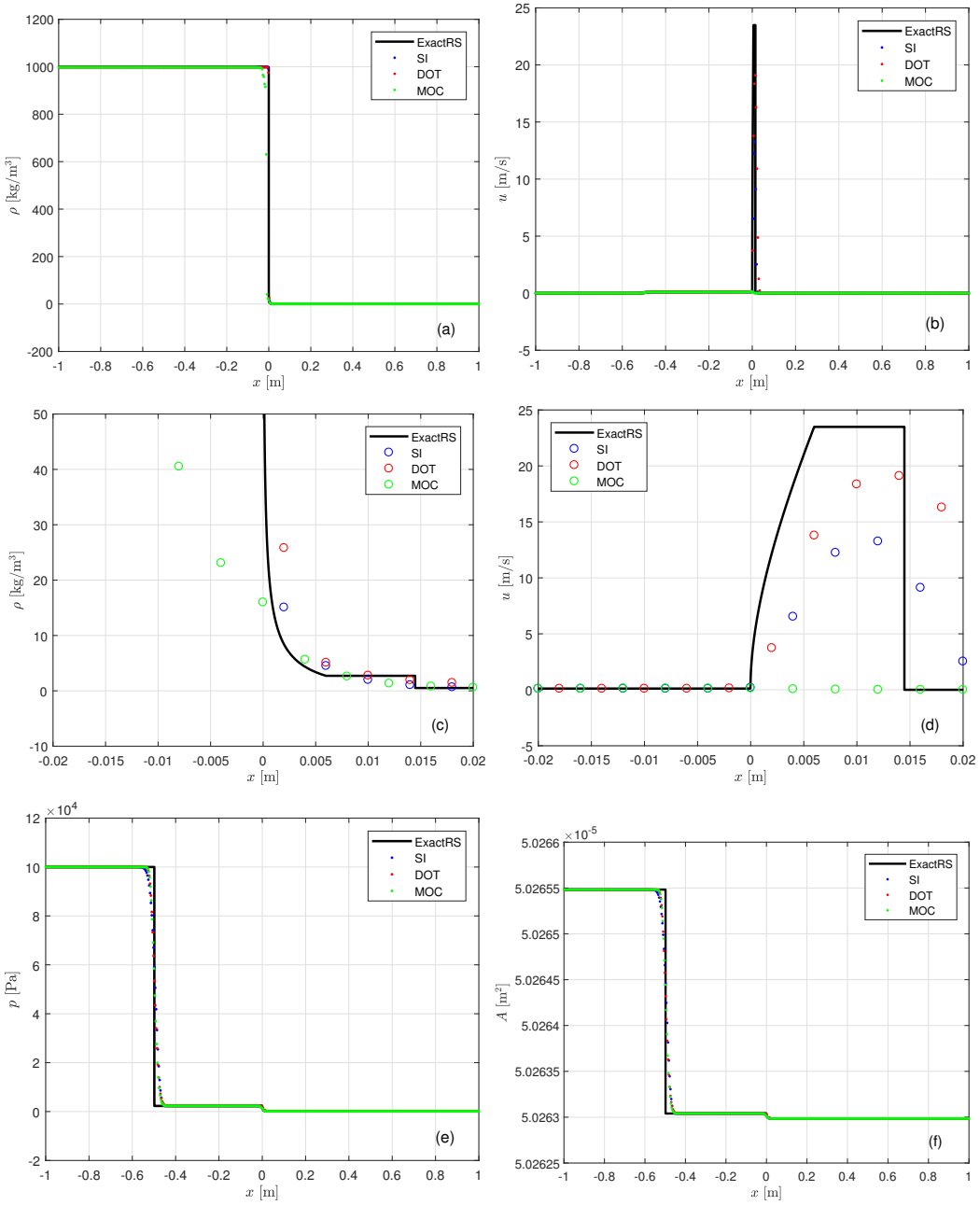

FIGURE 3.7: *Comparison of the numerical results obtained with MOC, DOT and SI against the quasi-exact solution (ExactRS) in Riemann problem RP3 at time t_{end} in terms of (a,c) density, (b,d) velocity, (e) pressure and (f) cross-sectional area. Figures (c) and (d) are zooms of (a) and (b) respectively, to show the complexity of the solution in the middle of the domain.*

RP2, while $\Delta t_{max} = 10^{-6}$ s in RP3. In addition, for all the simulations, $\theta = 0.80$ in order to reduce the numerical diffusion without generating excessive non-physical oscillations. Only for the RP3 the non-linear operator for the convective terms has been considered.

It has to be mentioned that, to obtain reliable results solving the Riemann problem test cases with the MOC, the Method of Specified Intervals (Wylie and Streeter, 1978) was used and computations were separated for the two parts of the domain with constant initial values. Moreover, for RP1 and RP2, it was also necessary to impose the total head and mass flow rate conservation at the interface to avoid an unrealistic jump of the flow rate in the middle of the domain. This aspect has to be underlined to make the reader understand that the simplest way to implement and use the MOC is generally not enough in case of more challenging problems.

Considering RP1 in Fig. 4.6, the less demanding Riemann problem, with a weakly non-linear response given by the material, the semi-implicit scheme appears a bit more diffusive along the shock wave than the other two numerical methods. This is due to the parameter θ, fixed equal to 0.8 (hence tending a bit more to a first order scheme) to avoid oscillations after the rarefaction and before the shock.

In RP2 (Fig. 4.7), in a fully non-linear context, both the DOT and the SI schemes present oscillations in proximity of the contact discontinuity, with the SI showing the same flaw also before the shock wave. In this very demanding situation, the DOT solver shows a deficiency in the correct conservation of the total head across the stronger contact discontinuity, which is more heavily transferred to the velocity (Fig. 4.7). This problem of oscillation is most probably due to the use of a linear path that doesn't correctly represent the non-linearity given by the material. Thus, recurring to a non-linear path, referring for example to Caleffi and Valiani (2017), the mentioned flaw might be reduced. On the other hand, in the SI method, the θ-method causes overshoots in the proximity of the strong gradients, as explained in Section 3.2.2.3. The MOC performs in the best way near the contact discontinuity (thanks to the separation in this point of the computations, imposing the conservation of the total head and of the mass flow rate at the interface) but it is the most diffusive scheme in the shock and rarefaction zone. However, in RP2 the Method of Characteristics needed another rearrangement of the code: to obtain correct wave speeds, non-straight characteristic curves (i.e. $^{dx}/_{dt} = u \pm a$) are considered, without neglecting the velocity with respect to the celerity. The reason for this distinct demand lays in the difference between the values of velocity and celerity in RP2 and RP1, already discussed and confirmed by Fig. 3.6.

Observing results of RP3, presented in Fig. 4.8, the rarefaction wave becomes evident in the density only when the pressure reaches values below the vapor pressure, as deduced from Eq. (3.17). On the other hand, the pressure starts to drop earlier, reaching the vapor pressure and maintaining a constant value until $x = 0$, with a mixture that is still liquid and hence represented by the typical water density value. The tail of the rarefaction wave is further ahead in the domain, before a very short constant state that separates the rarefaction from the shock wave in the wet steam region.
With this problem, the MOC demonstrates again to be not very robust. In this case, indeed, the scheme is not able to capture the correct evolution of the rarefaction and especially of the shock wave, clearly visible in the velocity plot of Fig. 4.8. The reason of this deficiency lays in the violation of one of the hypothesis made to obtain the classical Allievi-Joukowsky equations (3.13): the assumption of considering weakly compressible fluids, for which it is possible to neglect the spatial variation of the density (refer to Section 3.2.1). Thus, in these circumstances, the MOC cannot properly capture the whole

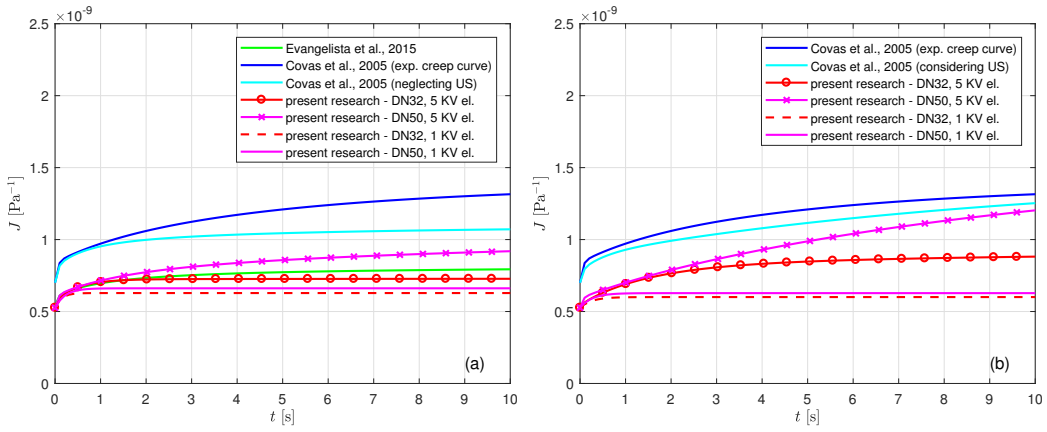

FIGURE 3.8: *Calibrated viscoelastic creep functions of the HDPE pipes considered in the present study, concerning the SLS and g-KV model, compared with creep functions for HDPE pipes taken from literature (Evangelista et al., 2015; Covas et al., 2005). Results (a) neglecting unsteady friction and (b) considering unsteady friction.*

complexity of the phenomenon because of its mathematical structure (e.g. the shock wave in the wet steam region is completely absent).

3.3.2 Water hammer problems

For the water hammer (WH) problems, two HDPE tubes have been chosen, considering the available experimental data (Evangelista et al., 2015; Pignatelli, 2014). Test WH1 concerns a straight DN50 pipe of length 203.3 m, while test WH2 regards a straight DN32 pipe of 101.9 m. The main features of the systems are listed in Tab. 3.2. The average wave speeds $\overline{a}$ were given from the laboratory experiments, estimated as mean values of those obtained as ratio between four times the total length of the pipe and the time elapsed between two pressure peaks. Pipelines were fixed to the ground by means of metal clamps along the entire length, to avoid any axial movement of the pipes. For this reason, in the WH simulations the geometric parameter W defined in Section 3.2.1.3 is multiplied by an

Test	DN [mm]	D [mm]	s_0 [mm]	L [m]	Q_0 [l/s]	$\overline{a}$ [m/s]	f [-]
WH1	50	44.0	3.0	203.3	2.00	350	0.02105
WH2	32	23.2	4.4	101.9	0.25	500	0.03006

TABLE 3.2: *Data of the water hammer tests WH1 and WH2.*

Parameter		WH1 - QS	WH1 - US	WH2 - QS	WH2 - US
E_0	[GPa]	1.90	1.90	1.90	1.90
E_∞	[GPa]	1.51	1.59	1.59	1.67
η	[GPa s]	0.085	0.080	0.043	0.060

TABLE 3.3: *Viscoelastic parameters calibrated for water hammer tests WH1 and WH2 solved with the SLS model in case of a quasi-steady friction model (QS) or considering the unsteady friction losses (US). Please refer to Section 3.2.4 for the calibration procedure.*

axial pipe-constraint dimensionless parameter (Wylie and Streeter, 1978):

$$\alpha_{pc} = \frac{s_0}{R_0}(1+\nu_p) + \frac{2R_0}{2R_0+s_0}\left(1+\nu_p^2\right),$$

finally being

$$W = \frac{\alpha_{pc} R_0}{s_0}. \tag{3.88}$$

In both cases, to experimentally generate a transient test, a fast and complete closure of the downstream ball valve is done, with a controlled closure time fixed at 0.1 s (set as outlet boundary condition in the computations). The discharge of the flow is provided upstream from a pressurized tank, whose pressure is measured at each time step and used as inlet boundary condition (see Fig. 3.3). For further details about the experimental setup and the procedure, the reader can refer to Evangelista et al. (2015) and Pignatelli (2014).

To solve WH problems considering the correct FSI between water and tube wall, both the SLS model and the g-KV model with 5 KV units (5-KV) are tested for all the numerical schemes. The viscoelastic parameters (calibrated as explained in Section 3.2.4) are listed in Tab. 3.3 and 3.4 for each case and for both the friction models taken into account, the simple quasi-steady (QS) and the unsteady (US) one (using the ODE friction model discussed in Section 3.2.1.2). In Fig. 3.8 it is possible to observe the trend of the calibrated creep functions adopted for the present study compared with those used by Evangelista et al. (2015), neglecting the unsteady friction effects with a 5 KV elements model, and

WH1 - QS						
Parameter		$k=1$	$k=2$	$k=3$	$k=4$	$k=5$
J_k	[10^{-11} Pa^{-1}]	8.14	1.55	14.53	0.0016	23.85
τ_{rk}	[s]	0.05	0.50	1.50	5.00	10.00
WH1 - US						
Parameter		$k=1$	$k=2$	$k=3$	$k=4$	$k=5$
J_k	[10^{-11} Pa^{-1}]	6.57	0.45	3.98	0.026	89.62
τ_{rk}	[s]	0.05	0.50	1.50	5.00	10.00
WH2 - QS						
Parameter		$k=1$	$k=2$	$k=3$	$k=4$	$k=5$
J_k	[10^{-11} Pa^{-1}]	4.40	15.41	0.013	0.021	0.43
τ_{rk}	[s]	0.05	0.50	1.50	5.00	10.00
WH2 - US						
Parameter		$k=1$	$k=2$	$k=3$	$k=4$	$k=5$
J_k	[10^{-11} Pa^{-1}]	1.91	1.00	25.64	0.93	9.78
τ_{rk}	[s]	0.05	0.50	1.50	5.00	10.00

TABLE 3.4: *Viscoelastic parameters calibrated for water hammer test WH1 and WH2 solved with the 5-KV model in case of a quasi-steady friction model (QS) or considering the unsteady friction losses (US), with $E_0 = 1.90$ GPa. Please refer to Section 3.2.4 for the calibration procedure.*

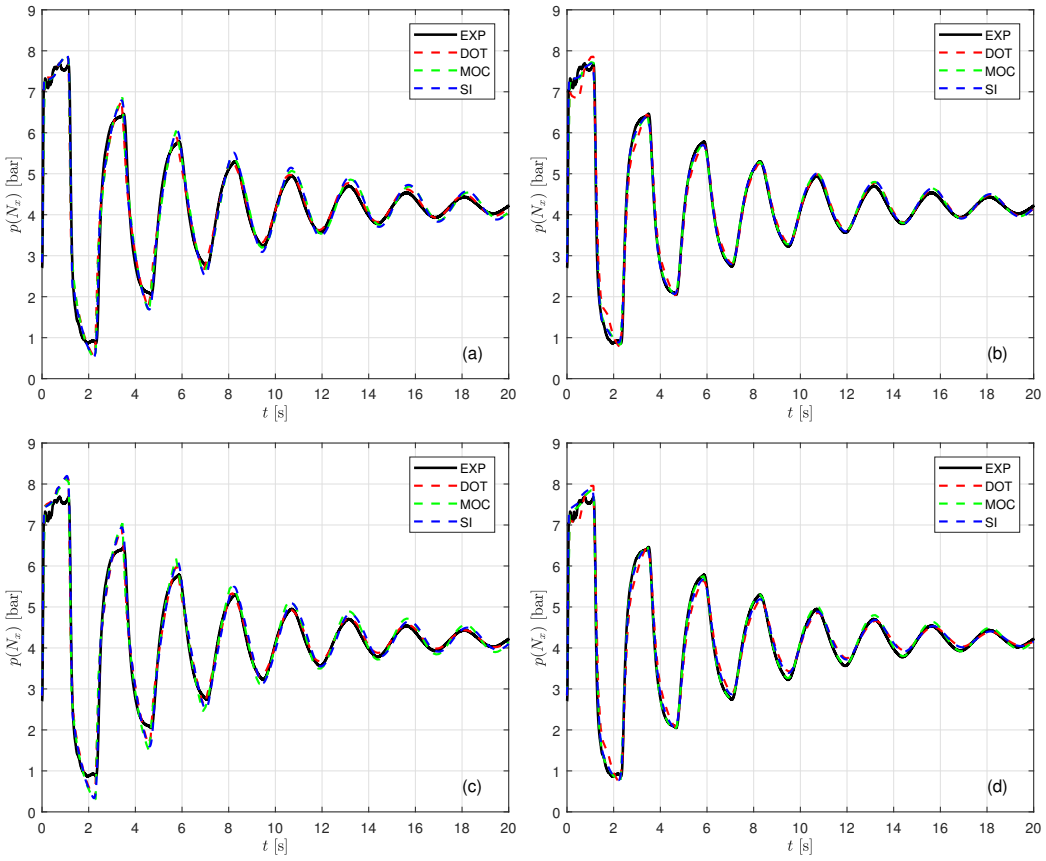

FIGURE 3.9: *Comparison of the numerical results obtained with MOC, DOT and SI against the experimental solution (EXP) of the water hammer test WH1 with each viscoelastic and friction model configuration: (a) SLS and quasi-steady friction model, (b) 5-KV and quasi-steady friction model, (c) SLS and unsteady friction model and (d) 5-KV and unsteady friction model. Pressure $p(N_x)$ at the downstream end.*

Covas et al. (2004) and Covas et al. (2005), neglecting the unsteady friction effects or considering them with the 5-KV model or using creep data experimentally determined by mechanical tests. It has to be mentioned that the creep function proposed by Covas et al. (2005) is referred to a PE pipe and an average pressure wave speed of 395 m/s, corresponding to an instantaneous Young modulus $E_0 = 1.43$ GPa. It can be noticed that the calibrated creep functions are really comparable to the one presented by Evangelista et al. (2015) neglecting the unsteady friction effects. On the other hand, considering the unsteady losses, the trend of the curves is similar to those calibrated by Covas et al. (2004) and Covas et al. (2005). In this case it is also visible an increment of the parameters J_k, with respect to the calibration made neglecting the unsteady friction, which confirms a reduction of the elastic modulus E_k due to the consideration of the unsteadiness as part of the damping. The difference between DN32 and DN50 creep functions can be attributed again to the different facilities and conditions of the two tests: being the viscoelastic models adopted for this work always considerably affected by these aspects, it is generally not possible to fix a unique set of parameters universally valid for a specific material. Finally, if we compare the curves obtained with 1 KV element (SLS model) with those with 5 KV elements (5-KV model) it can be clearly noticed that adding Kelvin-Voigt elements it is

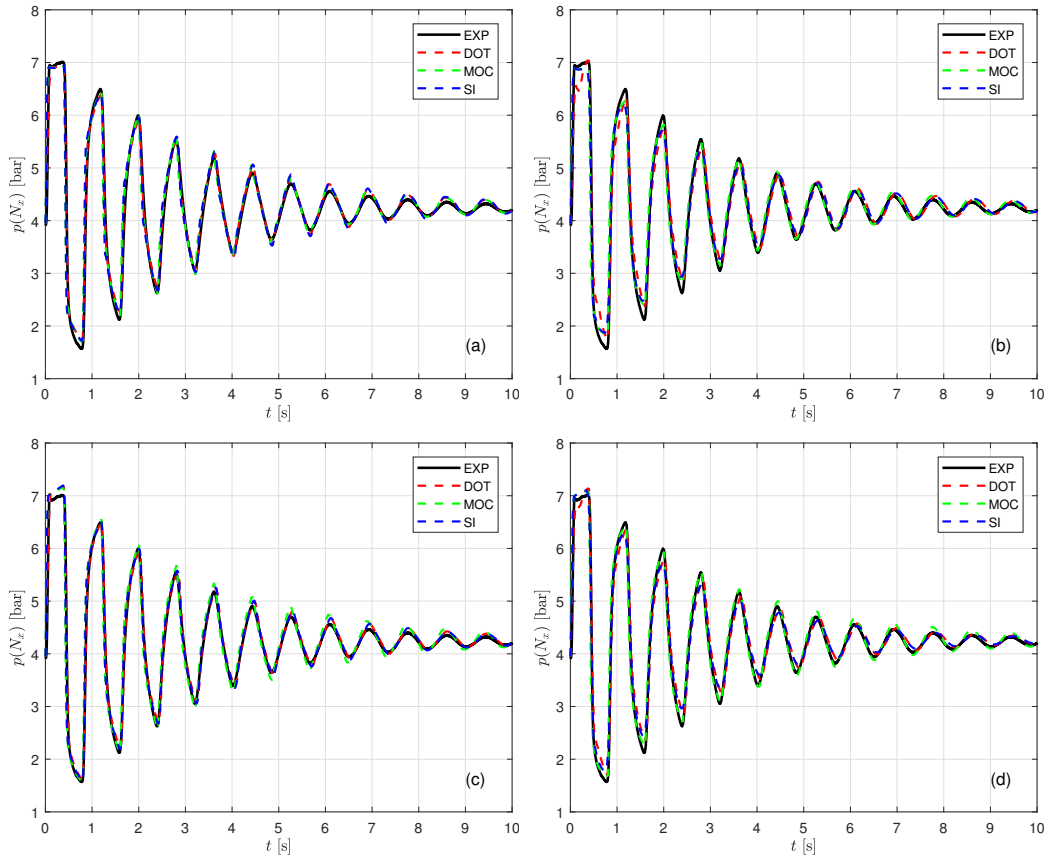

FIGURE 3.10: *Comparison of the numerical results obtained with MOC, DOT and SI against the experimental solution (EXP) of the water hammer test WH2 with each viscoelastic and friction model configuration: (a) SLS and quasi-steady friction model, (b) 5-KV and quasi-steady friction model, (c) SLS and unsteady friction model and (d) 5-KV and unsteady friction model. Pressure $p(N_x)$ at the downstream end.*

possible to obtain a behavior of the creep functions that is substantially not constant for increasing time.

Considering that the parameter P as defined in (3.18) is largely bigger than 1 for the systems analyzed in this study (respectively, $\mathrm{P} = 5.5$ in WH1 and $\mathrm{P} = 12.7$ in WH2), it was initially adopted a quasi-steady friction model inside all the numerical schemes. Nevertheless, the effect of the ODE unsteady friction model are also tested with respect to the steady one.

Comparisons between numerical and experimental pressure values in the immediate proximity of the closing valve are shown in Fig. 3.9 for test WH1 and in Fig. 3.10 for test WH2, with each viscoelastic model and friction configuration. For all the simulations the number of cells is maintained $N_x = 50$. With the semi-implicit scheme $\theta = 0.55$ and $\Delta t_{max} = 0.01$ s, except for WH2 with the SLS viscoelastic model, for which a smaller Δt was necessary to obtain an accurate result: $\Delta t_{max} = 0.001$ s. This behavior can be explained in terms of wave speed. In WH2, indeed, the wave speed is higher than in WH1, meaning that a higher resolution in terms of time steps is necessary if the viscoelastic model adopted is the simplest one.

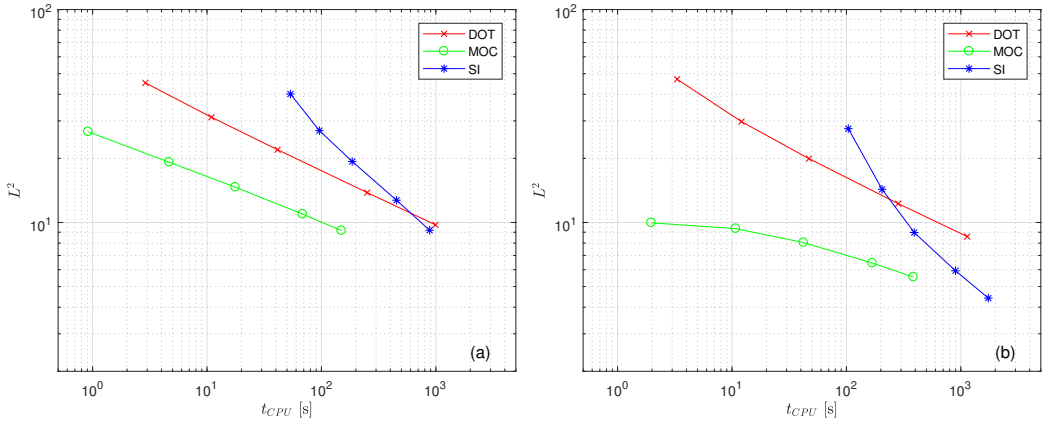

FIGURE 3.11: *Results of the efficiency analysis for the test WH1 with the (a) SLS and (b) 5-KV viscoelastic model, neglecting unsteady friction losses. Trend of the norm L^2 with respect to the CPU/computational time t_{CPU}.*

In general it can be noticed that the three numerical methods reproduce similar results in both the test cases. The first clear observation is related to the contribution of the unsteady friction model, which seems to be negligible, as already predictable by the parameter P related to the experiments (Ghidaoui, Mansour, and Zhao, 2002; Duan et al., 2010). This result underlines once more what established by Ghidaoui, Mansour, and Zhao (2002): the unsteady friction term assumes relevance only when the wave has to travel from one end of the pipe to another less than once in order to have the pre-existing turbulent characteristics, throughout the whole cross-section of the pipe, influenced by the wall shear pulse.
The second remark concerns the viscoelastic models: in the simulations it is visible that the increment of KV elements, from 1 to 5, does not yield to a consistent improvement of the results, weighting, on the other hand, in terms of computational costs and adding difficulties to the calibration procedure.

3.3.3 Efficiency analysis

For the water hammer test WH1, an efficiency analysis is computed to evaluate the performance of each numerical model adopted for the present study. In Fig. 3.11 errors in terms of norm L^2 are compared against the computational time t_{CPU}, separately using the SLS and the 5-KV viscoelastic models for each numerical scheme. Given a vector difference between the numerical values of the pressure p_{num} and the measured experimental values of the pressure p_{exp}, the norm L^2 is here defined as:

$$L^2 = \sqrt{\sum_{i=1}^{N_x} \left| p_{num,i} - p_{exp,i} \right|^2 \Delta x}. \tag{3.89}$$

Because of the low impact of the unsteady friction losses with respect to the accuracy of the results (as observed in Section 3.3.2), with these analysis only a quasi-steady friction model is considered. Solutions are computed for five different meshes: $N_x = 25$, 50, 100, 250, 500 for DOT and SI schemes and $N_x = 100$, 250, 500, 1000, 1500 for MOC (augmented because of the higher efficiency of this scheme).

Comparing the two graphs in Fig. 3.11, it is evident that the increment of viscoelastic parameters adopted to characterize the material mechanics leads to an inevitable increment of computational costs not balanced by a comparable error reduction. In the case of the 5-KV model, errors are less because the more parameters we have for describing the numerical pressure curve, the more adaptable to the experimental reference the curve itself will be. However, even if there is this error reduction adopting the 5-KV model instead of the SLS model (very small with DOT and SI methods), the consequent CPU time increment makes the choice fruitless. Considering both the viscoelastic models, it can clearly be deduced that the MOC is the most efficient scheme. The SI method starts to be competitive only when it is necessary to increase the number of cells of the domain, aiming to obtain very small errors. A parallel observation concerns the trend of each curve: while MOC and DOT maintain almost the same slope (typical of a second order scheme), the SI method presents a steeper slope, meaning a higher order of accuracy. Both these particular behaviors of the SI method are a consequence of the double condition that needs to be respected choosing the maximum admissible Δt. With these simulations, the CFL condition is always by-passed by the Δt_{max} fixed to avoid excessive numerical diffusion. In this way, the real order of the scheme is hidden and even with a limited number of cells the simulation remains slower than it could be without the fixed time step. Finally, the DOT is always less efficient than the MOC and more efficient than the SI only when fewer cells are considered for the discretization of the domain.

3.4 Concluding remarks

Accuracy, robustness and efficiency of three different numerical schemes have been analyzed and compared when applied for the resolution of hydraulic transients in flexible polymer tubes: the Method of Characteristics, the explicit path-conservative FVM with DOT solver (Dumbser and Toro, 2011b; Dumbser and Toro, 2011a) and the staggered semi-implicit FVM (Dumbser, Iben, and Ioriatti, 2015). Results show a good agreement with the experimental data for all the numerical methods, whether the SLS model or a g-KV chain is chosen for the characterization of the viscoelastic behavior of HDPE tube walls. This aspect encourages the adoption of less complex models, like the SLS, yet able to adequately capture the correct behavior of the material and ensuring in the meantime the minimum computational cost. The same applies concerning the friction term, for which it has been confirmed that, in the scenarios investigated in this study, the unsteady wall-shear stress can be neglected in favour of a quasi-steady friction model. It is worth remembering that the calibration of the model parameters for viscoelasticity and unsteady friction term is complicated by the fact that both these aspects are manifested in the damping effect of over-pressure and under-pressure waves. Therefore, a precise calibration of the specific coefficients is hard to achieve.
Furthermore, a new efficient resolution of the convolution integral of the unsteady wall-shear stress has been tested in turbulent flow conditions and an original formulation of the g-KV viscoelastic constitutive law for its applicability to augmented FSI finite volume schemes.

The Method of Characteristics results the most efficient numerical model, among those considered in this study, explaining why it is generally preferred for the resolution of hydraulic transients. Only the SI method becomes competitive with respect to the MOC when it is necessary to have a rich discretization of the domain, aiming to obtain very small errors. However, the Riemann problem test cases highlight that the

MOC is not as robust as DOT and SI schemes. To obtain adequate solutions considering more complex configurations in the analysis (e.g. cross-sectional changes) or more flexible materials (e.g. rubber), indeed, it is not possible to apply the MOC in its simplest way. The code needs to be rearranged for the specific request. In all the RPs here presented, the Method of Specified Intervals has been necessarily used and computations have been separated for the two parts of the domain with different initial values, imposing the variables congruence at the interface. Furthermore, in RP2, it had been necessary to consider non-straight characteristic curves, without neglecting the flow velocity with respect to the celerity. In addition, when considering cavitation cases, the MOC presents difficulties in the correct capture of the discontinuities inherent in the problem due to the simplifying hypothesis underlying its classical derivation. Aware of the existence of improved versions of the MOC with more complex cavitation models, such as the Discrete vapor Cavity model or the Discrete Gas Cavity model (Bergant, Simpson, and Tijsseling, 2006), it was not consistent to implement them to simulate the cavitation problem concerned in this study. In these models, indeed, is it assumed that the pressure cannot reach values below the vapor pressure or that the celerity of the mixture only depends on the liquid phase contribution. The purpose was to compare finite volume methods to the standard MOC, implemented in its classic and most used form, not recurring to very complex implementations, for an equilibrated analysis.

To summarize all the results achieved in the study presented, it can be said that while for simple systems the adoption of the MOC is generally encouraged, when dealing with complex configurations the choice of the numerical scheme becomes more complicated, requiring the evaluation of the critical aspects involved in the specific case and the maximum error admissible for the results.

Chapter 4

Viscoelasticity in blood vessels

4.1 Introduction

The availability of robust and efficient mathematical instruments, together with the engineering know-how in the fluid mechanics sector, represents an invaluable tool for a consistent support in hemodynamics studies. It is a proven fact that computational modeling can provide efficient approaches for the quantification of fluid dynamics phenomena in the cardiovascular network, supplying meaningful data that otherwise would require invasive techniques or simply would not be available with general clinical measurements (Pedley, 1980; Formaggia, Quarteroni, and Veneziani, 2009; Ambrosi, Quarteroni, and Rozza, 2012; Willemet, Vennin, and Alastruey, 2016). Mathematical models and numerical simulations can also help the prediction of the possible onset of diseases and development of pathologies (Cavallini, Caleffi, and Coscia, 2008; Delestre and Lagrée, 2013; Toro, 2016; Liang, Guan, and Alastruey, 2018; Müller et al., 2019). Numerical modeling of the entire cardiovascular system by means of 3D models is currently not affordable, because of the complexity of the computational domain, which is composed of thousands of arteries and veins and billions of arterioles, capillaries and venules, and the consequent demanding computational cost. For most applications, 1D models coupled to 0D/lumped-parameter models, derived from the full 3D models by means of simplifying assumptions on the flow, the structure, and their interaction, result one of the best realistic compromise (Toro, 2016). Optionally, these averaged models can be coupled with 3D ones. For instance, for cases involving the evaluation hemodynamic quantities such as the wall shear stress, when there is the formation of vortices, due to vessel occlusions and stenotic configurations (Caiazzo et al., 2014), or generally when localized (especially patient-specific) phenomena need to be analyzed (Blanco and Feijóo, 2013; Quarteroni, Manzoni, and Vergara, 2017). A thorough comparison of 1D and 3D computational hemodynamics in arterial models with compliant vessel walls is presented by Xiao, Alastruey, and Figueroa (2014). In this work, it is confirmed that accurate predictions can be made with a 1D model when the flow is predominantly unidirectional.

In recent years, mathematical models have been consistently developed, focusing on different aspects and fundamental issues that need to be addressed to successfully model the circulatory system. Among these, it has to be considered that blood flow mechanically interacts with vessel walls and tissue, giving rise to complex fluid-structure interactions whose mathematical analysis is difficult to properly describe and numerically simulate in an efficient manner (Holenstein, Niederer, and Anliker, 1980; Leguy, 2019). The wall of a blood vessel consists of three layers of different tissues: an epithelial inner lining, a middle layer consisting of a smooth muscle and elastic connective tissue, and a connective tissue outer covering. These three structural layers, from innermost to outermost, are called tunica interna (intima), tunica media and tunica externa (Tortora and Derrickson,

2013). The smooth muscle cells attribute a viscoelastic behavior to the wall (Valdez-Jasso et al., 2009; Battista, 2015), which assumes a fundamental role when high frequencies are dominant (Alastruey et al., 2012). Whereas when the stress is applied very slowly, the viscous aspects do not become apparent and the wall behaves as purely elastic (Westerhof et al., 2019). At a macroscopic level, indeed, the vessel wall can be seen as a complex multi-layer viscoelastic structure which deforms under the action of blood pressure (Nichols, O'Rourke, and Vlachlopoulos, 2011; Wang, Golob, and Chesler, 2016), even collapsing, in the case of veins, under certain circumstances (Shapiro, 1977; Pedley, 1983; Toro and Siviglia, 2013; Spiller et al., 2017). Modeling the interaction between blood flow and vessel wall mechanics requires the definition of a constitutive law which has to correctly describe the energy transfer between the two means, to accurately represent wave propagation phenomena (Pedley, 1980; Fung, 1997; Leguy, 2019). Moreover, as in all viscoelastic materials, the energy put into the system during strain is not totally recovered during relaxation, causing a viscous damping of the pulse waves. This phenomenon can be found in many biological tissues and it is visible when plotting pressure against area variations in time: the presence of a widening pressure-area loop (hysteresis) represents the effective energy dissipated during dilatation and contraction cycles (Valdez-Jasso et al., 2009; Raghu et al., 2011; Battista, 2015). When modeling the vessel wall mechanics simply by means of an elastic law, the whole information related to the loss of energy of the phenomenon vanishes and pressure peaks levels could be overestimated (Holenstein, Niederer, and Anliker, 1980; Alastruey et al., 2011; Montecinos, Müller, and Toro, 2014; Battista, 2015).

Even though frequently, in hemodynamics models, the viscosity of vessels is neglected for simplicity, there is an increasing number of contributions showing the benefits of modeling the mechanical behavior of the vessel wall using a viscoelastic rheological characterization. Bessems et al. (2008) formulate a 1D viscoelastic model whose results are compared with in-vitro data measured in single tapered polyurethane vessels, showing that wall viscoelasticity is necessary to accurately predict the propagation and attenuation of pressure and flow waves. Reymond et al. (2009) compare the simulations computed with a 1D viscoelastic model of the human arterial network with average pressure values and flow waveforms measured at several arterial locations in a group of young subjects. Both qualitative and quantitative comparisons of systolic, diastolic and mean pressure and flow suggest a significant importance of the viscous term of vessels walls, especially in peripheral branches. In fact, since pulse waves are subject to a viscoelastic response along each arterial segment, damping effects become more consistent as moving away from the heart (Valdez-Jasso et al., 2009; Alastruey et al., 2012; Mynard and Smolich, 2015). Similar results are presented by Alastruey et al., 2011 with the assessment of 1D viscoelastic simulations against measurements collected from a 37-branches network, in silicone material, representing the largest central systemic arteries of the human arterial tree. For these reasons, many attempts have recently been made to improve the rheological characterization of vessels wall on the basis of linear, quasilinear viscoelasticity or more complex non-linear models (Montecinos, Müller, and Toro, 2014; Battista, 2015; Ghigo et al., 2017).

In this Chapter, a novel 1D a-FSI system, able to capture viscoelastic wall effects, is presented for the blood flow modeling of both arterial and venous network and solved with a FVM with the implementation of a second-order strong-stability-preserving (SSP) Implicit-Explicit (IMEX) Runge-Kutta (RK) scheme (Pareschi and Russo, 2005). For the characterization of the wall mechanics, in this work it is proposed the use of the SLS model in its version with a KV unit (see Section 2.3.3). The same viscoelastic model

was already used by Bessems et al. (2008) and Valdez-Jasso et al. (2009), with successful comparisons of numerical results with experimental data. Moreover, Bessems et al. (2008) use a mathematical approach similar to the one presented in this work, based on an augmented system of equations, but with a different formulation of the final SLS model constitutive law and solely for the arterial network, associated to a spectral element discretization. Nevertheless, in the computational hemodynamics field, the most commonly used viscoelastic model is the KV model (see Fig. 2.4), due to its simplicity (Alastruey et al., 2011; Montecinos, Müller, and Toro, 2014; Wang, Fullana, and Lagrée, 2014; Mynard and Smolich, 2015; Liang, Guan, and Alastruey, 2018). This model, indeed, formulates pressure as a function of cross-sectional area, making it straightforward the incorporation into a fluid dynamics model. However, as already discussed in Section 2.3.2, the KV model has the lack of being able to describe an exponential relaxation of the stress (pressure) over time, which is one of the main attributes of viscoelastic materials (Lakes, 2009). Furthermore, when inserted into the system of equations in its general formulation, the KV viscoelastic law gives rise to a second-order derivative and consequent numerical issues related to the parabolic term. In literature this complication is treated in different manners. Alastruey et al. (2011) adopt a discontinuous Galerkin scheme with a spectral/hp spatial discretization. Montecinos, Müller, and Toro (2014) pass through a hyperbolic reformulation of the system introducing a numerical relaxation parameter (applying Cattaneo's law) and solving it with an ADER scheme. While, Formaggia, Lamponi, and Quarteroni (2003), Mynard and Smolich (2015), and Wang, Fullana, and Lagrée (2014) employ a specific operator-splitting procedure. The SLS model, together with the a-FSI system here proposed, directly overcome these issues, because the resulting system is natively hyperbolic. Still, it maintains ease of implementation and usage, with very good efficiency and robustness granted by the selected IMEX RK algorithm, and convergence is verified, even when dealing with viscoelastic arteries and veins. The model is validated for idealized and real case studies in single vessels, assessing its capability to serve as valuable tool even for practical medical applications, cardiovascular diagnosis and the study of circulatory pathologies. With this aim, in-vivo flow velocity and pressure measurements of human common carotid arteries (CCA) and common femoral arteries (CFA) are performed and compared with numerical results. Moreover, a preliminary effective strategy to estimate the viscoelastic parameters of the SLS model adopted is proposed, evaluating numerical hysteresis curves of different CCAs with corresponding literature ones.

4.2 Methods

4.2.1 Mathematical model

4.2.1.1 General one-dimensional formulation

The standard 1D mathematical model for blood flow, valid for medium to large-size vessels, is obtained averaging the incompressible Navier-Stokes equations over the cross-section, under the assumption of axial symmetry of the vessel and of the flow, obtaining the well established equations of conservation of mass and momentum (Formaggia,

Quarteroni, and Veneziani, 2009):

$$\partial_t A + \partial_x(Au) = 0 \tag{4.1a}$$

$$\partial_t(Au) + \partial_x(Au^2) + \frac{A}{\rho}\partial_x p = \frac{F_R}{\rho}. \tag{4.1b}$$

The reader can easily observe that this system coincides with system (3.1) when the considered fluid is incompressible (ρ constant in space and time).
To close the governing PDE system (4.1), a tube law, representative of the interaction between vessel wall displacement (through the cross-sectional area A) and blood pressure p, is required. As for water pipelines (Section 3.2), this can be performed through a constitutive model, relating strain and stress.

4.2.1.2 Friction model

The blood flow velocity profile is considered self-similar and axisymmetric even in sections with large curvature (e.g. in the aortic arch). The typical velocity profile used for blood flow satisfying the no-slip condition is (Alastruey, Parker, and Sherwin, 2012):

$$v(x,r,t) = u\frac{\zeta+2}{\zeta}\left[1-\left(\frac{r}{R}\right)^{\zeta}\right], \tag{4.2}$$

where r is the radial coordinate and $\zeta = \frac{2-\alpha_c}{\alpha_c-1}$ is the polynomial order depending on α_c, Coriolis coefficient, which accounts for the non-linearity of the sectional integration of the velocity. With Eq. (4.2) it is possible to define different profiles between close to flat ($\alpha_c \approx 1$) to parabolic ($\alpha_c = 3/4$, $\zeta = 2$). For blood flow in arteries it has been demonstrated that the velocity profile is on average rather blunt in central arteries and not parabolic (Quarteroni and Formaggia, 2004), with the consequence that the choice of $\alpha_c = 1.1$ ($\zeta = 9$) provides the best compromise to fit experimental data (Xiao, Alastruey, and Figueroa, 2014). A parabolic velocity profile is in any case more suitable for non-central arteries. For the velocity profile given by Eq. (4.2), the friction loss term finally results:

$$F_R = -2(\zeta+2)\mu\pi u\,, \tag{4.3}$$

where μ is the dynamic viscosity of blood.

4.2.1.3 Elastic constitutive tube law

In the simplest case, the pressure-area relationship is defined considering a perfectly elastic behavior of the vessel wall, with the widely adopted elastic constitutive tube law (Formaggia, Lamponi, and Quarteroni, 2003; Matthys et al., 2007; Müller and Toro, 2013):

$$p = p_{ext} + \psi_{el} = p_{ext} + K\left(\alpha^m - \alpha^n\right). \tag{4.4}$$

In this equation, p_{ext} is the external pressure, ψ_{el} is the elastic contribution of the transmural pressure which depends on α, K, which is the stiffness coefficient of the material, and m and n, specific parameters related to the behavior of the vessel wall, whether artery or vein. If dealing with arteries, this tube law corresponds to the well known Laplace law

presented in Eq. 3.30 in its linearized form (Wylie and Streeter, 1978). Indeed, considering the definition of the geometry parameter W in Eq. (3.32), for an artery we have:

$$K = \frac{E_0}{W}, \quad m = 1/2, \quad n = 0, \tag{4.5}$$

with the formulation of the stiffness parameter K coinciding with the one presented in Eq. (3.31). When dealing with veins, their possible collapse in case of large negative transmural pressures needs to be considered (Carpenter and Pedley, 2001; Toro and Siviglia, 2013; Murillo, Navas-Montilla, and García-Navarro, 2019). The collapsed state for veins is identified by a cross-sectional area assuming a buckled, dumbbell shape configuration, in which opposite sides of the interior wall touch each other, still leaving some fluid in the two extremes (Carpenter and Pedley, 2001; Spiller et al., 2017). This particular aspect leads to the assumption of different parameters for the mechanical characterization of the wall behavior (Shapiro, 1977):

$$K = \frac{E_0}{12W^3}, \quad m = 10, \quad n = -3/2. \tag{4.6}$$

Following what presented in Section 3.2.1.3, it is also possible to derive with respect to time Eq. (4.4) and to use the continuity Eq. (4.1a) to obtain a PDE representative of the elastic behavior of the vessel wall:

$$\partial_t p + \frac{K}{A}\left(m\alpha^m - n\alpha^n\right)\partial_x(Au) = 0, \tag{4.7}$$

with the same set of parameters K, m and n discussed above for the characterization of arteries (4.5) or veins (4.6).

4.2.1.4 Viscoelastic constitutive tube law

Even though mathematical models representing the blood circulation frequently neglect the viscous component of the vessel wall, it is well known that blood vessels (and living tissues in general) exhibit viscoelastic properties (Fung, 1997; Nichols, O'Rourke, and Vlachlopoulos, 2011; Salvi, 2012). Viscoelastic effects are simulated in literature using different more or less complex rheological models, whether linear or not (Holenstein, Niederer, and Anliker, 1980; Bessems et al., 2008; Valdez-Jasso et al., 2009; Wang, Golob, and Chesler, 2016; Ghigo et al., 2017; Mitsotakis et al., 2019). The most frequently used viscoelastic model results being the KV model (see Section 2.3.2 for details about the model). Considering initially a generic artery, the deformation of the wall is geometrically related to the cross-sectional area through equation $\epsilon = \alpha^m - \alpha^n = \sqrt{\alpha} - 1$. Involving Barlow's formula, for which $\sigma = W(p - p_{ext})$, as in Eq. (3.10), and the continuity Eq. (4.1a), it is possible to reformulate the constitutive law of the KV model, presented in Eq. (2.12), in the following pressure-area relation:

$$p = p_{ext} + K\left(\alpha^m - \alpha^n\right) - \frac{\Gamma}{A_0\sqrt{A}}\frac{\partial(Au)}{\partial x}, \tag{4.8}$$

with

$$\Gamma = \frac{\eta s_0\sqrt{\pi}}{2} \tag{4.9}$$

representing the viscous contribution of the material. With the same approach, considering $m = 10$ and $n = -3/2$ as in Eq. (4.6) for $\epsilon = \alpha^m - \alpha^n$ and assuming a relationship between stress and pressure defined as $\sigma = 12W^3(p - p_{ext})$, to take into account the potential collapsibility of the vessel wall, it is possible to obtain exactly the same equation (4.8), valid also for veins.
This viscoelastic law, which is widely adopted among literature's well recognized blood flow models (Alastruey et al., 2011; Montecinos, Müller, and Toro, 2014; Wang, Fullana, and Lagrée, 2014; Mynard and Smolich, 2015), has the deficiency of defining a relaxation response that is an impulse/spike plus a constant. Setting the strain to be a constant, indeed, the constitutive Eq. (2.12) reduces to the simple Hooke's law: $\sigma = E\epsilon$. In this way, the stress is taken up by the spring and is constant; so in fact there is no stress relaxation over time (Lakes, 2009).

A more realistic behavior can be modeled by the SLS model, represented in Fig. 2.5 (in this study chosen in its form with a KV unit). As already discussed in Section 2.3.3, the SLS model is yet able to exhibit all the three primary features of a viscoelastic material: creep, stress relaxation and hysteresis (Battista, 2015). Concerning hysteresis, indeed, it is possible to see vessels pressure-area loops representing the energy dissipated during expansion and contraction cycles (Nichols, O'Rourke, and Vlachlopoulos, 2011; Salvi, 2012). Moreover, with the SLS model, it is possible to define the so-called relaxation function, defined in Eq. (2.20), which describes, through the relaxation time τ_r, how the stiffness of the material changes in time, starting from the instantaneous value, E_0, and reaching the asymptotic one, E_∞. As previously presented for the KV model and in Section 3.2.1.3, it is possible to write the SLS model constitutive equation in terms of pressure and area. Taking into account a generic artery and parameters K, m and n as presented in Eq. (4.5), differentiating with respect to time equation $\epsilon = \alpha^m - \alpha^n$ and Barlow's formula, it follows that: $\mathrm{d}\epsilon/\mathrm{d}t = A^{-1}\left(m\alpha^m - n\alpha^n\right)\mathrm{d}A/\mathrm{d}t$ and $\mathrm{d}\sigma/\mathrm{d}t = W\mathrm{d}p/\mathrm{d}t$. Introducing these equations in the rheological law, presented in Eq. (2.16), and using the continuity equation (4.1a), the sought PDE is obtained:

$$\partial_t p + \frac{K}{A}\left(m\alpha^m - n\alpha^n\right)\partial_x(Au) = \frac{1}{\tau_r}\left[\frac{E_\infty}{E_0}\psi_{el} - (p - p_{ext})\right]. \tag{4.10}$$

Also with the SLS model it is possible to extend the applicability of the equation to the case of veins with the same procedure discussed for the KV model, considering in this case the set of parameters K, m and n presented in Eq. (4.6). It is here highlighted that the viscosity coefficient η of the SLS model can be reconducted to the KV model's viscosity parameter Γ directly through Eq. (4.9):

$$\eta = \frac{2\Gamma}{s_0\sqrt{\pi}}. \tag{4.11}$$

4.2.1.5 The augmented FSI system

Based on the choice on how to simulate the mechanical behavior of the vessel wall, whether elastic or viscoelastic, adding respectively Eq. (4.7) or Eq. (4.10) inside system (4.1), it is possible to obtain a novel 1D a-FSI system valid for the blood flow modeling. Furthermore, to accommodate longitudinal discontinuities of geometrical and mechanical properties, such as equilibrium cross-sectional area, instantaneous Young modulus E_0 (or eventually the asymptotic one, E_∞) and external pressure p_{ext}, it is necessary to introduce additional equations to the system, to allow a formally correct treatment (Müller

and Toro, 2013). Considering that these variables are constant in time, the additional equations result: $\partial_t A_0 = 0$, $\partial_t E_0 = 0$ and $\partial_t p_{ext} = 0$.
The complete coupled system of the FSI problem finally results:

$$\partial_t A + \partial_x(Au) = 0 \tag{4.12a}$$

$$\partial_t(Au) + \partial_x(Au^2) + \frac{A}{\rho}\partial_x p = \frac{F_R}{\rho} \tag{4.12b}$$

$$\partial_t p + d\,\partial_x(Au) = S \tag{4.12c}$$

$$\partial_t A_0 = 0 \tag{4.12d}$$

$$\partial_t E_0 = 0 \tag{4.12e}$$

$$\partial_t p_{ext} = 0. \tag{4.12f}$$

In Eq. (4.12c), the parameter $d(A, A_0, E_0)$ represents the elastic contribution of the tube law (as in Eq. (3.45c) in the case of compressible fluids systems), having indeed the same formulation if choosing an elastic or a viscoelastic characterization of the wall:

$$d = \frac{K}{A}\left(m\alpha^m - n\alpha^n\right). \tag{4.13}$$

In the same equation, the source term $S(x,t)$ takes into account the viscous information of the vessel wall behavior, hence simply being $S = 0$, as in Eq. (4.7), if an elastic wall behavior is considered, or

$$S = \frac{1}{\tau_r}\left[\frac{E_\infty}{E_0}\psi_{el} - (p - p_{ext})\right], \tag{4.14}$$

as in Eq. (4.10), if a more realistic viscoelastic behavior is chosen.

The reader is invited to observe how the formulation of the source term in Eq. (4.14) is coherent with the wall's mechanical behavior assumed. When one considers that the viscosity coefficient tends to zero, $\eta \to 0$, and therefore also the relaxation time $\tau_r \to 0$, one is asymptotically tending to a perfectly elastic behavior of the material, which automatically leads to $S \to 0$ through Eq. (4.12c). On the other hand, a relaxation time that tends to zero means, referring to the relaxation function presented in Eq. (2.20), that the Young modulus is constant in time, being $E_\infty \equiv E_0$, hence $E_\infty/E_0 \to 1$. This is, moreover, in accordance with the fact that, when tending to a perfectly elastic behavior, one direct consequence is that $\psi_{el} \to (p - p_{ext})$. These two final aspects, together, lead again to the result $S \to 0$.
It is also worth to underline that the choice of inserting the tube law in the form of a PDE straight inside the system of equations is even more advantageous when selecting a viscoelastic rheological characterization of the vessel wall. Indeed, if the classical formulation is followed, together with the choice of the KV viscoelastic model, Eq. (4.8) enters inside the system through Eq. (4.1b), and in particular through the derivative in space of the pressure. This procedure gives rise to a second order derivative in space of the flow rate Au, which leads to deal with a non-hyperbolic system and also to substantial numerical issues. In literature this problem is treated differently, e.g. resorting a hyperbolic reformulation of the system, introducing a numerical relaxation parameter mimic Cattaneo's law (Montecinos, Müller, and Toro, 2014), using a discontinuous Galerkin scheme (Alastruey et al., 2011), or considering a specific operator-splitting procedure (Formaggia, Lamponi, and Quarteroni, 2003; Mynard and Smolich, 2015). When considering the

proposed 1D a-FSI system, instead, the system persists to be natively hyperbolic.

Writing the non-linear non-conservative system (4.12) in the general compact form leads to:

$$\partial_t \boldsymbol{Q} + \partial_x \boldsymbol{f}(\boldsymbol{Q}) + \boldsymbol{B}(\boldsymbol{Q})\partial_x \boldsymbol{Q} = \boldsymbol{S}(\boldsymbol{Q}), \tag{4.15}$$

in which

$$\boldsymbol{Q} = \begin{pmatrix} A \\ Au \\ p \\ A_0 \\ E_0 \\ p_{ext} \end{pmatrix}, \quad \boldsymbol{f}(\boldsymbol{Q}) = \begin{pmatrix} Au \\ Au^2 \\ 0 \\ 0 \\ 0 \\ 0 \end{pmatrix}, \quad \boldsymbol{S}(\boldsymbol{Q}) = \begin{pmatrix} 0 \\ 0 \\ S \\ 0 \\ 0 \\ 0 \end{pmatrix}, \quad \boldsymbol{B}(\boldsymbol{Q}) = \begin{pmatrix} 0 & 0 & 0 & 0 & 0 & 0 \\ 0 & 0 & \frac{A}{\rho} & 0 & 0 & 0 \\ 0 & d & 0 & 0 & 0 & 0 \\ 0 & 0 & 0 & 0 & 0 & 0 \\ 0 & 0 & 0 & 0 & 0 & 0 \\ 0 & 0 & 0 & 0 & 0 & 0 \end{pmatrix}.$$

The system can also be written in the quasi-linear form,

$$\partial_t \boldsymbol{Q} + \boldsymbol{A}(\boldsymbol{Q})\partial_x \boldsymbol{Q} = \boldsymbol{S}(\boldsymbol{Q}), \tag{4.16}$$

considering $\boldsymbol{A}(\boldsymbol{Q}) = \partial \boldsymbol{f}/\partial \boldsymbol{Q} + \boldsymbol{B}(\boldsymbol{Q})$, with

$$\frac{\partial \boldsymbol{f}}{\partial \boldsymbol{Q}} = \begin{pmatrix} 0 & 1 & 0 & 0 & 0 & 0 \\ -u^2 & 2u & 0 & 0 & 0 & 0 \\ 0 & 0 & 0 & 0 & 0 & 0 \\ 0 & 0 & 0 & 0 & 0 & 0 \\ 0 & 0 & 0 & 0 & 0 & 0 \\ 0 & 0 & 0 & 0 & 0 & 0 \end{pmatrix}.$$

It can be demonstrated that the system is hyperbolic, being the matrix $\boldsymbol{A}(\boldsymbol{Q})$ diagonalizable, with a diagonal matrix $\boldsymbol{\Lambda}(\boldsymbol{Q})$ containing all real eigenvalues λ_l, with $l = 1, \cdots, N$ and N number of unknowns of the system (in this work $N = 6$), and a complete set of linearly independent eigenvectors represented by the columns of the matrix $\boldsymbol{R}(\boldsymbol{Q})$:

$$\boldsymbol{\Lambda}(\boldsymbol{Q}) = \begin{pmatrix} 0 & 0 & 0 & 0 & 0 & 0 \\ 0 & 0 & 0 & 0 & 0 & 0 \\ 0 & 0 & 0 & 0 & 0 & 0 \\ 0 & 0 & 0 & 0 & 0 & 0 \\ 0 & 0 & 0 & 0 & u+c & 0 \\ 0 & 0 & 0 & 0 & 0 & u-c \end{pmatrix}, \quad \boldsymbol{R}(\boldsymbol{Q}) = \begin{pmatrix} \frac{A}{\rho u^2} & 0 & 0 & 0 & \frac{1}{d} & \frac{1}{d} \\ 0 & 0 & 0 & 0 & \frac{u+c}{d} & \frac{u-c}{d} \\ 1 & 0 & 0 & 0 & 1 & 1 \\ 0 & 1 & 0 & 0 & 0 & 0 \\ 0 & 0 & 1 & 0 & 0 & 0 \\ 0 & 0 & 0 & 1 & 0 & 0 \end{pmatrix}.$$

In this system, since we are dealing with an incompressible fluid (in which the speed of sound c_s tends to infinity), the wave speed a coincides with the solely contribute c arising from the FSI (see Eqs. (3.14) and (3.16) for a comparison with the compressible case):

$$c = \sqrt{\frac{A}{\rho}\frac{\partial p}{\partial A}} = \sqrt{\frac{A}{\rho}d} = \sqrt{\frac{K}{\rho}\left(m\alpha^m - n\alpha^n\right)} \quad . \tag{4.17}$$

Concerning the eigenvectors, the fifth and the sixth characteristic fields are genuinely non-linear and are associated to shocks and rarefactions, whereas the remaining fields are linearly degenerate (LD) and are associated with stationary contact discontinuities. Evaluating the Riemann invariants (RI) of the system, those associated with the genuinely

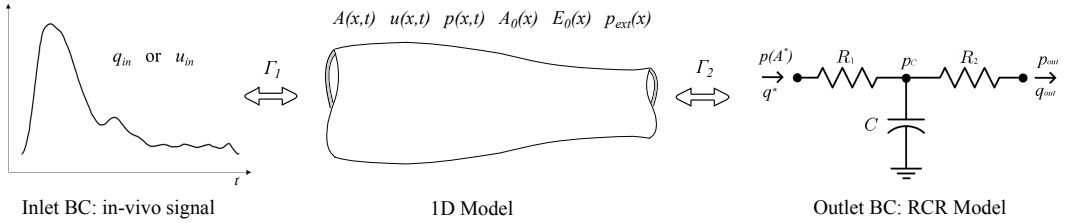

FIGURE 4.1: *Schematic representation of the hemodynamic model. Inlet boundary condition given by q_{in} or u_{in} and recurring to the first Riemann invariant Γ_1, defined in Eq. (4.18). The 1D a-FSI model is coupled to the 3-element Windkessel model (analogous to the RCR electric circuit) at the outlet through the solution of a Riemann problem at the 1D/0D interface, recurring to the second Riemann invariant Γ_2, defined in Eq. (4.18).*

non-linear fields are:

$$\Gamma_1 = u - \int \frac{c}{A} \mathrm{d}A, \quad \Gamma_2 = u + \int \frac{c}{A} \mathrm{d}A; \tag{4.18}$$

while those associated with the linearly degenerate fields result:

$$\Gamma_1^{LD} = p + \frac{1}{2}\rho u^2, \quad \Gamma_2^{LD} = Au, \quad \Gamma_3^{LD} = p - \int d \, \mathrm{d}A = p - \psi_{el}. \tag{4.19}$$

It has to be noticed that when dealing with arteries, integrals in the RI associated with the genuinely non-linear fields can be analytically resolved, resulting:

$$\Gamma_1 = u - 4c, \qquad \Gamma_2 = u + 4c.$$

Moreover, when dealing with a purely elastic system, the third RI associated with a linearly degenerate field results:

$$\Gamma_3^{LD} = p_{ext}.$$

Finally, it is here mentioned that, under physiological conditions, the source term of system (4.12) may become stiff, depending on the spatial discretization applied. Referring to Müller, Montecinos, and Toro (2013), indeed, a source term can be considered stiff if

$$\Delta x \frac{\max\{|\, \beta_l \,|\}}{\max\{|\, \lambda_l \,|\}} > 1, \quad l = 1, \cdots, N, \tag{4.20}$$

with β_l representing the *l-th* eigenvalue of the Jacobian of $\boldsymbol{S}(\boldsymbol{Q})$. It can be evaluated that $\max\{|\, \beta_l \,|\} = 1/\tau_r$, which could reach values up to 5 orders of magnitude more than $\max\{|\, \lambda_l \,|\} = u + c$. Additionally, it is evident that the relaxation time of the material τ_r, related to viscoelasticity, is the key parameter leading to stiffness.

4.2.1.6 Lumped-parameter models

Linearizing the continuity equation (4.12a) and the momentum equation (4.12b) with respect to a reference state $(A, Au, p) = (A_0, 0, 0)$ and integrating them along the length L of the vessel domain, the following system is obtained (Alastruey et al., 2008):

$$\begin{aligned} C\, \mathrm{d}_t(\hat{p} - p_{ext}) &= q_{in} - q_{out} \\ \mathcal{L}\, \mathrm{d}_t \hat{q} + R\, \hat{q} &= p_{in} - p_{out}, \end{aligned} \tag{4.21}$$

where $q_{in}(t) = q(0,t)$, $q_{out}(t) = q(L,t)$, $p_{in}(t) = p(0,t)$, $p_{out}(t) = p(L,t)$ are flow rates and pressures at the inlet and outlet interface of the domain, $\hat{p}(t) = \frac{1}{L}\int_0^L p\,\mathrm{d}x$, $\hat{q}(t) = \frac{1}{L}\int_0^L q\,\mathrm{d}x$ are mean pressure and flow rate over the entire domain and

$$R = -\frac{F_R L}{A_0^2 u}, \qquad \mathcal{L} = \frac{\rho L}{A_0}, \qquad C = \frac{A_0 L}{\rho c_0^2},$$

are respectively resistance related to the blood viscosity, inductance related to the blood inertia and capacitance related to the wall compliance of the vessel, with c_0 reference wave speed. System (4.21) can be equivalently regarded as the mathematical description of an electric circuit known as "$\mathcal{L}$-circuit". Indeed, in this hydraulic-electric analogy, pressure and flow rate correspond respectively to electric voltage/potential and current (Milišić and Quarteroni, 2004).

The 0D model commonly used to simulate the effects of peripheral resistance and compliance on pulse wave propagation in large 1D arteries is the so-called RCR model (or 3-element Windkessel model), which consists of a resistor with resistance R_1 connected in series with a parallel combination of a second resistor with resistance R_2 and a capacitor with compliance C, as shown in Fig. 4.1 (Boileau et al., 2015; Alastruey, Parker, and Sherwin, 2012; Reymond et al., 2009; Willemet, Vennin, and Alastruey, 2016; Xiao, Alastruey, and Figueroa, 2014). Note that in this model the inductance is neglected since peripheral inertias have a minor effect on reflected waves under normal conditions (Alastruey et al., 2008). In the present work, to impose outflow conditions, the RCR model has been chosen considering that the external pressure is constant in time, hence $\mathrm{d}_t p_{ext} = 0$. Thus, referring to Fig. 4.1 for the nomenclature, the resulting final system for the 0D model reads:

$$C\,\mathrm{d}_t p_C = q^* - q_{out} \tag{4.22a}$$
$$R_1 q^* = p(A^*) - p_C \tag{4.22b}$$
$$R_2 q_{out} = p_C - p_{out}\,, \tag{4.22c}$$

where p_C is the pressure at the capacitor and $q^* = A^* u^*$.
In the RCR model, the first resistance R_1 is introduced to absorb incoming waves and reduce artificial backward wave reflections in large arteries (Alastruey et al., 2008). Therefore, R_1 is fixed to match the characteristic impedance Z_0 of the terminal 1D vessel:

$$R_1 = Z_0 = \frac{\rho c_0}{A_0}. \tag{4.23}$$

4.2.2 Numerical model

To solve system (4.12), the IMEX RK schemes proposed by Pareschi and Russo (2005) for applications to hyperbolic systems with stiff relaxation terms have been considered. This scheme is asymptotic preserving (AP) and asymptotic accurate in the zero relaxation limit (i.e. the consistency of the scheme with the equilibrium system is guaranteed and the order of accuracy is maintained in the stiff limit), with an elevated robustness given by the use of an implicit Runge-Kutta scheme for the treatment of the stiff part. Usually, simpler splitting techniques are preferred to solve these kind of problems; for example Strang splitting provides second order of accuracy if each step is at least second order accurate in space (Strang, 1968). However, as shown in different references

(LeVeque and Yee, 1990; Descombes and Massot, 2004; Pareschi and Russo, 2005; Duarte, Massot, and Descombes, 2011) and confirmed here for the specific application discussed in section 4.3.4, this technique, which does not present the AP property, reduces to first order of accuracy when the problem becomes highly stiff. In these situations, indeed, the fastest time scales play a leading role in the global physics of the phenomenon and the composed solution of the splitting technique fails to capture the proper dynamics of the event. Recently developed RK schemes overcome this issue. Thus, a formally implicit finite volume discretization is adopted, applying a second-order L-stable diagonally implicit Runge-Kutta method (DIRK) to the stiff part and a second-order explicit strong-stability-preserving (SSP) method to the non-stiff terms, with the addition of the path-conservative DOT Riemann solver, as applied in Section 3.2.2.2 for compressible flows in polymer tubes.

4.2.2.1 IMEX Runge-Kutta scheme

The second-order IMEX RK finite volume discretization of system (4.15) is written as follows:

$$\boldsymbol{Q}_i^{(k)} = \boldsymbol{Q}_i^n - \frac{\Delta t}{\Delta x}\sum_{j=1}^{k-1}\tilde{a}_{kj}\left[\left(\boldsymbol{F}_{i+\frac{1}{2}}^{(j)} - \boldsymbol{F}_{i-\frac{1}{2}}^{(j)}\right) + \left(\boldsymbol{D}_{i+\frac{1}{2}}^{(j)} + \boldsymbol{D}_{i-\frac{1}{2}}^{(j)}\right) + \boldsymbol{B}\left(\boldsymbol{Q}_i^{(j)}\right)\Delta\boldsymbol{Q}_i^{(j)}\right] + \Delta t\sum_{j=1}^{k} a_{kj}\boldsymbol{S}\left(\boldsymbol{Q}_i^{(j)}\right) \tag{4.24a}$$

$$\boldsymbol{Q}_i^{n+1} = \boldsymbol{Q}_i^n - \frac{\Delta t}{\Delta x}\sum_{k=1}^{s}\tilde{\omega}_k\left[\left(\boldsymbol{F}_{i+\frac{1}{2}}^{(k)} - \boldsymbol{F}_{i-\frac{1}{2}}^{(k)}\right) + \left(\boldsymbol{D}_{i+\frac{1}{2}}^{(k)} + \boldsymbol{D}_{i-\frac{1}{2}}^{(k)}\right) + \boldsymbol{B}\left(\boldsymbol{Q}_i^{(k)}\right)\Delta\boldsymbol{Q}_i^{(k)}\right] + \Delta t\sum_{k=1}^{s}\omega_k\boldsymbol{S}\left(\boldsymbol{Q}_i^{(k)}\right) \tag{4.24b}$$

using a uniform grid of length L and N_x elements with mesh spacing $\Delta x = x_{i+\frac{1}{2}} - x_{i-\frac{1}{2}} = L/N_x$ and a time step size $\Delta t = t^{n+1} - t^n$ that follows the CFL condition of Eq. (3.54), with $\boldsymbol{Q}_i^n$ vector of the averaged variables on the *i-th* cell of the domain at time t^n.
Matrices $\tilde{A} = (\tilde{a}_{kj})$, with $\tilde{a}_{kj} = 0$ for $j \geq k$ and $A = (a_{kj})$ are $s \times s$ matrices such that the resulting scheme is implicit in $\boldsymbol{S}(\boldsymbol{Q})$ and explicit for all the rest, with s number of stages. Moreover, being a DIRK scheme, $a_{kj} = 0$ for $j > k$. An IMEX Runge-Kutta scheme is characterized by these two matrices and by the coefficient vectors $\tilde{\omega} = (\tilde{\omega}_1, ..., \tilde{\omega}_s)^T$, $\omega = (\omega_1, ..., \omega_s)^T$, which can be easily represented by a double tableau in the usual Butcher notation (Pareschi and Russo, 2005):

$$\begin{array}{c|c} \tilde{c}_k & \tilde{a}_{kj} \\ \hline & \tilde{\omega}_k^T \end{array} \qquad\qquad \begin{array}{c|c} c_k & a_{kj} \\ \hline & \omega_k^T \end{array}$$

where coefficient vectors $\tilde{c}_k$ and c_k are given by:

$$\tilde{c}_k = \sum_{j=1}^{k-1}\tilde{a}_{kj}, \qquad\qquad c_k = \sum_{j=1}^{k} a_{kj}.$$

In particular, in the present work it has been chosen the stiffly accurate IMEX-SSP2(3,3,2) Runge-Kutta scheme, characterized by $s = 3$ stages for the implicit part, 3 stages for the explicit part and 2^{nd} order of accuracy, which can be defined by the following tableau (explicit part on the left and implicit part on the right):

0	0	0	0
1/2	1/2	0	0
1	1/2	1/2	0
	1/3	1/3	1/3

1/4	1/4	0	0
1/4	0	1/4	0
1	1/3	1/3	1/3
	1/3	1/3	1/3

noticing that the explicit discretization coincides with an improved Euler method (Heun's method). The explicit RK methods are those in which the only non-zero entries in the $\tilde{A}$ matrix lie strictly below the diagonal. Entries at or above the diagonal will cause the right hand side of Eq. (4.24a) to involve $\boldsymbol{Q}_i^{(j)}$, giving a formally implicit method. Nevertheless, it is worth to highlight that, for the system of equations presented in this work, it is possible to obtain a totally explicit algorithm, which leads to a consistent reduction of the computational cost. More details concerning the implemented IMEX algorithm can be found in Appendix A, at the end of the Thesis.
For each step of the method, the numerical fluxes are obtained applying the DOT solver as defined by Dumbser and Toro (2011b) and Dumbser and Toro (2011a) and already discussed in Section 3.2.2.2. Hence, numerical fluxes are evaluated through Eq. (3.65) and fluctuations through Eq. (3.66), with integrals approximated by a simple 3-points Gauss-Legendre quadrature formula. The boundary-extrapolated values within cell i in this case are given by:

$$\boldsymbol{Q}^{-}_{i+\frac{1}{2}} = \boldsymbol{Q}_i + \frac{1}{2}\Delta\boldsymbol{Q}_i, \qquad \boldsymbol{Q}^{+}_{i-\frac{1}{2}} = \boldsymbol{Q}_i - \frac{1}{2}\Delta\boldsymbol{Q}_i.$$

with the slope $\Delta\boldsymbol{Q}_i$ again evaluated using the minmod slope limiter (Toro, 2009), to avoid spurious oscillations near discontinuities. Finally, the path Ψ connecting left to right boundary values in the phase-space (Parés, 2006) is linear, as presented in Eq. (3.68).

4.2.2.2 Well-balancing proof

A numerical scheme is here defined exactly well-balanced or, with the same connotation, satisfies the exact conservation property, i.e. C-property (Bermudez and Vazquez, 1994), if it is exact when applied to the stationary case in the zero flow rate condition. For the particular case of a scheme of the form (4.24) for system (4.12), this means that, for a given initial state of rest $\boldsymbol{Q}_i^n, \forall i \in [1, \cdots, N_x]$, for each RK stage it results that:

$$\boldsymbol{F}_{i+\frac{1}{2}} - \boldsymbol{F}_{i-\frac{1}{2}} = 0, \qquad \boldsymbol{D}_{i+\frac{1}{2}} + \boldsymbol{D}_{i-\frac{1}{2}} = 0, \qquad \boldsymbol{B}\left(\boldsymbol{Q}_i\right)\Delta\boldsymbol{Q}_i = 0, \qquad \forall i \in [1, \cdots, N_x].$$

In a condition of zero velocity ($u = 0$, $Au = 0$), observing system (4.12), p must be constant in x. Thus, both the second and the third component in $\Delta\boldsymbol{Q}_i$ are necessarily zero. Evaluating then the product $\boldsymbol{B}\left(\boldsymbol{Q}_i\right)\Delta\boldsymbol{Q}_i$, it can be noticed that the only non-zero columns in $\boldsymbol{B}\left(\boldsymbol{Q}_i\right)$ multiply exactly the two zero components in $\Delta\boldsymbol{Q}_i$, obtaining a null vector as result. Choosing a simple linear path Ψ, the same applies also to the term $\boldsymbol{B}\left(\Psi\right)\frac{\partial\Psi}{\partial s}$ when evaluating the fluctuations $\boldsymbol{D}_{i\pm\frac{1}{2}}$ through Eq. (3.66) and to the product $\left|\boldsymbol{A}\left(\Psi\right)\right|\frac{\partial\Psi}{\partial s}$ when evaluating the numerical fluxes $\boldsymbol{F}_{i\pm\frac{1}{2}}$ with Eq. (3.65). Finally, the analytical fluxes $\boldsymbol{f}\left(\boldsymbol{Q}^{\pm}_{i\pm\frac{1}{2}}\right)$ are automatically null when considering a zero flow rate state.
It is therefore proved that the numerical model here discussed is well-balanced for the a-FSI system of blood flow equations. It is also underlined that the C-property arises in a straightforward way from the construction of the explicit part of the scheme and not

from the implicit one, which leads to have more freedom when choosing the particular set of coefficients of the IMEX method.

4.2.2.3 Pressure update analysis

Evaluating the Rankine-Hugoniot conditions related to the continuity equation (4.12a) and to the additional elastic constitutive PDE (4.12c), it is observed that the celerity of the shock wave results respectively (Toro, 2009):

$$\xi = \frac{\Delta(Au)}{\Delta A}, \qquad \xi = \frac{\Delta(Au)}{\Delta p} \int_0^1 d\,\mathrm{d}s.$$

Since the celerity of the discontinuity is unique, it must be:

$$\frac{\Delta p}{\Delta A} = \int_0^1 d\,\mathrm{d}s = \int_0^1 \frac{\partial p}{\partial A}\,\mathrm{d}s.$$

This expression is always true when dealing with linear systems and can be considered a good approximation in case of mildly non-linear systems, but it is certainly not valid when working in a scenario of highly deformable and even collapsible veins (Carpenter and Pedley, 2001). In fact, adding the tube law inside the system of equations leads, in the elastic case, to an over-abundant system and a consequent inconsistency.
Hence, to correctly update through the tube law the non-conservative variable p, in accordance with the update of the related conservative variable A, even in the case of non-linear systems, an alternative evolution of the pressure is introduced in the scheme. Defining, for each *k-th* Runge-Kutta step, the pressure with physical sense if an elastic behavior of the vessel wall is considered as:

$$p_{el,i}^{(k)} = p_{ext,i} + \psi_{el,i}^{(k)}, \qquad p_{el,i}^{(k+1)} = p_{ext,i} + \psi_{el,i}^{(k+1)},$$

the contribution for the pressure variation in time exclusively linked to the area variation, both in the elastic and in the viscoelastic case, results:

$$\Delta p_{el,i}^{(k)} = p_{el,i}^{(k+1)} - p_{el,i}^{(k)}.$$

Thus, the additional pressure update, containing all the information of the time evolution, even regarding the viscoelastic contribute enclosed in the source term, results:

$$p_i^{(k+1)} = p_i^{(k)} + \Delta p_{el,i}^{(k)} + \Delta t \sum_{j=1}^{s} a_{kj} \mathcal{S}\left(\boldsymbol{Q}_i^{(j)}\right). \tag{4.25}$$

In the same way, the final pressure update between time t^n and t^{n+1} will be:

$$p_i^{n+1} = p_i^n + \Delta p_{el,i}^n + \Delta t \sum_{k=1}^{s} \omega_k \mathcal{S}\left(\boldsymbol{Q}_i^{(k)}\right). \tag{4.26}$$

Involving this additional evaluation, p is properly updated following the time evolution of the variable A through the constitutive law, with the due phase-synchronization of the two variables requested by the elastic part of the rheological model.

4.2.2.4 Boundary conditions

When simulating real case studies (see Fig. 4.1), inflow boundary conditions are defined prescribing the inlet flow rate q_{in} or the inlet velocity u_{in} (depending on the available data) and recurring to the first Riemann Invariant Γ_1 associated with the genuinely non-linear fields, defined in Eq. (4.18). The viscosity of the vessel wall is neglected when imposing boundary conditions, recurring to the simple elastic model relating p to A (Alastruey, Parker, and Sherwin, 2012).

At the outflow of the 1D domain, to simulate the effects of resistance and compliance of downstream vessels on the pulse wave propagation, the RCR model is coupled with the 1D model through the solution of the problem at the interface. A null outlet pressure, $p_{out} = 0$, which represents the pressure at which the flow arrives in the venous system, is prescribed (Xiao, Alastruey, and Figueroa, 2014). Referring again to Fig. 4.1 for the nomenclature, the discretization of system (4.22), considering the intermediate IMEX time step size $\Delta t = t^{(k+1)} - t^{(k)}$, leads to:

$$p_C^{(k+1)} - p_C^{(k)} = \frac{\Delta t}{C}\left[(q^*)^{(k+1)} - q_{out}^{(k+1)}\right] \tag{4.27a}$$

$$(q^*)^{(k+1)} = \frac{1}{R_1}\left[p(A^*)^{(k+1)} - p_C^{(k+1)}\right] \tag{4.27b}$$

$$q_{out}^{(k+1)} = \frac{1}{R_2}\left[p_C^{(k+1)} - p_{out}\right]. \tag{4.27c}$$

Subtracting Eq. (4.27c) from Eq. (4.27a) gives:

$$p_C^{(k+1)} = \frac{R_2}{\phi}(q^*)^{(k+1)} + \frac{\phi - 1}{\phi}p_C^{(k)} + \frac{p_{out}}{\phi}, \tag{4.28}$$

where $\phi = \frac{R_2 C}{\Delta t} + 1$. Using Eq. (4.28) into Eq. (4.27b) the expression for q^* is obtained, which reads:

$$(q^*)^{(k+1)} = \frac{p(A^*)^{(k+1)} - \tilde{p}}{R_1 + \frac{R_2}{\phi}}, \tag{4.29}$$

with $\tilde{p} = \phi^{-1}\left[p_{out} + (\phi - 1)p_C^{(k)}\right]$. Combining Eq. (4.29) with the second Riemann Invariant Γ_2 defined in Eq. (4.18), evaluated in the last cell and at the outlet interface of the 1D domain, yields to a non-linear equation in A^*, solved using Newton's method (Alastruey et al., 2008). Once A^* is obtained, u^* is calculated through Γ_2 and $p(A^*)$ is evaluated with the elastic tube law.

4.2.3 Human in-vivo blood flow velocity and pressure waveforms: data acquisition and extrapolation

To obtain in-vivo data useful to validate the proposed model, blood flow velocity and pressure waveforms are extrapolated from ad hoc measurements performed in six different healthy volunteers, from whom proper informed consent was previously obtained. The Doppler ultrasound technique (Xario 100, Toshiba Medical System, Shimoishagami, Japan) in combination with a 4.8/11 Hz linear transducer (Toshiba PLU-704BT) is used to record the time evolution of blood velocity (Gill, 1985; Hwang, 2017). Ultrasound images of velocity are essentially obtained from measurements of movement. In ultrasound scanners, a series of pulses is transmitted to detect movement of blood. Echoes from

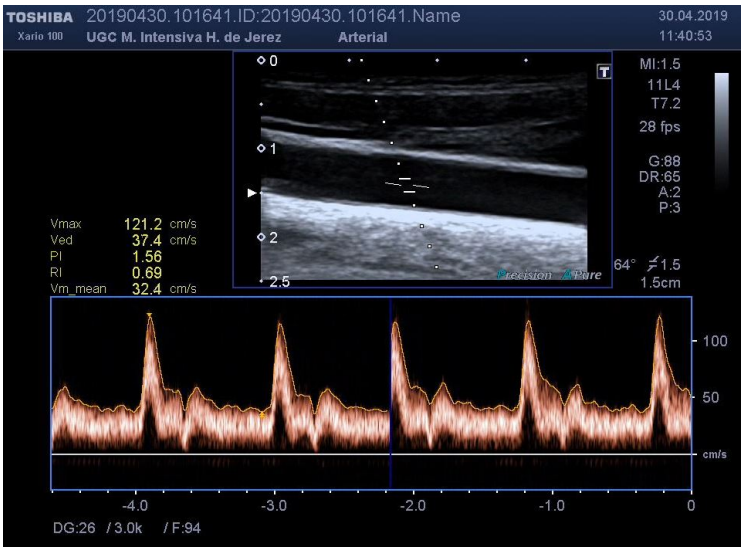

FIGURE 4.2: *Example of the display of a Doppler ultrasound record. On the top, the individuation of the sample volume, placed in the middle of the vessel. On the bottom, the pulse velocity signal recorded.*

stationary tissue are the same from pulse to pulse. Echoes from moving scatterers (red cells) exhibit slight differences in the time for the signal to be returned to the receiver. These differences can be measured as a direct time difference or, more usually, in terms of a phase shift from which the Doppler frequency is obtained. They are then processed to produce either a color flow display. In four volunteers blood velocity is measured in the right CCA, while in two volunteers measurements are executed in the right CFA. A beam-flow angle of 60° and a sample volume defined by a window size of 1.0-1.5 mm are chosen for the experiments. Aware of the possible sources of error and non-optimal accuracy of Doppler ultrasound measurements (Blanco et al., 2015; Gill, 1985; Park et al., 2012), this technique resulted the most applicable, since it is largely adopted for research experiments reported in literature and in hospitals. An example of the display of a Doppler ultrasound record is shown in Fig. 4.2.
In the post-processing, a threshold segmentation of the raw velocity is first applied to extract the maximum envelope of the signal. Then, considering the point of maximum derivative as starting point of a new cardiac cycle, an average of all the waves obtained for each cardiac cycle is carried out, obtaining a representative waveform for each case study. Finally, under the assumption of a parabolic velocity profile in non-central arteries (see Section 4.2.1.2), a scaling coefficient of 0.5 is used to estimate the average cross-sectional velocity signal.

To measure pressure waveforms, the arterial applanation tonometry technique is used (Giannattasio et al., 2008; O'Rourke and Hashimoto, 2007; Townsend et al., 2015; Salvi et al., 2004; Salvi, 2012; Spronck et al., 2016). A PulsePen tonometer (DiaTecne srl, Milan, Italy), which consists of a tonometric probe and an electrocardiography (EKG) unit, is chosen for this purpose (Salvi et al., 2004). The measurement is performed by placing the sensor over the skin, applying a moderate pressure to partially flatten the artery (applanation tonometry) with a balance of the circumferential forces inside the vessel. In this way the sensor records the pressure in the middle of the compressed artery.
In the post-processing, a detrending of the signal is applied to remove the low-frequency oscillations caused by the respiration of the subject, recurring to a low-pass filter. To carry

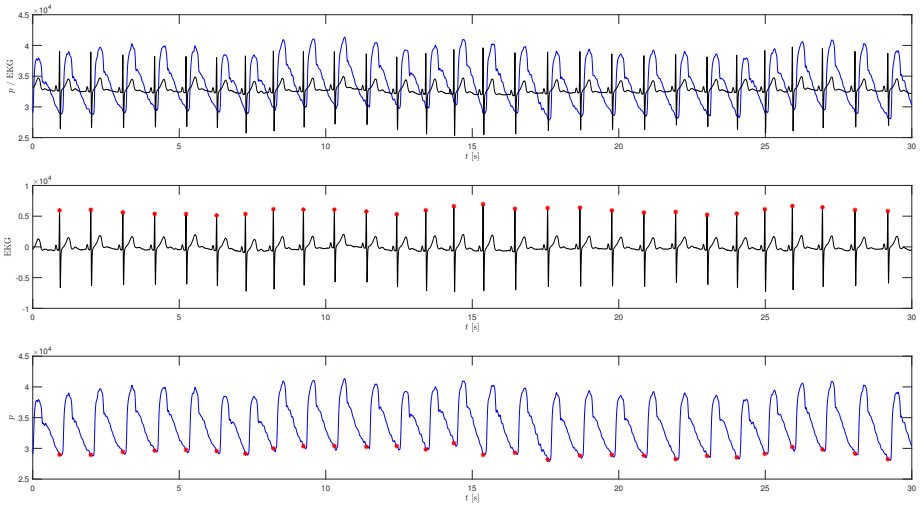

FIGURE 4.3: *Different steps of the post-processing for pressure data recorded by a tonometer. The first row represents the initial measured pressure and EKG signal; the following rows show the thresholding procedure (red stars), made using the EKG signal (second row) and then transposed to the pressure waveform (third row).*

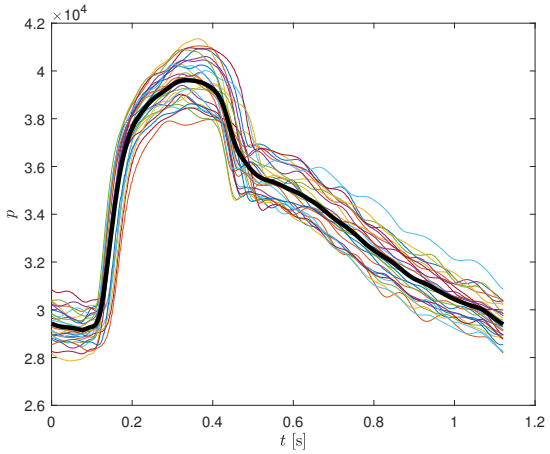

FIGURE 4.4: *Example of the overlapping of the pressure waveforms extracted from the post-processed pressure signal. The thick black line represents the mean curve.*

out a phase averaging, the EKG is used as baseline signal to estimate the duration of the cardiac cycles, through a peak-detection algorithm. An explanatory example is presented in Fig. 4.3. For all the cardiac cycles, the pressure waveform is re-sampled and averaged into a representative one (see Fig. 4.4). Finally, for the calibration of the phase-averaged pressure waveform, the diastolic and systolic pressure of the subject measured in the brachial artery (by means of a sphygmomanometer at the beginning of the experiment) are used as reference values. It is indeed recalled that mean arterial pressure remains constant from the aorta to the peripheral arteries, as the diastolic pressure, which tends to decrease insignificantly from the center to the periphery (Salvi, 2012).

4.2.4 FSI parameters estimation

In the case of a purely elastic model, the single Young modulus E_0 is evaluated through a given reference celerity c_0, taken from literature (Müller and Toro, 2014a). Inverting the wave speed Eq. (4.17), considering a reference state (in this work the diastolic state) in which $A = A_0$ (Alastruey, Parker, and Sherwin, 2012; Alastruey et al., 2012), leads to:

$$E_0 = \frac{2R_0\rho c_0^2}{s_0}. \tag{4.30}$$

When the viscosity of the vessel wall is taken into account considering the SLS model (Fig. 2.5), the elastic component is represented by two different Young modulus: the instantaneous, E_0, and the asymptotic one, E_∞, defined in Eq. (2.18). The elastic modulus of the system $E(x,t)$ changes in time, from the instantaneous to the asymptotic value, following the so-called relaxation function presented in Eq. (2.20). How rapidly the viscoelastic material reaches the asymptotic condition depends on the third parameter of the model: the relaxation time, τ_r. Moreover, when the viscoelastic material undergoes cyclic loading and unloading, the amount of energy dissipated (represented by the hysteresis loop) does not only depend on the viscous parameter η, but also on the ratio E_∞/E_0, hence on how much the behavior of the material differs from the elastic one (for which $E_\infty \equiv E_0$).

The estimation of the three viscoelastic parameters defining the SLS model aims to obtain a viscoelastic system that correctly matches with the corresponding elastic in the asymptotic case. When considering the SLS model with $\eta = 0$, the equivalent elastic system is represented by two springs in series for which the equivalent Young modulus exactly results E_∞. Therefore, when switching from elastic to viscoelastic simulations, E_∞ is imposed equal to the previously calculated E_0 in the elastic case through Eq. (4.30).
For the determination of the viscosity parameter η, we refer to parameters estimated by Alastruey et al. (2012) for the viscosity coefficient Γ of the viscoelastic KV model, for which the linear relationship with η (neglecting Poisson's ratio) is presented in Eq. (4.11) (Alastruey et al., 2011; Montecinos, Müller, and Toro, 2014; Mynard and Smolich, 2015; Wang, Fullana, and Lagrée, 2014).
Finally, the ratio E_∞/E_0 is evaluated in order to obtain numerical results reproducing realistic energy losses, based on published hysteresis loops from in-vivo pressure-diameter measurements of human CCAs (Giannattasio et al., 2008; Salvi, 2012), shown in grey-scale in Fig. 4.5 for subjects with different ages. The energy dissipated in literature hysteresis curves is numerically evaluated by an integral, being the area inside the loop in the p-A plane. Observing Fig. 4.5, it can be noticed that there is a high variability of hysteresis loops recorded in young subjects from those in elderly subjects, this also being the case for subjects with a higher compared with a lower blood pressure level, as highlighted by Giannattasio et al. (2008). To cope with these large fluctuations of energy losses, values of energy dissipated by viscoelastic effects are converted to energy fractions dividing them for the reference stored energy. The area of the triangle below the pulse pressure line, again in the p-A plane (refer to Fig. 4.5), is assumed as reference stored energy (Wang and Chesler, 2012). The weighted average over age is then taken as target for the comparisons with simulated dissipations.
The empirical relation which returned the best fit with reference data in CCAs is:

$$\frac{E_\infty}{E_0} = e^{-1.3\cdot10^{-5}\eta}, \tag{4.31}$$

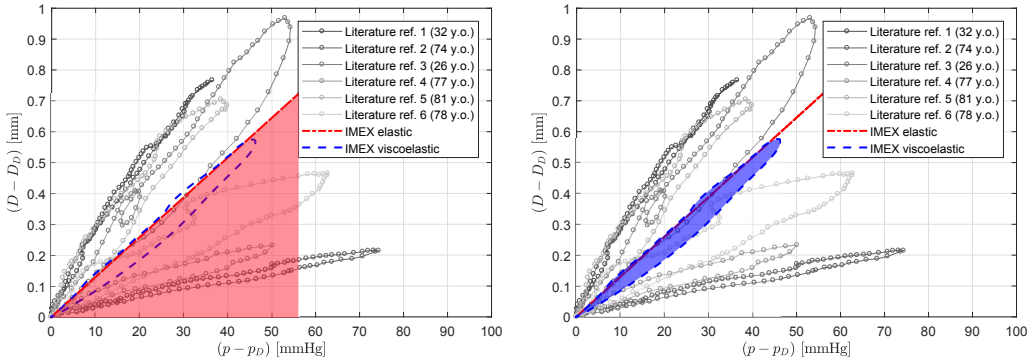

FIGURE 4.5: *Hysteresis curves of one cardiac cycle presented in terms of relative pressure and relative diameter. A representative numerical result compared to hysteresis curves available in literature (Giannattasio et al., 2008; Salvi, 2012). The highlighted areas represent an example of the evaluation of the reference stored energy (red, left) and of the dissipated energy (blue, right) used for the viscoelastic parameters calibration discussed in Section 4.2.4.*

through which the viscoelastic E_0 can be imposed. Eq. (4.31) is used for the estimation of Young modulus ratios in all the arteries of the studies further presented due to the limited *p-D* data available in literature concerning other human vessels. The reader is invited to notice that the proposed relation respects the elastic asymptotic limit, being $E_\infty/E_0 = 1$ when $\eta = 0$. For a more robust estimation of viscoelastic parameters for the entire human cardiovascular network, further measurements should be made by collecting additional in-vivo data from humans.
A schematic algorithm of the above discussed procedure is available in Appendix B.

Variable	RP1	RP2	RP3	RP4	RP5
A_L [mm^2]	6.4138	2.5082	0.9900	4.7030	2.0000
A_R [mm^2]	3.1282	3.2921	2.0800	2.1947	0.2222
u_L [m/s]	0.00	1.00	0.00	0.00	0.00
u_R [m/s]	0.00	0.00	0.00	0.00	0.00
p_L [mmHg]	80.00	146.67	9.97	178.99	43.38
p_R [mmHg]	80.00	108.78	46.05	8.05	4.58
$A_{0,L}$ [mm^2]	6.2706	1.5677	1.1000	3.1353	1.0000
$A_{0,R}$ [mm^2]	3.1353	3.1353	1.3000	3.1353	1.0000
$E_{0,L}$ [MPa]	2.7655	1.3828	0.4604	1.9555	0.3991
$E_{0,R}$ [MPa]	1.9555	1.9555	5.9153	1.9555	0.3991
$p_{ext,L}$ [mmHg]	75.00	30.00	10.00	80.00	5.00
$p_{ext,R}$ [mmHg]	85.00	0.00	5.00	80.00	5.00
x_0 [m]	0.10	0.05	0.05	0.10	0.15

TABLE 4.1: *Initial states for the Riemann problems. Subscripts L and R stand respectively for left and right state of the piece-wise constant initial values, while x_0 indicates the position of the initial discontinuity. For all the tests, L = 0.2 m, s_0 = 0.3 mm, CFL = 0.9 and N_x = 100.*

4.3 Numerical results and Discussion

To check the accuracy and the robustness of the proposed model, for ranges of parameters found in the human body and reported in applications regarding cardiovascular mathematics, different types of tests have been set up. Initially, five Riemann problems have been selected, considering only an elastic behavior of the vessel wall, for which an exact solution is available (Toro and Siviglia, 2013). The first of these RPs (RP1) aims to verify the well-balancing of the scheme in a state of rest condition, while the second (RP2) and the third (RP3) are related to unsteady problems in a 1D segment representative of a portion of the aorta and of the internal jugular vein (reproduced referring to Müller and Toro (2013)). Successively, in RP4 and RP5, the C-property of the scheme (as defined in Section 4.2.2.2) is tested also when, on the left and on the right side of the discontinuity, smooth functions are defined, in the case of a generic artery and a generic vein segment. Furthermore, since an exact solution of the problem does not exist when considering vessels viscoelasticity, to validate the contribution given by the viscoelastic source term in Eq. (4.14), the Method of Manufactured Solutions (MMS) is applied (Roache, 2002). Thus, a problem for a modified non-linear system of equations that is a perturbation of the original one via a source term vector has been designed, applying it to a generic artery and a generic vein segment. In addition, with these validation problems, the accuracy of the proposed scheme is verified. Accuracy results obtained with the IMEX RK scheme are also compared to those obtained adopting the Strang splitting technique, with which a reduction of the expected order of accuracy is observed.

For the geometrical and mechanical parameters of the vessels, Müller and Toro (2013), Müller and Toro (2014a), and Xiao, Alastruey, and Figueroa (2014) are taken as reference. The computational code, written in MATLAB (MathWorks Inc.) language, with the implementation of the above presented tests, is available in Mendeley Data repository (Bertaglia, Caleffi, and Valiani, 2020).

Further tests are designed to evaluate the applicability of the proposed model to real case studies in single vessels, assessing its capability to serve as valuable tool even for practical medical applications, cardiovascular diagnosis and the study of circulatory pathologies. Additional simulations are initially performed considering the elastic tube law to compare numerical results with benchmark data sets available in literature. The upper TA and the CCA, are first analyzed considering a constant radius (Boileau et al., 2015) and then with a linearly tapered radius (Xiao, Alastruey, and Figueroa, 2014). Simulations for the tapered vessel cases are also run using the viscoelastic SLS model.
Furthermore, specific test cases regarding the CCA and the CFA are designed using the recorded in-vivo data discussed in Section 4.2.3: the velocity waveform extrapolated from each Doppler measurement is imposed at the inlet boundary (u_{in}) as described in 4.2.2.4, while the pressure waveform measured by the PulsePen tonometer is compared to the computed pressure obtained in the last cell of the domain (this being, for both types of vessels, the position that is considered closest to the data measurement position). For these tests, simulations are performed comparing results using the elastic and the viscoelastic model, to assess the effects of the wall viscoelasticity.

In all the presented problems, when switching from the elastic to the viscoelastic tube law, only the viscoelastic parameters are activated, without changing other properties, including inlet and outlet boundary conditions. Outflow RCR parameters are calibrated following the procedure proposed by Alastruey et al., 2012 and Xiao, Alastruey, and Figueroa, 2014. Viscoelastic parameters are estimated with the procedure presented in Section 4.2.4 and summarized in Appendix B.

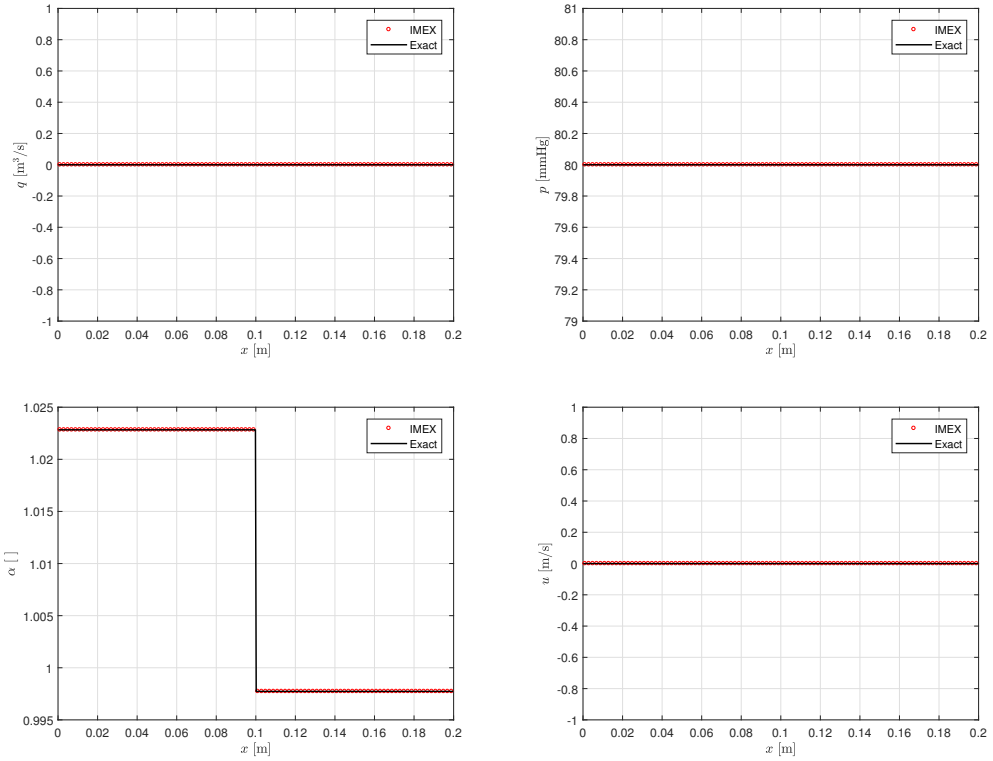

FIGURE 4.6: *Results obtained in test RP1, at time t_{end} = 0.01 s, solving the 1D a-FSI system with the IMEX Runge-Kutta scheme, in terms of flow rate q, pressure p, non-dimensional cross-sectional area α and velocity u, with respect to the exact solution.*

4.3.1 Riemann problems

The first Riemann problem, RP1, is designed to verify the well-balancing, in a rest state, of the IMEX RK scheme here proposed for the resolution of the a-FSI system (4.12). The problem presents an initial discontinuity in A, A_0, E_0 and p_{ext}. Results of RP1 at $t_{end} = 0.01$ s (after 94 complete time iterations), shown in Fig. 4.6 confirm that the scheme is able to preserve the initial condition in the case of zero flow rate. Indeed, the L^2 norm calculated for the evolutive variables A, Au and p results, respectively: $3.83 \times 10^{-20}, 0$ and 0 (values in SI units).

The second Riemann problem, RP2, schematically represents a systolic pressure and peak flow rate arriving in a portion of the thoracic aorta. In this problem, the left side of the aorta, so the part that in the initial state was already reached by the systolic peak (represented in Fig. 4.7 by the shock wave on the right), is compressed, while on the right of the initial discontinuity the aorta is 10 times stiffer than the part on the left. This idealized configuration leads to a partial reflection of the incoming wave, which can be noticed in Fig. 4.7 by the presence of the shock wave on the left. From the same Figure it is possible to observe that a good agreement between the exact solution and the numerical results is achieved for all the variables.

In RP3, the effects of an idealized Valsalva maneuver on a portion of the internal jugular vein are depicted. The Valsalva maneuver consists in the practice of exhaling while closing all the airways, producing a sharp increase of the central venous pressure of the

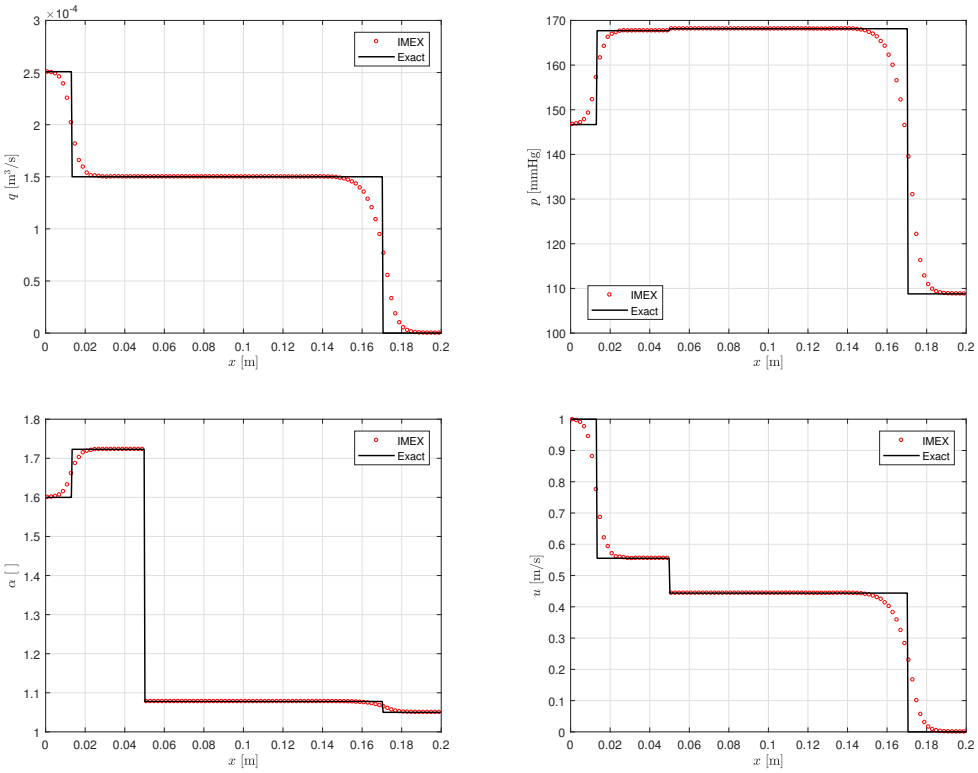

FIGURE 4.7: *Results obtained in test RP2, at time t_{end} = 0.007 s, solving the 1D a-FSI system with the IMEX Runge-Kutta scheme, in terms of flow rate q, pressure p, non-dimensional cross-sectional area α and velocity u, with respect to the exact solution.*

analyzed subject. Moreover, in this test it is considered that downstream, in the correspondence of the heart, there is an incompetent valve causing a venous reflux towards the head (represented in Fig. 4.8 by the elastic jump traveling to the left). Even in this very challenging test, in which there is also the presence of a rarefaction wave traveling to the right, numerical results agree very well with the exact solution.

RP4 and RP5, presented in Fig. 4.9 and 4.10, concern, again, a single 1D segment having geometrical and mechanical properties representative of the thoracic aorta and of the internal jugular vein, respectively. In these problems, a single initial jump in the cross-sectional area (and thereby in the pressure, being evaluated through the tube law) is considered, to assess the effects of a solely geometrical discontinuity. Even in these tests, numerical results correctly capture the exact solution, confirming once more the suitability of the model to solve also unsteady problems, both in arteries and veins. It is here underlined that, in RP5, the small undershoot/overshoot of the numerical solution of α and u in correspondence of the tail of the rarefaction wave (Fig. 4.10 bottom) depends on the chosen slope limiter. This irregularity, indeed, would not appear if using the superbee limiter instead of the minmod. Nevertheless, it was decided to present the results using a single slope limiter for all the simulations in a uniform manner, with the minmod being the most accurate among all the tests. Additionally, comparing the rarefaction wave in the pressure plot with the one in the adimensional area plot, it is possible to observe the typical neither concave nor convex behavior of veins (Spiller et al., 2017) given by the specific parameters adopted in the tube law, presented in Eq. (4.6).

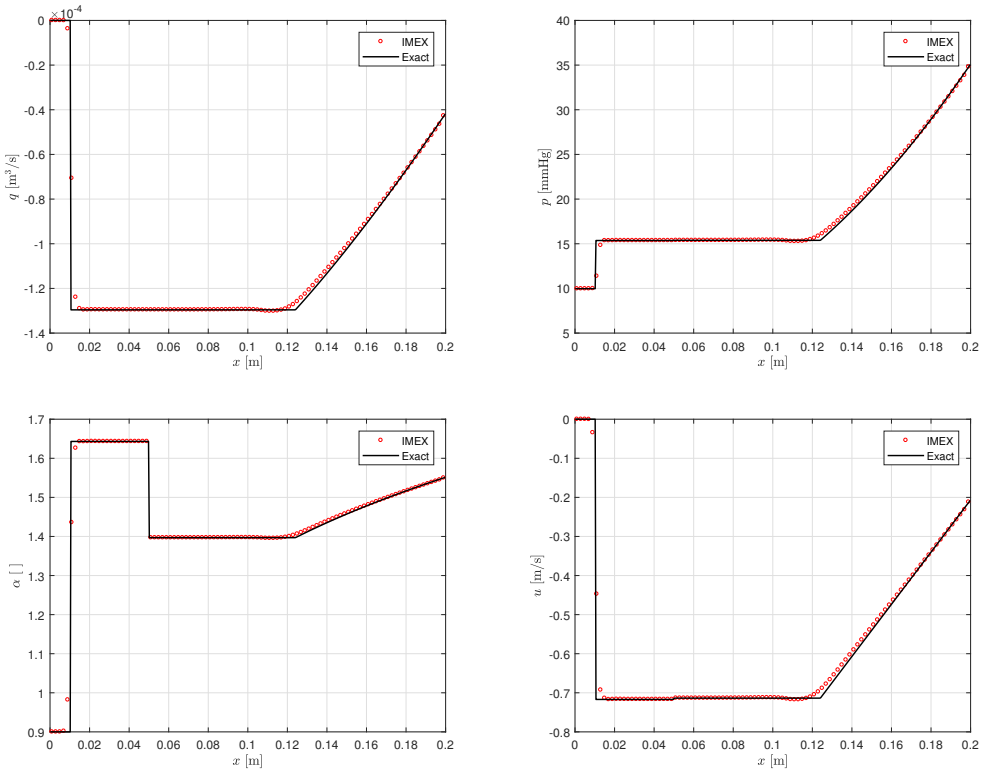

FIGURE 4.8: *Results obtained in test RP3, at time t_{end} = 0.025 s, solving the 1D a-FSI system with the IMEX Runge-Kutta scheme, in terms of flow rate q, pressure p, non-dimensional cross-sectional area α and velocity u, with respect to the exact solution.*

The complete set of initial data is listed, for each RP, in Tab. 4.1.

4.3.2 C-property problems

To test the C-property of the scheme even in the case in which smooth functions are defined on the left and on the right side of a central initial discontinuity (and not piecewise constant values), two additional problems have been designed. The first test (CP1) takes into account a portion of a generic artery, while the second one (CP2) a portion of a generic vein, in both the cases simply concerning an elastic behavior of the wall. Mechanical and geometrical reference data are given in Tab. 4.2, whereas initial conditions are specified in Tab. 4.3. The non-trivial initial conditions regard variables A_0, E_0 and p_{ext}, all influencing the initial condition of the area, evaluated involving the tube law. Results

Test	L [m]	s_0 [mm]	u_0 [m/s]	p_0 [mmHg]	a_0 [mm^2]	e_0 [MPa]	p_e [mmHg]
CP1	0.10	1.50	0.00	80.00	1.00	1.00	80.00
CP2	0.10	0.30	0.00	10.00	0.01	0.10	10.00

TABLE 4.2: *Parameters used for the C-property tests: domain length L, vessel wall thickness s_0, reference velocity u_0, reference pressure p_0, reference cross-sectional area a_0, reference instantaneous Young modulus e_0, reference external pressure p_e. In both the tests,* CFL *= 0.9 and N_x = 100.*

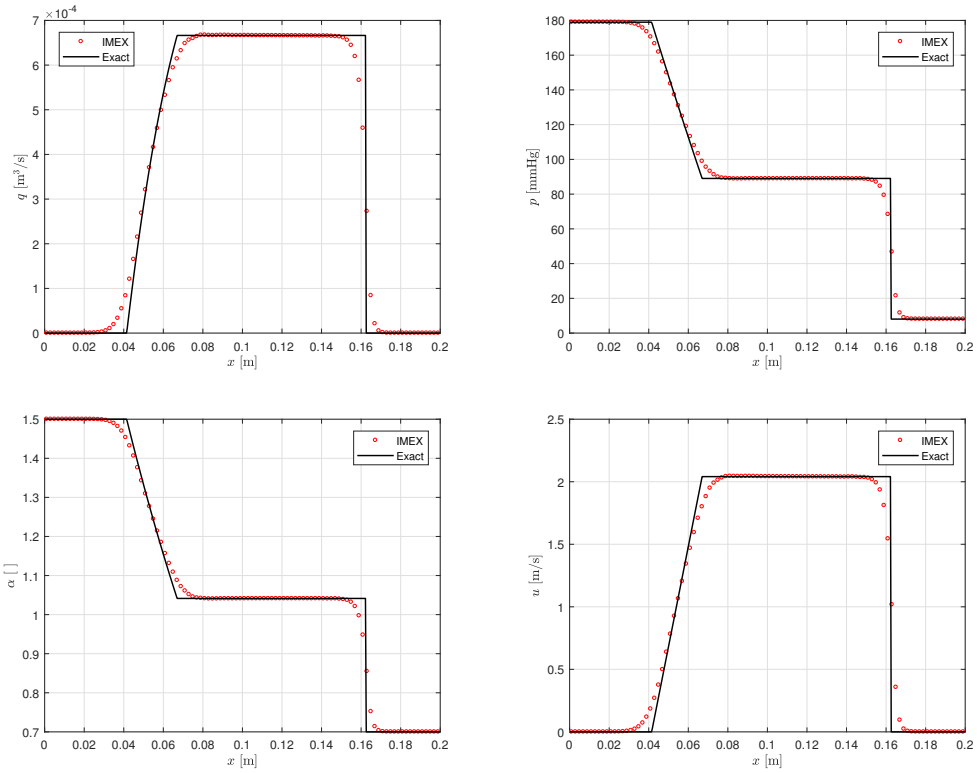

FIGURE 4.9: *Results obtained in test RP4, at time t_{end} = 0.01 s, solving the 1D a-FSI system with the IMEX Runge-Kutta scheme, in terms of flow rate q, pressure p, non-dimensional cross-sectional area α and velocity u, with respect to the exact solution.*

Variable	IC
u_L [m/s]	u_0
u_R [m/s]	u_0
p_L [mmHg]	p_0
p_R [mmHg]	p_0
$A_{0,L}$ [mm^2]	$a_0 + \frac{a_0}{2}\sin\left(\frac{8\pi x}{L}\right)$
$A_{0,R}$ [mm^2]	$2a_0 + \frac{a_0}{2}\sin\left(\frac{8\pi x}{L}\right)$
$E_{0,L}$ [MPa]	$e_0 + \frac{e_0}{2}\sin\left(\frac{8\pi x}{L}\right)$
$E_{0,R}$ [MPa]	$2e_0 + \frac{e_0}{2}\sin\left(\frac{8\pi x}{L}\right)$
$p_{ext,L}$ [mmHg]	$p_e + \frac{p_e}{2}\sin\left(\frac{8\pi x}{L}\right)$
$p_{ext,R}$ [mmHg]	$2p_e + \frac{p_e}{2}\sin\left(\frac{8\pi x}{L}\right)$
x_0 [m]	$0.5\,L$

TABLE 4.3: *Initial conditions for the C-property tests CP1 and CP2. Subscripts L and R stand for the smooth initial values respectively on the left and on the right of the initial discontinuity, located in x_0. The initial condition of the area A is evaluated solving the tube law presented in Eq. (4.4). For parameters u_0, p_0, a_0, e_0 and p_e refer to Tab. 4.2.*

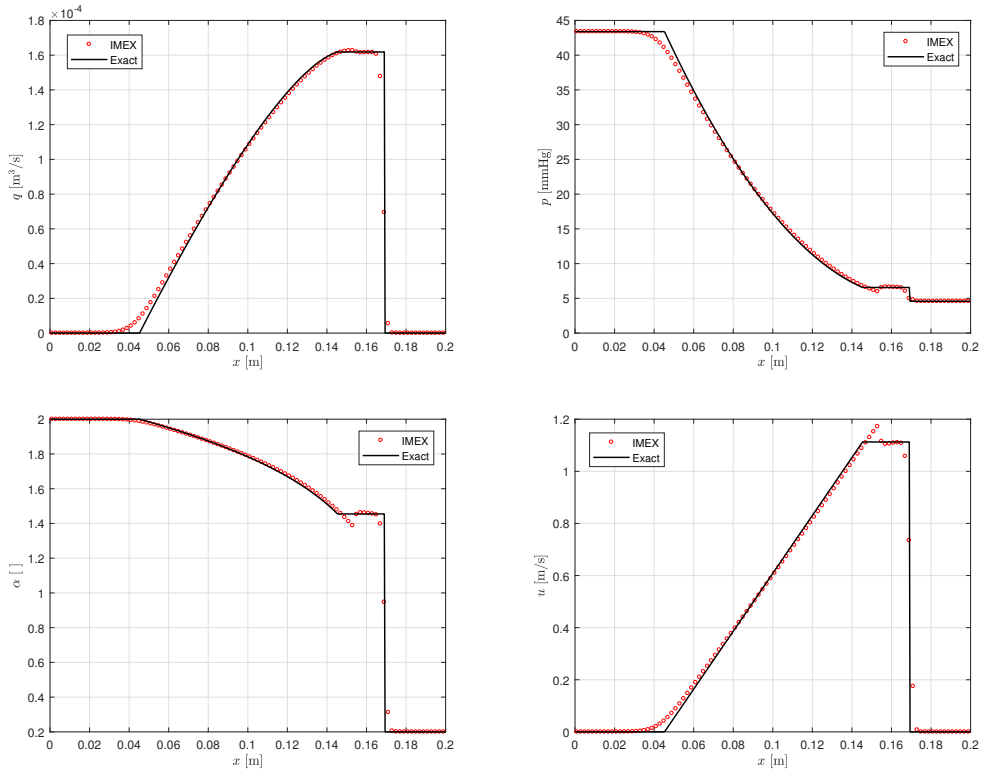

FIGURE 4.10: *Results obtained in test RP5, at time t_{end} = 0.015 s, solving the 1D a-FSI system with the IMEX Runge-Kutta scheme, in terms of flow rate q, pressure p, non-dimensional cross-sectional area α and velocity u, with respect to the exact solution.*

are graphically shown in Fig. 4.11 for CP1 and in Fig. 4.12 for CP2.
Furthermore, errors are evaluated in terms of L^2 norm at time $t_{end} = 0.25$ s for both the tests. It is here specified that, with the chosen t_{end}, the number of complete time iterations is 4208 in CP1 and 1896 in CP2, being in fact fairly large. The L^2 norm for the evolutive variables A, Au and p results, respectively: 1.18×10^{-20}, 0, 0 in CP1 and 1.34×10^{-22}, 0, 0 in CP2 (values in SI units). By consequence, the well-balancing proof presented in Section 4.2.2.2 is here confirmed even by numerical results.

Test	s_0 [mm]	$\tilde{A}_0$ [mm^2]	$\tilde{a}_0$ [mm^2]	$\tilde{P}$ [kPa]	$\tilde{p}$ [kPa]	$\tilde{E}_0$ [MPa]	$\tilde{e}_0$ [MPa]	E_∞ [MPa]	τ_r [ms]
VV1	1.50	4.00	0.40	10.00	2.00	2.00	0.20	1.60	0.36
VV2	0.30	0.40	0.04	1.50	0.30	1.75	0.10	1.50	0.06

TABLE 4.4: *Parameters used in the tests designed with the MMS to validate the viscoelastic term for a generic artery (VV1) and for a generic vein (VV2). Values chosen or calibrated in accordance with standard ranges found in the human body. In both the tests,* CFL *= 0.9 and N_x = 100.*

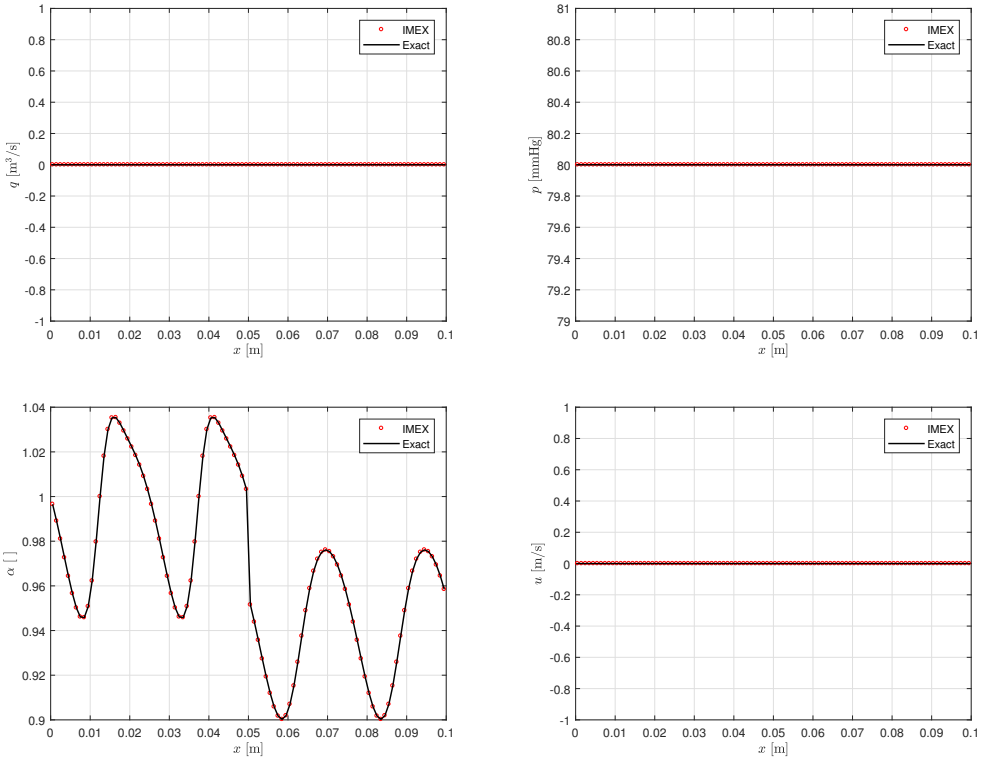

FIGURE 4.11: *Results obtained in the C-property problem CP1, at time t_{end} = 0.25 s, solving the 1D a-FSI system with the IMEX Runge-Kutta scheme for a generic artery, in terms of flow rate q, pressure p, non-dimensional cross-sectional area α and velocity u, with respect to the exact solution in the state of rest.*

4.3.3 Problems for the validation of the viscoelastic term

To validate also the additional contribution given by viscoelasticity in the proposed model, the Method of Manufactured Solutions (Roache, 2002) is used. Manufactured solutions are exact solutions to a set of governing equations that have been modified with forcing terms. Hence, starting from system (4.16), a smooth, exact solution of the perturbed system, which is a non-homogeneous non-linear system, is prescribed as follows:

$$\hat{\boldsymbol{Q}}(x,t) = \begin{pmatrix} \hat{A}(x,t) \\ \hat{A}u(x,t) \\ \hat{p}(x,t) \\ \hat{A}_0(x) \\ \hat{E}_0(x) \\ \hat{p}_{ext}(x) \end{pmatrix} = \begin{pmatrix} \tilde{A}_0 + \tilde{a}_0 \sin\left(\frac{2\pi}{L}x\right)\cos\left(\frac{2\pi}{T}t\right) \\ \tilde{A}_0 u - \tilde{a}_0 \frac{L}{T}\cos\left(\frac{2\pi}{L}x\right)\sin\left(\frac{2\pi}{T}t\right) \\ \tilde{P} + \tilde{p}\cos\left(\frac{2\pi}{L}x\right)\sin\left(\frac{2\pi}{T}t\right) \\ \tilde{A}_0 + \tilde{a}_0 \sin\left(\frac{2\pi}{L}x\right) \\ \tilde{E}_0 + \tilde{e}_0 \sin\left(\frac{2\pi}{L}x\right) \\ \tilde{P}_{ext} + \tilde{p}_{ext} \sin\left(\frac{2\pi}{L}x\right) \end{pmatrix}$$

with $L = 1.0$ m, $T = 1.0$ s, $\tilde{A}_0 u = 0.0$ m^3/s, $\tilde{P}_{ext} = 0.0$ Pa and $\tilde{p}_{ext} = 50.0$ Pa. The rest of the parameters, characterized for each of the two tests, are listed in Tab. 4.4. Introducing the prescribed solution in system (4.16), a non-homogeneous system with a residual source term $\boldsymbol{R}(x,t)$ (arising because $\hat{\boldsymbol{Q}}$ is not the exact solution) is obtained:

$$\partial_t \hat{\boldsymbol{Q}} + \boldsymbol{A}(\hat{\boldsymbol{Q}})\partial_x \hat{\boldsymbol{Q}} - \boldsymbol{S}(\hat{\boldsymbol{Q}}) = \boldsymbol{R}(x,t)\,. \tag{4.32}$$

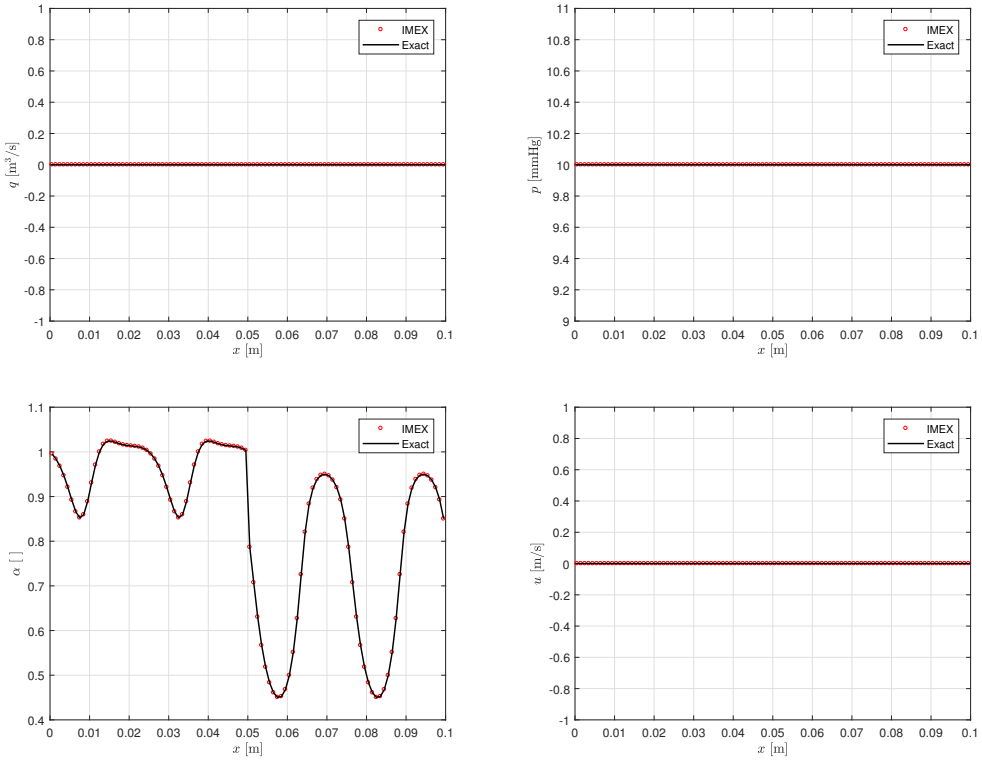

FIGURE 4.12: *Results obtained in the C-property problem CP2, at time t_{end} = 0.25 s, solving the 1D a-FSI system with the IMEX Runge-Kutta scheme for a generic artery, in terms of flow rate q, pressure p, non-dimensional cross-sectional area α and velocity u, with respect to the exact solution in the state of rest.*

Knowing $\boldsymbol{R}(x,t)$, which can be analytically obtained with algebraic manipulations, it is possible to solve the system enriched by the additional source term:

$$\partial_t \boldsymbol{Q} + \boldsymbol{A}(\boldsymbol{Q})\partial_x \boldsymbol{Q} = \boldsymbol{S}(\boldsymbol{Q}) + \boldsymbol{R}(x,t)\,. \tag{4.33}$$

The numerical scheme must therefore reproduce the prescribed $\hat{\boldsymbol{Q}}$ as unique solution. The initial condition is fixed as $\hat{\boldsymbol{Q}}(x,0)$. For this type of test, periodic boundary conditions are imposed, in accordance with the periodicity of the expected solution. Results are reported in Fig. 4.13 (test VV1, concerning an artery) and Fig. 4.14 (test VV2, concerning a vein) and confirm the validity of the model discussed in the present work also with respect to the proposed treatment of viscoelasticity in vessels.

4.3.4 Accuracy analysis

With the same test cases discussed in the previous section 4.3.3, for which the prescribed solution is intended as the exact one, it is also performed an accuracy analysis. It can be noticed, observing results reported in Tab. 4.5, that the expected second-order of accuracy is confirmed for all the evolutive variables. Given the set of parameters presented in Tab. 4.4 for each test case, following what stated in Eq. (4.20), it is worth to highlight that when considering a discretization with $\Delta x > 1.0 \times 10^{-4}$ m the two problems become stiff. Therefore, this analysis confirms the AP property of the chosen IMEX

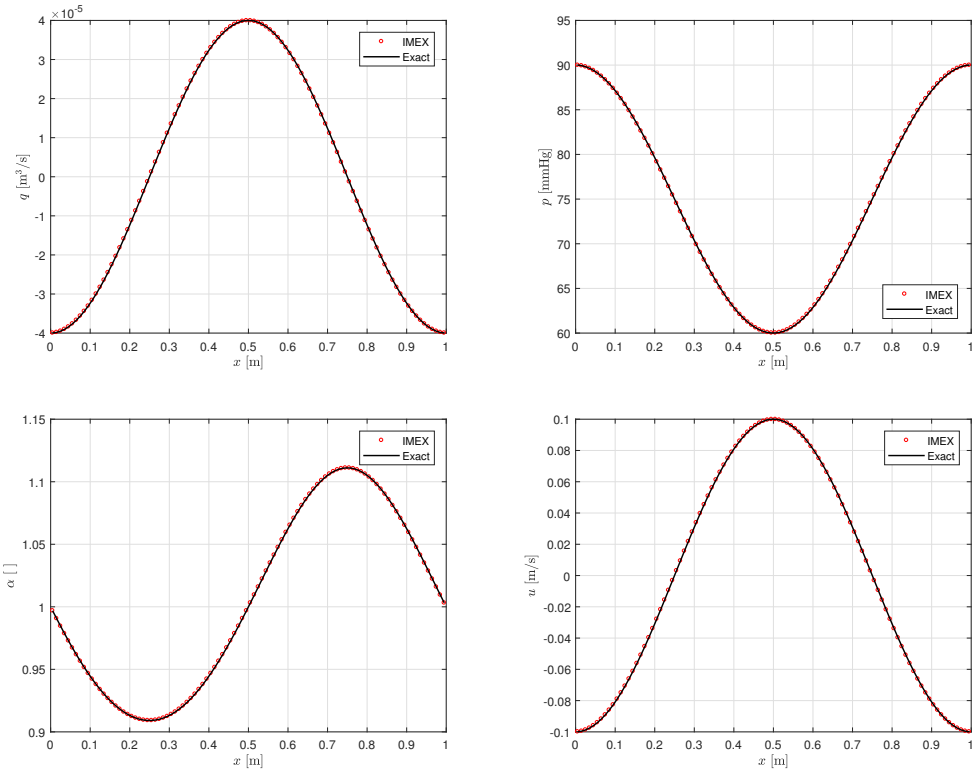

FIGURE 4.13: *Results obtained in test VV1, designed with the MMS to validate the viscoelastic term with configuration of a generic artery, at time t_{end} = 0.75 s, solving the 1D a-FSI system with the IMEX Runge-Kutta scheme, in terms of flow rate q, pressure p, non-dimensional cross-sectional area α and velocity u, with respect to the exact solution.*

RK scheme, which preserves the expected order of accuracy also in the zero relaxation limit.
On the other hand, it is verified that resolving the same problems with a simpler Strang splitting technique (Strang, 1968), which should provide second-order of accuracy if each step is at least second order accurate in space, leads to a reduction of the expected accuracy to first-order, as shown in Tab. 4.6 for test VV1. The non-asymptotic preserving behavior of this technique in the stiff limit was already discussed in literature for different contexts (LeVeque and Yee, 1990; Descombes and Massot, 2004; Pareschi and Russo, 2005; Duarte, Massot, and Descombes, 2011). In the present study, this aspect is confirmed even for the specific application of blood flow modeling. A qualitative comparison highlighting the difference between numerical results obtained with the selected IMEX RK and with the Strang splitting technique is also shown in Fig. 4.15.

4.3.5 Benchmark test cases

Parameters for the benchmark test cases, simulated referring to Boileau et al. (2015) and Xiao, Alastruey, and Figueroa (2014), concerning a constant-radius upper thoracic aorta (cTA), a tapered-radius upper thoracic aorta (tTA), a constant-radius common carotid artery (cCCA) and a tapered-radius common carotid artery (tCCA) are given in Tab. 4.7. In all the benchmark tests $\rho = 1060$ kg/m^3, $\mu = 0.004$ Pa s and CFL $= 0.9$.

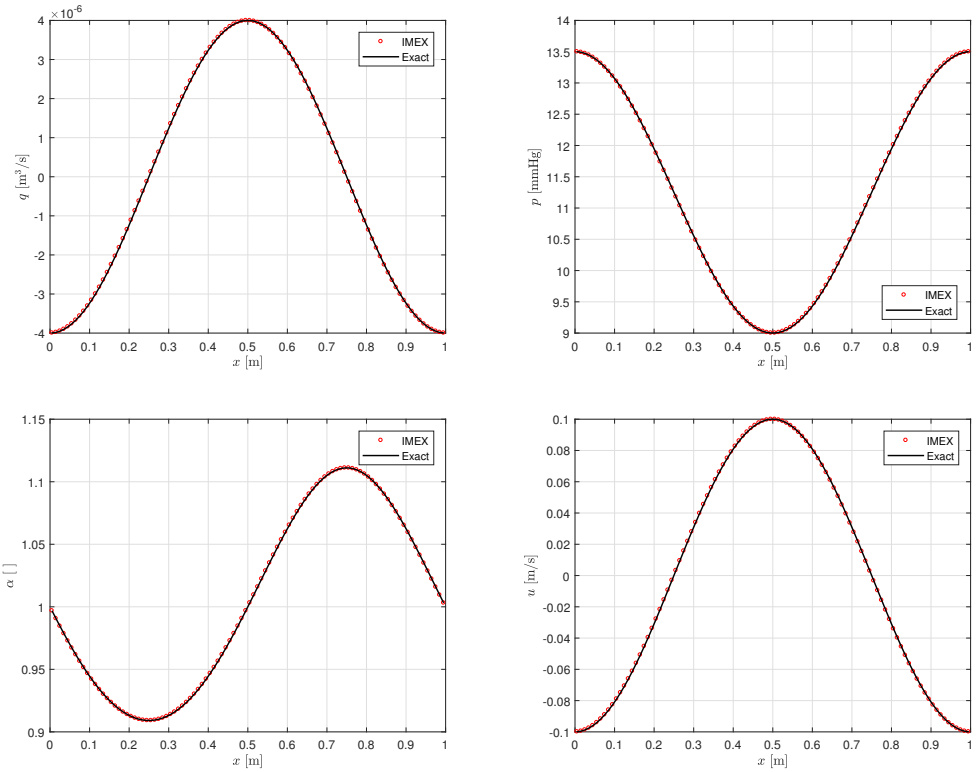

FIGURE 4.14: *Results obtained in test VV2, designed with the MMS to validate the viscoelastic term with configuration of a generic vein, at time t_{end} = 0.75 s, solving the 1D a-FSI system with the IMEX Runge-Kutta scheme, in terms of flow rate q, pressure p, non-dimensional cross-sectional area α and velocity u, with respect to the exact solution.*

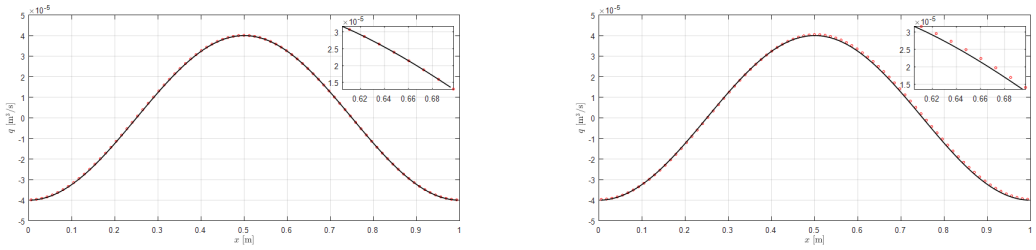

FIGURE 4.15: *Qualitative comparison of numerical results obtained with the selected IMEX RK (left) and with the Strang splitting technique (right) in test VV1, in terms of flow rate q.*

4.3.5.1 Thoracic aorta benchmark test cases

The constant radius upper thoracic aorta test case (cTA) is simulated using a purely elastic wall model to allow comparisons with solely elastic benchmark available data by Boileau et al. (2015), from which also the flow rate signal imposed at the inlet q_{in} is taken. Fig. 4.16 shows a comparison of the numerical results obtained solving the a-FSI system (4.12) with the IMEX RK scheme against benchmark data. Such data were obtained using a three-dimensional (3D) model and six different 1D numerical methods: discontinous Galerkin (Alastruey, Parker, and Sherwin, 2012), locally conservative Galerkin (Sherwin

et al., 2003), Galerkin least-squares finite elements (Watanabe, Blanco, and Feijóo, 2013), finite volumes (Müller and Toro, 2013), finite difference MacCormack (Leinan, 2012) and simplified trapezium rule method (Kroon et al., 2012). It can be observed that, for all the variables, IMEX results are in perfect agreement with 1D benchmark solutions. Larger but still acceptable differences are observed when compared to the 3D benchmark.

To account for spatial variations of the properties along the vessel length, the problem with a linearly tapered upper thoracic aorta (tTA) is simulated, following Xiao, Alastruey, and Figueroa (2014). All other geometrical and mechanical parameters are unaltered with respect to the baseline model, including inflow and outflow Windkessel total resistance, $R_T = R_1 + R_2$, and compliance. To evaluate the relevance, in terms of damping mechanism, of viscoelastic effects in a large central artery like the aorta, the tTA simulation is run also considering the viscoelastic SLS model. Results are presented in Fig. 4.17 for three different points in the domain (inlet, midpoint and outlet) and compared to the reference elastic solution. It can be noticed that IMEX elastic results totally agree with the

Test	Variable	N_x	L^1	$\mathcal{O}(L^1)$	L^2	$\mathcal{O}(L^2)$	L^∞	$\mathcal{O}(L^\infty)$	t_{CPU} [s]
VV1	A	9	4.70×10^{-07}	-	5.19×10^{-07}	-	7.52×10^{-07}	-	0.5
		27	6.25×10^{-08}	1.84	6.97×10^{-08}	1.83	1.02×10^{-07}	1.82	3.7
		81	7.27×10^{-09}	1.96	8.09×10^{-09}	1.96	1.18×10^{-08}	1.96	30.3
		243	8.20×10^{-10}	1.99	9.12×10^{-10}	1.99	1.33×10^{-9}	1.99	276.5
		729	9.15×10^{-11}	2.00	1.02×10^{-10}	2.00	1.49×10^{-10}	2.00	2478.7
	Au	9	2.08×10^{-06}	-	2.37×10^{-06}	-	3.66×10^{-06}	-	0.5
		27	1.71×10^{-07}	2.27	1.98×10^{-07}	2.26	3.34×10^{-07}	2.18	3.7
		81	1.91×10^{-08}	1.99	2.21×10^{-08}	1.99	3.74×10^{-08}	1.99	30.3
		243	2.16×10^{-09}	1.98	2.50×10^{-09}	1.98	4.23×10^{-09}	1.99	276.5
		729	2.36×10^{-10}	2.02	2.73×10^{-10}	2.02	4.62×10^{-10}	2.02	2478.7
	p	9	$6.89\times10^{+01}$	-	$7.67\times10^{+01}$	-	$1.23\times10^{+02}$	-	0.5
		27	$8.20\times10^{+00}$	1.94	$9.18\times10^{+00}$	1.93	$1.45\times10^{+01}$	1.94	3.7
		81	9.03×10^{-01}	2.01	$1.01\times10^{+00}$	2.01	$1.59\times10^{+00}$	2.01	30.3
		243	1.02×10^{-01}	1.99	1.14×10^{-01}	1.99	1.79×10^{-01}	1.99	276.5
		729	1.10×10^{-02}	2.02	1.23×10^{-02}	2.02	1.94×10^{-02}	2.02	2478.7
VV2	A	9	2.49×10^{-07}	-	2.83×10^{-07}	-	4.04×10^{-07}	-	0.1
		27	1.99×10^{-08}	2.30	2.27×10^{-08}	2.30	3.65×10^{-08}	2.19	0.5
		81	1.91×10^{-09}	2.14	2.22×10^{-09}	2.12	3.93×10^{-09}	2.03	3.4
		243	2.04×10^{-10}	2.03	2.38×10^{-10}	2.03	4.31×10^{-10}	2.01	29.2
		729	2.25×10^{-11}	2.01	2.62×10^{-11}	2.01	4.77×10^{-11}	2.00	257.5
	Au	9	2.47×10^{-07}	-	2.74×10^{-07}	-	4.36×10^{-07}	-	0.1
		27	4.23×10^{-08}	1.61	4.74×10^{-08}	1.60	8.17×10^{-08}	1.52	0.5
		81	5.11×10^{-09}	1.92	5.71×10^{-09}	1.92	9.59×10^{-09}	1.95	3.4
		243	5.82×10^{-10}	1.98	6.50×10^{-10}	1.98	1.09×10^{-09}	1.98	29.2
		729	6.52×10^{-11}	1.99	7.28×10^{-11}	1.99	1.21×10^{-10}	1.99	257.5
	p	9	$5.98\times10^{+00}$	-	$6.68\times10^{+00}$	-	$1.18\times10^{+01}$	-	0.1
		27	4.95×10^{-01}	2.27	5.97×10^{-01}	2.20	$1.30\times10^{+00}$	2.00	0.5
		81	5.20×10^{-02}	2.05	7.33×10^{-02}	1.91	1.76×10^{-01}	1.82	3.4
		243	5.54×10^{-03}	2.04	7.98×10^{-03}	2.02	1.95×10^{-02}	2.00	29.2
		729	6.15×10^{-04}	2.00	9.04×10^{-04}	1.98	2.21×10^{-03}	1.98	257.5

TABLE 4.5: *Results of the accuracy analysis for the tests designed with the MMS to validate the viscoelastic term solved with the IMEX-SSP2 scheme, with configuration of a generic artery (VV1) and of a generic vein (VV2). Errors computed for variables A, Au and p in terms of norms L^1, L^2 and L^∞, using the International System of Units. CPU times listed for each simulation.*

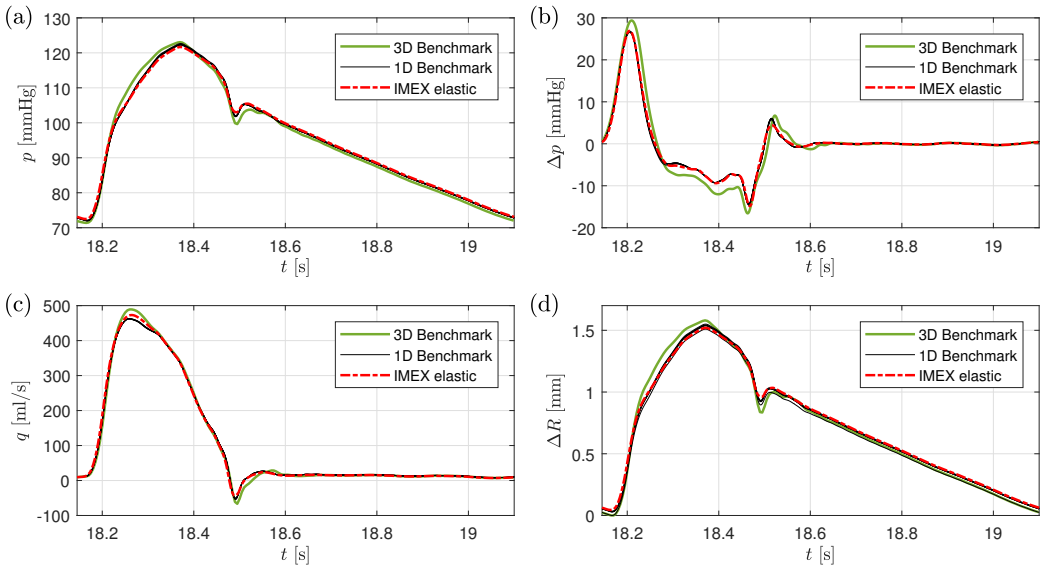

FIGURE 4.16: *Baseline thoracic aorta case (cTA). Solution of the 1D a-FSI system with the IMEX scheme with elastic tube law compared to six 1D and one 3D benchmark solutions, all taken from Boileau et al. (2015). Results presented in terms of pressure at the midpoint (a), inlet-outlet pressure difference (b), flow rate at the midpoint (c) and change in radius from diastole at the midpoint (d).*

1D elastic benchmark in all the locations. On the other hand, wall viscosity in IMEX viscoelastic results already plays an important role in the TA, being the viscoelastic behavior of vessels mainly attributed to smooth muscle cells (Gow and Taylor, 1968; Valdez-Jasso et al., 2009; Battista, 2015).

Test	Variable	N_x	L^1	$\mathcal{O}(L^1)$	L^2	$\mathcal{O}(L^2)$	L^∞	$\mathcal{O}(L^\infty)$
VV1	A	9	1.44×10^{-06}	-	1.61×10^{-06}	-	2.32×10^{-06}	-
		27	3.78×10^{-07}	1.22	4.20×10^{-07}	1.22	6.32×10^{-07}	1.18
		81	1.34×10^{-07}	0.94	1.49×10^{-07}	0.94	2.20×10^{-07}	0.96
		243	4.61×10^{-08}	0.97	5.12×10^{-08}	0.97	7.50×10^{-08}	0.98
		729	1.55×10^{-08}	0.99	1.72×10^{-08}	0.99	2.52×10^{-08}	0.99
	Au	9	4.98×10^{-06}	-	5.95×10^{-06}	-	1.00×10^{-05}	-
		27	1.79×10^{-06}	0.93	2.04×10^{-06}	0.98	3.31×10^{-06}	1.01
		81	5.91×10^{-07}	1.00	6.71×10^{-07}	1.01	1.09×10^{-06}	1.01
		243	1.96×10^{-07}	1.00	2.22×10^{-07}	1.00	3.60×10^{-07}	1.00
		729	6.53×10^{-08}	1.00	7.40×10^{-08}	1.00	1.20×10^{-07}	1.00
	p	9	$7.10\times10^{+01}$	-	$8.01\times10^{+01}$	-	$1.22\times10^{+02}$	-
		27	$1.24\times10^{+00}$	1.58	$1.38\times10^{+00}$	1.60	$2.05\times10^{+01}$	1.62
		81	$5.60\times10^{+00}$	0.73	$6.25\times10^{+00}$	0.72	$9.52\times10^{+00}$	0.70
		243	$1.24\times10^{+00}$	1.37	$1.39\times10^{+00}$	1.37	$2.19\times10^{+00}$	1.34
		729	2.18×10^{-01}	1.58	2.43×10^{-01}	1.59	3.66×10^{-01}	1.63

TABLE 4.6: *Results of the accuracy analysis for the test VV1 (configuration of a generic artery) solved with the Strang splitting technique. Errors computed for variables A, Au and p in terms of norms L^1, L^2 and L^∞, using the International System of Units.*

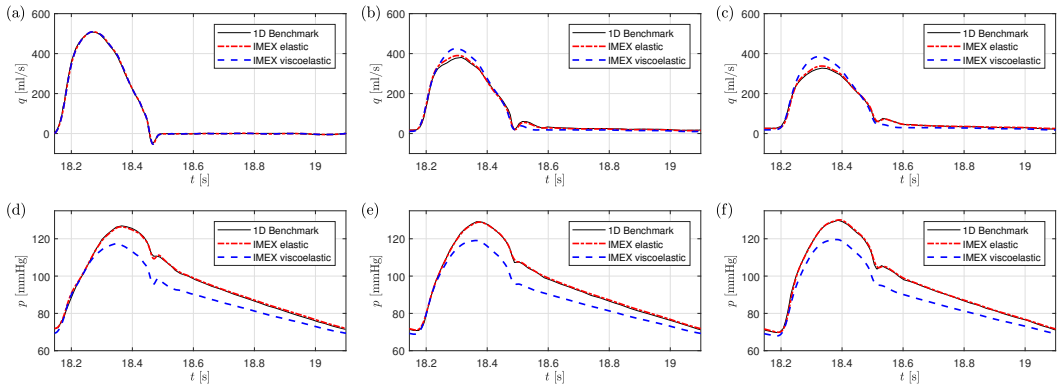

FIGURE 4.17: *Tapered thoracic aorta case (tTA). Results obtained solving the 1D a-FSI system with the IMEX scheme with elastic and viscoelastic tube law compared to 1D elastic benchmark, taken from Xiao, Alastruey, and Figueroa (2014), presented in terms of flow rate at the inlet (a), flow rate at the midpoint (b), flow rate at the outlet (c), pressure at the inlet (d), pressure at the midpoint (e), pressure at the outlet (f).*

Parameter	cTA	tTA	cCCA	tCCA
L [cm]	24.137	24.137	12.60	12.60
$R_{0,in}$ [mm]	12.0	15.0	3.0	4.0
$R_{0,out}$ [mm]	12.0	10.0	3.0	2.0
s_0 [mm]	1.2	1.2	0.3	0.3
$p(x,0)$ [kPa]	0	0	0	0
$u(x,0)$ [m/s]	0	0	0	0
α_c [-]	1.1	1.1	4/3	4/3
p_D [kPa]	9.467	9.467	10.933	10.933
p_{out} [kPa]	0	0	0	0
R_1 [MPa s m^{-3}]	11.752	18.503	248.75	685.48
R_2 [MPa s m^{-3}]	111.67	104.92	1869.7	1433.0
C [m^3 GPa^{-1}]	10.163	10.163	0.17529	0.17529
E_0 [MPa]	0.5333	0.7275	0.9333	1.7367
E_∞ [MPa]	-	0.5333	-	0.9333
η [kPa s]	-	23.884	-	47.768
τ_r [s]	-	0.009	-	0.013

TABLE 4.7: *Model parameters of the TA and the CCA, with constant or tapered radius, taken from Xiao, Alastruey, and Figueroa (2014) and Boileau et al. (2015): vessel length L, inlet equilibrium radius $R_{0,in}$, outlet equilibrium radius $R_{0,in}$, vessel wall thickness s_0, initial pressure $p(x,0)$, initial velocity $u(x,0)$, Coriolis coefficient α_c, diastolic pressure p_D (in this model coincident with the external pressure p_{ext} for the equilibrium), outflow pressure p_{out}, Windkessel resistance R_1, Windkessel resistance R_2, Windkessel compliance C, instantaneous Young modulus E_0, asymptotic Young modulus E_∞, viscosity coefficient η, relaxation time τ_r. The number of cells in the domain is $N_x = 12$ for tests in the TA and $N_x = 6$ for tests in the CCA; for the TA cases 20 cardiac cycles are simulated, corresponding to a final time $t_{end} = 19.10$ s, while for the CCA cases 9 cardiac cycles are simulated, corresponding to a final time $t_{end} = 9.90$ s.*

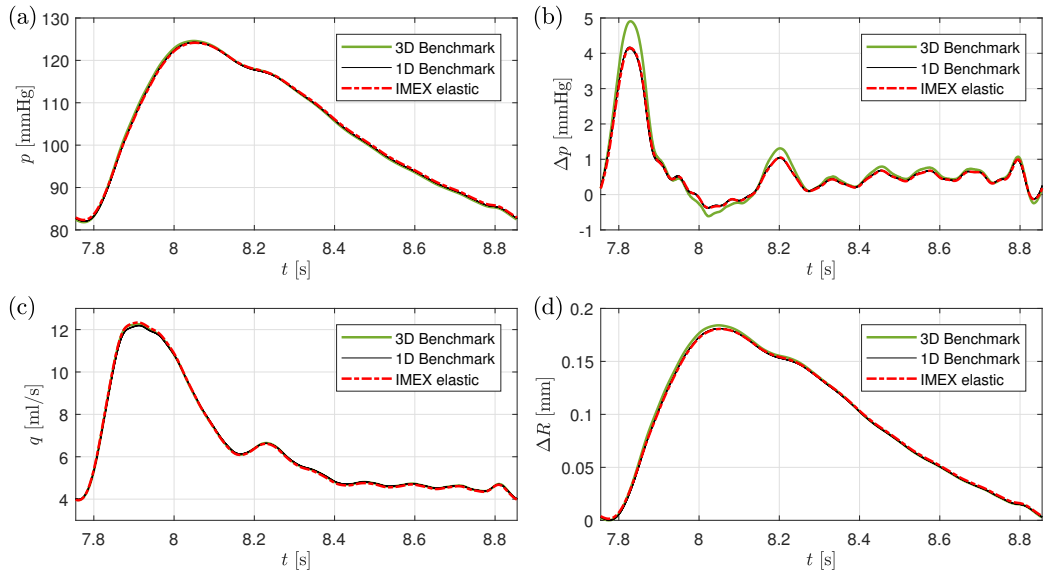

FIGURE 4.18: *Baseline common carotid artery case (cCCA). Solution of the 1D a-FSI system with the IMEX scheme with elastic tube law compared to six 1D and one 3D benchmark solutions, all taken from Boileau et al. (2015). Results presented in terms of pressure at the midpoint (a), inlet-outlet pressure difference (b), flow rate at the midpoint (c) and change in radius from diastole at the midpoint (d).*

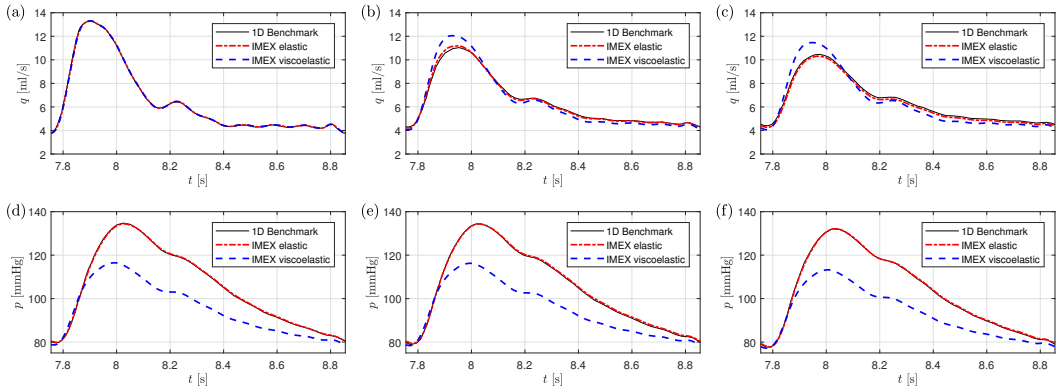

FIGURE 4.19: *Tapered common carotid artery case (tCCA). Results obtained solving the 1D a-FSI system with the IMEX scheme with elastic and viscoelastic tube law compared to 1D elastic benchmark, taken from Xiao, Alastruey, and Figueroa (2014), presented in terms of flow rate at the inlet (a), flow rate at the midpoint (b), flow rate at the outlet (c), pressure at the inlet (d), pressure at the midpoint (e), pressure at the outlet (f).*

4.3.5.2 Common carotid artery benchmark test cases

The constant radius common carotid artery test case (cCCA) is simulated using a purely elastic configuration of the wall mechanics to allow comparisons with solely elastic benchmark available data, from which also the inlet flow rate q_{in} is taken (Boileau et al., 2015). Figure 4.18 shows results obtained solving the a-FSI system (4.12) with the IMEX scheme against the benchmark solution. All the IMEX waveforms are almost indistinguishable from the reference ones, confirming the ability of the model to correctly

simulate pulse wave hemodynamics in single arterial segments.

Also for the CCA, the problem with a linearly tapered radius (tCCA) is performed as presented by Xiao, Alastruey, and Figueroa (2014). Designed in the same manner as for the TA, the simulation is executed initially considering a simple elastic behavior of the vessel wall and further taking into account viscoelasticity. In Fig. 4.19 it is possible to observe an excellent correspondence between IMEX elastic results and the 1D elastic benchmark along the whole length of the vessel. All other parameters being equal, the introduction of the viscoelastic model entails a significant damping effect of pressure waves, associated with a loss of energy of the system. Since the pulse wave is subject to a viscoelastic response along each arterial segment, the damping effect increases toward the periphery of the cardiovascular system: the frequency of the wave increases as the wall viscosity η, while the equilibrium radius R_0 decreases (Alastruey, Parker, and Sherwin, 2012; Alastruey et al., 2012; Mynard and Smolich, 2015; Valdez-Jasso et al., 2009), with a relaxation time of the wall that behaves almost like a biological constant (Ghigo et al., 2017). It can be verified that this concept is well reproduced by the proposed model when comparing damping effects in the TA (Fig. 4.17) to those in the CCA (Fig. 4.19).

Parameter	CCA-A	CCA-B	CCA-C	CCA-D	FA-E	FA-F
Age [years]	29	28	44	28	44	32
L [cm]	17.70	17.70	17.70	17.70	14.50	14.50
$R_{0,in}$ [mm]	4.0	4.0	4.0	4.0	3.7	3.7
$R_{0,out}$ [mm]	3.7	3.7	3.7	3.7	3.14	3.14
s_0 [mm]	0.3	0.3	0.3	0.3	0.3	0.3
$p(x,0)$ [mmHg]	0	0	0	0	0	0
$u(x,0)$ [m/s]	0	0	0	0	0	0
α_c [-]	4/3	4/3	4/3	4/3	4/3	4/3
p_D [mmHg]	90.0	70.0	80.0	75.0	90.0	90.0
p_{out} [mmHg]	0	0	0	0	0	0
R_1 [MPa s m^{-3}]	145.91	145.91	145.91	145.91	241.26	241.26
R_2 [MPa s m^{-3}]	768.17	588.83	702.28	756.13	4140.0	2352.1
C [m^3 GPa^{-1}]	0.29178	0.24997	0.49551	0.11168	0.11155	0.13208
E_0 [MPa]	1.7742	1.7742	1.7742	1.7742	2.2352	2.2352
E_∞ [MPa]	0.9535	0.9535	0.9535	0.9535	1.2012	1.2012
η [kPa s]	47.768	47.768	47.768	47.768	47.768	47.768
τ_r [s]	0.0125	0.0125	0.0125	0.0125	0.010	0.010

TABLE 4.8: *Model parameters of the CCA and CFA test cases for the 6 different subjects (A-F) from whom in-vivo velocity and pressure data were measured: subject age, vessel length L, inlet equilibrium radius $R_{0,in}$, outlet equilibrium radius $R_{0,in}$, vessel wall thickness s_0, initial pressure $p(x,0)$, initial velocity $u(x,0)$, Coriolis coefficient α_c, diastolic pressure p_D (in this model coincident with the external pressure p_{ext} for the equilibrium), outflow pressure p_{out}, Windkessel resistance R_1, Windkessel resistance R_2, Windkessel compliance C, instantaneous Young modulus E_0, asymptotic Young modulus E_∞, viscosity coefficient η, relaxation time τ_r. The number of cells in the domain is $N_x = 7$ and 10 cardiac cycles are simulated, corresponding to a final time $t_{end} = 10.00$ s.*

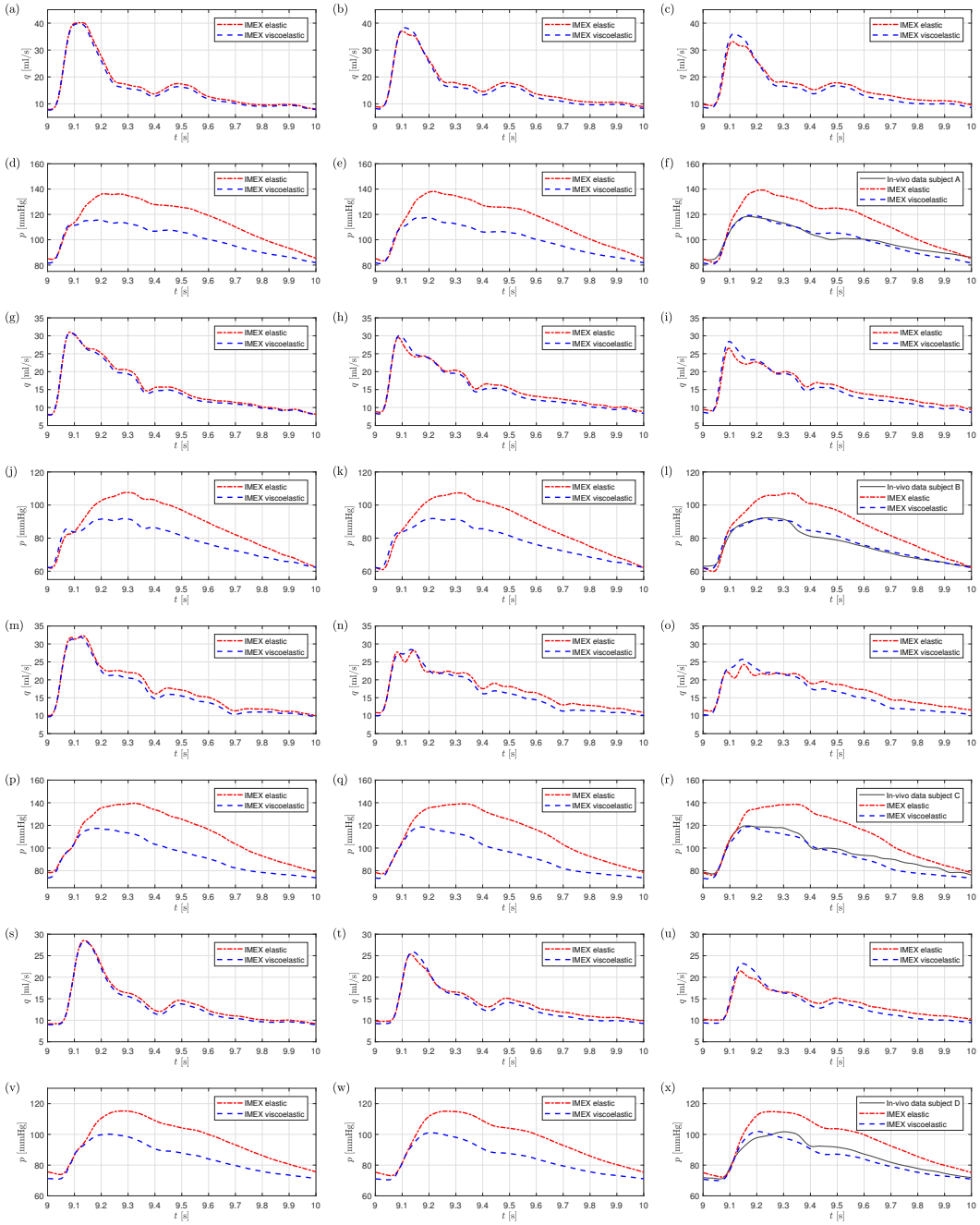

FIGURE 4.20: *Common carotid artery (CCA) cases with in-vivo data. Results obtained solving the 1D a-FSI system with the IMEX RK scheme, with elastic and viscoelastic tube law, for four different subjects. First (flow rate) and second (pressure) rows related to subject A; third (flow rate) and forth (pressure) rows related to subject B; fifth (flow rate) and sixth (pressure) rows related to subject C; seventh (flow rate) and eight (pressure) rows related to subject D. First column shows results in the first cell of the domain, second column shows results in the central cell of the domain, third column shows results in the last cell of the domain. Inlet velocity waveform obtained for each subject from Doppler measurements. Computed pressure obtained in the last cell of the domain compared to pressure waveforms measured for each subject with the PulsePen tonometer.*

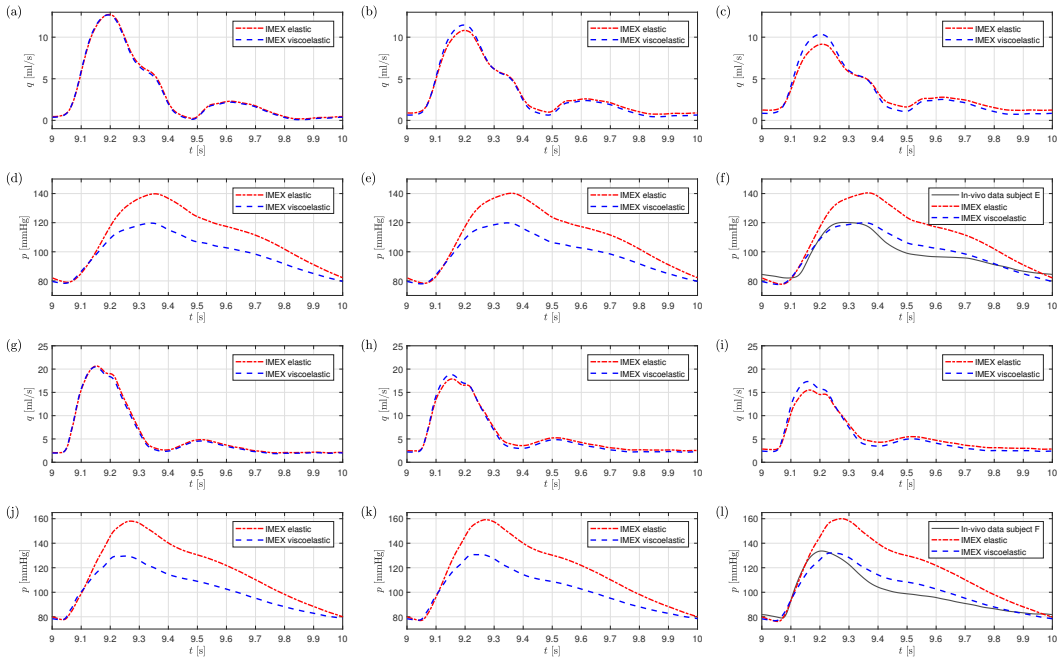

FIGURE 4.21: *Common femoral artery (CFA) cases with in-vivo data. Results obtained solving the 1D a-FSI system with the IMEX RK scheme, with elastic and viscoelastic tube law, for two different subjects. First (flow rate) and second (pressure) rows related to subject E; third (flow rate) and forth (pressure) rows related to subject F. First column shows results in the first cell of the domain, second column shows results in the central cell of the domain, third column shows results in the last cell of the domain. Inlet velocity waveform obtained for each subject from Doppler measurements. Computed pressure obtained in the last cell of the domain compared to pressure waveforms measured for each subject with the PulsePen tonometer.*

4.3.6 In-vivo data test cases

Not having found benchmark test cases of blood flow in single viscoelastic vessels in literature, data measured in-vivo in human CCAs and CFAs (see Section 4.2.3) are used as reference for the validation of the proposed model in its viscoelastic form. The velocity waveform extrapolated from each Doppler measurements (for four subjects in the CCA and for two subjects in the CFA) is imposed at the inlet boundary as described in Section 4.2.2.4. The pressure waveform measured with the PulsePen tonometer is compared to the computed pressure obtained in the last cell of the domain, this being, for both type of vessels, the position that is considered closest to the data measurement position. Model parameters for each in-vivo data test case are listed in Tab. 4.8. Physiological data for arteries are chosen referring to Müller and Toro (2014a), while the diastolic pressure is fixed based on values measured in the brachial artery for each patient. Outflow parameters are calibrated following the procedure proposed by Alastruey et al. (2012) and Xiao, Alastruey, and Figueroa (2014) and viscoelastic parameters are estimated as presented in Section 4.2.4. In all the cases, $\rho = 1060$ kg/m^3, $\mu = 0.004$ Pa s and CFL $= 0.9$.

Figures 4.20 and 4.21 show flow rate and pressure results, obtained solving the a-FSI system, considering the simple elastic and the SLS viscoelastic model, with the chosen IMEX RK scheme, in three different positions along the domain of each CCA and CFA, respectively. It can be noticed that IMEX viscoelastic results correctly capture the shape

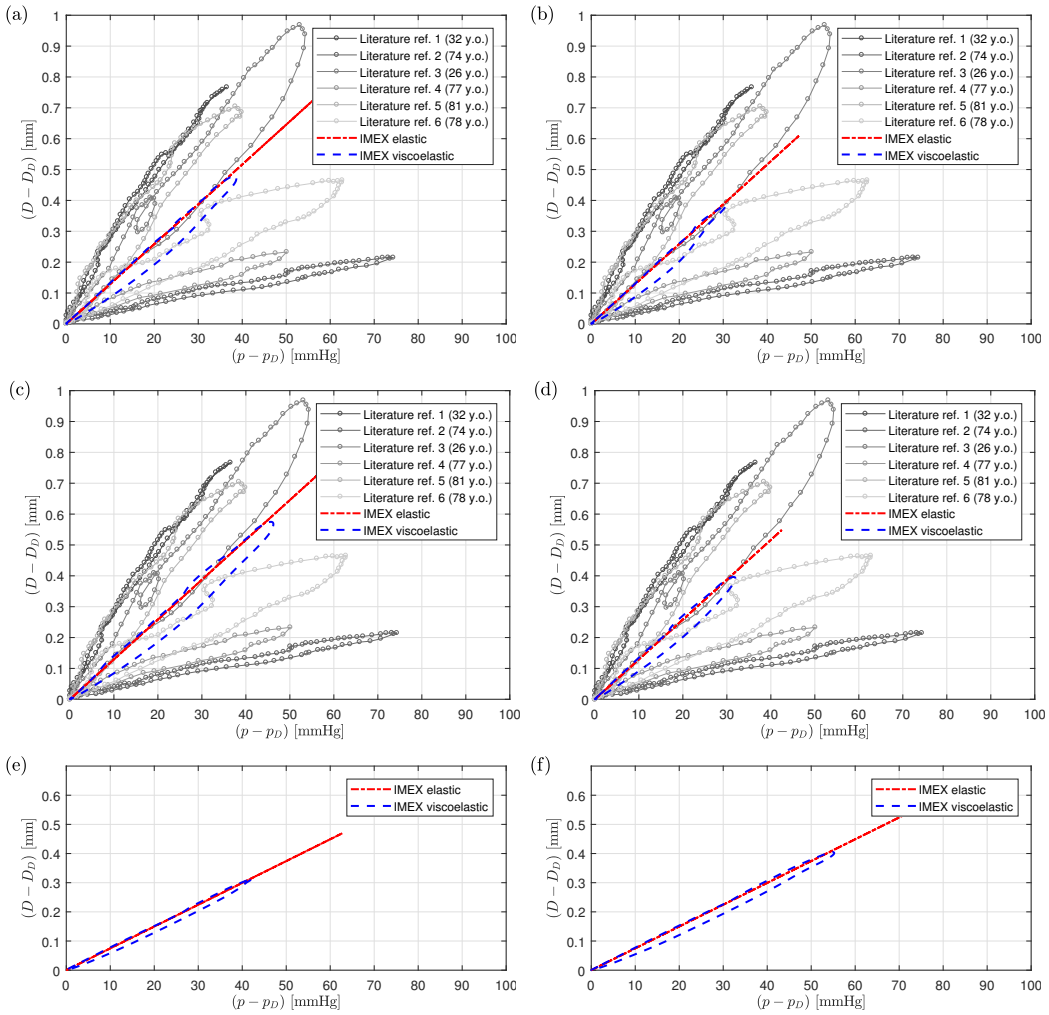

FIGURE 4.22: *Hysteresis curves representative of one cardiac cycle presented in terms of relative pressure and relative diameter, with respect to diastolic values, p_D and D_D respectively. Results obtained solving the 1D a-FSI system with the IMEX RK scheme, with elastic and viscoelastic tube law, for each subject of the study. Curves for the CCA of subjects A (a), B (b), C (c), D (d) and for the CFA of subjects E (e), F (f). Numerical results obtained for each CCA are compared to hysteresis curves available in literature, produced correlating in-vivo diameter and pressure simultaneous records made in volunteers of different ages (Giannattasio et al., 2008; Salvi, 2012). Curves develop in time counter-clockwise.*

and magnitude of the pressure waveforms of all the volunteers, concerning both the types of arteries. These results confirm the capability of the proposed model to reproduce realistic pressure signals and the importance of taking into account the viscosity of the vessel wall in order not to overestimate systolic pressure values (Alastruey et al., 2011; Battista, 2015; Westerhof and Noordergraaf, 1970).

In Fig. 4.22, computed *p-D* hysteresis loops are presented, comparing those related to CCAs with reference literature hysteresis (Giannattasio et al., 2008; Salvi, 2012). It was not possible to do the same for CFA results, due to lack of sufficient reference data available in literature. Comparisons of the dissipated energy fractions, carried out for each subject from literature loops and computed hysteresis curves (as described in Section

4.2.4), confirm the correct reproduction of energy losses. Numerical dissipation percentage in CCA tests results 21.5%, 20.0%, 22.5% and 23.1%, respectively for subjects from A to D, while the average over age of the corresponding literature curves results 19.2%, 23.7%, 22.0% and 23.7%. Numerical results in CFA tests reproduce a dissipation percentage of 12.6% and 13.7%, respectively for subject E and F, asserting the presence of smaller areas of hysteresis in more peripheral vessels (Alastruey et al., 2012).

4.4 Concluding remarks

In the present study, an innovative augmented fluid-structure interaction system is proposed for the blood flow modeling with regards to the viscoelastic effects of arterial and venous walls. The model has been validated through idealized time-dependent tests for situations close to reality, considered as a tool for checking the accuracy and the robustness of hemodynamics models. It has been demonstrated that the selected IMEX Runge-Kutta scheme preserves the expected in order of accuracy also when dealing with stiff source terms, confirming the AP property also in the blood flow context here discussed. Furthermore, results obtained considering a simple elastic behavior of single arteries arise in perfect agreement with 1D and 3D benchmark data available in literature. Comparisons with in-vivo data, collected from different human healthy volunteers in CCAs and CFAs, demonstrate that the proposed model is able to correctly simulate pressure trends in different subjects, serving as a valuable tool to improve cardiovascular diagnostics and the treatment of diseases.

An effective procedure to estimate viscoelastic parameters of the SLS model is proposed, which returns CCA hysteresis curves dissipating energy fractions in line with values calculated from literature hysteresis loops in the same vessel. Considering literature physiological data (for R_0, s_0, L and c_0 in vessels), the procedure presented in Section 4.2.4 permits to obtain all the necessary elastic and viscoelastic parameters. Only brachial systolic and diastolic pressure values (which can easily be recorded) are needed to correctly impose reference pressure values and define outlet lumped parameters (Alastruey et al., 2012; Xiao, Alastruey, and Figueroa, 2014), without the need of specific parameter adjustments. Given the satisfactory results obtained in all the test cases, it is believed that the proposed 1D a-FSI system of blood flow equations can be a valid tool for modeling the human circulation, both in arteries and veins, representing a valuable resource for different real medical applications. The chosen asymptotic-preserving IMEX-SSP2 RK scheme ensures at the same time robustness (given by the usage of an implicit discretization of the stiff terms) and efficiency (being possible to obtain a totally explicit algorithm for the specific resolution, as discussed in Appendix A). A simple shift from elastic to viscoelastic characterization of the vessel wall is ensured by the straightforward addition of a source term. Recurring to the a-FSI system, in fact, would be mostly advantageous when taking into account the viscoelastic wall behavior of vessels: all the viscosity information would be enclosed within a source term, avoiding the presence of second order derivatives in the system. Moreover, in this manner the governing system of equations remains natively hyperbolic.

Finally, the impact of characterizing the mechanics of the vessel wall concerning viscoelastic effects and not solely the elastic ones has been pointed out, especially comparing computed pressure waveforms with experimental measurements. In this context, the viscoelastic SLS model better describes the complex behavior of a viscoelastic material if compared with the KV model, frequently adopted in the biofluid dynamics literature

(Alastruey et al., 2011; Montecinos, Müller, and Toro, 2014; Wang, Fullana, and Lagrée, 2014; Mynard and Smolich, 2015), still maintaining ease of implementation and usage.

Chapter 5

Application study on arterial hypertension

5.1 Introduction

The viscoelastic behaviour of arterial and venous walls plays a determinant role in setting the functional level of the cardiovascular system under physiological and, especially, under pathological conditions such hypertension (Bia et al., 2003).
Arterial hypertension, or persistent high blood pressure, is a well-known pathology, affecting around 30% of the population, with a steep increase with aging. It is the most common disorder affecting the heart and blood vessels and represents the leading global risk factor for cardiovascular diseases, chronic kidney diseases, strokes and mortality (Williams et al., 2018; Hart, 2016; Tortora and Derrickson, 2013). The pathology is also known as the "silent killer" because it can cause considerable damage to blood vessels, heart, brain and kidneys before it causes pain or other noticeable symptoms. In blood vessels, hypertension causes thickening of the tunica media, accelerates development of atherosclerosis and coronary artery disease and increases systemic vascular resistance. In the heart, hypertension increases the afterload, which forces the ventricles to work harder to eject blood (Tortora and Derrickson, 2013).

The latest guidelines for hypertension, published in 2013 by the Task Force for the management of arterial hypertension of the European Society of Hypertension (ESH) and of the European Society of Cardiology (ESC), define and classify the following blood pressure levels, in terms of diastolic pressure (p_D) and systolic pressure (p_S) expressed in mmHg (Williams et al., 2018):

- Optimal: $p_D < 80$ and $p_S < 120$;
- Normal: $80 < p_D < 84$ and/or $120 < p_S < 129$;
- High normal: $85 < p_D < 89$ and/or $130 < p_S < 139$;
- Grade 1 of hypertension: $90 < p_D < 99$ and/or $140 < p_S < 159$;
- Grade 2 of hypertension: $100 < p_D < 109$ and/or $160 < p_S < 179$;
- Grade 3 of hypertension: $p_D \geq 110$ and/or $p_S \geq 180$;
- Isolated systolic hypertension: $p_D < 90$ and $p_S \geq 140$;

The recommended classification is unchanged from the 2003, 2007 and 2013 ESH/ESC guidelines, being hypertension still defined as office systolic pressure values at least 140 mmHg and/or diastolic values at least 90 mmHg.

The number of people with raised blood pressure in the world is increased by 90% during the four decades between 1975 and 2015, with the majority of the increase occurring in low-income and middle-income countries, largely driven by the growth and aging of the population (NCD Risk Factor Collaboration (NCD-RisC), 2017). Between 90 and 95% of the hypertensive patients are affected by essential/primary hypertension, a persistent elevated blood pressure state that cannot be attributed to any identifiable cause. The remaining 5-10% of cases are secondary hypertension, which has an identifiable underlying cause, like obstruction of renal blood flow, hypersecretion of aldosterone and hypersecretion of epinephrine and norepinephrine (Tortora and Derrickson, 2013).

Many people are successfully treated with diuretics, agents that decrease blood pressure by decreasing blood volume because they increase the elimination of water and salt in the urine. Angiotensin converting enzyme inhibitors block the formation of angiotensin II and thereby promote vasodilation and decrease the secretion of aldosterone. Beta blockers reduce blood pressure by inhibiting the secretion of renin and by decreasing heart rate (HR) and contractility. Vasodilators relax the smooth muscle in arterial walls, causing vasodilation and lowering blood pressure by lowering systemic vascular resistance (Tortora and Derrickson, 2013). The alarming aspect, however, is that approximately one-third of people receiving anti-hypertensive medication still have uncontrolled high blood pressure, which reflects the limited understanding of the pathophysiology underlying the onset of elevated blood pressure and how this could represent a significant economic problem for public health-care (Hart, 2016).

For a concrete step forward on hypertension studies as well as other medical researches, quantitative data and non-invasive measurements are increasingly required. In this context, the available mathematical instruments, together with the engineering know-how in the field of fluid mechanics, represent a valuable tool for a faster progress in the knowledge of human hemodynamics. Having this perspective in mind, the aim of the following study is to model a hypertensive patient with one of the few global multiscale closed-loop blood flow models available in literature, the Müller-Toro model (Müller and Toro, 2014a; Müller and Toro, 2014b), examining results obtained with a sensitivity analysis to investigate correlations between hemodynamics variations and the development of arterial hypertension. Furthermore, since recent findings highlight that congenital cerebrovascular abnormalities, i.e. vertebral artery hypoplasia (VAH) and incomplete posterior Circle of Willis (CoW), may play a fundamental role in triggering high blood pressure (Warnert et al., 2016), some studies are conducted, concerning both normotensive and hypertensive subjects, to assess the effects of the suspected anatomical variations.

5.1.1 The Selfish Brain Hypothesis of essential hypertension

One of the historical theories which tries to give an explanation to the development of essential hypertension is termed "the Cushing's mechanism" (Paton, Dickinson, and Mitchell, 2009), recently re-proposed under the appellation of "the Selfish Brain Hypothesis" of hypertension by Paton and Hart and their collaborators from the University of Bristol (Cates et al., 2012). This theory considers it possible that an increase in cerebrovascular resistances (CVR), leading to cerebral hypoperfusion (a reduction of normal cerebral perfusion pressure levels, associated with a reduction of cerebral blood flow), may cause the onset of high sympathetic nerve activity and the consequent rise of blood pressure, inverting in this way the undisputed cause-effect relationship between hypertension and high cerebrovascular resistance (Hart, 2016). The increment of CVR could be

due to inflammations, oxidative stresses, changes in collagen and/or elastin content in the arterial walls or even congenital cerebrovascular abnormalities, i.e. VAH and incomplete CoW.

The first researcher starting to speculate about this novel explanation to the rise of blood pressure is Harvey Cushing, from whom, indeed, the theory takes the name. At the beginning of the twentieth century, Cushing, conducting experimental analysis in dogs, verified the presence of a regulatory mechanism of the vasomotor center (located in the brainstem) which controls blood pressure levels during cerebral compression (Cushing, 1901). First measurements of cerebral blood flow (CBF) and cerebral vascular resistance in humans concerning what is termed "the Cushing's response" were presented only almost 50 years later by Kety and Schmidt (1948). Thereafter, Dickinson and Thomson, with ante-mortem and post-mortem studies in hypertensive patients, hypothesized a connection between the narrowing of vertebral arteries, the brainstem hypoperfusion and the development of essential hypertension (Dickinson and Thomson, 1959; Dickinson and Thomson, 1960).

For the introduction of the term "Cushing's mechanism" (which has a different meaning than the "Cushing's response", since the latter is intended as a 'last ditch' self-protection for a critically ischemic brain, while the former is seen as a physiological mechanism for long-term control of mean arterial pressure levels) we have to wait until the beginning of the current century. Paton, Dickinson, and Mitchell (2009), in fact, revisited the Dickinson hypothesis, focusing on the aspect that brainstem hypoperfusion could cause the onset of sympathetic hyperactivity and consequent hypertension, by taking a firm stand on the side of an inverse cause-effect relationship between increased CVR (always accepted as a consequence of hypertension) and high blood pressure. Two years later, experimental studies in pre-hypertensive spontaneously hypertensive rats conducted by Cates et al. (2011) demonstrated the presence of VAH before the onset of hypertension. This gave a concrete support to the hypothesis that "the Cushing's mechanism" could effectively be activated by narrowing of the arteries supplying the brainstem, with a consequent rise in cerebrovascular resistance. In particular, the authors hypothesized that the narrowing of these cerebral arteries might be a consequence of inflammation-mediated alterations in the connective tissue types and elastin.
Recently, thorough reviews of the theory have been presented by Cates et al. (2012) and Hart (2016), with the introduction of the name "the Selfish Brain Hypothesis", being this process seen as a fundamental self-protective mechanism of the brain to maintain adequate levels of cerebral blood flow.
Finally, in recent studies performed by Warnert et al. (2016), first findings concerning normotensive, pre-hypertensive and hypertensive humans demonstrate that congenital posterior cerebrovascular variants, here specifically intended as VAH and incomplete posterior CoW, and the associated cerebral hypoperfusion may be a factor in triggering high blood pressure, highlighting that lowering blood pressure with specific antihypertensive drugs may therefore worsen cerebral perfusion in susceptible individuals, putting patients at risk of developing cognitive impairment and vascular dementia.

5.1.2 Anatomy of the Circle of Willis and Vertebral Artery Hypoplasia

Referring to Fig. 5.1, the CBF is governed by four inlet vessels: two anterior internal carotid arteries and two posterior vertebral arteries (VA) which unite into the basilar artery (BA). These vessels feed a circle of communicating arteries known as circle of Willis, which represents the major source of blood supply of the human brain. From

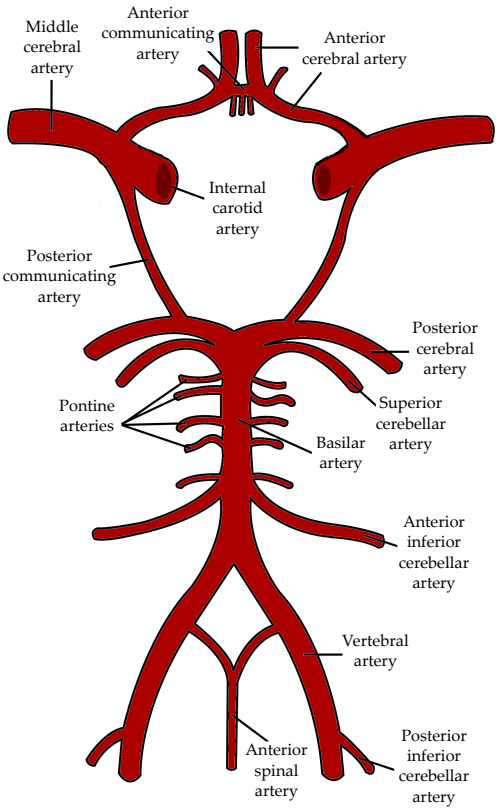

FIGURE 5.1: *Anatomy of the Circle of Willis, circulatory anastomosis that supplies blood to the brain and surrounding structures.*

the CoW, other arteries, namely anterior cerebral arteries, middle cerebral arteries and posterior cerebral arteries, arise and travel to all the parts of the brain. Posteriorly, the basilar artery divides into left and right posterior cerebral artery and each one communicates with the ipsilateral internal carotid artery by the respective posterior communicating artery (PcoA). In the anterior part of the brain, internal carotid arteries divide into the anterior and middle cerebral arteries. Left and right anterior cerebral arteries are connected by the anterior communicating artery (Cipolla, 2010). In the posterior region, the brainstem is supplied by superior cerebellar arteries and anterior inferior cerebellar arteries, which originate from the BA, and the posterior inferior cerebellar arteries, which originate directly from each vertebral artery.
The brainstem is composed by thalamus, midbrain, pons and medulla (medulla oblongata). The vasomotor center (VMC) is a portion of the medulla oblongata that, together with cardiovascular center and respiratory center, regulates blood pressure and other homeostatic processes. Embedded in the medulla, in fact, there is a series of purely sensory nuclei (clusters of nerve cell bodies) forming a vertical column of gray matter: the nucleus of the solitary tract (nucleus tractus solitarii, NTS), which is one of the most effective central sites for modulating the baroreceptor reflex function, a process that is critically important for blood pressure homeostasis. This tract is known to be heavily vascularized compared to the other compartments of the brainstem, suggesting that it exhibits a high level of oxygen demand (Waki et al., 2011), being really sensitive to an eventual hypoperfusion. A complete CoW exists only in almost 50% of the population, with different incomplete CoW configurations existing in the rest of the population. An

incomplete CoW, due to the absence of one or other posterior arteries, might be linked to cerebrovascular disorders, such as aneurysms, infarctions and other vascular anomalies, especially if associated to inferior cerebral arteries stenoses (Alastruey et al., 2007).

Another consistent cerebrovascular abormality concerns the vertebral arteries configuration and a possible hypoplasia (underdevelopment or incomplete development of the tissue which is read as a reduced lumen of the vessel) of one of the two. According to recent studies about frequency and effects on cerebellar blood flow characteristics of VAH, in the literature there is a high incongruence concerning its prevalence and ranges between 1.9 and $\leq$ 26.5% (Thierfelder et al., 2014). This discrepancy is in part related to the fact that there is no consensus on a standard definition of this cerebrovascular variant, with a cut-off diameter range between 2.0 and 3.0 mm (Katsanos et al., 2013). Despite its presumably high prevalence, relatively little is known about the clinical relevance of VAH and there has always been a long-prevailing opinion that this anatomic variant is harmless. Only recently, VAH has obtained increased attention, mainly because of evidence suggesting that this abnormality confers an increased probability of ischaemic stroke, especially infarction in the posterior inferior cerebellar arteries and in the lateral medulla (Chuang et al., 2012; Katsanos et al., 2013; Park, Kim, and Roh, 2007; Thierfelder et al., 2014). Thierfelder et al. (2014) define VAH by a diameter of the fourth segment of the VA $\leq$ 2.0 mm and a concomitant diameter asymmetry ratio $\leq 1 : 1.7$ in all of the 4 vertebral segments. Park, Kim, and Roh (2007) define as hypoplastic the vetebral artery whose diameter is $<$ 2.2 mm. Chen et al. (2010) determined that a VA diameter $\leq$ 2.5 mm is an ideal value to define VAH and discriminate marked flow asymmetry and low flow volume of VA.

5.2 Methods

5.2.1 The Müller-Toro global closed-loop model

The Müller-Toro model is a global multi-scale closed-loop mathematical model for the human circulation composed by a 1D representation of the network of major arteries and major veins and lumped-parameter (0D) models for microvasculature (arterioles, capillaries and venules), heart, pulmonary circulation and cerebrospinal fluid (CSF) circulation, taking into account the Starling-resistor like behavior of cerebral veins and the presence of venous valves (Müller and Toro, 2014a; Müller and Toro, 2014b; Celant, 2018). The 1D FSI between vessel wall and blood flow is here described using the viscoelastic KV model (presented in Section 2.3.2) with the general 1D formulation of the PDE system (see Section 4.2.1.1), treating the resulting second order derivative in space of the flow rate introducing a numerical relaxation parameter, as discussed in Section 4.2.1.5 (Montecinos, Müller, and Toro, 2014).

With respect to the model presented by Müller and Toro (2014b) and further developed by Celant (2018) (to which the reader is invited to refer for details of the model and physiological data of the cardiovascular network), for the analysis conducted in this study related to the Selfish Brain Hypothesis, the cerebral autoregulation model (intrinsic ability of the organ to maintain constant blood flow despite changes in perfusion pressure) is deactivated, aiming to depict cerebral pressure levels changes not affected by secondary mechanisms. Moreover, the velocity profile chosen follows the simple Poiseuille law, avoiding the adoption of the not very beneficial and more complex Womersley pulsatile flow profiles (Womersley, 1957).

The 1D blood flow equations are solved using a high-order well-balanced non-linear numerical scheme in space and time based on ADER (Arbitrary high-order DERivatives) finite volume scheme (Müller and Toro, 2013), with a high-order local time stepping (LTS) scheme based on a high-order coupling strategy and a synchronization approach of the solution at junctions, as the one proposed by Müller et al. (2016).
Geometrical and physical parameters of the starting model are representative of a healthy young male aged 25 years at rest. The simulated subject is assumed to have a weight of 75 kg and height of 175 cm, with a body surface area (BSA) of 1.92 m^2 and HR equal to 75 beats/min, which corresponds to a heart cycle duration of 0.8 s.

The development of the model in this study consists in the recalibration of the parameters involved in the representation of a proper hypertensive scenario. To proceed with a proper comparison between hypertensive and normotensive subjects, without influences due to aging effects more than hypertension, parameters are firstly rearranged in order to represent a healthy adult male aged 55 years (maintaining the same BSA and HR) and further to represent a hypertensive adult male of the same age, as presented in the following Sections.

5.2.2 Modeling aging effects

Aging effects are imposed referring to previous computational studies published by Liang et al. (2009) and main references therein (Avolio et al., 1983; McEniery et al., 2005; Nichols et al., 1985). In addition, calibrations are adapted in accordance to what reported in other more recent medical papers of the field of interest (Franklin et al., 1997; Maksuti et al., 2016; Mitchell et al., 2004; O'Rourke and Hashimoto, 2007; Palatini et al., 2011; Rogers et al., 2001; Scuteri et al., 2014; Strait and Lakatta, 2012; Sugawara and Tanaka, 2015; Tarumi and Zhang, 2018).
Hence, to simulate an adult male aged 55 years, the following parameters are rearranged:

- Aortic radius: as result of an augmented left ventricle afterload, the ascending aorta inlet radius is increased by 28%, corresponding to an inlet radius of 1.83 cm (Nichols et al., 1985), with a consequent proportional adaptation of the whole branch until the abdomen region, maintaining the previous tapering effect.
- Pulse wave celerity of arteries: since the celerity of the blood flow reflects changes in both thickness and Young elastic modulus, as presented in Eq. (4.17) with the caracterization of Eq. (4.5), to simulate thickening and stiffening of central arteries, it was decided to act directly on the celerity on the basis of the body location of the vessel, referring to pulse wave velocities reported by McEniery et al. (2005) for central arteries and by Avolio et al. (1983) for peripheral arteries. In this way, celerity of vessels in the thorax are increased by 40%, celerity of vessels in the abdomen and in the upper limbs by 30% and celerity of vessels in the pelvis and lower limbs by 20%. All the other vessels maintained the initial celerity value.
- Total terminal arteries resistance: the total terminal arteries resistance is increased by 15% to account for the verified increment of the total peripheral resistance with aging.

5.2.3 Modeling hypertension effects

Research studies reporting other computational analysis on arterial hypertension, developed by Blanco, Müller, and Spence (2017) and Liang, Guan, and Alastruey (2018),

are considered as main references to simulate a hypertensive adult male aged 55 years. Therefore, to obtain a hypertensive scenario, in accordance with literature pressure trends (Asmar et al., 1995; Cox et al., 1991; De Giusti et al., 2012; Ganau et al., 1992; Laurent et al., 1994; Palatini et al., 2011), the following parameters of the adult normotensive subject have been rearranged:

- Pulse wave celerity of arteries: to match carotid-femoral pulse wave velocity (cf-PWV) measurements (Asmar et al., 1995), wave speeds in arteries are increased by 20% in all the locations, considering an overall increment of the arterial stiffness by 50%.
- Total terminal arteries resistance: the total terminal arteries resistance is increased by 45% to account for a proper augmented peripheral resistance.
- Total terminal arteries compliance: since in large vessels the compliance is inversely proportional to the celerity, $C \propto \frac{1}{a}$, the total terminal arteries compliance is decreased by 17%.
- Left ventricle elastance: as an adaptation to the elevated arterial load induced by hypertension, the contractility of the left ventricle might slightly increase; thus, the left ventricle elastance is increased by 30% to match literature cardiac output (CO) and cardiac index (CI = CO/BSA) values (Ganau et al., 1992).

It has to be underlined that, in this case, no vessel radius changes are applied following Laurent et al. (1994). Finally, it is important to stress that, in all the simulations of the present study, the total blood volume is kept constant (with a circulating part corresponding to 2,63 l).

5.3 Numerical Results and Discussion

The obtained adult normotensive and adult hypertensive scenarios are first validated comparing numerical results in terms of central and peripheral pressure levels, CO and cfPWV with reference literature values (McEniery et al., 2005; Asmar et al., 1995; Benetos et al., 2002; Cox et al., 1991; De Giusti et al., 2012; Laurent et al., 1994; Ganau et al., 1992). Subsequently, a sensitivity analysis of the parameters involved in the development of a hypertensive state is carried out, analyzing the effects of a percentage variation of arterial stiffness, total terminal arteries resistance, total terminal arteries compliance, heart contractility (left ventricle elastance) and cardiac cycle duration, with respect to a baseline hypertensive state. Finally, to assess the effects of the presence of a hypoplastic vertebral artery and an eventual incomplete circle of Willis, based on recent findings presented by Warnert et al. (2016) concerning the Selfish Brain Hypothesis of hypertension, a preliminary computational study has been conducted, taking into account three different configurations of anatomical cerebrovascular variants concerning adult normotensive and hypertensive subjects.

5.3.1 Validation of adult and hypertensive scenarios

Comparing results obtained for the young and adult subject against measured pressure ranges taken from McEniery et al. (2005), we observe from Figs. 5.2 - 5.4 that blood pressure trends are correct in all the regions. Mean arterial pressure (MAP) changes from

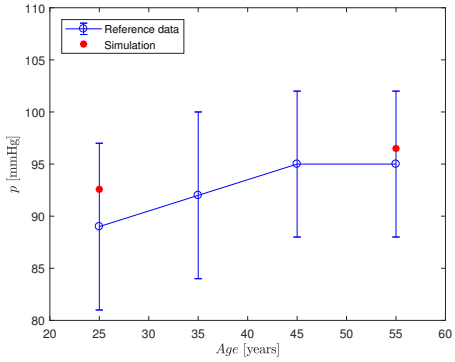

FIGURE 5.2: *Mean/brachial arterial pressure of simulated young and adult normotensive patients: aging trend. Reference data range taken from McEniery et al. (2005).*

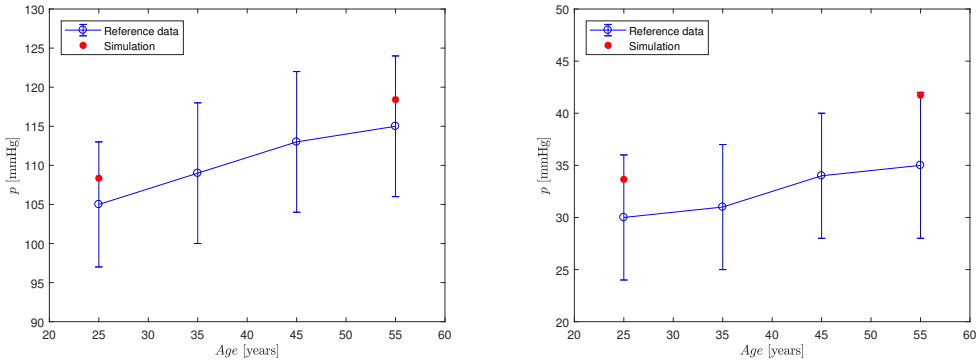

FIGURE 5.3: *Central/aortic systolic (left) and pulse pressure (right) of simulated young and adult normotensive patients: aging trend. Reference data range taken from McEniery et al. (2005).*

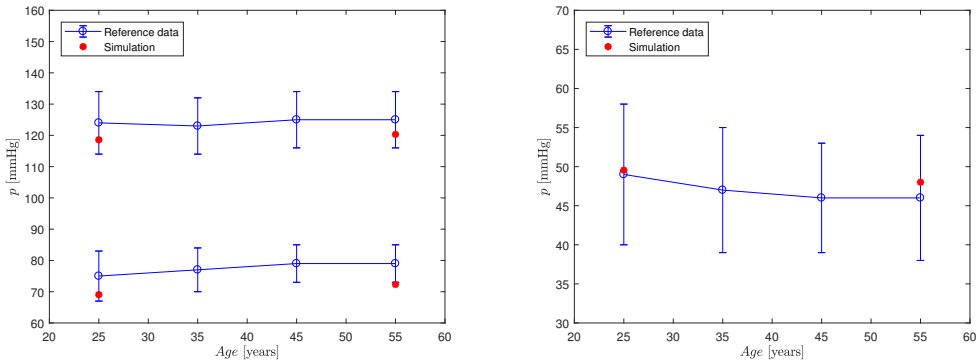

FIGURE 5.4: *Radial systolic and diastolic pressure (left) and pulse pressure (right) of simulated young and adult normotensive patients: aging trend. Reference data range taken from McEniery et al. (2005).*

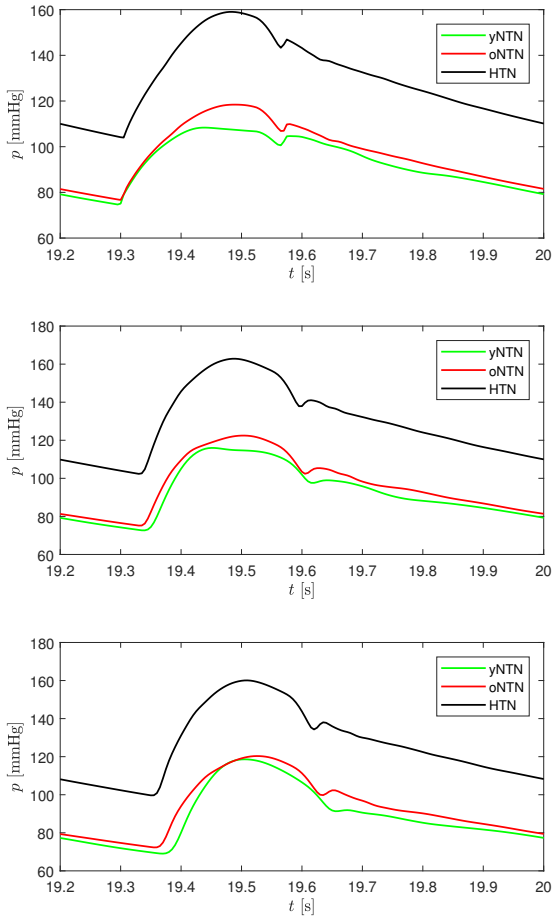

FIGURE 5.5: *Pressure wave in ascending aorta (top), left subclavian artery II (middle) and left radius (bottom) of the simulated young normotensive (yNTN) patient, the adult normotensive (oNTN) patient and the adult hypertensive (HTN) patient.*

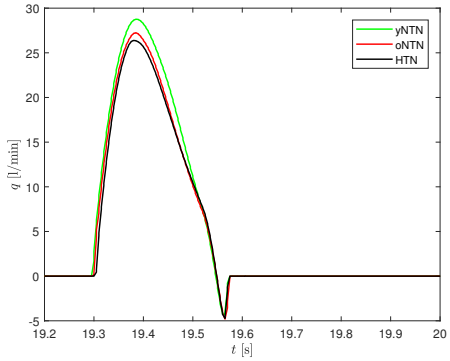

FIGURE 5.6: *Cardiac output of the simulated young normotensive (yNTN) patient, adult normotensive (oNTN) patient and adult hypertensive (HTN) patient.*

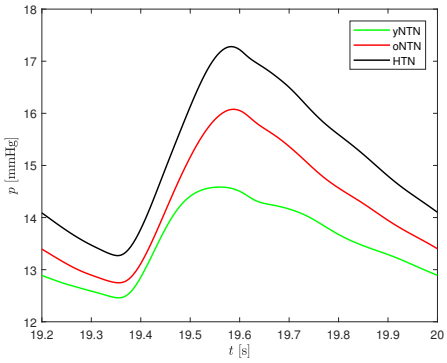

FIGURE 5.7: *Intracranial pressure of the simulated young normotensive (yNTN) patient, adult normotensive (oNTN) patient and adult hypertensive (HTN) patient.*

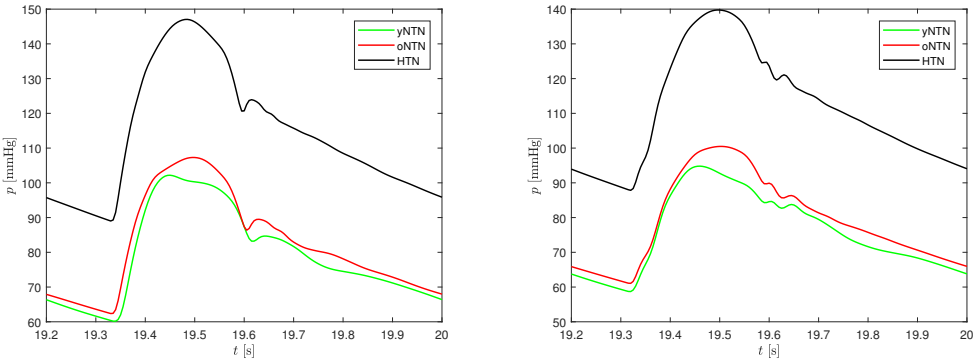

FIGURE 5.8: *Mean perfusion pressure, intended as the difference between mean arterial pressure and intracranial pressure, (left) and posterior cerebral perfusion pressure, intended as the difference between the basilar pressure and the intracranial pressure, (right) of the simulated young normotensive (yNTN) patient, adult normotensive (oNTN) patient and adult hypertensive (HTN) patient.*

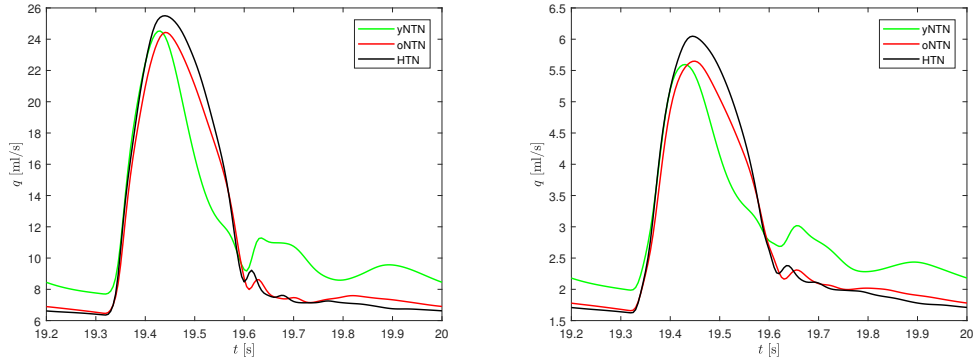

FIGURE 5.9: *Total cerebral blood flow (left) and posterior cerebral blood flow (right) of the simulated young normotensive (yNTN) patient, adult normotensive (oNTN) patient and adult hypertensive (HTN) patient.*

93 to 96.5 mmHg and also in the central region both systolic and pulse pressure considerably increase. On the other hand, in the peripheral region of the network, changes are less evident in the aging process, and indeed systolic, diastolic and consequently pulse pressure maintain more or less unvaried values. All these results are consistent with recent medical findings (Franklin et al., 1997; Maksuti et al., 2016; Mitchell et al., 2004; O'Rourke and Hashimoto, 2007; Palatini et al., 2011; Rogers et al., 2001; Scuteri et al., 2014; Strait and Lakatta, 2012; Sugawara and Tanaka, 2015; Tarumi and Zhang, 2018).
In Tabs. 5.1 and 5.2, brachial pressure values, cardiac index and carotid-femoral pulse wave velocity obtained in the simulation respectively of the adult normotensive and of the hypertensive subject are reported together with reference data taken from Asmar et al. (1995), Benetos et al. (2002), Cox et al. (1991), De Giusti et al. (2012), Ganau et al. (1992), and Laurent et al. (1994): again it is confirmed that both the calibrations made return valid results if compared to literature measurements and, according to the 2018 ESH/ESC guidelines (Williams et al., 2018), the modeled hypertensive patient is exactly at the beginning of grade 2 of hypertension.

Results of the three simulations of young normotensive, adult normotensive and hypertensive patient are shown in Figs. 5.5 - 5.9. Pressure waves forms here presented appear correct if compared to classical measurements. The effects of aging become less evident when leaving the central aortic region and reaching the radial peripheral zone, while hypertension acts with a systematic shift of pressures in all the body regions, as visible from Fig. 5.5. The CO slightly decrease as a consequence of both aging and hypertension (Fig. 5.6). On the other hand, concentrating on the cerebral area, observing respectively Fig. 5.7 and Fig. 5.8 right, the intracranial pressure p_{IC} and the posterior perfusion pressure (in this study intended as the difference between pressure in the basilar artery, which is the inlet vessel for the posterior CBF, and the intracranial pressure) increase consistently with the increase in blood pressure. In the same manner, also the mean perfusion pressure, obtained as the classical difference between MAP and p_{IC}, reaches elevated values in the hypertensive subject (Fig. 5.8 left). Concerning Fig. 5.9, a discrete decrement of the total CBF, and also of the posterior CBF, is observed with aging: total CBF changes from 700 ml/min in the young normotensive subject to 650 ml/min in the adult normotensive subject, which is a result consistent with literature trends (Tarumi and Zhang, 2018). With the development of hypertension, there is then a very slight increase to 660 ml/min of total CBF. In this study, the total CBF is considered as the sum of the inlet contributes arriving from the two internal carotid arteries (anterior) and the basilar artery (posterior), which collects incoming blood from the two vertebral arteries; while the posterior cerebral blood flow is obtained as the sum of the outgoing blood in anterior inferior cerebellar arteries and posterior cerebral arteries.

5.3.2 Sensitivity analysis

A sensitivity analysis of the parameters involved in the development of a hypertensive state is performed to observe the effects of a percentage variation of arterial stiffness (i.e. the product Eh, which affects the pulse wave celerity), total terminal arteries resistance, total terminal arteries compliance, heart contractility (i.e. left ventricle elastance) and cardiac cycle duration (i.e. heart rate) with respect to a baseline hypertensive state. The reference hypertensive state is assumed to be the result of calibrations discussed in Section 5.2.3, starting from which the parameters of intereste are varied in an univariate manner; hence, when a parameter is varied, all the others are fixed at their baseline state. Percentage variations considered for each parameter are listed in Table 5.3. Again, it has

Data	BSP	BDP	BPP	BMP	CI	cfPWV
Simulation	122	75	47	96.5	2.65	9.87
Asmar et al. (1995)	125 ± 9	77 ± 8	-	-	-	8.5 ± 1.5
Benetos et al. (2002)	129.5 ± 0.9	82.4 ± 0.6	47.1 ± 0.7	98.1 ± 0.6	-	10.35 ± 0.1
Cox et al. (1991)	136 ± 16	77 ± 9	-	-	-	-
Laurent et al. (1994)	128 ± 21	71 ± 13	-	90 ± 15	-	-
Ganau et al. (1992)	-	-	-	-	2.9 ± 0.7	-

TABLE 5.1: *Results obtained in the adult normotensive patient simulation (first row) compared to literature data ranges. BSP = brachial systolic pressure [mmHg], BDP = brachial diastolic pressure [mmHg], BPP = brachial pulse pressure [mmHg], BMP = brachial mean pressure [mmHg], CI = cardiac index [l m^{-2}/min], cfPWV = carotid-femoral pulse wave velocity [m/s], calculated with the foot-to-foot method.*

Data	BSP	BDP	BPP	BMP	CI	cfPWV
Simulation	163	102	60.5	129	2.56	11.52
Asmar et al. (1995)	164 ± 13	102 ± 9	-	-	-	11.8 ± 2.7
Cox et al. (1991)	180 ± 22	96 ± 13	-	-	-	-
De Giusti et al. (2012)	145.6 ± 15.8	87.8 ± 10.4	-	-	-	-
Laurent et al. (1994)	165 ± 25	96 ± 24	-	121 ± 24	-	-
Ganau et al. (1992)	-	-	-	-	2.4 ± 0.5	-

TABLE 5.2: *Results obtained in the adult hypertensive patient simulation (first row) compared to literature data ranges. BSP = brachial systolic pressure [mmHg], BDP = brachial diastolic pressure [mmHg], BPP = brachial pulse pressure [mmHg], BMP = brachial mean pressure [mmHg], CI = cardiac index [l m^{-2}/min], cfPWV = carotid-femoral pulse wave velocity [m/s], calculated with the foot-to-foot method.*

to be reminded that for each simulation the total blood volume is kept constant and equal to 2.63 l.
Results of the sensitivity analysis are reported in Figs. 5.10-5.44 with respect to pressure waves in different compartments, cardiac output, intracranial pressure, mean and posterior cerebral perfusion and cerebral blood flow. Moreover, two summary conclusive plots accounting for variation trends of mean arterial pressure, central systolic pressure, central diastolic pressure, central pulse pressure, intracranial pressure, mean perfusion, cardiac output, total cerebral blood flow and total cerebrovascular resistance are presented.
It is here underlined that for the estimation of the CVR it is followed the standard indirect clinical definition: CVR = MAP/CBF.

Parameter	(- -%)	(-%)	(+%)	(++%)
Arterial stiffness	-75%	-50%	+50%	+75%
Total terminal arteries resistance	-40%	-20%	+20%	+40%
Total terminal arteries compliance	-40%	-20%	+20%	+40%
Heart contractility (elastance)	-30%	-10%	+10%	+30%
Cardiac cycle duration	-20%	-10%	+10%	+20%

TABLE 5.3: *List of the percentage variations considered for each parameter of interest in the sensitivity analysis of the hypertensive scenario with respect to the baseline state.*

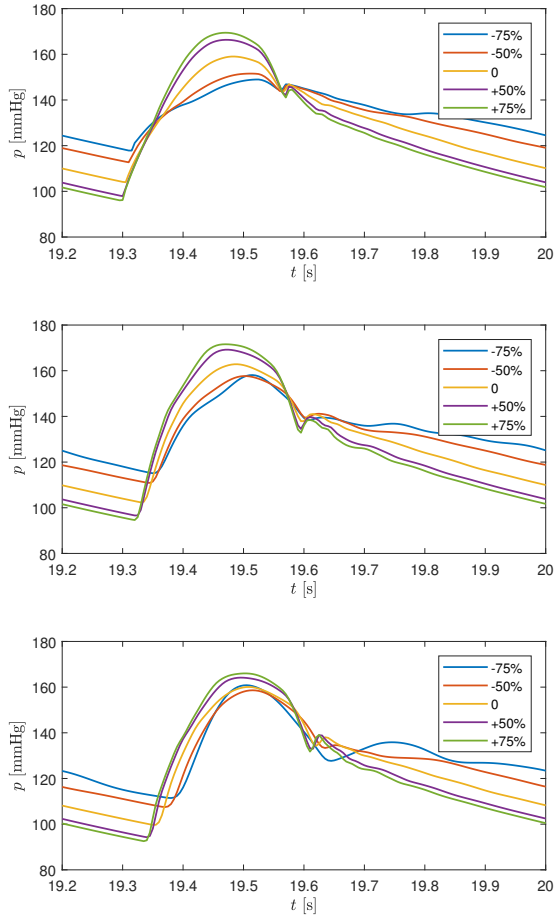

FIGURE 5.10: *Sensitivity analysis results concerning arterial stiffness variation: pressure wave in ascending aorta (top), left subclavian artery II (centre) and left radius (bottom). Percentage variation of the parameter in legend.*

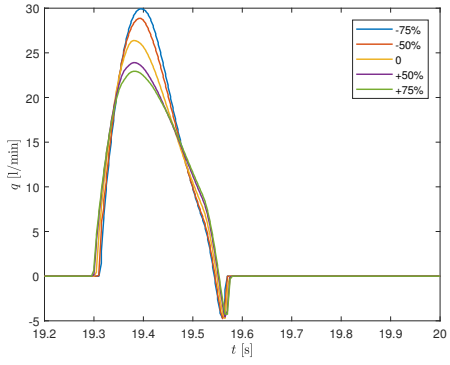

FIGURE 5.11: *Sensitivity analysis results concerning arterial stiffness variation: cardiac output. Percentage variation of the parameter in legend.*

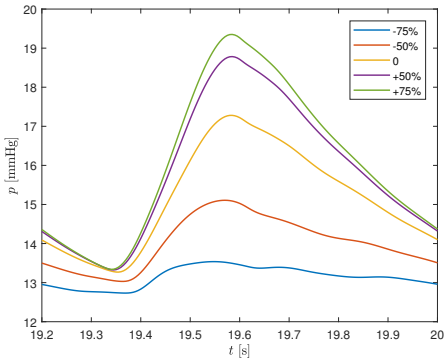

FIGURE 5.12: *Sensitivity analysis results concerning arterial stiffness variation: intracranial pressure. Percentage variation of the parameter in legend.*

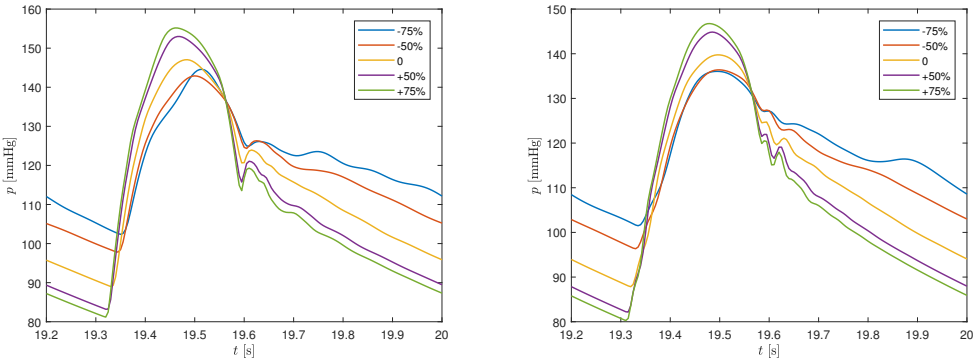

FIGURE 5.13: *Sensitivity analysis results concerning arterial stiffness variation: mean perfusion pressure (left) and posterior cerebral perfusion pressure (right). Percentage variation of the parameter in legend.*

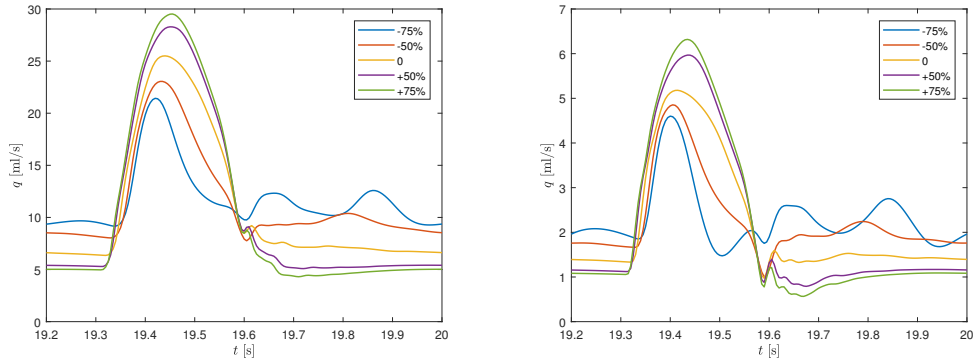

FIGURE 5.14: *Sensitivity analysis results concerning arterial stiffness variation: total cerebral blood flow (left) and posterior cerebral blood flow (right). Percentage variation of the parameter in legend.*

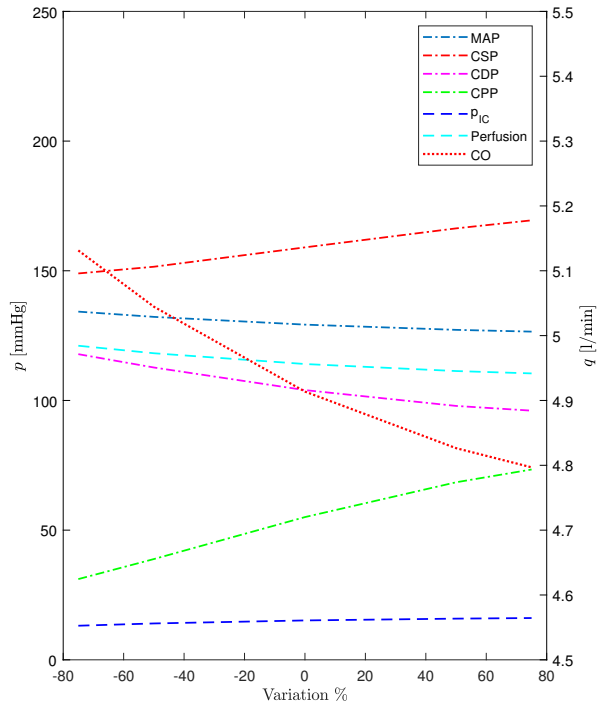

FIGURE 5.15: *Sensitivity analysis summary results concerning arterial stiffness variation: trends of mean arterial pressure (MAP), central systolic pressure (CSP), central diastolic pressure (CDP), central pulse pressure (CPP), intracranial pressure (p_{IC}), mean perfusion pressure and cardiac output (CO).*

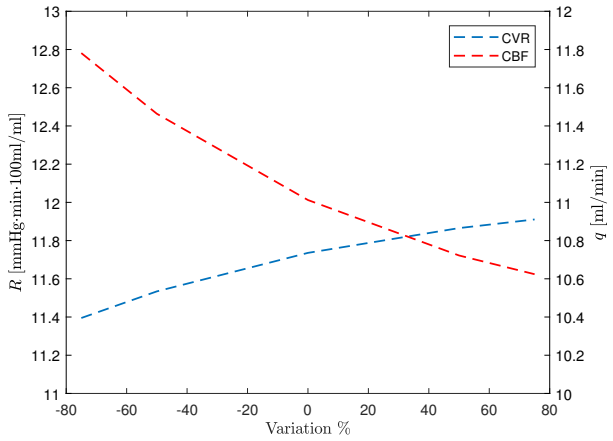

FIGURE 5.16: *Sensitivity analysis summary results concerning arterial stiffness variation: trends of total cerebrovascular resistance (CVR) and total cerebral blood flow (CBF).*

5.3.2.1 Arterial stiffness variation

Figures from 5.10 to 5.16 show changes in the main hemodynamic aspects when varying the arterial stiffness in a reference hypertensive subject. In particular, it is evident that increasing the arterial stiffness, the systolic pressure rises (especially in the central region), while the diastolic pressure decreases, with a consequent increment of the pulse pressure. The mean arterial pressure is only mildly affected by the variation of this parameter, while a stronger impact is observed in the total cerebral blood flow, which decreases while the arterial stiffness increases. These last two results explain why the cerebrovascular resistance increases with the arterial stiffness. In the meantime, cardiac output decreases while intracranial pressure increases and consequently the perfusion pressure decreases.

5.3.2.2 Total terminal arteries resistance variation

Figures from 5.17 to 5.23 show changes in the main hemodynamic aspects when varying the total terminal arteries resistance in a reference hypertensive subject. In particular, it is evident that increasing the total terminal arterial resistance, both the systolic and the diastolic pressure rise deeply, with a consequent almost invariance of the pulse pressure. The same increment applies to the mean arterial pressure. Also in the total cerebral blood flow a strong impact is observed, even if not with a linear trend, with a decrement of this parameter while the arterial resistance increases, while the cerebrovascular resistance increases with the arterial resistance with a linear trend. The cardiac output is deeply affected by the increment of the arterial resistance, and indeed a decisive drop is observed. Finally, even though the intracranial pressure rises with the growth of the resistance, the perfusion pressure still increase, due to the major rise of the mean arterial pressure.

5.3.2.3 Total terminal arteries compliance variation

Figures from 5.24 to 5.30 show changes in the main hemodynamic aspects when varying the total terminal arteries compliance in a reference hypertensive subject. In particular, it is observed that increasing the total terminal arterial compliance, the systolic pressure decreases, while the diastolic pressure remains almost stable, with a consequent slight decrement of the pulse pressure. The mean arterial pressure is only mildly affected by the variation of this parameter, while a stronger impact is observed in the total cerebral blood flow, which decreases while the arterial compliance increases. These last two results explain why in parallel the cerebrovascular resistance increases with the arterial compliance. Moreover, also the cardiac output presents a decisive drops. Finally, the intracranial pressure increases, with a consequent light decrement of the perfusion pressure.

5.3.2.4 Heart contractility variation

Figures from 5.31 to 5.37 show changes in the main hemodynamic aspects when varying the heart contractility in a reference hypertensive subject. In particular, it is evident that increasing the left ventricle elastance, the systolic and the diastolic pressure rise, with a parallel slight increment of the pulse pressure. The same growth is read in the mean arterial pressure, while a stronger impact is observed in the total cerebral blood

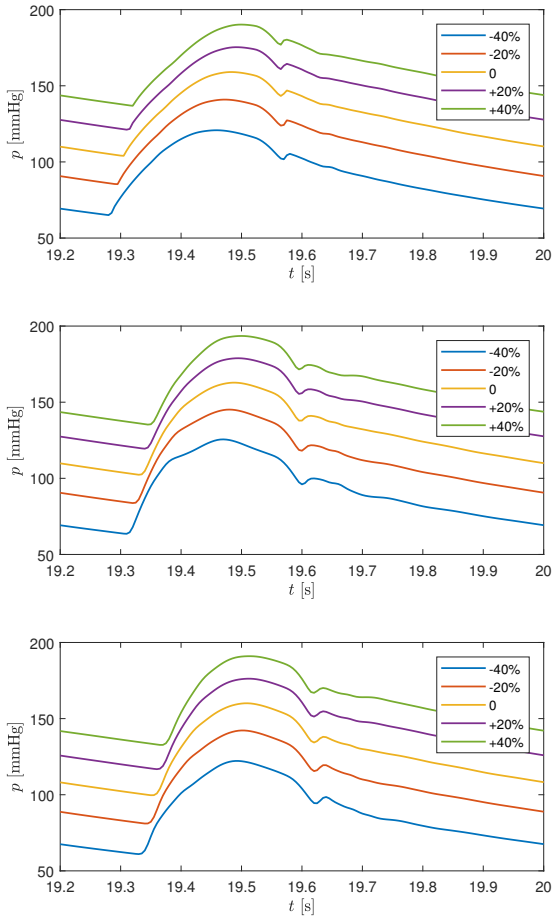

FIGURE 5.17: *Sensitivity analysis results concerning total terminal arteries resistance variation: pressure wave in ascending aorta (top), left subclavian artery II (centre) and left radius (bottom). Percentage variation of the parameter in legend.*

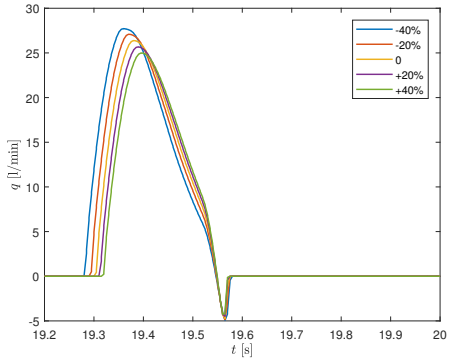

FIGURE 5.18: *Sensitivity analysis results concerning total terminal arteries resistance variation: cardiac output. Percentage variation of the parameter in legend.*

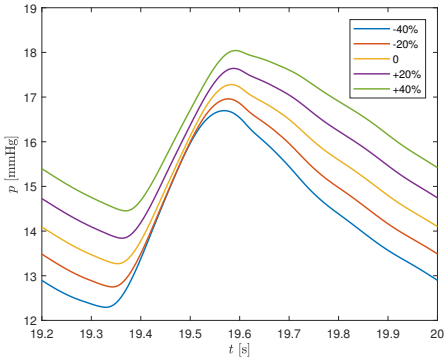

FIGURE 5.19: *Sensitivity analysis results concerning total terminal arteries resistance variation: intracranial pressure. Percentage variation of the parameter in legend.*

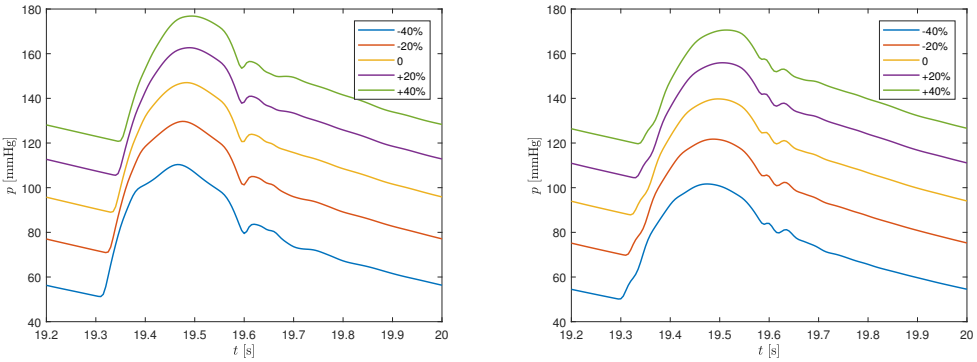

FIGURE 5.20: *Sensitivity analysis results concerning total terminal arteries resistance variation: mean perfusion pressure (left) and posterior cerebral perfusion pressure (right). Percentage variation of the parameter in legend.*

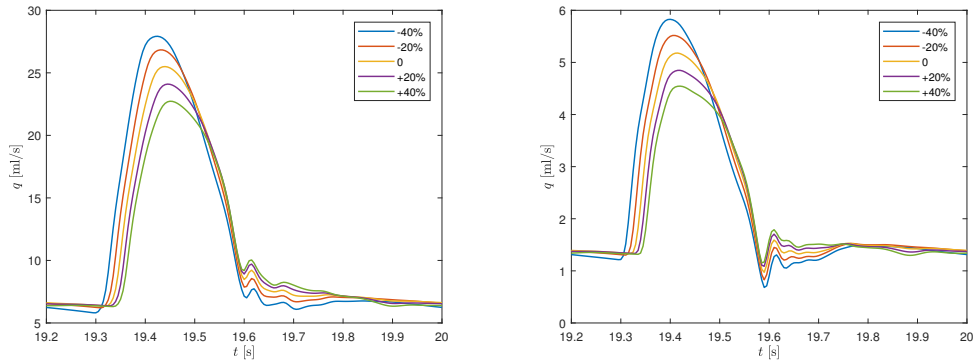

FIGURE 5.21: *Sensitivity analysis results concerning total terminal arteries resistance variation: total cerebral blood flow (left) and posterior cerebral blood flow (right). Percentage variation of the parameter in legend.*

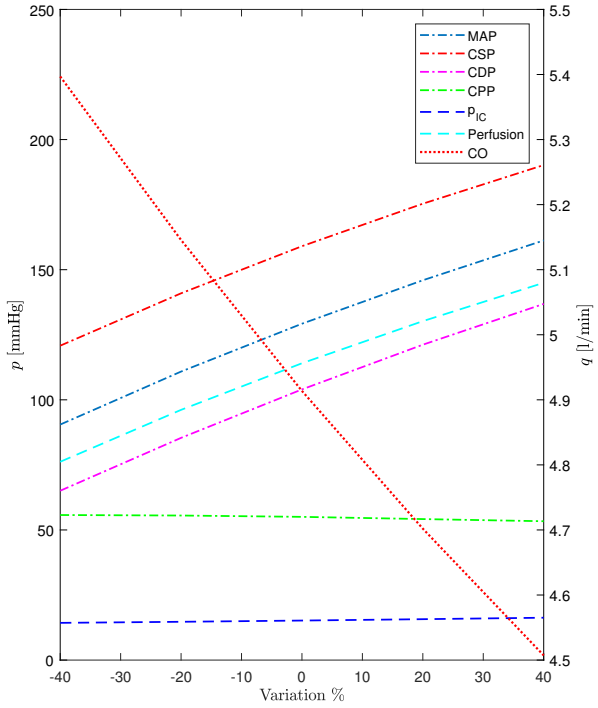

FIGURE 5.22: *Sensitivity analysis summary results concerning total terminal arteries resistance variation: trends of mean arterial pressure (MAP), central systolic pressure (CSP), central diastolic pressure (CDP), central pulse pressure (CPP), intracranial pressure (p_{IC}), mean perfusion pressure and cardiac output (CO).*

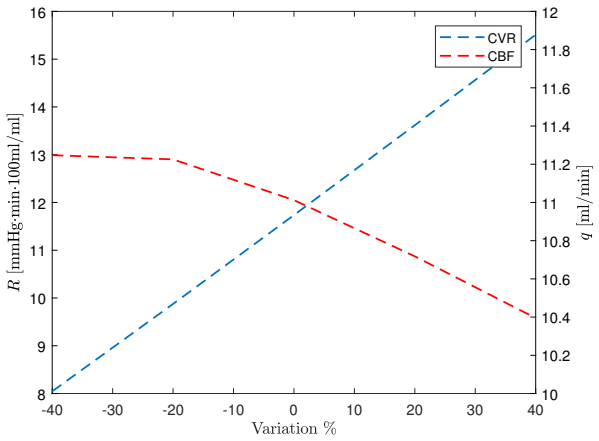

FIGURE 5.23: *Sensitivity analysis summary results concerning total terminal arteries resistance variation: trends of total cerebrovascular resistance (CVR) and total cerebral blood flow (CBF).*

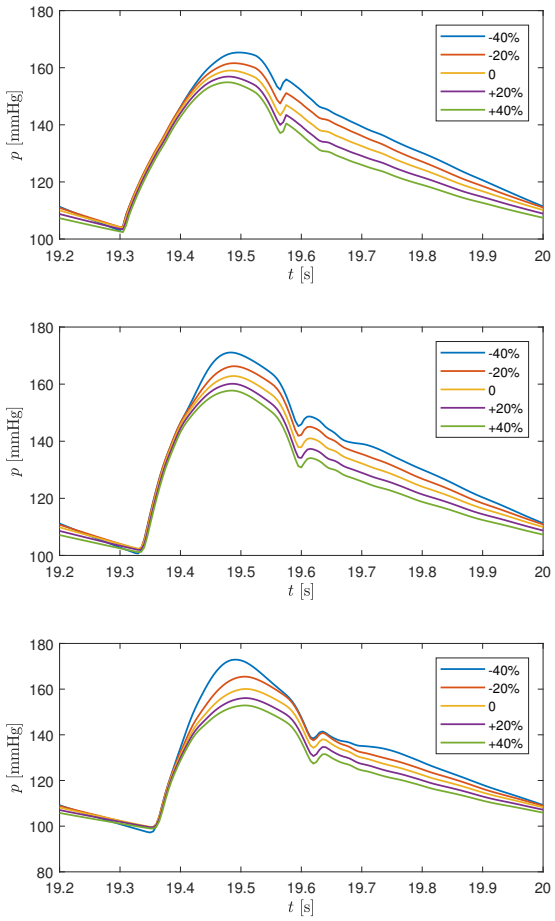

FIGURE 5.24: *Sensitivity analysis results concerning total terminal arteries compliance variation: pressure wave in ascending aorta (top), left subclavian artery II (centre) and left radius (bottom). Percentage variation of the parameter in legend.*

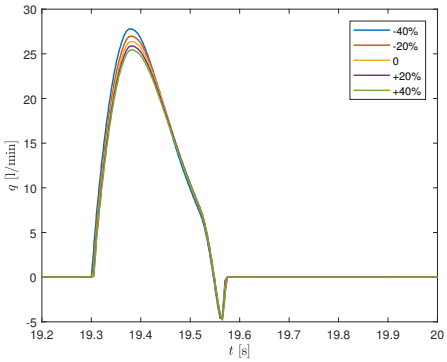

FIGURE 5.25: *Sensitivity analysis results concerning total terminal arteries compliance variation: cardiac output. Percentage variation of the parameter in legend.*

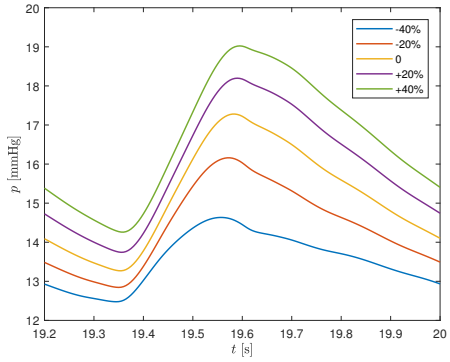

FIGURE 5.26: *Sensitivity analysis results concerning total terminal arteries compliance variation: intracranial pressure. Percentage variation of the parameter in legend.*

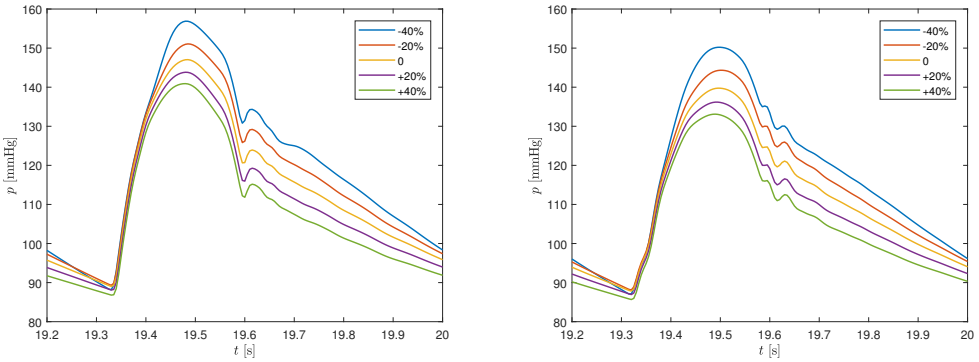

FIGURE 5.27: *Sensitivity analysis results concerning total terminal arteries compliance variation: mean perfusion pressure (left) and posterior cerebral perfusion pressure (right). Percentage variation of the parameter in legend.*

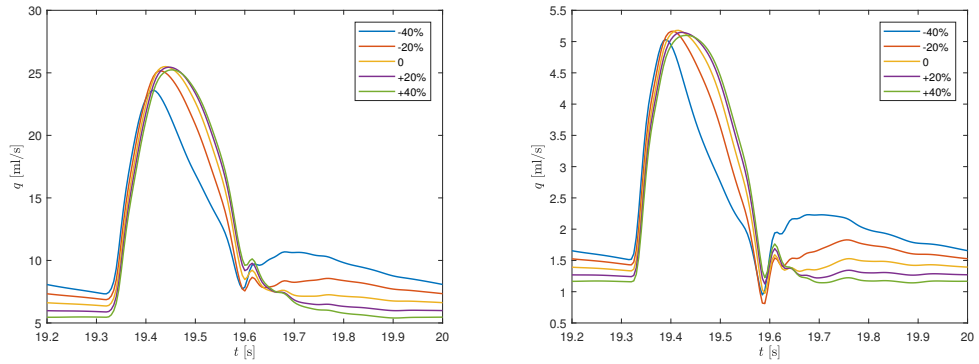

FIGURE 5.28: *Sensitivity analysis results concerning total terminal arteries compliance variation: total cerebral blood flow (left) and posterior cerebral blood flow (right). Percentage variation of the parameter in legend.*

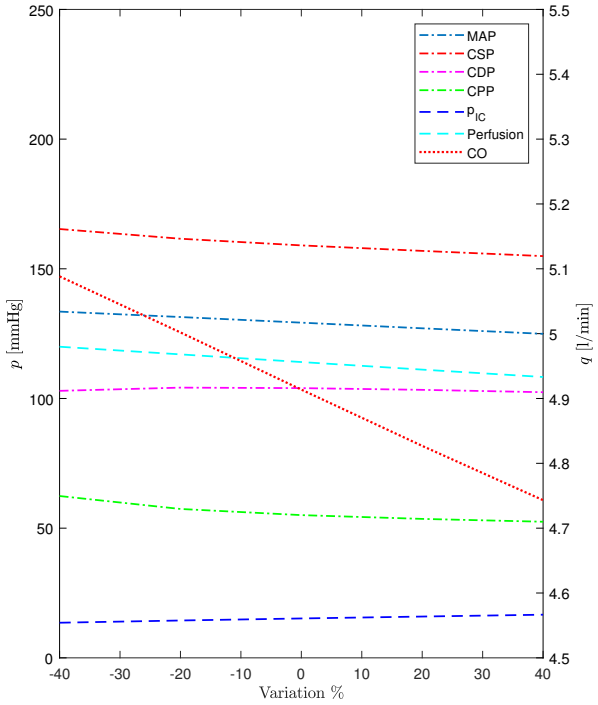

FIGURE 5.29: *Sensitivity analysis summary results concerning total terminal arteries compliance variation: trends of mean arterial pressure (MAP), central systolic pressure (CSP), central diastolic pressure (CDP), central pulse pressure (CPP), intracranial pressure (p_{IC}), mean perfusion pressure and cardiac output (CO).*

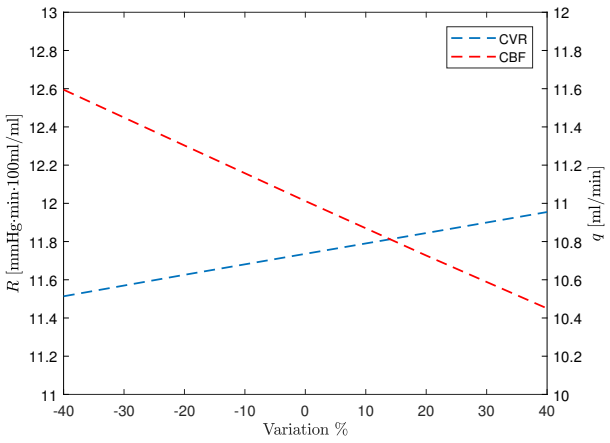

FIGURE 5.30: *Sensitivity analysis summary results concerning total terminal arteries compliance variation: trends of total cerebrovascular resistance (CVR) and total cerebral blood flow (CBF).*

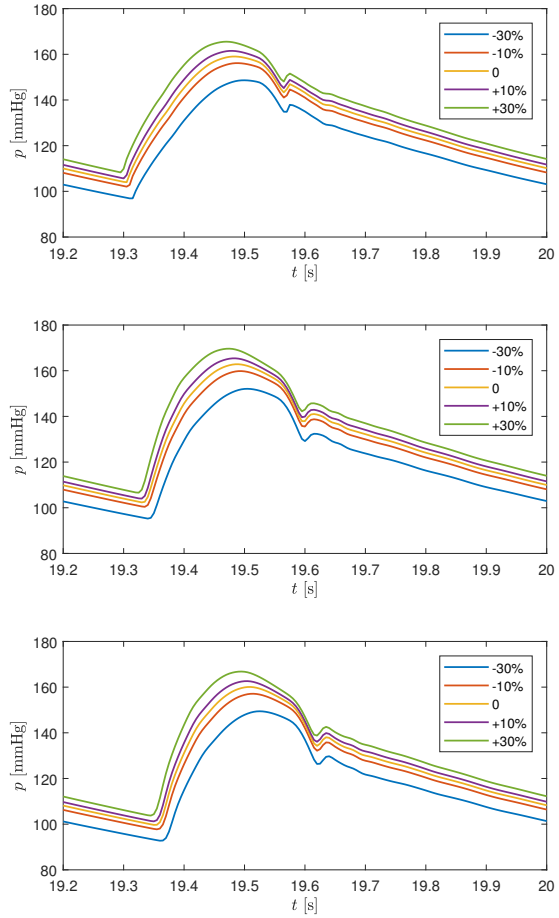

FIGURE 5.31: *Sensitivity analysis results concerning left ventricle elastance variation: pressure wave in ascending aorta (top), left subclavian artery II (centre) and left radius (bottom). Percentage variation of the parameter in legend.*

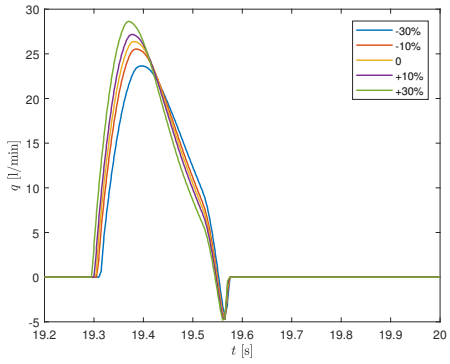

FIGURE 5.32: *Sensitivity analysis results concerning left ventricle elastance variation: cardiac output. Percentage variation of the parameter in legend.*

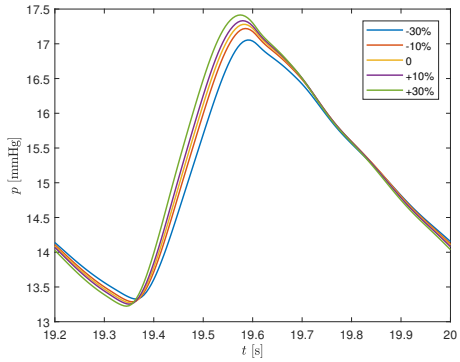

FIGURE 5.33: *Sensitivity analysis results concerning left ventricle elastance variation: intracranial pressure. Percentage variation of the parameter in legend.*

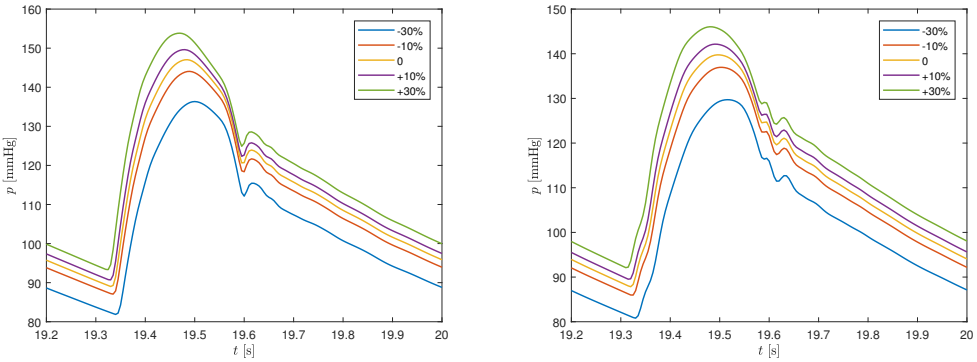

FIGURE 5.34: *Sensitivity analysis results concerning left ventricle elastance variation: mean perfusion pressure (left) and posterior cerebral perfusion pressure (right). Percentage variation of the parameter in legend.*

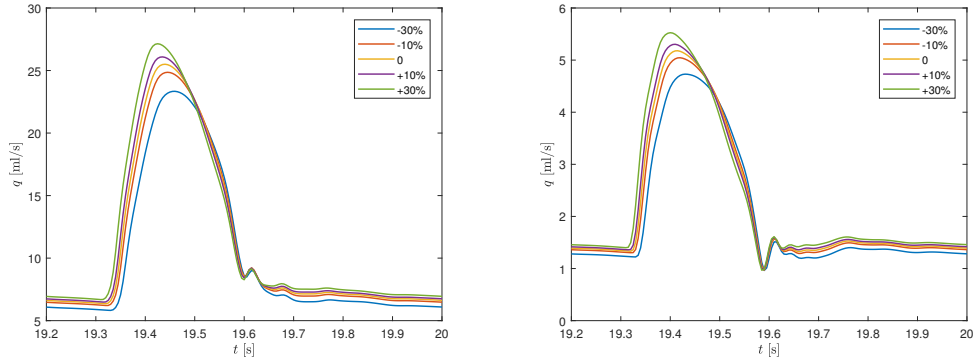

FIGURE 5.35: *Sensitivity analysis results concerning left ventricle elastance variation: total cerebral blood flow (left) and posterior cerebral blood flow (right). Percentage variation of the parameter in legend.*

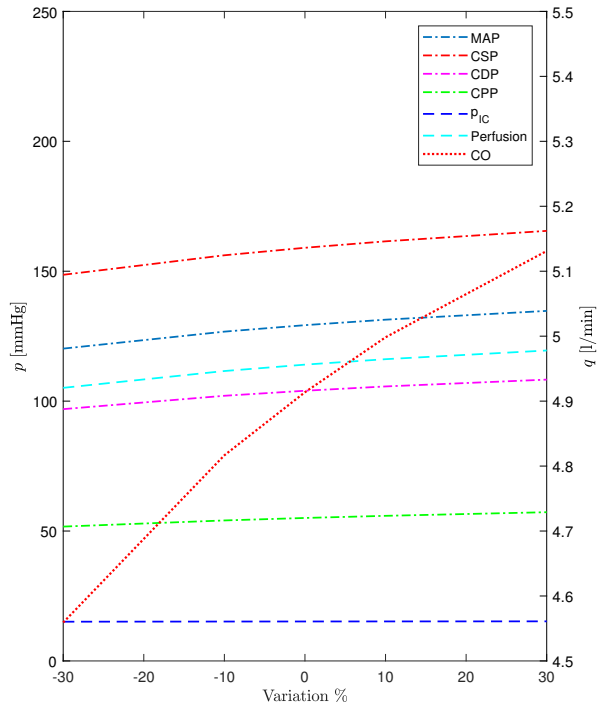

FIGURE 5.36: *Sensitivity analysis summary results concerning left ventricle elastance variation: trends of mean arterial pressure (MAP), central systolic pressure (CSP), central diastolic pressure (CDP), central pulse pressure (CPP), intracranial pressure (p_{IC}), mean perfusion pressure and cardiac output (CO).*

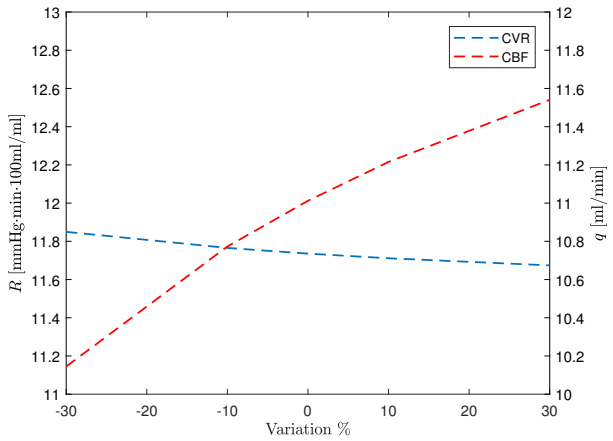

FIGURE 5.37: *Sensitivity analysis summary results concerning left ventricle elastance variation: trends of total cerebrovascular resistance (CVR) and total cerebral blood flow (CBF).*

flow, which increases while the heart contractility increases. As a consequence, the cerebrovascular resistance decreases inversely to the gain in heart contractility. Concerning the cardiac output, it can be verified its increment, while intracranial pressure remains almost constant, resulting in a slight increase of perfusion pressure.

5.3.2.5 Cardiac cycle duration variation

Figures from 5.38 to 5.44 show changes in the main hemodynamic aspects when varying the cardiac cycle duration in a reference hypertensive subject. In particular, it is observed that increasing the cardiac cycle duration, both the systolic and the diastolic pressure decrease, with a little increase of the pulse pressure. Also the mean arterial pressure and the total cerebral blood flow decrease, even if the latter not with a linear trend. This last result explains why in parallel the cerebrovascular resistance has a non-monotone behaviour. The same applies to the intracranial pressure, while perfusion pressure, mostly affected by mean arterial pressure trend, decreases. Finally, the cardiac output presents a significant drop, as expected.

5.3.2.6 Final remarks

If considering the 2018 ESH/ESC guidelines for the management of arterial hypertension (Williams et al., 2018), it is possible to highlight which parameters determine a change of the hypertension grade with their variation, with respect to the reference state (represented by a grade 2 of hypertension), or even the transition to a normal pressure level. Observing Tab. 5.4, it is evident that, to obtain a pressure level change, the most decisive parameter on which action should be taken is the total terminal arteries resistance, which substantially determines a shift in the pressure grade for each 20% of variation. At the same time, it can be noticed that also the HR plays an important role when aiming to reduce arterial pressure values.

5.3.3 Application study to the medical case: the Selfish Brain Hypothesis

To assess the effects of the presence of hypoplastic vertebral artery and eventual additional incomplete circle of Willis, a preliminary computational study is conducted, taking into account three different configurations of anatomical cerebrovascular variants.
Since the vertebral artery hypoplasia is found more frequently on the right side (Park,

	(- -%)		(-%)		(+%)		(++%)	
Variation parameter	p_S	p_D	p_S	p_D	p_S	p_D	p_S	p_D
Arterial stiffness	158	115	158	110	169	96	171	94
Total terminal arteries resistance	125	63	145	83	179	119	193	134
Total terminal arteries compliance	171	100	166	101	160	101	158	101
Heart contractility (elastance)	152	95	160	100	165	104	170	106
Heart rate	168	111	166	107	158	96	153	89

TABLE 5.4: *Summary of the sensitivity analysis: systolic (p_S) and diastolic (p_D) pressure levels expressed in mmHg for each parameter univariation. Different cell colours identify different pressure level shifts: green represents normotensive levels, orange represents grade 1 of hypertension, red represents grade 3 of hypertension and blue represents the isolated systolic hypertension.*

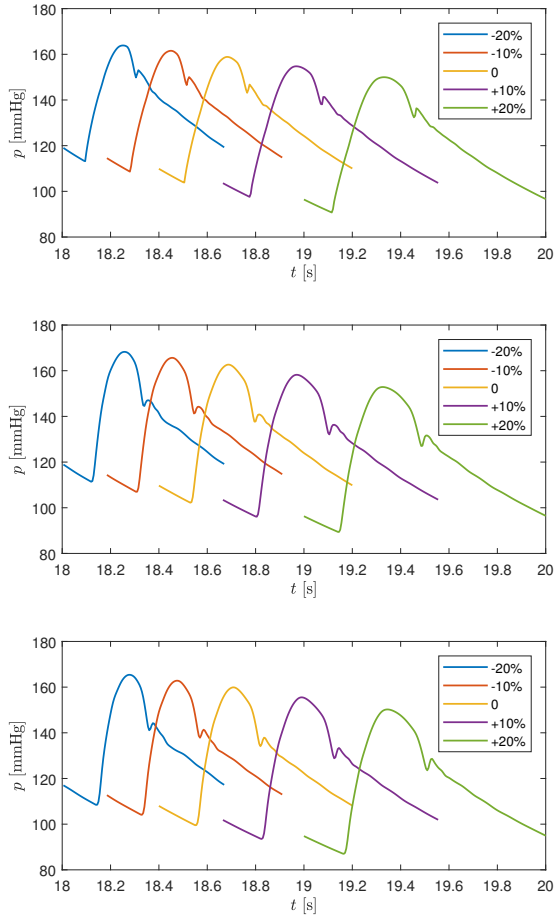

FIGURE 5.38: *Sensitivity analysis results concerning heart rate variation: pressure wave in ascending aorta (top), left subclavian artery II (centre) and left radius (bottom). Percentage variation of the parameter in legend.*

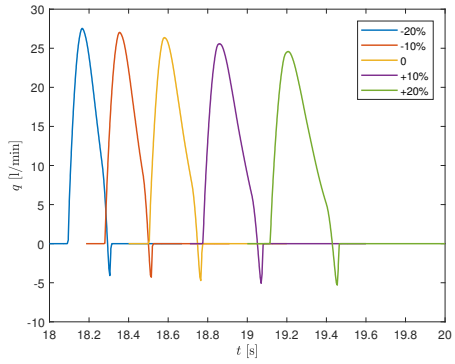

FIGURE 5.39: *Sensitivity analysis results concerning heart rate variation: cardiac output. Percentage variation of the parameter in legend.*

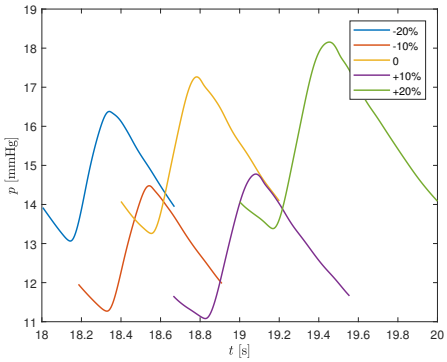

FIGURE 5.40: *Sensitivity analysis results concerning heart rate variation: intracranial pressure. Percentage variation of the parameter in legend.*

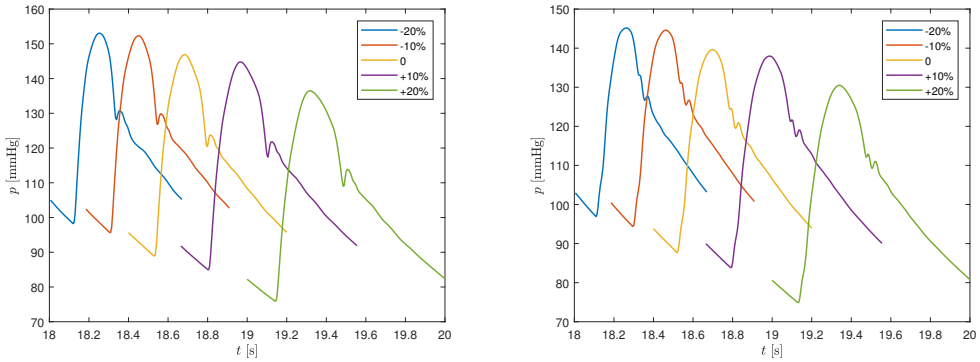

FIGURE 5.41: *Sensitivity analysis results concerning heart rate variation: mean perfusion pressure (left) and posterior cerebral perfusion pressure (right). Percentage variation of the parameter in legend.*

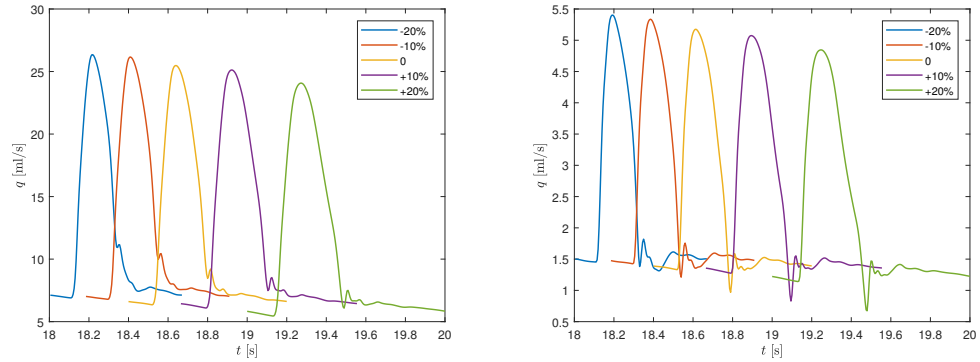

FIGURE 5.42: *Sensitivity analysis results concerning heart rate variation: total cerebral blood flow (left) and posterior cerebral blood flow (right). Percentage variation of the parameter in legend.*

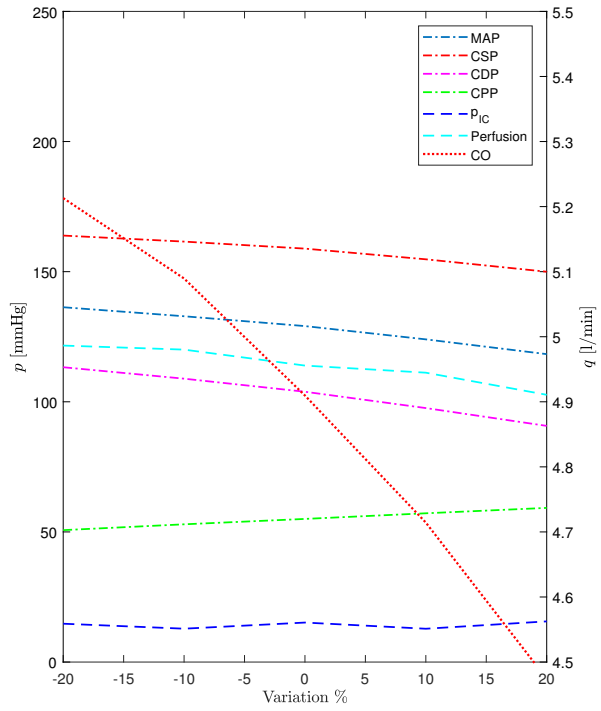

FIGURE 5.43: *Sensitivity analysis summary results concerning heart rate variation: trends of mean arterial pressure (MAP), central systolic pressure (CSP), central diastolic pressure (CDP), central pulse pressure (CPP), intracranial pressure (p_{IC}), mean perfusion pressure and cardiac output (CO).*

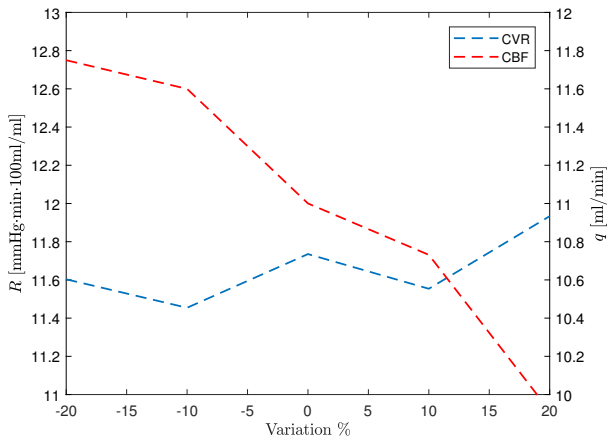

FIGURE 5.44: *Sensitivity analysis summary results concerning heart rate variation: trends of total cerebrovascular resistance (CVR) and total cerebral blood flow (CBF).*

Kim, and Roh, 2007; Chen et al., 2010), in the following VAH case simulations it is assumed hypoplastic the right VA. To evaluate a very critic case, in the present study it is applied a 75% occlusion of the vessel, corresponding to an average diameter of 0.715 mm. The effects of the presence of VAH, in terms of cerebral blood flow variation, are evaluated first considering an adult, 55 years old, normotensive (NTN) subject (with parameters calibrated as presented in Section 5.2.2) and then considering an adult hypertensive (HTN) subject (following the calibration discussed in Section 5.2.3). Moreover, for the NTN configuration, it is also analyzed a more critic scenario, corresponding to the simultaneous presence of VAH and absence of the two PcoAs, hence an incomplete CoW with total separation of the anterior region to the posterior region.

5.3.3.1 Vertebral artery hypoplasia in an adult patient

Observing cerebral blood flow variations reported in Fig. 5.5 concerning the adult NTN case with VAH, compared to arterial CBF baseline values, it can be noticed that the controlateral VA is able to partially compensate the reduction of flow rate due to the hypoplastic VA, increasing the flowing rate in its path by 50%. Even though, the flow rate arriving in the BA is not totally recovered, indeed presenting a considerable reduction of 26%. However, the total arterial CBF does not seem to be affected by the presence of VAH, since the part of blood flow missing from the posterior inlet is almost fully compensated by the anterior inlet with the internal carotid arteries.
Focusing on the posterior region, where the VMC is located (see Section 5.1.2), a discrete reduction of blood flow is observed only in the first part of the posterior cerebral arteries, as this section of the artery cannot benefit from the compensatory percentage of flow arriving from the front. Globally, considering the posterior CBF in the model composed by the sum of the contributes outgoing posterior cerebral arteries and anterior inferior cerebellar arteries, the posterior region presents solely a small decrease of blood flow rate in the subject with a hypoplastic VA.

	q [ml/min]		
Location	baseline	VAH	Δq
Total CBF	651	647	-0.6%
right internal carotid artery	257	273	$+6.2\%$
left internal carotid artery	254	270	$+6.3\%$
basilar artery	141	105	-26%
right vertebral artery	70	0.40	-99%
left vertebral artery	70	105	$+50\%$
Posterior CBF	164	161	-1.8%
right posterior cerebral artery (I)	65	47	-28%
left posterior cerebral artery (I)	65	47	-28%
right posterior cerebral artery (II)	77	75	-2.6%
left posterior cerebral artery (II)	77	75	-2.6%
right anterior inferior cerebellar artery	5.1	5.0	-2.0%
left anterior inferior cerebellar artery	5.5	5.4	-1.8%

TABLE 5.5: *Cerebral blood flow values, with a focus on the posterior region, for all the arteries of interest concerning the NTN subject, with or without VAH, and the difference in percentage (Δq) between the two configurations.*

5.3.3.2 Vertebral artery hypoplasia and absence of posterior communicating arteries in an adult patient

An interesting aspect worth to be noticed regards the compensatory capacity of the controlateral VA when a configuration of adult NTN with VAH and additional absence of the two PcoAs is studied. In this scenario, in which the controlateral VA is the only vessel supplying the posterior region of the brain, the artery demonstrates to be able to totally compensate the lower blood flow in the hypoplastic VA. Referring to Tab. 5.6, the blood flow entering in the BA is even increased by 11% with respect to the baseline state, while a contemporary reduction of the inlet flow from the internal carotid arteries is observed. In total, the CBF is maintained under an almost constant value.
The second interesting aspect concerns the posterior CBF. It is indeed highlighted that in the present configuration there is almost 5% less of blood supplying the brainstem. Since the NTS here located is very sensitive to alteration of perfusion levels, this decrement of flow rate (and consequent decrement of perfusion) could be seen as triggering factor for the activation of the response of the Selfish Brain, in agreement with studies performed by Warnert et al. (2016), Hart (2016), and Cates et al. (2012).

5.3.3.3 Vertebral artery hypoplasia in a hypertensive patient

Tab. 5.7 shows computational results of the study of the effects of the presence of VAH in a HTN subject when arterial CBF values are analyzed with respect to a baseline state. These results present an evident agreement with those obtained in the respective NTN configuration, suggesting that the presence or not of high blood pressure levels do not affect the redistribution of cerebrovascular flow rates when the subject has a hypoplastic VA. In fact, even though the controlateral VA increases by 49% the level of blood flowing within it, the total CBF and also the posterior CBF levels present an irrelevant reduction thanks to the additional compensation arriving from the internal carotid arteries.

	q [ml/min]		
Location	baseline	VAH & no PcoAs	Δq
Total CBF	651	645	-0.9%
right internal carotid artery	257	245	-4.7%
left internal carotid artery	254	243	-4.3%
basilar artery	141	156	$+11\%$
right vertebral artery	70	0.60	-99%
left vertebral artery	70	156	$+123\%$
Posterior CBF	164	156	-4.9%
right posterior cerebral artery (I)	65	73	$+12\%$
left posterior cerebral artery (I)	65	73	$+12\%$
right posterior cerebral artery (II)	77	73	-5.2%
left posterior cerebral artery (II)	77	73	-5.2%
right anterior inferior cerebellar artery	5.1	4.8	-5.9%
left anterior inferior cerebellar artery	5.5	5.2	-5.5%

TABLE 5.6: *Cerebral blood flow values, with a focus on the posterior region, for all the arteries of interest concerning the NTN subject, with or without VAH and absence of the posterior communicating arteries (PcoAs), and the difference in percentage (Δq) between the two configurations.*

5.4 Concluding remarks

In the present work, some preliminary studies have been conducted concerning representative 55 years old normotensive and hypertensive subjects, to assess the effects of congenital anatomical variations concentrated in the cerebral vasculature: vertebral artery hypoplasia and incomplete posterior Circle of Willis, which have been found to play a possible role in triggering high arterial pressure (Hart, 2016).
With this aim, the Müller-Toro model (Müller and Toro, 2014a; Müller and Toro, 2014b; Celant, 2018), a global multiscale closed-loop blood flow model, has been extended considering changes in the vessels network due to aging and hypertension processes. Results obtained simulating the hypertensive subject have been investigated through a sensitivity analysis to assess correlations between hemodynamic variations and the development of arterial hypertension. This analysis confirmed that the parameter affecting the most changes in pressure levels is the total terminal arteries resistance, which determined a shift in the pressure grade for each 20% of variation.

Simulations, regarding both the NTN and the HTN subject, highlight that a VAH state do not generally lead to a decreased total arterial CBF thanks to the compensatory capability of the other vessels supplying the brain, especially the controlateral VA. The cerebral circulation network, in fact, has an innate oversizing which guarantees enough resources to the system when small geometrical abnormalities are present. A possible reduction of total CBF could eventually occur when this compensatory capacity is limited (Celant, 2018). We could speculate that when the abnormality continue in time with excessive/prolonged stress, there could be more chances for the system to not be able to properly react, activating the Cushing's mechanism.
What is more interesting about numerical results, is that, in case of simultaneous absence of posterior communicating arteries and presence of VAH, there is a significant reduction of the posterior cerebral blood flow (4,9%) associated with a decrease up to 5.9% of the blood flow in the anterior inferior cerebellar arteries. This finding could lead to hypothesize that there might be a constant total CBF value but with a diminished local CBF in

	q [ml/min]		
Location	baseline	VAH	Δq
Total CBF	661	658	-0.5%
right internal carotid artery	261	277	$+6.1\%$
left internal carotid artery	258	274	$+6.2\%$
basilar artery	142	107	-24.6%
right vertebral artery	71	0.40	-99%
left vertebral artery	71	106	$+49\%$
Posterior CBF	167	166	-0.6%
right posterior cerebral artery (I)	66	48	-27%
left posterior cerebral artery (I)	66	48	-27%
right posterior cerebral artery (II)	78	77	-1.3%
left posterior cerebral artery (II)	78	77	-1.3%
right anterior inferior cerebellar artery	5.1	5.1	-1.2%
left anterior inferior cerebellar artery	5.5	5.4	-1.3%

TABLE 5.7: *Cerebral blood flow values, with a focus on the posterior region, for all the arteries of interest concerning the HTN subject, with or without VAH, and the difference in percentage (Δq) between the two configurations.*

the area of the medulla, hence a localized hypoperfusion in a specific posterior region, triggering the Selfish Brain mechanism.

It is important to underline that the work here presented is the result of a preliminary study on the Selfish Brain Hypothesis of essential hypertension. One limitation is related to the vessel network implemented in the model, which does not include the posterior inferior cerebellar arteries, the anterior spinal artery and the superior cerebellar arteries. These last are necessary for the complete representation of the posterior circulation, while posterior inferior cerebellar arteries and anterior spinal artery, which originate directly from the vertebral arteries, need to be included because supplying the upper and caudal medulla, where the VMC is located. Another aspect regards the concept of perfusion. In this work, the hypoperfusion is solely associated to a reduction of blood flow, which is not totally correct since a limited perfusion could be determined solely by the decrease of oxygen supplied. This feature could be improved adding a global gas transport model to evaluate the oxygen and carbon dioxide transfer from vessels to body organs by convection and diffusion to the model adopted. In this way, cases of brainstem hypoxia (deficiency in the amount of oxygen reaching the tissues) could be individuated and analyzed in relation with high blood pressure levels.

Other triggering factors taken into account by the Selfish Brain Hypothesis, such as inflammation and alterations in the collagen/elastic content of cerebral vessels, were not included in the present study. Future works could be developed analyzing the effects of an augmented blood viscosity and alterations of the Young modulus of cerebral vessels with respect to the variation of perfusion levels, not only concerning geometrical abnormalities. It could also be interesting to evaluate the VAH not only related to a reduction of the lumen, but also to a thickening of the wall. In fact, in the sensitivity analysis here reported, variations of the thickness and the Young modulus, considered together in the product Eh, were already found to be related to a reduction of CBF levels.

Chapter 6

Conclusions

6.1 Overview

The goal of this PhD research was to propose a mathematical model able to predict the behavior of the fluid-structure interaction mechanism that underlies the dynamics of flows in different compliant ducts. Starting from the purely civil engineering sector, with the study of plastic water pipelines, the final application of the proposed tool is linked to the field of medical research, to reproduce the fluid mechanics of blood flow in both arteries and veins. The correct characterization of the interactions occurring between the fluid and the wall, when the latter is deformable, is a fundamental aspect of the proposed method. To do so, various linear viscoelastic models, from the simplest to the more sophisticated, have been applied and extended to permit the obtaining of augmented fluid-structure interaction systems, in which the constitutive equation of the material is directly inserted into the system as partial differential equation. These systems are solved recurring to second-order Finite Volume Methods that take into account the recent evolution in the computational literature of hyperbolic balance laws systems. To validate the models, numerical results have been compared with quasi-exact solutions of idealized time-dependent tests for situations close to reality or reference values obtained with numerical schemes generally adopted in the specific research field investigated. Furthermore, comparisons with experimental data have been considered both for the water pipelines scenario and the blood flow modeling, recurring to ad hoc in-vivo measurements for the latter. Accuracy and efficiency analyses have been performed in different contexts, as well as a sensitivity analysis with regards to the final, more applicative, part of the project.

6.2 Main Findings and Original Contributions

As done throughout this Thesis, the achievements of the presented research can be differentiated in three main parts: the water pipelines modeling, the blood flow modeling and the application study on arterial hypertension.

6.2.1 Water pipelines modeling

The mathematical system for modeling compressible fluids in flexible tubes has been presented with a particular focus on its augmented FSI form. The proposed model has been proved to correctly simulate the mechanical behavior of the viscoelastic material analyzed, using two different constitutive models: the Standard Linear Solid model (three-parameter model) and the more complex generalized Kelvin-Voigt chain (general multi-parameter model). Original extensions of existing techniques for the numerical treatment

of the latter have been introduced for this research project for the first time. Two different models have also been considered for the definition of friction losses: taking into account the unsteady wall shear stress, with a new approach tested for turbulent flows, or simply considering a quasi-steady friction model. A predominance of the damping effects due to viscoelasticity with respect to the one related to the unsteady friction is confirmed in the contexts studied.

Three numerical schemes, the Method of Characteristics, an Explicit path-conservative FVM and a staggered Semi-Implicit FVM have been analyzed with respect to the simulation of hydraulic transients in flexible polymeric tubes and compared in terms of accuracy, robustness and efficiency. All the three models show a good agreement with reference solutions, with the MOC turning out to be the most efficient model among those considered, explaining the usual preference for using this model in literature studies of water hammers. However, the MOC does not result as robust as the other two FVMs when non-standard conditions are taken into account, such as cavitation cases.
Moreover, numerical results do not highlight significant differences if the SLS model or a g-KV chain is chosen to characterize the rheological behavior of the plastic pipe wall. This aspect encourages the adoption of less complex models, yet able to adequately capture the dynamics of the phenomenon, ensuring in the meantime the minimum computational cost, with a reduced number of parameters to be calibrated. The same applies to the friction term, for which it has been confirmed that, for the scenarios investigated, the unsteady wall shear stress can be neglected in favor of a quasi-steady model.

6.2.2 Blood flow modeling

An innovative 1D augmented FSI system has been proposed for the blood flow modeling with regards to the mechanical effects of arterial and venous walls. An easy shift from the simple elastic to the more realistic viscoelastic characterization of the vessel wall is ensured by the straightforward addition of a source term. Recurring to the a-FSI system, in fact, would be mostly advantageous when taking into account the viscoelastic wall behavior of vessels: all the viscosity information would be enclosed within a source term, avoiding the presence of second order derivatives and permitting to work with a purely hyperbolic system of equations.
The chosen IMEX-SSP2 RK scheme has been demonstrated to preserve the expected order of accuracy also when dealing with stiff source terms, confirming its asymptotic-preserving property. The implemented IMEX RK scheme ensures at the same time robustness, given by the usage of an implicit discretization of the stiff terms, and efficiency, being possible to obtain a totally explicit algorithm for the resolution of the system of interest.

The model has been extensively validated with success, showing results in perfect agreement with 1D and 3D benchmark data. The impact of modeling the mechanics of the vessel wall concerning viscoelastic effects and not solely the elastic ones has been pointed out, especially comparing computed pressure waveforms with in-vivo measurements. In this context, the viscoelastic SLS model better describes the complex behavior of a viscoelastic material if compared with the KV model, frequently adopted in the biofluid dynamics literature, still maintaining ease of implementation and usage.

An effective procedure to estimate the FSI parameters of the adopted SLS model has been presented, returning hysteresis curves dissipating energy fractions similar to values evaluated from literature hysteresis loops in the same vessels. Starting from literature

physiological data (for radius, thickness, length and reference celerity of vessels), the proposed procedure permits to obtain all the necessary FSI parameters, without additional specific adjustments.

6.2.3 Application study on arterial hypertension

Some preliminary studies have been conducted concerning representative 55 years old normotensive and hypertensive subjects, to assess the effects of congenital anatomical variations concentrated in the cerebral vasculature: vertebral artery hypoplasia and incomplete posterior Circle of Willis, which have been found to play a possible role in triggering high arterial pressure.
With this aim, the Müller-Toro model, a global multiscale closed-loop blood flow model, has been extended considering changes in the vessels network due to aging and hypertension processes. Results obtained simulating the hypertensive subject have been investigated through a sensitivity analysis to assess correlations between hemodynamic variations and the development of arterial hypertension. This analysis confirmed that the parameter affecting the most changes in pressure levels is the total terminal arteries resistance, which determined a shift in the pressure grade for each 20% of variation.

Simulations, regarding both the NTN and the HTN subject, highlight that VAH do not generally lead to a decreased total arterial CBF thanks to the compensatory capability of the other vessels supplying the brain, especially the controlateral VA. The cerebral circulation network, in fact, has an innate oversizing which guarantees enough resources to the system when small geometrical abnormalities are present. The most interesting aspect concerning numerical results, is that, in case of simultaneous absence of posterior communicating arteries and presence of VAH, there is a significant reduction of almost 5% of the posterior cerebral blood flow associated with a decrease up to almost 6% of the blood flow in the anterior inferior cerebellar arteries. This finding could lead to hypothesize that there might be a constant total CBF value but with a diminished local CBF in the area of the medulla, hence a localized hypoperfusion in a specific posterior region, triggering the Selfish Brain mechanism.

6.3 Future work

One of the main future goals, for a further development of this PhD research project, consists on the extension of the 1D a-FSI systems here presented through the complex and delicate implementation of junctions. A challenging aspect consists in taking into account the viscous component even in the numerical treatment of bifurcations, without neglecting it as generally happens in the existing reference literature, still maintaining the desired order of accuracy of the model. Concerning water pipelines, this would allow the design of more complex networks, increasingly faithful to case studies of real practical interest, especially for design companies and industries. With respect to the blood flow modeling, to include a network of the major arteries and veins of the human cardiovascular system (still maintaining a 0D treatment of secondary vessels) would provide an even more effective tool to substantially support studies of circulatory diseases and broad-spectrum medical applications, allowing to obtain clinical data that would otherwise be accessible only through invasive measurements on patients.
At the same time, the application of the uncertainty quantification theory is desirable for

a quantitative characterization and reduction of uncertainties underlying the parameters involved for the modeling of human hemodynamics.

Other considerations need to be highlighted with respect to the final application study. It is indeed worth to be mentioned that the work concerning the Selfish Brain Hypothesis of essential hypertension is the result of a purely preliminary study. To improve the analysis carried out and the subsequent observations, it would be important to include the posterior inferior cerebellar arteries, the anterior spinal artery and the superior cerebellar arteries in the modeled network, to complete the representation of the posterior circulation. In particular, posterior inferior cerebellar arteries and anterior spinal artery, which originate directly from the vertebral arteries, need to be included because supplying the upper and caudal medulla, where the VMC is located.

Another aspect regards the concept of perfusion. In this work, the hypoperfusion is solely associated to a reduction of blood flow, which is not totally correct since a limited perfusion could be determined by the decrease of oxygen supplied alone. This feature could be improved in further researches adding a global gas transport model to evaluate the oxygen and carbon dioxide transfer from vessels to body organs by convection and diffusion to the model adopted. In this way, cases of brainstem hypoxia (deficiency in the amount of oxygen reaching the tissues) could be individuated and analyzed in relation with high blood pressure levels.

Finally, other triggering factors taken into account by the Selfish Brain Hypothesis, such as inflammation and alterations in the collagen/elastic content of cerebral vessels, were not included in the present study. Future work could be developed analyzing the effects of an augmented blood viscosity and alterations of the Young modulus of cerebral vessels with respect to the variation of perfusion levels, not only concerning geometrical abnormalities. It could also be interesting to evaluate the VAH not only related to a reduction of the lumen, but also to a thickening of the wall.

Appendix A

Explicit formulation of the IMEX-SSP2(3,3,2) method

Analysing each of the $s = 3$ Runge-Kutta steps necessary to apply the chosen IMEX-SSP2(3,3,2) method, the following is obtained:

$$
\begin{aligned}
\boldsymbol{Q}_i^{(1)} &= \boldsymbol{Q}_i^n + \Delta t a_{11} \boldsymbol{S}\left(\boldsymbol{Q}_i^{(1)}\right) \\
\boldsymbol{Q}_i^{(2)} &= \boldsymbol{Q}_i^n - \frac{\Delta t}{\Delta x}\tilde{a}_{21}\left[\left(\boldsymbol{F}_{i+\frac{1}{2}}^{(1)} - \boldsymbol{F}_{i-\frac{1}{2}}^{(1)}\right) + \left(\boldsymbol{D}_{i+\frac{1}{2}}^{(1)} + \boldsymbol{D}_{i-\frac{1}{2}}^{(1)}\right) + \boldsymbol{B}\left(\boldsymbol{Q}_i^{(1)}\right)\Delta \boldsymbol{Q}_i^{(1)}\right] \\
&\quad + \Delta t\left[a_{21}\boldsymbol{S}\left(\boldsymbol{Q}_i^{(1)}\right) + a_{22}\boldsymbol{S}\left(\boldsymbol{Q}_i^{(2)}\right)\right] \\
\boldsymbol{Q}_i^{(3)} &= \boldsymbol{Q}_i^n - \frac{\Delta t}{\Delta x}\Bigg\{\tilde{a}_{31}\left[\left(\boldsymbol{F}_{i+\frac{1}{2}}^{(1)} - \boldsymbol{F}_{i-\frac{1}{2}}^{(1)}\right) + \left(\boldsymbol{D}_{i+\frac{1}{2}}^{(1)} + \boldsymbol{D}_{i-\frac{1}{2}}^{(1)}\right) + \boldsymbol{B}\left(\boldsymbol{Q}_i^{(1)}\right)\Delta \boldsymbol{Q}_i^{(1)}\right] \\
&\quad + \tilde{a}_{32}\left[\left(\boldsymbol{F}_{i+\frac{1}{2}}^{(2)} - \boldsymbol{F}_{i-\frac{1}{2}}^{(2)}\right) + \left(\boldsymbol{D}_{i+\frac{1}{2}}^{(2)} + \boldsymbol{D}_{i-\frac{1}{2}}^{(2)}\right) + \boldsymbol{B}\left(\boldsymbol{Q}_i^{(2)}\right)\Delta \boldsymbol{Q}_i^{(2)}\right]\Bigg\} \\
&\quad + \Delta t\left[a_{31}\boldsymbol{S}\left(\boldsymbol{Q}_i^{(1)}\right) + a_{32}\boldsymbol{S}\left(\boldsymbol{Q}_i^{(2)}\right) + a_{33}\boldsymbol{S}\left(\boldsymbol{Q}_i^{(3)}\right)\right].
\end{aligned}
$$

In particular, analysing the structure of the system, it can be observed that each step can be analytically linearised, avoiding the adoption of a Newton-Raphson method (or similar ones) for the evaluation of the implicit part. Replacing the already explicit contributions of the convective part,

$$
\boldsymbol{EX}^{(1)} = \frac{\Delta t}{\Delta x}\tilde{a}_{21}\left[\left(\boldsymbol{F}_{i+\frac{1}{2}}^{(1)} - \boldsymbol{F}_{i-\frac{1}{2}}^{(1)}\right) + \left(\boldsymbol{D}_{i+\frac{1}{2}}^{(1)} + \boldsymbol{D}_{i-\frac{1}{2}}^{(1)}\right) + \boldsymbol{B}\left(\boldsymbol{Q}_i^{(1)}\right)\Delta \boldsymbol{Q}_i^{(1)}\right]
$$

$$
\begin{aligned}
\boldsymbol{EX}^{(2)} = \frac{\Delta t}{\Delta x}\Bigg\{&\tilde{a}_{31}\left[\left(\boldsymbol{F}_{i+\frac{1}{2}}^{(1)} - \boldsymbol{F}_{i-\frac{1}{2}}^{(1)}\right) + \left(\boldsymbol{D}_{i+\frac{1}{2}}^{(1)} + \boldsymbol{D}_{i-\frac{1}{2}}^{(1)}\right) + \boldsymbol{B}\left(\boldsymbol{Q}_i^{(1)}\right)\Delta \boldsymbol{Q}_i^{(1)}\right] \\
&+ \tilde{a}_{32}\left[\left(\boldsymbol{F}_{i+\frac{1}{2}}^{(2)} - \boldsymbol{F}_{i-\frac{1}{2}}^{(2)}\right) + \left(\boldsymbol{D}_{i+\frac{1}{2}}^{(2)} + \boldsymbol{D}_{i-\frac{1}{2}}^{(2)}\right) + \boldsymbol{B}\left(\boldsymbol{Q}_i^{(2)}\right)\Delta \boldsymbol{Q}_i^{(2)}\right]\Bigg\}
\end{aligned}
$$

the final totally explicit formulation is here presented in details, for each of the 3 Runge-Kutta steps, only for the first three equations of system (4.12):

$$
\begin{aligned}
A_i^{(1)} &= A_i^n \\
(Au)_i^{(1)} &= (Au)_i^n \\
p_i^{(1)} &= \frac{\tau_r}{\tau_r + \Delta t a_{11}} p_i^n + \frac{\Delta t a_{11}}{\tau_r + \Delta t a_{11}} \left[\frac{E_{\infty,i}}{E_{0,i}} \psi_{el}\left(A_i^{(1)}, A_{0,i}, E_{0,i}\right) + p_{ext,i} \right]
\end{aligned}
$$

$$
\begin{aligned}
A_i^{(2)} &= A_i^n - EX_{(A)}^{(1)} \\
(Au)_i^{(2)} &= (Au)_i^n - EX_{(Au)}^{(1)} \\
p_i^{(2)} &= \frac{\tau_r}{\tau_r + \Delta t a_{22}} \left\{ p_i^n - EX_{(p)}^{(1)} + \frac{\Delta t a_{21}}{\tau_r} \left[\frac{E_{\infty,i}}{E_{0,i}} \psi_{el}\left(A_i^{(1)}, A_{0,i}, E_{0,i}\right) - \left(p_i^{(1)} - p_{ext,i}\right) \right] \right\} \\
&\quad + \frac{\Delta t a_{22}}{\tau_r + \Delta t a_{22}} \left[\frac{E_{\infty,i}}{E_{0,i}} \psi_{el}\left(A_i^{(2)}, A_{0,i}, E_{0,i}\right) + p_{ext,i} \right]
\end{aligned}
$$

$$
\begin{aligned}
A_i^{(3)} &= A_i^n - EX_{(A)}^{(2)} \\
(Au)_i^{(3)} &= (Au)_i^n - EX_{(Au)}^{(2)} \\
p_i^{(3)} &= \frac{\tau_r}{\tau_r + \Delta t a_{33}} \left\{ p_i^n - EX_{(p)}^{(2)} + \frac{\Delta t a_{31}}{\tau_r} \left[\frac{E_{\infty,i}}{E_{0,i}} \psi_{el}\left(A_i^{(1)}, A_{0,i}, E_{0,i}\right) - \left(p_i^{(1)} - p_{ext,i}\right) \right] \right. \\
&\quad \left. + \frac{\Delta t a_{32}}{\tau_r} \left[\frac{E_{\infty,i}}{E_{0,i}} \psi_{el}\left(A_i^{(2)}, A_{0,i}, E_{0,i}\right) - \left(p_i^{(2)} - p_{ext,i}\right) \right] \right\} \\
&\quad + \frac{\Delta t a_{33}}{\tau_r + \Delta t a_{33}} \left[\frac{E_{\infty,i}}{E_{0,i}} \psi_{el}\left(A_i^{(3)}, A_{0,i}, E_{0,i}\right) + p_{ext,i} \right]
\end{aligned}
$$

The time update of the variables finally results:

$$
\begin{aligned}
\boldsymbol{Q}_i^{n+1} = \boldsymbol{Q}_i^n - \frac{\Delta t}{\Delta x} \Bigg\{ & \tilde{\omega}_1 \left[\left(\boldsymbol{F}_{i+\frac{1}{2}}^{(1)} - \boldsymbol{F}_{i-\frac{1}{2}}^{(1)} \right) + \left(\boldsymbol{D}_{i+\frac{1}{2}}^{(1)} + \boldsymbol{D}_{i-\frac{1}{2}}^{(1)} \right) + \boldsymbol{B}\left(\boldsymbol{Q}_i^{(1)}\right) \Delta \boldsymbol{Q}_i^{(1)} \right] \\
& + \tilde{\omega}_2 \left[\left(\boldsymbol{F}_{i+\frac{1}{2}}^{(2)} - \boldsymbol{F}_{i-\frac{1}{2}}^{(2)} \right) + \left(\boldsymbol{D}_{i+\frac{1}{2}}^{(2)} + \boldsymbol{D}_{i-\frac{1}{2}}^{(2)} \right) + \boldsymbol{B}\left(\boldsymbol{Q}_i^{(2)}\right) \Delta \boldsymbol{Q}_i^{(2)} \right] \\
& + \tilde{\omega}_3 \left[\left(\boldsymbol{F}_{i+\frac{1}{2}}^{(3)} - \boldsymbol{F}_{i-\frac{1}{2}}^{(3)} \right) + \left(\boldsymbol{D}_{i+\frac{1}{2}}^{(3)} + \boldsymbol{D}_{i-\frac{1}{2}}^{(3)} \right) + \boldsymbol{B}\left(\boldsymbol{Q}_i^{(3)}\right) \Delta \boldsymbol{Q}_i^{(3)} \right] \Bigg\} \\
& + \Delta t \left[\omega_1 \boldsymbol{S}\left(\boldsymbol{Q}_i^{(1)}\right) + \omega_2 \boldsymbol{S}\left(\boldsymbol{Q}_i^{(2)}\right) + \omega_3 \boldsymbol{S}\left(\boldsymbol{Q}_i^{(3)}\right) \right].
\end{aligned}
$$

Appendix B

Algorithm for the estimation of elastic and viscoelastic arterial wall parameters

- Elastic model:
  - Input: ρ, R_0, s_0 and c_0 from literature (Müller and Toro, 2014a; Liang et al., 2009; Alastruey et al., 2012; Xiao, Alastruey, and Figueroa, 2014),
  - E_0 evaluated with Eq. (4.30),
  - K evaluated with Eq. (4.5).
- Viscoelastic model:
  - Input: ρ, R_0, s_0, c_0 and Γ from literature (Müller and Toro, 2014a; Liang et al., 2009; Alastruey et al., 2012; Xiao, Alastruey, and Figueroa, 2014),
  - E_∞ evaluated adapting Eq. (4.30) for the viscoelastic Young modulus:

$$E_\infty = \frac{2R_0\rho c_0^2}{s_0},$$

  - η evaluated with Eq. (4.11),
  - E_0 evaluated inverting Eq. (4.31):

$$E_0 = \frac{E_\infty}{e^{-1.3\cdot 10^{-5}\eta}}$$

  - K evaluated with Eq. (4.5).

Bibliography

Alastruey, J., A. W. Khir, K. S. Matthys, P. Segers, S. J. Sherwin, P. R. Verdonck, K. H. Parker, and J. Peiró (2011). "Pulse wave propagation in a model human arterial network: Assessment of 1-D visco-elastic simulations against in vitro measurements". In: *Journal of Biomechanics* 44.12, pp. 2250–2258.

Alastruey, J., K. H. Parker, J. Peiró, S. M. Byrd, and S. J. Sherwin (2007). "Modelling the circle of Willis to assess the effects of anatomical variations and occlusions on cerebral flows". In: *Journal of Biomechanics* 40.8, pp. 1794–1805.

Alastruey, J., K. H. Parker, J. Peiró, and S. J. Sherwin (2008). "Lumped parameter outflow models for 1-D blood flow simulations: Effect on pulse waves and parameter estimation". In: *Communications in Computational Physics* 4.2, pp. 317–336.

Alastruey, J., K. H. Parker, and S. J. Sherwin (2012). "Arterial pulse wave haemodynamics". In: *Proceedings BHR Group's 11th International Conference on Pressure Surges*, pp. 401–443.

Alastruey, J., T. Passerini, L. Formaggia, and J. Peiró (2012). "Physical determining factors of the arterial pulse waveform: Theoretical analysis and calculation using the 1-D formulation". In: *Journal of Engineering Mathematics* 77.1, pp. 19–37.

Ambrosi, D., A. Quarteroni, and G. Rozza (2012). *Modeling of Physiological Flows*. Springer.

Apollonio, C., D. I. Covas, G. de Marinis, A. Leopardi, and H. Ramos (2014). "Creep functions for transients in HDPE pipes". In: *Urban Water Journal* 11.2, pp. 160–166.

Asmar, R., A. Benetos, G. London, C. Hugue, Y. Weiss, J. Topouchian, B. Laloux, and M. Safar (1995). "Aortic distensibility in normotensive, untreated and treated hypertensive patients". In: *Blood Pressure* 4.1, pp. 48–54.

Avallone, E. A. and T. Baumeister III (1916). *Standard handbook for mechanical engineers*. McGraw-Hill Inc.

Avolio, A., S. Chen, R. Wang, C. Zang, M. Li, and M. O'Rourke (1983). "Effect of aging on changing arterial compliance and left ventricle load in a northern Chinese urban community". In: *Circulation* 68, pp. 50–58.

Battista, C. (2015). "Parameter Estimation of Viscoelastic Wall Models in a One-Dimensional Circulatory Network". PhD thesis. North Carolina State University.

Benetos, A., C. Adamopoulos, J. M. Bureau, M. Temmar, C. Labat, K. Bean, F. Thomas, B. Pannier, R. Asmar, M. Zureik, M. Safar, and L. Guize (2002). "Determinants of accelerated progression of arterial stiffness in normotensive subjects and in treated hypertensive subjects over a 6-year period". In: *Circulation* 105.10, pp. 1202–1207.

Bergant, A., A. R. Simpson, and A. S. Tijsseling (2006). "Water hammer with column separation: A historical review". In: *Journal of Fluids and Structures* 22.2, pp. 135–171.

Bermudez, A. and M. E. Vazquez (1994). "Upwind methods for hyperbolic conservation laws with source terms". In: *Computers & Fluids* 23.8, pp. 1049–1071.

Bertaglia, G., V. Caleffi, and A. Valiani (2020). *Data for: Modeling blood flow in viscoelastic vessels: the 1D augmented fluid-structure interaction system*. http://dx.doi.org/10.17632/zz4zw9kyz7.1. Mendeley Data, v1.

Bessems, D., C. G. Giannopapa, M. C. M. Rutten, and F. N. van de Vosse (2008). "Experimental validation of a time-domain-based wave propagation model of blood flow in viscoelastic vessels". In: *Journal of Biomechanics* 41.2, pp. 284–291.

Bia, D., R. L. Armentano, J. C. Grignola, Y. A. Zócalo, F. F. Ginés, D. Craiem, and J. Levenson (2003). "The vascular smooth muscle of great arteries: Local control site of arterial buffering function?" In: *Revista Espanola de Cardiologia* 56.12, pp. 1202–1209.

Blanco, P. J. and R. A. Feijóo (2013). "A dimensionally-heterogeneous closed-loop model for the cardiovascular system and its applications". In: *Medical Engineering and Physics* 35.5, pp. 652–667.

Blanco, P. J., L. O. Müller, and J. D. Spence (2017). "Blood pressure gradients in cerebral arteries: a clue to pathogenesis of cerebral small vessel disease". In: *Stroke and Vascular Neurology* 2.3, pp. 108–117.

Blanco, P. J., S. M. Watanabe, M. A. R. Passos, P. A. Lemos, and R. A. Feijóo (2015). "An anatomically detailed arterial network model for one-dimensional computational hemodynamics". In: *IEEE Transactions on Biomedical Engineering* 62.2, pp. 736–753.

Boileau, E., P. Nithiarasu, P. J. Blanco, L. O. Müller, F. E. Fossan, L. R. Hellevik, W. P. Donders, W. Huberts, M. Willemet, and J. Alastruey (2015). "A benchmark study of numerical schemes for one-dimensional arterial blood flow modelling". In: *International Journal for Numerical Methods in Biomedical Engineering* e02732, pp. 1–33.

Brugnano, L. and V. Casulli (2008). "Iterative Solution of Piecewise Linear Systems". In: *SIAM Journal on Scientific Computing* 30.1, pp. 463–472.

Brugnano, L. and V. Casulli (2009). "Iterative Solution of Piecewise Linear Systems and Applications to Flows in Porous Media". In: *SIAM Journal on Scientific Computing* 31.3, pp. 1858–1873.

Brunone, B., B. W. Karney, M. Mecarelli, and M. Ferrante (2000). "Velocity Profiles and Unsteady Pipe Friction". In: *Journal of Water Resources Planning and Management* 126.4, pp. 236–244.

Caiazzo, A., G. I. Montecinos, L. O. Müller, E. M. Haacke, and E. F. Toro (2014). "Computational haemodynamics in stenotic internal jugular veins". In: *Journal of Mathematical Biology* 70.4, pp. 745–772.

Caleffi, V. and A. Valiani (2017). "Well balancing of the SWE schemes for moving-water steady flows". In: *Journal of Computational Physics* 342, pp. 85–116.

Carpenter, P. W. and T. J. Pedley (2001). "Flow past Highly Compliant Boundaries and in Collapsible Tubes". In: *Proceedings of the IUTAM Symposium*. Springer.

Casulli, V., M. Dumbser, and E. F. Toro (2012). "Semi-implicit numerical modeling of axially symmetric flows in compliant arterial systems". In: *International Journal for Numerical Methods in Biomedical Engineering* 28.2, pp. 257–272.

Casulli, V. and P. Zanolli (2010). "A Nested Newton-Type Algorithm for Finite Volume Methods Solving Richards' Equation in Mixed Form". In: *SIAM Journal on Scientific Computing* 32.4, pp. 2255–2273.

Casulli, V. and P. Zanolli (2012). "Iterative solutions of mildly nonlinear systems". In: *Journal of Computational and Applied Mathematics* 236.16, pp. 3937 –3947.

Cates, M. J., C. J. Dickinson, E. C. J. Hart, and J. F. R. Paton (2012). "Neurogenic hypertension and elevated vertebrobasilar arterial resistance: Is there a causative link?" In: *Current Hypertension Reports* 14.3, pp. 261–269.

Cates, M. J., P. W. Steed, A. P. L. Abdala, P. D. Langton, and J. F. R. Paton (2011). "Elevated vertebrobasilar artery resistance in neonatal spontaneously hypertensive rats." In: *Journal of applied physiology* 111.1, pp. 149–56.

Cavallini, N., V. Caleffi, and V. Coscia (2008). "Finite volume and WENO scheme in one-dimensional vascular system modelling". In: *Computers and Mathematics with Applications* 56.9, pp. 2382–2397.

Celant, M. (2018). "A global multiscale closed-loop mathematical model of the human circulation applied to the selfish-brain hypothesis of arterial hypertension". PhD thesis. University of Trento.

Chaudhry, M. H. (1979). *Applied Hydraulic Transients*. Springer Verlag.

Chen, Y. Y., A. C. Chao, H. Y. Hsu, C. P. Chung, and H. H. Hu (2010). "Vertebral Artery Hypoplasia is Associated With A Decrease in Net Vertebral Flow Volume". In: *Ultrasound in Medicine and Biology* 36.1, pp. 38–43.

Christensen, R. M. (1982). *Theory of Viscoelasticity*. Academic Press, Inc.

Chuang, Y. M., L. Chan, H. M. Wu, S. P. Lee, and Y. T. Chu (2012). "The clinical relevance of vertebral artery hypoplasia". In: *Acta Neurologica Taiwanica* 21.1, pp. 1–7.

Cipolla, M. J. (2010). *The Cerebral Circulation*. Morgan & Claypool Life Science, pp. 1–59.

Covas, D. I. (2003). "Inverse transient analysis for leak detection and calibration of water pipe systems modelling special dynamic effects". PhD thesis. University of London.

Covas, D. I., I. Stoianov, J. F. Mano, H. Ramos, N. Graham, and C. Maksimovic (2005). "The dynamic effect of pipe-wall viscoelasticity in hydraulic transients. Part II - model development, calibration and verification". In: *Journal of Hydraulic Research* 43.1, pp. 56–70.

Covas, D. I., I. Stoianov, H. Ramos, N. Graham, and C. Maksimovic (2004). "The dynamic effect of pipe-wall viscoelasticity in hydraulic transients. Part I - experimental analysis and creep characterization". In: *Journal of Hydraulic Research* 42.5, pp. 517–532.

Cox, J, K O'Malley, N Atkins, and E O'Brien (1991). "A comparison of the twenty-four-hour blood pressure profile in normotensive and hypertensive subjects." In: *Journal of hypertension. Supplement : official journal of the International Society of Hypertension* 9.1, S3–6.

Cushing, H. (1901). "Concerning a definite regulatory mechanism of the vaso-motor centre which controls blood pressure during cerebral compression". In: *Bull Johns Hopk Hosp*, pp. 290–292.

De Giusti, M., E. Dito, B. Pagliaro, S. Burocchi, F. I. Laurino, G. Tocci, M. Volpe, and S. Rubattu (2012). "A survey on blood pressure levels and hypertension control in a sample of the italian general population". In: *High Blood Pressure and Cardiovascular Prevention* 19.3, pp. 129–135.

Delestre, O. and P.-Y. Lagrée (2013). "A 'well-balanced' finite volume scheme for blood flow simulation". In: *International Journal for Numerical Methods in Fluids* 72.2, pp. 177–205.

Descombes, S. and M. Massot (2004). "Operator splitting for nonlinear reaction-diffusion systems with an entropic structure: singular perturbation and order reduction". In: *Numerische Mathematik* 97, pp. 667–698.

Dickinson, C. J. and A. D. Thomson (1959). "Vertebral and internal carotid arteries in relation to hypertension and cerebrovascular disease". In: *Lancet* 2, pp. 46–48.

Dickinson, C. J. and A. D. Thomson (1960). "A post mortem study of the main cerebral arteries with special reference to their possible role in blood pressure regulation". In: *Clinical Science* 19, pp. 513–538.

Duan, H.-F., M. S. Ghidaoui, P. J. Lee, and Y.-K. Tung (2010). "Unsteady friction and viscoelasticity in pipe fluid transients". In: *Journal of Hydraulic Research* 48.3, pp. 354–362.

Duan, Q. Y., V. K. Gupta, and S. Sorooshian (1993). "Shuffled complex evolution approach for effective and efficient global minimization". In: *Journal of Optimization Theory and Applications* 76.3, pp. 501–521.

Duan, Q. Y., S. Sorooshian, and V. K. Gupta (1992). "Effective and efficient global optimization for conceptual rainfall-runoff models". In: *Water Resources Research* 28.4, pp. 1015–1031.

Duarte, M., M. Massot, and S. Descombes (2011). "Parareal operator splitting techniques for multi-scale reaction waves: numerical analysis and strategies". In: *Mathematical Modelling and Numerical Analysis* 5.45, pp. 825–852.

Dumbser, M., U. Iben, and M. Ioriatti (2015). "An efficient semi-implicit finite volume method for axially symmetric compressible flows in compliant tubes". In: *Applied Numerical Mathematics* 89, pp. 24–44.

Dumbser, M. and E. F. Toro (2011a). "A simple extension of the Osher Riemann solver to non-conservative hyperbolic systems". In: *Journal of Scientific Computing* 48.1-3, pp. 70–88.

Dumbser, M. and E. F. Toro (2011b). "On universal Osher-type schemes for general nonlinear hyperbolic conservation laws". In: *Communications in Computational Physics* 10.3, pp. 635–671.

Evangelista, S., A. Leopardi, R. Pignatelli, and G. de Marinis (2015). "Hydraulic Transients in Viscoelastic Branched Pipelines". In: *Journal of Hydraulic Engineering* 141.8, p. 04015016.

Fambri, F., M. Dumbser, and V. Casulli (2014). "An efficient semi-implicit method for three-dimensional non-hydrostatic flows in compliant arterial vessels". In: *International Journal for Numerical Methods in Biomedical Engineering* 30.11, pp. 1170–1198.

Ferrante, M. and C. Capponi (2017). "Viscoelastic models for the simulation of transients in polymeric pipes". In: *Journal of Hydraulic Research* 55.5, pp. 599–612.

Ferràs, D., P. A. Manso, A. J. Schleiss, and D. I. Covas (2016). "Experimental distinction of damping mechanisms during hydraulic transients in pipe flow". In: *Journal of Fluids and Structures* 66, pp. 424–446.

Formaggia, L., D. Lamponi, and A. Quarteroni (2003). "One-dimensional models for blood flow in arteries". In: *Journal of Engineering Mathematics* 47.3-4, pp. 251–276.

Formaggia, L., A. Quarteroni, and A. Veneziani (2009). *Cardiovascular Mathematics: Modeling and simulation of the circulatory system*. Springer.

Franke, P. and F. Seyler (1983). "Computation of Unsteady Pipe Flow With Respect To Visco-Elastic Material Properties". In: *Journal of Hydraulic Research* 21.5, pp. 345–353.

Franklin, S. S., W. Gustin, N. D. Wong, M. G. Larson, M. A. Weber, W. B. Kannel, and D. Levy (1997). "Hemodynamic Patterns of Age-Related Changes in Blood". In: *Circulation* 96, pp. 308–315.

Fung, Y. C. (1997). *Biomechanics: Circulation*. 2nd. Springer.

Gallardo, J. M., C. Parés, and M. J. Castro (2007). "On a well-balanced high-order finite volume scheme for shallow water equations with topography and dry areas". In: *Journal of Computational Physics* 227.1, pp. 574–601.

Ganau, A., R. B. Devereux, M. J. Roman, G. de Simone, T. G. Pickering, P. S. Saba, P. Vargiu, I. Simongini, and J. H. Laragh (1992). "Patterns of left ventricular hypertrophy and geometric remodeling in essential hypertension". In: *Journal of the American College of Cardiology* 19.7, pp. 1550–1558.

Ghidaoui, M. S., G. S. Mansour, and M. Zhao (2002). "Applicability of Quasisteady and Axisymmetric Turbulence Models in Water Hammer". In: *Journal of Hydraulic Engineering* 128.10, pp. 917–924.

Ghidaoui, M. S., M. Zhao, D. A. McInnis, and D. H. Axworthy (2005). "A Review of Water Hammer Theory and Practice". In: *Applied Mechanics Reviews* 58.1, pp. 49–76.

Ghigo, A. R., X. Wang, R. Armentano, P.-Y. Lagrée, and J.-M. Fullana (2017). "Linear and nonlinear viscoelastic arterial wall models: application on animals". In: *Journal of Biomechanical Engineering* 139, p. 011003.

Giannattasio, C., P. Salvi, F. Valbusa, A. Kearney-Schwartz, A. Capra, M. Amigoni, M. Failla, L. Boffi, F. Madotto, A. Benetos, and G. Mancia (2008). "Simultaneous measurement of beat-to-beat carotid diameter and pressure changes to assess arterial mechanical properties". In: *Hypertension* 52.5, pp. 896–902.

Gill, R. W. (1985). "Measurement of blood flow by ultrasound: Accuracy and sources of error". In: *Ultrasound in Medicine and Biology* 11.4, pp. 625–641.

Gow, B. S. and M. G. Taylor (1968). "Measurement of viscoelastic properties of arteries in the living dog". In: *Circulation research* 23.1, pp. 111–122.

Gurtin, M. and E. Sternberg (1962). "On the Linear Theory of Viscoelasticity". In: *Archive for Rational Mechanics and Analysis* 11, pp. 291–354.

Hart, E. C. J. (2016). "Human hypertension, sympathetic activity and the selfish brain". In: *Experimental Physiology* 101.12, pp. 1451–1462.

Holenstein, R., P. Niederer, and M. Anliker (1980). "A Viscoelastic Model for Use in Predicting Arterial Pulse Waves". In: *Journal of Biomechanical Engineering* 102.4, pp. 318–325.

Hwang, J. Y. (2017). "Doppler ultrasonography of the lower extremity arteries: anatomy and scanning guidelines". In: *Ultrasonography* 36.2, pp. 111–119.

Ioriatti, M., M. Dumbser, and U. Iben (2017). "A comparison of explicit and semi-implicit finite volume schemes for viscous compressible flows in elastic pipes in fast transient regime". In: *ZAMM Zeitschrift fur Angewandte Mathematik und Mechanik* 23, pp. 1–23.

Kagawa, T., I. Lee, A. Kitagawa, and T. Takenaka (1983). "High Speed and Accurate Computing Method of Frequency-Dependent Friction in Laminar Pipe Flow for Characteristics Method". In: *Transactions of the Japan Society of Mechanical Engineers Series B* 49.447, pp. 2638–2644.

Katsanos, A. H., M. Kosmidou, A. P. Kyritsis, and S. Giannopoulos (2013). "Is vertebral artery hypoplasia a predisposing factor for posterior circulation cerebral ischemic events? A comprehensive review". In: *European Neurology* 70.1-2, pp. 78–83.

Kety, S. S. and C. F. Schmidt (1948). "The Nitrous Oxide Method for the Quantitative Determination of Cerebral Blood Flow in Man: Theory, Procedure and Normal Values". In: *The Journal of clinical investigation* 27.4, pp. 476–483.

Kroon, W., W. Huberts, M. Bosboom, and F. Van De Vosse (2012). "A numerical method of reduced complexity for simulating vascular hemodynamics using coupled 0D lumped and 1D wave propagation models". In: *Computational and Mathematical Methods in Medicine* 2012.

Lakes, R. (2009). *Viscoelastic Materials*. Cambridge University Press.

Laurent, S., X Girerd, J. J. Mourad, P Lacolley, L Beck, P Boutouyrie, J. P. Mignot, and M Safar (1994). "Elastic modulus of the radial artery wall material is not increased in patients with essential hypertension". In: *Arteriosclerosis, Thrombosis, and Vascular Biology* 14.7, pp. 1223–1231.

Leguy, C. (2019). *Cardiovascular Computing: Methodologies and Clinical Applications. Chapter 11: Mathematical and Computational Modelling of Blood Pressure and Flow*. Springer, pp. 231–246.

Leibinger, J., M. Dumbser, U. Iben, and I. Wayand (2016). "A path-conservative Osher-type scheme for axially symmetric compressible flows in flexible visco-elastic tubes". In: *Applied Numerical Mathematics* 105.June, pp. 47–63.

Leinan, P. R. (2012). "Biomechanical modeling of fetal veins: The umbilical vein and ductus venosus bifurcation". PhD thesis. Norwegian University of Science and Technology (NTNU), Trondheim, Norway.

LeVeque, R. J. and H. C. Yee (1990). "A Study of Numerical Methods for Hyperbolic Conservation Laws with Stiff Source Terms". In: *Journal of Computational Physics* 86, pp. 187–210.

Liang, F., D. Guan, and J. Alastruey (2018). "Determinant factors for arterial hemodynamics in hypertension: theoretical insights from a computational model-based study". In: *Journal of Biomechanical Engineering* 140.3, p. 031006.

Liang, F., S. Takagi, R. Himeno, and H. Liu (2009). "Biomechanical characterization of ventricular-arterial coupling during aging: A multi-scale model study". In: *Journal of Biomechanics* 42.6, pp. 692–704.

Maksuti, E., N. Westerhof, B. E. Westerhof, M. Broomé, and N. Stergiopulos (2016). "Contribution of the arterial system and the heart to blood pressure during normal aging - A simulation study". In: *PLoS ONE* 11.6, pp. 1–12.

Matthys, K. S., J. Alastruey, J. Peiró, A. W. Khir, P. Segers, P. R. Verdonck, K. H. Parker, and S. J. Sherwin (2007). "Pulse wave propagation in a model human arterial network: Assessment of 1-D numerical simulations against in vitro measurements". In: *Journal of Biomechanics* 40.15, pp. 3476–3486.

McEniery, C. M., Yasmin, I. R. Hall, A. Qasem, I. B. Wilkinson, and J. R. Cockcroft (2005). "Normal vascular aging: Differential effects on wave reflection and aortic pulse wave velocity - The Anglo-Cardiff Collaborative Trial (ACCT)". In: *Journal of the American College of Cardiology* 46.9, pp. 1753–1760.

Meniconi, S., B. Brunone, and M. Ferrante (2012). "Water-hammer pressure waves interaction at cross-section changes in series in viscoelastic pipes". In: *Journal of Fluids and Structures* 33, pp. 44–58.

Meniconi, S., B. Brunone, M. Ferrante, and C. Massari (2014). "Energy dissipation and pressure decay during transients in viscoelastic pipes with an in-line valve". In: *Journal of Fluids and Structures* 45, pp. 235–249.

Milišić, V. and A. Quarteroni (2004). "Analysis of lumped parameter models for blood flow simulations and their relation with 1D models". In: *Mathematical Modelling and Numerical Analysis* 38.4, pp. 613–632.

Mitchell, G. F., H. Parise, E. J. Benjamin, M. G. Larson, M. J. Keyes, J. A. Vita, R. S. Vasan, and D. Levy (2004). "Changes in arterial stiffness and wave reflection with advancing age in healthy men and women: The Framingham Heart Study". In: *Hypertension* 43.6, pp. 1239–1245.

Mitsotakis, D., D. Dutykh, Q. Li, and E. Peach (2019). "On some model equations for pulsatile flow in viscoelastic vessels". In: *Wave motion* 90, pp. 139–151.

Montecinos, G. I., L. O. Müller, and E. F. Toro (2014). "Hyperbolic reformulation of a 1D viscoelastic blood flow model and ADER finite volume schemes". In: *Journal of Computational Physics* 266, pp. 101–123.

Müller, L. O., P. J. Blanco, S. M. Watanabe, and R. A. Feijóo (2016). "A high-order local time stepping finite volume solver for one-dimensional blood flow simulations: application to the ADAN model". In: *International Journal for Numerical Methods in Biomedical Engineering* 32.10.

Müller, L. O., M. Celant, E. F. Toro, P. J. Blanco, G. Bertaglia, V. Caleffi, and A. Valiani (2019). "The Selfish-Brain Hypothesis as possible cause of arterial hypertension: a

modelling study". In: *6th International Conference on Computational & Mathematical Biomedical Engineering*. Sendai City, Japan, pp. 592–595.

Müller, L. O., G. I. Montecinos, and E. F. Toro (2013). "Some issues in modelling venous haemodynamics". In: *Numerical Methods for Hyperbolic Equations: Theory and Applications. An international conference to honour Professor EF Toro*, pp. 347–354.

Müller, L. O. and E. F. Toro (2013). "Well-balanced high-order solver for blood flow in networks of vessels with variable properties". In: *International Journal for Numerical Methods in Biomedical Engineering* 29.12, pp. 1388–1411.

Müller, L. O. and E. F. Toro (2014a). "A global multiscale mathematical model for the human circulation with emphasis on the venous system". In: *International Journal for Numerical Methods in Biomedical Engineering* 30.7, pp. 681–725.

Müller, L. O. and E. F. Toro (2014b). "Enhanced global mathematical model for studying cerebral venous blood flow". In: *Journal of Biomechanics* 47.13, pp. 3361–3372.

Murillo, J., A. Navas-Montilla, and P. García-Navarro (2019). "Formulation of exactly balanced solvers for blood flow in elastic vessels and their application to collapsed states". In: *Computers & Fluids* 186, pp. 74–98.

Mynard, J. P. and J. J. Smolich (2015). "One-Dimensional Haemodynamic Modeling and Wave Dynamics in the Entire Adult Circulation". In: *Annals of Biomedical Engineering* 43.6, pp. 1443–1460.

NCD Risk Factor Collaboration (NCD-RisC) (2017). "Worldwide trends in blood pressure from 1975 to 2015: a pooled analysis of 1479 population-based measurement studies with 19·1 million participants". In: *The Lancet* 389.10064, pp. 37–55.

Nichols, W. W., M. F. O'Rourke, A. P. Avolio, T. Yaginuma, J. P. Murgo, C. J. Pepine, and C. R. Conti (1985). "Effects of age on ventricular-vascular coupling". In: *The American Journal of Cardiology* 55.9, pp. 1179–1184.

Nichols, W. W., M. F. O'Rourke, and C. Vlachlopoulos (2011). *McDonald's Blood Flow in Arteries*. 6th. Hodder Arnold.

O'Rourke, M. F. and J. Hashimoto (2007). "Mechanical Factors in Arterial Aging. A Clinical Perspective". In: *Journal of the American College of Cardiology* 50.1, pp. 1–13.

Palatini, P., E. Casiglia, J. Gasowski, J. Głuszek, P. Jankowski, K. Narkiewicz, F. Saladini, K. Stolarz-Skrzypek, V. Tikhonoff, L. Van Bortel, W. Wojciechowska, and K. Kawecka-Jaszcz (2011). "Arterial stiffness, central hemodynamics, and cardiovascular risk in hypertension". In: *Vascular Health and Risk Management* 7.1, pp. 725–739.

Parés, C. (2006). "Numerical methods for nonconservative hyperbolic systems: a theoretical framework". In: *SIAM Journal on Numerical Analysis* 44.1, pp. 300–321.

Pareschi, L. and G. Russo (2005). "Implicit-explicit Runge-Kutta schemes and applications to hyperbolic systems with relaxation". In: *Journal of Scientific Computing* 25.1, pp. 129–155.

Park, J. H., J. M. Kim, and J. K. Roh (2007). "Hypoplastic vertebral artery: Frequency and associations with ischaemic stroke territory". In: *Journal of Neurology, Neurosurgery and Psychiatry* 78.9, pp. 954–958.

Park, M. Y., S. E. Jung, J. Y. Byun, J. H. Kim, and G. E. Joo (2012). "Effect of beam-flow angle on velocity measurements in modern doppler ultrasound systems". In: *American Journal of Roentgenology* 198.5, pp. 1139–1143.

Paton, J. F. R., C. J. Dickinson, and G. Mitchell (2009). "Harvey Cushing and the regulation of blood pressure in giraffe, rat and man: Introducing 'Cushing's mechanism'". In: *Experimental Physiology* 94.1, pp. 11–17.

Pedley, T. J. (1980). *The Fluid Mechanics of Large Blood Vessels*. Cambridge Monographs on Mechanics. Cambridge University Press.

Pedley, T. J. (1983). "Waves in physiological flows". In: *Eighth Australasian Fluid Mechanics Conference*, K8.1–8.

Pezzinga, G. (2014). "Evaluation of Time Evolution of Mechanical Parameters of Polymeric Pipes by Unsteady Flow Runs". In: *Journal of Hydraulic Engineering* 140.12, p. 04014057.

Pignatelli, R. (2014). "Pipe-wall viscoelasticity during water hammer in branched pipelines. Experimental tests and numerical analysis". PhD thesis. Università degli Studi di Cassino e del Lazio Meridionale.

Quarteroni, A. and L. Formaggia (2004). "Mathematical Modelling and Numerical Simulation of the Cardiovascular System". In: *Handbook of Numerical Analysis* 12.03, pp. 3–127.

Quarteroni, A., A. Manzoni, and C. Vergara (2017). "The cardiovascular system: Mathematical modelling, numerical algorithms and clinical applications". In: *Acta Numerica* 26, pp. 365–590.

Raghu, R., I. E. Vignon-Clementel, C. A. Figueroa, and C. A. Taylor (2011). "Comparative Study of Viscoelastic Arterial Wall Models in Nonlinear One-Dimensional Finite Element Simulations of Blood Flow". In: *Journal of Biomechanical Engineering* 133.8, p. 081003.

Ramos, H., D. I. Covas, A. Borga, and D. Loureiro (2004). "Surge damping analysis in pipe systems: modelling and experiments". In: *Journal of Hydraulic Research* 42.4, pp. 413–425.

Reymond, P., F. Merenda, F. Perren, D. Rufenacht, N. Stergiopulos, and D. Ru (2009). "Validation of a one-dimensional model of the systemic arterial tree". In: *AJP: Heart and Circulatory Physiology* 297.1, H208–H222.

Roache, P. J. (2002). "Code Verification by the Method of Manufactured Solutions". In: *Journal of Fluids Engineering* 124.3, pp. 4–10.

Rogers, W. J., Y. L. Hu, D. Coast, D. A. Vido, C. M. Kramer, R. E. Pyeritz, and N. Reichek (2001). "Age-associated changes in regional aortic pulse wave velocity". In: *Journal of the American College of Cardiology* 38.4, pp. 1123–1129.

Salvi, P. (2012). *Pulse Waves: How vascular hemodynamics affects blood pressure*. Springer Verlag.

Salvi, P., G. Lio, C. Labat, E. Ricci, B. Pannier, and A. Benetos (2004). "Validation of a new non-invasive portable tonometer for determining arterial pressure wave and pulse wave velocity". In: *Journal of Hypertension* 22.12, pp. 2285–2293.

Scuteri, A., C. H. Morrell, M. Orrù, J. B. Strait, K. V. Tarasov, L. A. P. Ferreli, F. Loi, M. G. Pilia, A. Delitala, H. Spurgeon, S. S. Najjar, M. Alghatrif, and E. G. Lakatta (2014). "Longitudinal perspective on the conundrum of central arterial stiffness, blood pressure, and aging". In: *Hypertension* 64.6, pp. 1219–1227.

Seck, A., M. Fuamba, and R. Kahawita (2017). "Finite-Volume Solutions to the Water-Hammer Equations in Conservation Form Incorporating Dynamic Friction Using the Godunov Scheme". In: *Journal of Hydraulic Engineering* 143.9, p. 04017029.

Shamloo, H., R. Norooz, and M. Mousavifard (2015). "A review of one-dimensional unsteady friction models for transient pipe flow". In: *Cumhuriyet Science Journal* 36.3, pp. 2278–2288.

Shapiro, A. H. (1977). "Steady Flow in Collapsible Tubes". In: *Journal of Biomechanical Engineering* 99, pp. 126–147.

Shaw, M. T. and W. J. MacKnight (2005). *Introduction to Polymer Viscoelasticity*. 3rd. John Wiley & Sons, Inc.

Sherwin, S. J., L. Formaggia, J. Peiró, and V. Franke (2003). "Computational modelling of 1D blood flow with variable mechanical properties and its application to the simulation of wave propagation in the human arterial system". In: *International Journal for Numerical Methods in Fluids* 43, pp. 673–700.

Soares, A. K., D. I. Covas, and L. F. Reis (2008). "Analysis of PVC Pipe-Wall Viscoelasticity during Water Hammer". In: *Journal of Hydraulic Engineering* 134.9, pp. 1389–1394.

Spiller, C., E. F. Toro, M. E. Vázquez-Cendón, and C. Contarino (2017). "On the exact solution of the Riemann problem for blood flow in human veins, including collapse". In: *Applied Mathematics and Computation* 303, pp. 178–189.

Spronck, B., T. Delhaas, J. Op'T Roodt, and K. D. Reesink (2016). "Carotid Artery Applanation Tonometry Does Not Cause Significant Baroreceptor Activation". In: *American Journal of Hypertension* 29.3, pp. 299–302.

Strait, J. and E. Lakatta (2012). "Aging-associated cardiovascular changes and their relationship to heart failure". In: *Heart failure clinics* 8.1, pp. 143–164.

Strang, G. (1968). "On the Construction and Comparison of Difference Schemes". In: *SIAM Journal on Numerical Analysis* 5.3, pp. 506–517.

Sugawara, J. and H. Tanaka (2015). "Brachial-Ankle Pulse Wave Velocity: Myths, Misconceptions, and Realities". In: *Pulse* 3.2, pp. 106–113.

Tarumi, T. and R. Zhang (2018). "Cerebral blood flow in normal aging adults: cardiovascular determinants, clinical implications, and aerobic fitness". In: *Journal of Neurochemistry* 144.5, pp. 595–608.

Tavelli, M., M. Dumbser, and V. Casulli (Dec. 2013). "High Resolution Methods for Scalar Transport Problems in Compliant Systems of Arteries". In: *Appl. Numer. Math.* 74, pp. 62–82.

Thierfelder, K. M., A. B. Baumann, W. H. Sommer, M. Armbruster, C. Opherk, H. Janssen, M. F. Reiser, A. Straube, and L. Von Baumgarten (2014). "Vertebral artery hypoplasia: Frequency and effect on cerebellar blood flow characteristics". In: *Stroke* 45.5, pp. 1363–1368.

Toro, E. F. (2009). *Riemann Solvers and Numerical Methods for Fluid Dynamics*. 3rd. Springer Verlag.

Toro, E. F. (2016). "Brain venous haemodynamics, neurological diseases and mathematical modelling. A review". In: *Applied Mathematics and Computation* 272, pp. 542–579.

Toro, E. F. and A. Siviglia (2013). "Flow in collapsible tubes with discontinuous mechanical properties: Mathematical model and exact Solutions". In: *Communications in Computational Physics* 13.2, pp. 361–385.

Tortora, G. J. and B. Derrickson (2013). *Principles of anatomy and phisiology*. 12th. John Wiley & Sons, Inc.

Townsend, R. R., I. B. Wilkinson, E. L. Schiffrin, A. P. Avolio, J. A. Chirinos, J. R. Cockcroft, K. S. Heffernan, E. G. Lakatta, C. M. McEniery, G. F. Mitchell, S. S. Najjar, W. W. Nichols, E. M. Urbina, and T. Weber (2015). *Recommendations for Improving and Standardizing Vascular Research on Arterial Stiffness: A Scientific Statement from the American Heart Association*. Vol. 66. 3, pp. 698–722.

Trikha, A. K. (1975). "An Efficient Method for Simulating Frequency-Dependent Friction in Transient Liquid Flow". In: *Journal of Fluids Engineering* 97.1, pp. 97–105.

Urbanowicz, K. and Z. Zarzycki (2012). "New efficient approximation of weighting functions for simulations of unsteady friction losses in liquid pipe flow". In: *Journal of Theoretical and Applied Mechanics* 50.2, pp. 487–508.

Valdez-Jasso, D., M. A. Haider, H. T. Banks, D. B. Santana, Y. Z. German, R. L. Armentano, and M. S. Olufsen (2009). "Analysis of Viscoelastic Wall Properties in Ovine Arteries". In: *IEEE Transactions on Biomedical Engineering* 56.2, pp. 210–219.

Vardy, A. E. and J. M. Brown (1995). "Transient, turbulent, smooth pipe friction". In: *Journal of Hydraulic Research* 33.4, pp. 435–456.

Vardy, A. E. and J. M. Brown (2003). "Transient Turbulent Friction in Smooth Pipe Flows". In: *Journal of Sound and Vibration* 259.5, pp. 1011–1036.

Waki, H., M. E. R. Bhuiyan, S. S. Gouraud, M. Takagishi, A. Hatada, A. Kohsaka, J. F. R. Paton, and M. Maeda (2011). "Acute reductions in blood flow restricted to the dorsomedial medulla induce a pressor response in rats". In: *Journal of Hypertension* 29.8, pp. 1536–1545.

Wang, X., J.-M. Fullana, and P.-Y. Lagrée (2014). "Verification and comparison of four numerical schemes for a 1D viscoelastic blood flow model". In: *Computer Methods in Biomechanics and Biomedical Engineering* 23.16, pp. 37–41.

Wang, Z. and N. C. Chesler (2012). "Role of collagen content and cross-linking in large pulmonary arterial stiffening after chronic hypoxia". In: *Biomechanics and Modeling in Mechanobiology* 11.1-2, pp. 279–289.

Wang, Z., M. J. Golob, and N. C. Chesler (2016). *Viscoelastic and Viscoplastic Materials. Chapter 7: Viscoelastic Properties of Cardiovascular Tissues*. InTech, pp. 141–163.

Warnert, E. A. H., J. C. L. Rodrigues, A. E. Burchell, S. Neumann, L. E. K. Ratcliffe, N. E. Manghat, A. D. Harris, Z. Adams, A. K. Nightingale, R. G. Wise, J. F. R. Paton, and E. C. J. Hart (2016). "Is High Blood Pressure Self-Protection for the Brain?" In: *Circulation Research* 119.12, e140–e151.

Watanabe, S. M., P. J. Blanco, and R. A. Feijóo (2013). "Mathematical Model of Blood Flow in an Anatomically Detailed Arterial Network of the Arm". In: *ESAIM: Mathematical Modelling and Numerical Analysis* 47.4, pp. 961–985.

Westerhof, N. and A. Noordergraaf (1970). "Arterial viscoelasticity: A generalized model". In: *Journal of Biomechanics* 3.3, pp. 357–379.

Westerhof, N., N. Stergiopulos, M. I. M. Noble, and B. E. Westerhof (2019). *Snapshots of Hemodynamics: An Aid for Clinical Research and Graduate Education*. 3rd. Springer.

Willemet, M., S. Vennin, and J. Alastruey (2016). "Computational assessment of hemodynamics-based diagnostic tools using a database of virtual subjects: Application to three case studies". In: *Journal of Biomechanics* 49.16, pp. 3908–3914.

Williams, B., G. Mancia, W. Spiering, E. A. Rosei, M. Azizi, M Burnier, D. L. Clement, A. Coca, G. de Simone, A. Dominiczak, T. Kahan, F. Mahfoud, J. Redon, L. Ruilope, A. Zanchetti, M. Kerins, S. E. Kjeldsen, R. Kreutz, S. Laurent, G. Y. H. Lip, R. McManus, K. Narkiewicz, F. Ruschitzka, R. E. Schmieder, E. Shlyakhto, C. Tsioufis, V. Aboyans,

and I. Desormais (2018). “2018 ESC/ESH Guidelines for the management of arterial hypertension”. In: *Journal of Hypertension* 36, pp. 1953–2041.

Womersley, J. R. (1957). “Oscillatory flow in arteries: the constrained elastic tube as a model of arterial flow and pulse transmission.” In: *Physics in medicine and biology* 2.2, pp. 178–187.

Wylie, E. and V. Streeter (1978). *Fluid Transients*. McGraw-Hill Inc.

Xiao, N., J. Alastruey, and C. A. Figueroa (2014). “A systematic comparison between 1-D and 3-D hemodynamics in compliant arterial models”. In: *International Journal for Numerical Methods in Biomedical Engineering* 30.2, pp. 204–231.

Zielke, W. (1968). “Frequency-dependent friction in transient pipe flow”. In: *Journal of Basic Engineering* 90, pp. 109–115.